Department für Frauengesundheit Tübingen
Forschungsinstitut für Frauengesundheit

Development of Non-Invasive Technologies for Investigating Cardiac Tissue in a Novel Heart-on-Chip Platform

Thesis submitted as requirement to fulfill the degree ,,Doctor of Philosophy" in *Experimental Medicine* (PhD)

at the
Faculty of Medicine
Eberhard Karls Universität
Tübingen

presented by

Moruzzi, Alessia

2024

Dean: Professor Dr. B. Pichler

1st reviewer: Professor Dr. P. M. Loskill

2nd reviewer: Professor Dr. R. Lukowski

Date of oral examination: 09.10.2024

Contents

List of Tables and Figures 4

List of abbreviations 6

1 Introduction and state of the art 9

1.1 Cardiac models 13

1.1.1 Heart anatomy and cellular composition 13

1.1.2 Cardiomyocyte development and current cell sources used for cardiac models 16

1.1.3 Current cardiac models and applications 17

1.2 Readouts: challenges and opportunities in OoC 21

1.2.1 Structural readouts 21

1.2.2 Functional readouts 23

1.2.3 Metabolic readouts 24

1.3 Engineered skeletal muscle tissues 28

1.3.1 Skeletal muscle physiology 28

1.3.2 Current approaches for generation of skeletal muscle models 30

2 Materials and Methods 33

2.1 Cell culture 33

2.1.1 hiPSC culture 33

2.1.2 Cardiomyocytes differentiation and Lactate purification 33

2.1.3 Cardiac fibroblasts differentiation protocols 34

2.1.4 PhDF culture 35

2.1.5 haCFv culture 36

2.1.6 Skeletal muscle cells culture 36

2.2 Spheroids formation 37

2.3 Microfluidic systems fabrication 37

2.3.1 Centrifugal HoC 38

2.3.2 Spheroflow HoC 38

2.4 Skeletal muscle fibre in 3D mould 40

2.5 Chip injection and culture 41

2.5.1 Centrifugal HoC loading 41

2.5.2 Spheroflow HoC loading 42

2.5.3 Chip culture 42

2.6 On-chip experimental procedures 43
2.6.1 Electrical Stimulation 44
2.6.2 O_2 sensor readout 44
2.6.3 Drug injection automation 44
2.7 Staining and imaging 45
2.7.1 Flow cytometry 45
2.7.2 Immunocytochemistry 46
2.7.3 Live/Dead staining 48
2.7.4 Raman imaging 48
2.8 Effluent assays 48
2.8.1 LDH-Glo 48
2.8.2 MTS 49
2.8.3 Glucose QuantiChrom 49
2.8.4 Lactate-Glo 50
2.8.5 Drug retention analysis by HPLC-UV 50
2.9 ImageJ analyses 51
2.10 OpenHeartWare analyses 51
2.11 Statistical analysis 51
3 Results 53
3.1 Differentiation and characterization of cardiomyocytes and cardiac fibroblasts 53
3.1.1 hiPSC maintenance and cardiomyocytes differentiation 53
3.1.2 Differentiation of cardiac fibroblasts 57
3.1.3 Media optimization for co-culture of cardiomyocytes and fibroblasts 61
3.1.4 Cardiac spheroid formation 63
3.2 Cardiac tissue formation in HoC systems 66
3.2.1 Spheroids and hydrogel integration within the Centrifugal HoC platform 66
3.2.2 Establishment of the Spheroflow HoC platform 71
3.2.3 Cardiac tissue formation and characterization within the Spheroflow HoC 76
3.3 Readouts 83
3.3.1 Establishment of O_2 sensors readouts 83
3.3.2 On-chip mitochondrial respiration assay 86
3.3.3 Drug response – Optical and O_2 sensors readouts 88
3.3.4 Effluent Analysis 90

3.3.5 Raman Spectroscopy 93
3.4 Skeletal muscle-on-chip 101
4 Discussion 107
4.1 Validation of cell types used in this study 107
4.2 HoC platforms and tissue validation 110
4.3 Non-invasive monitoring of cardiac metabolic changes under external stimuli 114
4.4 Skeletal muscle tissue establishment 120
5 Outlook and Perspectives 122
6 Summary 125
7 Appendix 128
8 Bibliography 131
9 Declaration of own contribution 160
10 Publications 161
11 Acknowledgement 162

List of Tables and Figures

Table 2.1.1 Cardiomyocyte selective medium composition 34
Table 2.1.2 Cardiac fibroblasts basal medium composition.....35
Table 2.1.3 Media composition for myocytes expansion and fusion into myotubules. 37
Table 2.7.1 Antibodies and respective dilutions used for flowcytometry analyses. 46
Table 2.7.2 Antibodies and dyes with respective dilutions used for 2D staining procedures. 47
Figure 1.1.1 Heart anatomy and cellular composition. 15
Figure 1.1.2 Phenotype differences between adult and hiPSC-CMs. 17
Figure 1.2.1 Optical sensors schematic. 26
Figure 3.1.1 hiPSC culture under chemically defined culture conditions. 54
Figure 3.1.2 Cardiomyocyte differentiation, GM25256 hiPSC-line. 55
Figure 3.1.3 Cardiomyocytes purity characterization. 56
Figure 3.1.4 Cardiac fibroblasts differentiation protocol 1. 58
Figure 3.1.5 *Cardiac fibroblasts differentiation protocol 2.* 60
Figure 3.1.6 Assessment of media compatibility of cardiomyocyte medium with fibroblast types 61
Figure 3.1.7 Assessment of co-culture medium compositions on haCFv. 62
Figure 3.1.8 Assessment of co-culture media compositions on hiPSC-CM. 63
Figure 3.1.9 Cardiac aggregation concept and performance. 65
Figure 3.2.1 Centrifugal HoC design 67
Figure 3.2.2 Representative pictures of Centrifugal HoC chambers. 68
Figure 3.2.3 Representative images of a Centrifugal HoC chamber loaded with spheroids and hydrogel. 69
Figure 3.2.4 Representative images of the Centrifugal HoC chamber loaded with spheroids and hydrogel at day 3. 70
Figure 3.2.5 Representative images of the Centrifugal HoC chamber loaded with spheroids and hydrogel at day 6. 71
Figure 3.2.6 Concept of the Spheroflow HoC.....72
Figure 3.2.7 Design of the Spheroflow HoC. 73
Figure 3.2.8 Resin compatibility testing.....74
Figure 3.2.9 Drug absorption during perfusion by Spheroflow platforms made out of different materials. 76
Figure 3.2.10 Spheroflow HoC loading and tissue formation. 77
Figure 3.2.11 Spheroflow HoC tissue characterization 78
Figure 3.2.12 Electrical stimulation set up.....79
Figure 3.2.13 Beating analysis of electrically stimulated tissues 80
Figure 3.2.14 Tissue viability after prolonged continuous pacing. 81
Figure 3.2.15 Tissue functionality at day 5 and day 14 after prolonged continuous pacing. 82
Figure 3.3.1 Assessment of O_2 sensors stability under experimental conditions 84
Figure 3.3.2 O_2 levels recording by integrated optical sensors 85
Figure 3.3.3 Recording of O_2 partial pressures (hPa) of 2 tissues over 8 days. 86

Figure 3.3.4 On-chip mitochondrial respiration assay. 88
Figure 3.3.5 Functional response to Verapamil and Isoproterenol drugs. 89
Figure 3.3.6 Consumption of O_2 in cardiac tissues treated with 10 μM of Verapamil or 100 nM Isoproterenol. 90
Figure 3.3.7 Analysis of glucose consumption in chip effluent. 91
Figure 3.3.8 Analysis of lactate secretion in chip effluent. 93
Figure 3.3.9 TCA results of Raman imaging of fixed sample of fibroblasts in Spheroflow HoC 94
Figure 3.3.10 Raman spectra detected in Spheroflow HoC tissue. 95
Figure 3.3.11 Raman Imaging in fixed Spheroflow HoC fibroblasts tissue sample on the Z-axis. 96
Figure 3.3.12 Raman imaging of a cardiac tissue at day 5 in the Spheroflow HoC. 97
Figure 3.3.13 PCA of the Raman proteins spectrum. 99
Figure 3.3.14 PCA of the Raman lipids spectrum. 101
Figure 3.4.1 Myotubule formation and functionality in 2D culture. 102
Figure 3.4.2 Myobundle formation in 3D. 103
Figure 3.4.3 Generation of the skeletal muscle tissue into the Spheroflow chip. 104
Figure 3.4.4 Tissue formation and functionality in hydrogels. 105
Figure 3.4.5 Tissue viability and myotubules structure. 106

Supplementary Table 1 Compatibility of different materials to clearing solutions. 128

Supplementary Figure 1 Automated injection set up. 129
Supplementary Figure 2 Perfusion set ups. 130
Supplementary Figure 3 HPLC analysis of pipet tip plasticware absorbance of Verapamil and Isoproterenol. 130

List of abbreviations

2D two-dimensional

3D three-dimensional

ADME absorption, distribution, metabolism, and excretion

APTES (3-Aminopropyl)triethoxysilane

ATP Adenosine tri-phosphate

bFGF Basic fibroblast growth factor

CF cardiac fibroblast

CM cardiomyocyte

Col1A1 Collagen type I alpha 1

CPC cardiac progenitor cell

cTnT cardiac Troponin-T

Cx43 Connexin-43

DAPI 4',6-Diamidino-2-phenylindole dihydrochloride

DDR2 Discoidin domain-containing receptor 2

DI de-ionized

DMSO Dimethyl sulfoxide

EC endothelial cell

ECAR extracellular acidification rate

ECM extracellular matrix

EHT engineered heart tissue

EPC epicardial progenitor cell

FA fatty acid

FCS foetal calf serum

GLUT Glucose transporter

haCFv primary human adult cardiac fibroblasts ventricular

hESC human embryonic stem cell

hiPSC human induced pluripotent stem cell

HoC Heart-on-Chip

HPLC High-performance liquid chromatography

IGF-1 insulin-like growth factor-1

IPA isopropyl alcohol

LDH Lactate dehydrogenase

LOD Limit of detection

LOQ Limit of quantification

LSM laser scanning microscope

MEA multi electrode array

MHT microphysiological heart tissues

MPS microphysiological systems

NAD+/NADH Nicotinamide adenine dinucleotide

NADP+/NADPH Nicotinamide adenine dinucleotide phosphate

OCR oxygen consumption rate

OHW OpenHeartWare

OoC Organ-on-Chip

PBS phosphate-buffered saline

PC polycarbonate

PCA Principal component analysis

PDMS polydimethylsiloxane

PET polyethylene terephthalate

phDF primary human dermal fibroblasts

PMMA polymethylmethacrylate

RH relative humidity

rhVTN-N Vitronectin Recombinant Human Protein, Truncated

RI Rock Inhibitor

RT room temperature

SD standard deviation

SEM standard error of the mean

SERCA Sarco-Endoplasmic Reticulum Calcium ATPase

SLA stereolithography

TCA True component analysis

TPE thermoplastic elastomer

UV ultraviolet

ZO1 Zonula occludens-1

1 Introduction and state of the art

The use of animals in scientific research is a highly debated topic among both the public and scientific community. However, in biomedical research, animal models are still essential, especially at the preclinical stages of drug development. Preclinical studies currently still rely on *in vitro* and *in vivo* experiments to determine efficacy, safety, and potential dosages of drug candidates (pharmacokinetics and pharmacodynamics) before clinical testing in humans (Shegokar, 2020).

While standard two-dimensional (**2D**) cellular models allow for high-throughput experimentation and can provide a human genetic background, they present several limitations ranging from cell sources to culture conditions. The most common cell sources are immortalised cell lines, primary cells, and stem cell-derived cells. While primary cells may offer a close approximation of native functions and responses, they are not widely available for certain cell types, for example cardiomyocytes and neurons. Because they may also have a limited life span in culture, and present high biological variability due to patient-to-patient variability, immortalised cell lines may be used instead. However, immortalised cell lines often feature altered cellular functions and are not representative of normal cells (Gordon et al., 2013; White et al., 2004; Yang et al., 2012). Over the years, human induced pluripotent stem cells (**hiPSCs**) revealed a great potential for generating terminally differentiated cell types as well as offering the chance to generate personalized models (Matsa et al., 2016; Ye et al., 2018); still, they exhibit immature phenotypes compared to the respective adult primary cells (Birket & Mummery, 2015; M. C. Ribeiro et al., 2015). In terms of culture conditions, standard cell culture models used for drug screening are typically single cell type monolayers on hard-plastic surfaces, providing only a limited reproduction of native morphology and cellular organization and lacking proper cell-cell contacts as well as cell-matrix interaction (Wikswo, 2014). Cell culture media and supplements are, moreover, usually designed to maximize the growth of specific cell types and often contain nutrient concentrations far higher than the physiological level. For example, most cell culture media contain glucose levels ≥ 10 mM (equivalent to a diabetic condition), which is significantly higher than the 5.5 mM in physiological conditions *in vivo* (Koobotse et al., 2020). Another important aspect of static culture condition is the progressive reduction of nutrients and accumulation of waste metabolites, followed by media replacement which causes sudden fluctuation in the cellular microenvironment, by replenishing the nutrients but also disrupting the autocrine and paracrine cellular signalling (Vis et al., 2020).

Animal models are used as the golden standard to bypass the limitations of *in vitro* models. They are physiologically complex and allow the studying of long-term and systemic effects of drug candidates on the whole organism, such as overall absorption, distribution, metabolism, and excretion (**ADME**) (Yang et al., 2012). Nevertheless, their different physiology and genetic background can yield misleading results. For example, different animals have very different gene expression of ion channels, which limit the predictability of ion channel targeted drugs in humans, bearing different IC_{50} and EC_{50} in different species (Beeton, 2018).

Bringing one drug to the market nowadays costs an average of 2 billion US$ and takes 10-18 years, of which the preclinical stage only takes about 5-21 million US$, and 1-4 years to be completed, depending on the drug archetype (Shegokar, 2020). In the end, however, only less than 10% of candidates in the clinical phase reach the final stage (Dowden & Munro, 2019). The effort to find better alternatives to animal models not only stems from the need to achieve a more efficient drug development process but also in response to the ethical concerns that animal experimentation entails. Between 2014 and 2016, approximately 10 million experimental procedures involving animals were conducted annually in Europe (Taylor, 2019), despite the existence of the 3R principles (*Refine, Reduce, Replace),* formulated by William Russell and Rex Burch in 1959 (Russell & Burch, 1959).

In the context of the 3R principle “Replace”, complex alternative tissue models, such as microphysiological systems (**MPS**), are developed to closely replicate the three-dimensional (**3D**) environment of human organs, including the specific cell types, extracellular matrix (**ECM**) and perfusion. In this thesis, I distinguished microphysiological heart tissues (**MHT**) in three categories: organoids, engineered heart tissues (**EHTs**), and Organ-on-Chips (**OoCs**), as defined in Arslan, Moruzzi, Novacka *et al*. 2022. (Arslan et al., 2022). To summarize, organoids (or microtissues) are self-organized cellular aggregates, while in EHTs, 3D distribution and organization of cells relies on the use of biomaterials. Lastly, OoC systems strive to faithfully replicate human physiology by incorporating diverse cell types within a customized microenvironment. These systems not only aim to mimic the specific cellular organization of the target organ but also simulate a circulatory-like system by integrating media perfusion. The devices are usually comprised of two compartments, a tissue layer where the target tissue is hosted and a media layer where media perfusion occurs. A porous membrane, located between the tissue and the media layers, acts as an endothelial-like barrier, allowing diffusion of nutrients and waste metabolites while protecting the tissue from shear stress during media perfusion.

Going beyond conventional cell culture platforms, OoCs facilitate the application of biophysical stimuli (Thompson et al., 2020). Whereas tailored approaches for the application of biomechanical cues in 2D culture involve the placement of cells onto matrices with varying stiffness, OoC platforms offer the ability to incorporate dynamic modulation of stretching and/or compression, as well as the application of shear forces and electrical actuation. For instance, LaBarge et al. demonstrated gene expression changes in hiPSC-derived cardiomyocytes (**hiPSC-CMs**) towards a more mature phenotype after exposure to cyclic, uniaxial stretch and electrical stimulation (LaBarge et al., 2019). While Silvani *et al.*, showed how shear-stress induces changes in morphology and cell-cell contacts in endothelial cells (Silvani et al., 2021). Application of stimuli can be coupled with sensing capabilities, such as integrated electrodes (i.e., multi electrode arrays - **MEAs**) to measure action potentials (Maoz et al., 2017) or cantilevers to detect forces applied by the tissues (Agarwal et al., 2013; Feric et al., 2019). Other sensors offer the possibility to detect molecules present in the extracellular environment such as oxygen, pH, or metabolites (Fuchs et al., 2021; Shin et al., 2017). Additionally, OoCs can be designed to connect several organs to study systemic response to stimuli (i.e., drug compounds) (Loskill et al., 2015; Shroff et al., 2022).

Recently, Ronaldson-Bouchard *et al.* developed a 4-organ system (heart, liver, bone, and skin) perfused within the same recirculating vascular flow (Ronaldson-Bouchard et al., 2022). They proved that all the organs could retain functionality over 4 weeks of culture and could reproduce the pharmacokinetic and pharmacodynamic profiles of doxorubicin in humans. Ultimately, OoCs hold the potential to enhance the translatability between in-vitro results and clinical trials, potentially *reducing* or completely *replacing* the need for animal testing (Ma et al., 2021).

Accurately predicting the effects of drugs on the human heart is of utmost importance in preclinical drug development, not only to predict the ability to regulate cardiac function to treat heart conditions (i.e., heart failure and arrhythmias) but also to assess the cardiotoxicity of drugs designed for treatment of other diseases. Models of the human heart play a crucial role in drug testing studies, particularly due to cardiotoxicity being a leading cause of drug withdrawal in advanced clinical trials (Onakpoya et al., 2016). However, existing strategies have significant limitations, as they often fail to detect cardiotoxic drugs or mistakenly flag potentially life-saving therapies as toxic. In response to these challenges, Heart-on-Chip (**HoC**) systems have been developed to create aligned cardiac muscle fibres within a perfused microfluidic device (Ellis et al., 2017; Marsano et al., 2016; Mathur et al., 2016; Vivas et al., 2022).

These HoC models have made significant strides in replicating the structural organization and mechanical cues of the heart, and often incorporate both mechanical and electrical stimulation approaches. However, the effects of such applied stimuli cannot be assumed to be uniform across the tissue, a fact that is often overlooked. Despite being claimed to be suitable for drug screening purposes, the retention of drugs (absorption and adsorption) by the materials used in the platforms is not addressed in these studies. *In situ* tissue analysis primarily rely on capturing brightfield videos to assess beating kinetics, detecting tissue exerted forces, and measuring action potentials, but they lack integrated sensing capabilities for metabolites and small molecules (i.e., O_2, lactate, glucose, cytokines).

This thesis presents an innovative HoC platform specifically designed for robust 3D tissue generation of contractile tissues. Two different cell injection approaches were employed to create both cardiac and skeletal muscle tissues. To achieve formation of 3D cardiac tissue with high density, spheroids were loaded into the chip. For the formation of skeletal muscle fibres, a mixture of single cells and hydrogel was injected, resulting in the formation of myotubules over a 10-day culture period. Both tissues exhibited structural organization equivalent to their respective organs and displayed full functionality within 14 days of culture. In addition to cultivation, the tissues were characterized by brightfield video microscopy for analysis of beating kinetics, and immunostaining to verify tissue morphology. With a specific focus on cardiac tissues, the goal was to establish non-invasive measurements that could be applied to investigate different biological questions. Integration of electrodes into the developed HoC allowed for successful electrical stimulation of both cardiac and skeletal muscle tissues. Furthermore, oxygen sensors were integrated to enable real-time measurement of tissue consumption during applied stimulation. Moreover, to enhance the versatility of the platform, an automated drug injection and readout procedure was implemented. This enabled not only potential drug screening but also the performance of

seahorse experiments within the chip itself, eliminating the need for external machines or modifications to the chip design to accommodate the use of an analyser.

The thesis is structured into four chapters: *Chapter 1,* “State of the Art”, covers cardiac models (organoids, EHTs and HoC) advancement and limitations, readouts opportunities but also challenges that the HoC platforms offers and a brief overview of current limitations in skeletal muscle tissues generation for diabetes research. In *Chapter 2,* “Material and Methods”, all the methodologies developed for platform establishment and investigation of tissues within the HoC platforms are explained. While in *Chapter 3,* “Results”, the characterization of differentiated cardiac cell types and cardiac tissue models within HoC platforms are presented and the application of novel non-invasive techniques for investigation of tissue metabolism is also explored. Furthermore, the integration of other contractile tissue models within the platform is demonstrated as proof of concept. In *Chapter 4*, “Discussion”, the results are compared to current literature and an overview of the platform’s novel features as well as its limitations is offered. The thesis concludes with *Chapter 5,* “Outlook and Perspectives”, which builds on the conclusions drawn in Chapter 4. This section explores potential enhancements to the model and provides an outlook on the platform's future applications.

1.1 Cardiac models

1.1.1 Heart anatomy and cellular composition

The heart holds a central function within the human body; by pumping blood throughout the vascular network, it resupplies all organs with oxygenated blood, maintaining the homeostasis of the whole biological system. In mammals, the heart consists of four chambers (two atria and two ventricles) surrounded by the heart walls and is connected to the vascular network by valves that regulate the flow of the blood between the different cavities. Blood circulation is orchestrated via the electrical conduction system between heart cavities which leads to their sequential contractions or “beating” (Moorman & Christoffels, 2003).

To function properly, the heart depends on the interplay between distinct cardiac cell types organized in the different parts of the heart (**Fig. 1.1.1 A**).

Despite constituting only 20-30% of the total cell count in the human heart, cardiomyocytes (**CMs**), are the main cellular components of the myocardium (Rubart & Field, 2006). During development, they originate from cardiac progenitor cells (**CPC**) and mature in different specialized CMs under the guidance of specific growth factors such as WNT, BMP and TGF-β (Moorman & Christoffels, 2003; Wiesinger et al., 2022; Xin et al., 2013).

Atrial and ventricular CMs are chamber specific CMs responsible for muscle contraction. Pacemaker cells and Purkinje fibres form the mammalian cardiac conduction system, with the pacemaker cells located in the sinoatrial node and the Purkinje fibres spreading from the sinoatrial node to the ventricular sub-endocardium (Xin et al., 2013). These populations of CMs, possess distinct morphology and electrophysiology properties and their disfunction plays major roles in several cardiac disorders such as arrhythmias, channelopathies and cardiomyopathies.

Endothelial cells (**ECs**), constitute the endocardium, capillaries, and coronary vessels and, depending on their specific location, display diverse characteristics in terms of morphology, function, and genetic composition (Aird, 2012). These metabolically active cells regulate the vasomotor tone, angiogenesis, immunity, and blood vessel permeability. Moreover, cardiac-specific ECs supply oxygen and fatty acids (**FA**) to CMs and, through EC-CM crosstalk, influence CMs metabolism, maturation, and function (Brutsaert, 2003; Narmoneva et al., 2004).

Cardiac fibroblasts (**CFs**) represent a significant portion of the heart's cellular composition. During embryonic development, the primary population of CFs originates from the epicardium (Tallquist & Molkentin, 2017). CFs contribute to maintaining the ECM and myocardial integrity, particularly in cases of cardiac cell death (Dostal et al., 2015). Their interconnection with other cardiac cells, especially CMs, plays a crucial role in cardiac development and disease progression (Furtado et al., 2016).

A minor population of cardiac cells include cardiac resident macrophages, which are located in the atrioventricular node and are involved in the electrical conduction from the atria to the ventricles. Studies show that these specialized cells can interact with CMs regulating their

electrical activity by increasing the excitability and decreasing the refractory period (Harari et al., 2017; Hulsmans et al., 2017) in addition to modulating the inflammatory response (Bajpai et al., 2018). Another small percentage of cardiac cells comprises the intrinsic cardiac nervous system, which is mainly located in the cardiac ganglia (Ardell & Armour, 2016), and connects the heart to the brain. The intrinsic cardiac nervous system is composed of sensory, motor, and interconnecting neurons that contribute to heart rate, contractility, conduction, and blood flow regulation (Zipes et al., 2017). While some studies have suggested potential roles for cardiac resident macrophages (Dutta & Nahrendorf, 2015) and the intrinsic cardiac nervous system (Wake & Brack, 2016) in cardiac pathophysiology, their precise involvement requires further investigation. Notably, these cell types have yet to be integrated into 3D cardiac models *in vitro*.

Nevertheless, all of these cell types contribute to structural, biochemical, mechanical, and electrical properties of the functional heart, and communicate amongst themselves through cell-cell contacts and endocrine, paracrine and autocrine signals (Tirziu et al., 2010).

Most *in vitro* 3D models aim to recapitulate the structural organization of the heart cell walls and specifically, the myocardium; therefore, they only focus on three main cell types: CMs (ventricular and atrial), CFs, ECs and their ECM.

Within the myocardium (**Fig. 1.1.1 B**), CMs exhibit a branched morphology and are tightly connected to each other by gap junction and intercalated discs, forming uniaxially aligned myocardial fibres. This structure allows for a faster propagation of the electrical signal in 3D and results in a coordinated contraction of the muscle, while the surrounding ECM provides support to the repetitive tissue contraction and relaxation and hosts resident CFs and capillaries (Ausoni & Sartore, 2009; Godier-Furnémont et al., 2011).

The ECM is mainly secreted by the CFs, and it is predominantly composed of fibrillar collagens (I and III), which constitute mainly the interstitial matrix. These, together with the basement membrane components (non-fibrillar collagens IV and VI, fibronectin and hyaluronic acids) contribute to cell adhesion, geometry, and force transmission (Rienks et al., 2014). Moreover, during development, aging, and as a consequence of cardiac trauma, the cardiac ECM goes through major remodelling and changes in its component ratios (Silva et al., 2021); both changes are important in terms of *in vitro* modelling of developmental processes and diseases. Another important aspect of various cardiac ECM proteins (Collagen I and IV, laminin, and fibronectin) is their ability to engage integrins, which have a crucial role in cell adhesion, ion channel regulation and mechano-transduction in CMs (Israeli-Rosenberg et al., 2014).

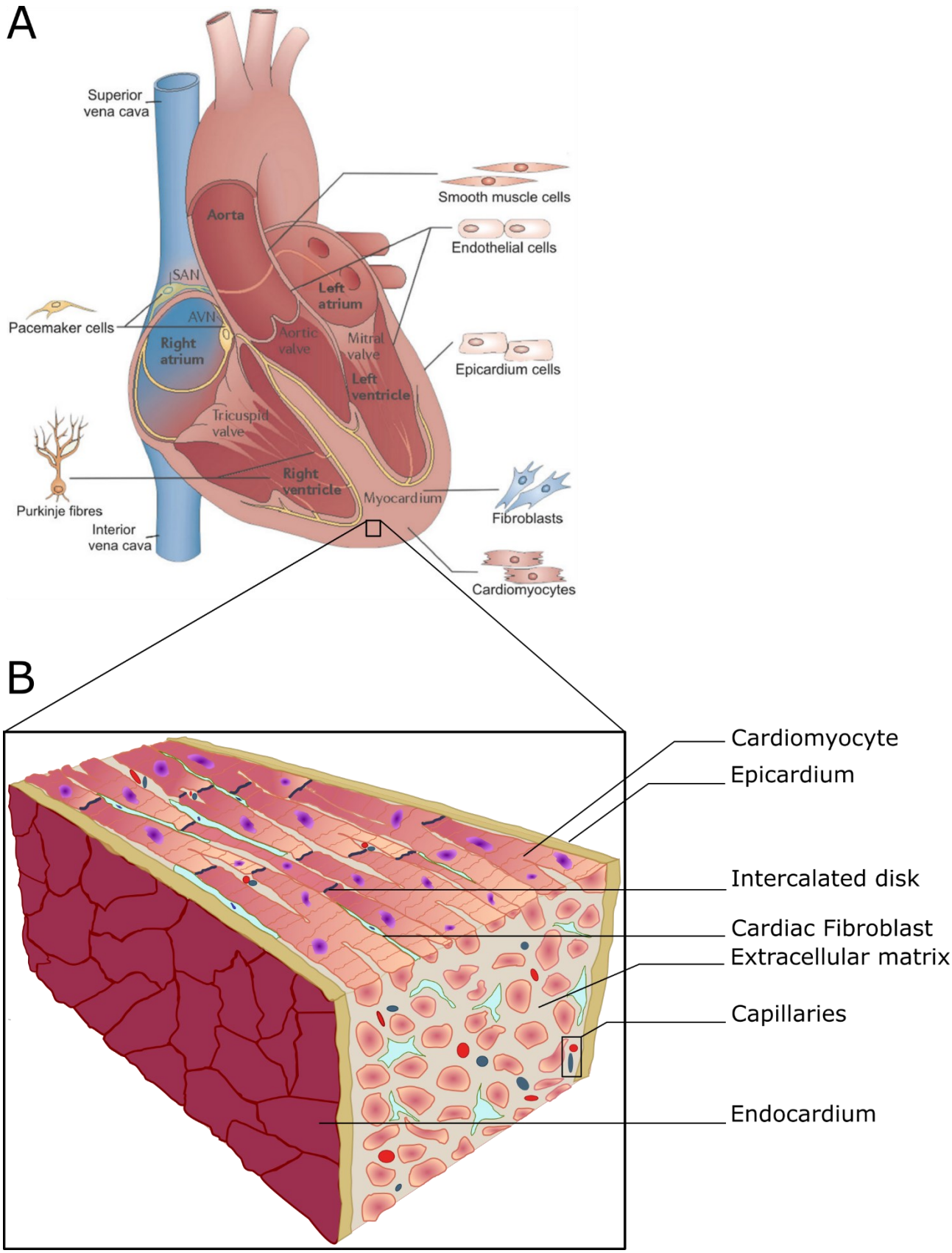

Figure 1.1.1 *Heart anatomy and cellular composition.* ***(A)*** *Illustration of the cardiac cell types and their location within the heart anatomy. Adapted from* Y. S. Zhang et al., 2015. ***(B)*** *Schematic of the myocardium cellular composition and organization.*

1.1.2 Cardiomyocyte development and current cell sources used for cardiac models

Although patient-specific human adult primary CMs would be an optimal cell source for disease modelling and drug screening, the limited access to human cardiac tissue for isolation and the inability to expand CMs in culture due to terminal differentiation pose significant challenges.

While human immortalized cell lines are also available (Davidson et al., 2005), a recent study compared similarities of the immortalized cell line, AC16, to hiPSC-CMs and primary adult CMs and revealed that AC16 presents a significantly different expression profile of cardiac genes compared to both primary CMs and hiPSC-CMs, with a non-functional contractile machinery and response to hypertrophic or ischemic stimuli (Onódi et al., 2022). Therefore, the scientific community mostly disregards their use as cardiac models in favour of hiPSC-CMs.

Even though, advances in the stem cell field now offer possibilities for large scale generation of different cardiac cell types (Giacomelli et al., 2020; Wiesinger et al., 2022), a major issue still, is that hiPSC-CMs resemble foetal CMs more than adult ones (**Fig. 1.1.2**) with respect to their morphology, contractility, electrophysiology, and gene expression (Birket & Mummery, 2015; M. C. Ribeiro et al., 2015; Vučković et al., 2022).

Adult CMs are elongated and exhibit increased cytoskeletal organization. Their sarcomeres are uniaxially organized into myofibrils and they exhibit increased expression of MYH7 compared to the foetal isoform MYH6 (Y. Guo & Pu, 2020). They possess a higher mitochondria content, with mitochondria aligned along the myofibrils. Adult CMs are also often binucleated and display robust T-tubules, with an increased expression of L-type Ca^{2+} channels and Sarco-Endoplasmic Reticulum Calcium ATPase (**SERCA**), allowing for a more efficient signal transduction for contraction. Their higher expression of Connexin-43 and N-cadherin (gap junction proteins) and their localization at the cellular extremities allows for the formation of intercalated disks for cell-cell contacts. Additionally, compared to foetal CMs they switch their main source of energy from glycolysis to FA (metabolic switch) (Breckenridge et al., 2013; Lopaschuk & Jaswal, 2010). Foetal CMs, on the other hand, are smaller and rounder, do not possess the highly specialized subcellular organization of both cytoskeletal and membrane proteins and still rely mainly on glucose and lactate, as their main metabolic process is still glycolysis.

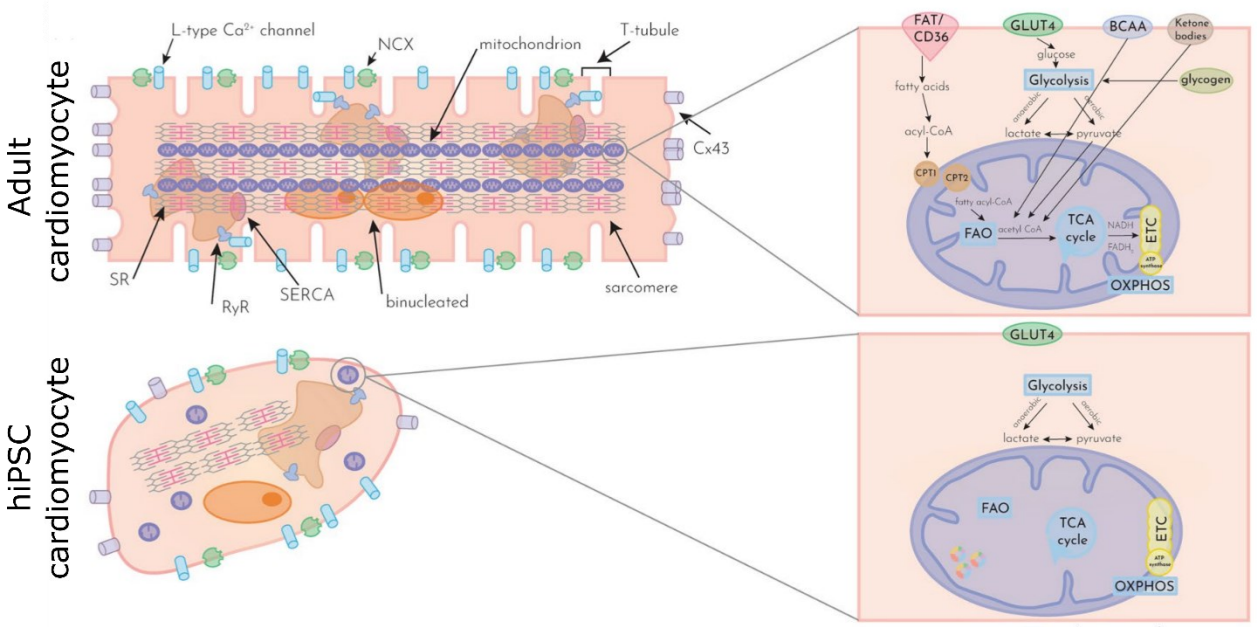

Figure 1.1.2 *Phenotype differences between adult and hiPSC-CMs adapted from* Vučković et al., 2022*. Binucleated adult CMs show organization of membrane proteins, such as L-type Ca^{2+} and NCX channels in the T-tubules and the Connexin-43 (**Cx43**) at the CM extremities (intercalated disks). Mitochondria are adjacent to the uniaxially aligned sarcomeres. Their metabolism consists of both glycolysis and FA oxidation. hiPSC-CMs are mononucleated and exhibit unorganized membrane proteins distribution with no defined T-tubules or intercalated disks. The contraction apparatus does not exhibit structural organization and has low mitochondrial content. Their metabolism relies solely on glycolysis.*

Like CMs, CFs have also been shown to go through such phenotypic changes during development (Jonsson et al., 2016). The heart ECM changes as well with aging and becomes stiffer over time going from 0.2 kPa at the embryonic stage to 10-20 kPa in the adult heart (Gaetani et al., 2020; Huyer et al., 2015).

From developmental studies, it became clear that multiple environmental cues, such as mechanical and electrical stimuli, ECM interactions, and interactions with non-CMs drive the gradual maturation of CMs. Therefore, with the aim to study disease and drug responses, microphysiological tissue engineering approaches have been developed to provide these cues to patient derived hiPSCs with the aim of achieving models that closely mimic specific aspects of the native heart tissue.

1.1.3 Current cardiac models and applications

Generation of spheroids/organoids was one of the first approaches to reproduce the myocardium physiology and consisted of mixing pre-differentiated CMs, CFs and cardiac ECs into 3D self-organized aggregates. These beating aggregates can be formed entirely scaffold-free as CFs produce their own matrix, which consists mainly of collagen I and fibronectin (Campostrini et al., 2021; Y. Li et al., 2017; J. Zhang et al., 2019). These models are mainly used to study early heart development and investigate how co-culture of CMs

with non-myocyte cell types can drive tissue maturation. Giacomelli at al., showed that spheroids made from hiPSC-derived CMs, CFs and ECs, exhibit improved sarcomeric structures with T-tubules, enhanced contractility, and mitochondrial respiration and were electro-physiologically more mature. CMs and CFs coupling occurred through Connexin-43 (Cx43) gap junctions and increased intracellular cyclic adenosine monophosphate (cAMP). Additionally, their organoids could reproduce arrhythmogenic cardiomyopathy through the inclusion of patient derived CFs within the organoids (Giacomelli et al., 2020). Another group mimicked myocardial infraction by embedding spheroids in hydrogel and applying an oxygen gradient (Richards et al., 2020). Toxicity testing on cardiac organoids revealed that these models can distinguish between negative and positive inotropic compounds as opposed to previous studies on hiPSC-CM monolayer cultures (Pointon et al., 2015) and this confirms an improved risk assessment of compounds (Pointon et al., 2017). Later, the same model was used to test the structural cardiotoxicity of FDA approved compounds (Archer et al., 2018). Morphology assessments of drug-exposed spheroid models showed changes in their structural integrity and cellular viability.

These organoids are robust and highly scalable but lack the cellular organization of the myocardium and its interspersed ECM. Even though they integrate ECs, they do not develop perfused vasculature and tend to develop an anoxic core.

To mimic the cellular organization of the native myocardium, EHTs rely on geometric confinement and the addition of extracellular scaffolds. Seeding CMs in frames of different shapes revealed that a rectangular frame induces CMs to exhibit a more rod-shape morphology, uniaxial calcium flow and improved sarcomeric organization compared to square frames or monolayer culture in multi-well plates (Huebsch et al., 2016; A. J. S. Ribeiro et al., 2015). Recently, Gepstein's group generated a ring-shaped EHT with atrial-ventricular polarization (Goldfracht et al., 2020). The same results can be achieved by seeding a cell hydrogel mixture between two posts, leading elongated cardiac fibres to form between them while they serve as anchor points (Feric et al., 2019; Mills et al., 2018). In the Biowire II platform, the 3D engineered cardiac tissue was generated between two flexible wires, that allowed for non-invasive measurement of contractility frequency and force (Feric et al., 2019; Zhao et al., 2020); long term pacing training was showed to improve contractile properties and the tissue proved to be responsive to a large set of inotropic compounds, validating this model for early drug discovery and development testing. In a later study, the same platform was employed to model human myocardial fibrosis and to aid in the screening of antifibrotic drugs (E. Y. Wang et al., 2019). Additionally, the platform offers the possibility to generate atrial-ventricular polarized tissues (Zhao et al., 2020). Similar concepts were also present in the *Heart-Dyno* platform (Mills et al., 2019), which, upon testing of pro-proliferative drug compounds, revealed detrimental effects of many hit compounds compared to 2D assays, as well as in the "*Flexible Thin-Film*" system from Lind et al., which integrated contraction sensors within the flexible leaflet (Lind et al., 2017).

Physiological mechanical stretching is important for heart development (Hong et al., 2023); therefore, several versions of stretching apparatus have been built to provide EHTs with tuneable mechanical loads (Fink et al., 2000; Zimmermann et al., 2002). The simplest approach to study the effect of stretching on an EHT consists of applying a static acute

uniaxial stretch. Yang and colleagues studied the impact of longitudinal and lateral stretching on the elongation and re-organization of sarcomeres through single live-cell microscopy (H. Yang et al., 2016). The effects of different cyclic afterload regimes on EHTs suspended between flexible posts were studied by Leonard and colleagues, showing that the degree of mechanical load correlates positively with the twitch force and negatively with the twitch velocity. At a lower afterload, sarcomere length, contractility, calcium kinetics, and the expression profile (of MYH6, MYH7, MYL2, ACTC1 and TNNI3) indicated a more mature phenotype. However, tissues under excessive afterload displayed upregulation of pathological hypertrophy/fibrosis markers, while contractility and sarcomere length remained constant (Leonard et al., 2018). Therefore, mechanical stretching can also be used to trigger pathological conditions for disease modelling (Garoffolo & Pesce, 2019; Lindsey et al., 2014).

All of these strategies for EHT formation can be combined with pacing training (Eng et al., 2016; Radisic et al., 2004) or metabolic strategies (Ulmer & Eschenhagen, 2020), allowing the development of highly complex experimental set ups in which several cues work together to improve tissue functions. EHTs do not rely on the self-organization of cells within a round MHT and provide ECM cues which are not present in the MHTs. However, they are still cultured in static conditions and require high cell density for tissue generation. Moreover, the unequal distribution of different cell types within the tissue may limit comparative analysis between replicates and the lack of perfusable vessel-like structures limit the diffusion of oxygen and nutrients to the inner parts of the tissue.

Introducing microfluidic channels to these *in vitro* tissue models may help in eliminating these drawbacks as they provide continuous flow which provides a consistent delivery of oxygen and nutrient to the tissue core. Another important aspect is that microfluidic systems are easier to automate and scale-up.

Some of these EHT models were later converted to OoC, specifically HoC devices. Agarwal *et al.* placed a cover plate connected to perfusion tubes on top of the previously designed "*Flexible Thin-Film*" system (Agarwal et al., 2013). However, in this set up there was no porous barrier between the medium and the cells, thus exposing the CMs to sheer stress. In the HoC of Mathur *et al.*, the cardiac microtissue was protected from sheer stress via a barrier between the media-channels and the microtissue-chamber featuring micropores which allowed for passive nutrient exchange (Mathur et al., 2015). As similar chip design was also used to integrate organoids within a hydrogel, interspersed with ECs, in an attempt to induce angiogenesis and vascularisation of the cardiac organoids (Arslan et al., 2023). In this case not only were the media channels of the HoC platform perfused, but the micro-vessels generated by the ECs within the hydrogels also showed a bidirectional flow of media, which was induced by the cardiac organoids' contraction. As the HoC design developed, micropores were replaced by a porous membrane between upper media-channel and lower tissue chamber (O. Schneider et al., 2019). This perfusion approach not only allows for continuous supply of nutrients and avoids excessive accumulation of waste metabolites, which maintaines the system homeostasis, but also decreases the handling of the culture for media "change". However, OoC culture requires proficient handling of perfusion tubings and electrical cables for sensor-based readouts/connection to stimulation

devices (i.e., pacers) and syringe pumps, thus increasing the complexity of experimental set ups.

Various commercial platforms have sought to simplify chip handling by eliminating the need for tubes and syringe pumps for perfusion purposes. One notable example is the Emulate chip, which can be conveniently placed into their custom-made perfusion system, Human Emulation System (Jang et al., 2019). Similarly, the Mimetas' OrganoPlate utilizes a rocking motion to induce flow between reservoirs located at the ends of the media channel, eliminating the requirement for external pumps (Trietsch et al., 2013).

HoCs are suitable for parallelization, reducing batch effects that arise from technical and biological variations. Therefore, implementation of technical replicates in a single OoC improves the readout robustness (Ren et al., 2020; O. Schneider et al., 2019). Schneider et al. tailored their HoC to hold eight independent-tissue chambers that can be loaded at once via centrifugation (O. Schneider et al., 2019). For one time-use OoC platforms, scalable production of such systems can be achieved by microfabrication techniques such as lithography or laser cutting (Ahadian et al., 2018). However, another approach consists usage of autoclavable materials that allows the chip to be re-used (Agarwal et al., 2013).

Additionally, HoCs as EHTs, can integrate stimulation approaches as well as on-line readouts (see readouts in section 1.2). For example, Marsano *et al.* introduced an underlying flexible polymer layer to apply defined medium pressure in the chip, mimicking the pulsating flow of the bloodstream and the mechanical environment of native myocardium (Marsano et al., 2016). Similarly, Kong and colleagues, applied cyclic stress to CFs cultured within a OoC platform to study cardiac fibrotic remodelling. They proved that the magnitude of the strain could either maintain or attenuate the myofibroblast activation (physiological strains of 5-10%) or promote the phenotype transition toward myofibroblasts (pathological strains 15-20%) (Kong et al., 2019). Electrical stimulation is another relevant stimulus to be applied in HoC devices; Ren *et al*., integrated a comb-patterned gold electrode array for electrical stimulation (Ren et al., 2020).

In the last years, HoC have been also connected to relevant tissues, with the most common being liver (Oleaga, Riu, et al., 2018; Yin et al., 2021), in order to study systemic effects. In Skardal and colleagues' study, they connected three tissues, heart, liver, and lung to a common fluid routing breadboard that allows the connection of the systems in a *"plug-and-play*" fashion. Additionally, they integrated in-line sensors for detection of albumin, α-glutathione-S-transferase (α-GST), and creatine kinase. They first connected the liver upstream of the cardiac tissue and monitored changes in secreted metabolites after epinephrine and propranolol injections compared to when only the heart was connected. Then the lung-on-chip was added downstream of the heart and the response to Bleomycin, an anticancer drug that causes fibrosis and inflammation, was monitored. When perfused with the drug, the three-organ system showed loss of functionality of the cardiac tissue; conversely, when only the HoC was treated with the drug, no effect was observed (Skardal et al., 2017). In a later study by Gordana's group, the heart was connected to liver, bone, and skin tissues (Ronaldson-Bouchard et al., 2022). The system consists of a linear sequence of trans-well on top of the same vasculature barrier, so that they share the

perfusion system. The interconnected tissues maintained molecular, structural, and functional characteristics over four weeks of culture. When challenged with doxorubicin, they replicated the pharmacokinetic and pharmacodynamic profiles and miRNA responses observed in humans better than the isolated tissue cultures or fluidically interconnected tissues that lacked endothelial barriers.

All of these features demonstrate the relevance that OoC may have in preclinical drug screening, however the differences between different designs have created challenges for standardization, leading to independent implementation of readout technologies and making it difficult to compare results from different platforms with each other.

Standardization involves various aspects, including materials, devices, interfaces, assays, and data formatting. Despite several commercial OoC devices being available by companies such as Hesperos, Aim Biotech, InSphero, Nortis, Mimetas and Emulate, they differ in size and format, lacking easy interoperability. To address this, various OoC platforms that offers standardization, automation, and high throughput OoC culture and assays, are being developed, such as the Translational OoC Platform (TOP), Predict96, and the smart multi-well plate (SMWP) project called "Moore4Medical" (Mastrangeli & van den Eijnden-van Raaij, 2021).

1.2 Readouts: challenges and opportunities in OoC

The readouts implemented for 3D microphysiological models can be categorized in structural, functional, and metabolic readouts.

1.2.1 Structural readouts

Transmitted light microscopy techniques, such as bright-field or phase contrast microscopy, provides information about microtissue shape and size without the need for additional labelling or fixation. Therefore, the techniques enable live and non-disruptive imaging on-chip. Bright-field microscopy has been used for imaging microtissue shape changes over time. Compaction of cells was observed on platforms with anchoring points (Zhao et al., 2020) or in dog-bone-shaped tissue chambers (O. Schneider et al., 2019). Likewise, faster aggregation of cells in MHTs was observed when CFs were included in the culture (T. Y. Kim et al., 2018). However, transmitted light microscopy techniques lack specificity in identifying cells and their structures.

Structural readouts mainly rely on immunofluorescent microscopic imaging. This allows for the investigation of, for instance, sarcomere organization, formation of gap junction and matrix deposition in both healthy and disease phenotypes. In OoCs, structural analysis is preferable done directly on chip since removing the microtissue is not always feasible and most likely affects its structure. Therefore, OoC platforms should be compatible with microscope holders and, in the best case, fit an SBS-plate (Trietsch et al., 2013) or a glass slide format (Rennert et al., 2015; Ronaldson-Bouchard et al., 2022). Additionally, chip materials may introduce additional distance between the tissue and the objective lenses, or not being made of optically clear materials, impairing the achievable resolution. Ordinarily, in fully polydimethylsiloxane (**PDMS**) based microfluidic devices, the thickness of the layer

in which the channels are engraved is at least three millimetres (Chen et al., 2017; Mu et al., 2015), while the working distance of high magnification objectives is less than 0.3 mm. Several approaches have been developed to shorten the path between tissue and objective, such as PDMS exclusion molding (Rogal et al., 2020) or the use of polymethylmethacrylate (**PMMA**), polycarbonate (**PC**) and thermoplastic elastomer (**TPE**) as substrates (Busek et al., 2021; S. Schneider et al., 2021; Trinh et al., 2020).

3D tissues often require imaging, not only in the XY plane but also on the Z axis, which allows for internal structure analysis. Confocal fluorescence microscopy has thus become a popular tool for imaging 3D samples, primarily because of its ability to remove signal from outside the image focal plane. Optical sectioning, imaging in the Z axis, and 3D-reconstruction have provided views into the inner microtissue structure and the distribution of cells within the microtissue. Localization of ECs (Giacomelli, Bellin, Orlova, et al., 2017) and the distribution of CFs (Lee et al., 2019) has, for example, been assessed via imaging in spheroids. Atrial and ventricular CMs were distinguished in the chamber specific Biowire II (Zhao et al., 2019). Furthermore, confocal microscopy allows imaging of sub-cellular components such as sarcomeres (Giacomelli et al., 2020), adhesive proteins in junctions between cells (Marsano et al., 2016) and mitochondrial networks (Kolanowski et al., 2020). However, the penetration depth of confocal microscopy is ≤ 100 µm, while multi-photon microscopy can achieve a penetration depth ≥ 500 µm. A commonly used approach to improve penetration depth in 3D tissues is the use of clearing solutions, either solvent- or aqueous-based. In thick 3D tissues, lipids, intracellular and extracellular fluids scatter the light. Tissue clearing dissolves these components, allowing light to penetrate the tissue (Kolesová et al., 2021; Richardson & Lichtman, 2015). As a result, thicker tissue samples can be visualized by different microscopic techniques while preserving the 3D integrity of the sample. Nevertheless, chips materials may not be compatible with all clearing solutions. For example, the aqueous clearing solution SCALES can be used on PDMS-based microfluidic devices, instead of the solvent-based solution CLARITY (Clear Lipid-exchanged Acrylamide-hybridized Rigid Imaging/Immunostaining/In situ hybridization-compatible Tissue-hYdrogel), which is not PDMS compatible (Ondatje et al., 2022).

Despite its usefulness, immunofluorescence is a terminal assay, meaning that changes at the structural level within the same tissue cannot be followed, but a different tissue must be sacrificed at each time point. This results in an increase in the sample number needed for the experiments as well as increasing data noise due to tissue biological variability between samples. A solution is using reporter cell lines for live cell imaging; however, genetically modifying patient cells is a labour-intensive process. Genetic fluorescent reporter cell lines have also been used to monitor sarcomere structure in live tissue (M. C. Ribeiro et al., 2020).

To preserve tissue viability while extracting structural and molecular information, label-free and live imaging techniques are gaining popularity. Second harmonic generation can image non-centrosymmetric structures without additional labelling (e.g., collagen type I) (Lopez III & Larina, 2019). Second harmonic generation was also used to visualize extensive collagen deposition in a fibrosis-on-chip model (Mastikhina et al., 2020) and to image on the Z axis, providing optical sections at 3µm and 30µm depths of engineered heart slices (Blazeski et al., 2015). When coupled with two-photon autofluorescence microscopy, imaging of

unstained CMs (Wallace et al., 2015) and myofibrillogenesis (H. Liu et al., 2011) was possible.

Another microscopy technique to visualize cellular content is Raman spectroscopy. Raman spectroscopy has been used on cardiac biopsies to detect fibrotic tissue (Yamamoto et al., 2018), ECM deposition (Brauchle & Schenke-Layland, 2013; Votteler et al., 2012) and to characterize hiPSC-CMs subpopulations (Brauchle et al., 2016; Shen et al., 2017). Despite its novelty, it has rarely been used for imaging of OoC since the PDMS spectrum presents strong scattering (Zahid et al., 2017) that could interfere with the detection of biological components compared to glass (Mikoliunaite et al., 2015). Nonetheless, this technique was successfully applied for the characterization of the pancreatic islet on chip, where it identified nuclei, mitochondria and lipids and managed to detect a metabolic shift in response to glucose concentration changes (Zbinden et al., 2020). These studies demonstrate the versatility of Raman imaging as a tool for both monitoring tissue structural changes (i.e., collagen secretion, cell identification and organization) as well as for tracking metabolism.

1.2.2 Functional readouts

Most of the functional assays in EHTs and HoCs rely on the optical tracking of cells, tissues or cantilevers (Feric et al., 2019; Mathur et al., 2015; O. Schneider et al., 2019) around which tissues are compacted as a way to retrieve contraction parameters as relative pixel displacement or absolute contraction force. Software such as MuscleMotion (Sala et al., 2018) and *OpenHeartWare* (O. Schneider et al., 2019) are user-friendly and open access tools for optical tracking of live contracting tissue from video recordings or image stacks. This automated contraction analysis enables quantification of contraction changes in disease and healthy states or as response to drugs and can also be applied to MPS (O. Schneider et al., 2019; van Meer et al., 2018). However, the tissue contraction Force (N) cannot be directly measured with these optical tools, therefore Lind and colleagues integrated flexible sensors in their microphysiological system for continuous monitoring of contractile force and beat rate (Lind et al., 2017).

Excitation-contraction coupling is a key indicator of a functional cardiac tissue. Calcium (Ca^{2+}) plays a pivotal role as an essential ion. During the action potential (AP) plateau phase, the sarcoplasmic reticulum responds to electrical excitation by releasing Ca^{2+} ions, thereby elevating the intracellular Ca^{2+} level. This increase in intracellular Ca^{2+} facilitates the coupling of troponin C with intracellular Ca^{2+} in myofilaments, leading to contraction activation. Ca^{2+} fluorescent dyes, in a variety of excitation ranges and Ca^{2+} affinity, are used to study Ca^{2+} flux propagation in 3D cardiac tissues. Although this real-time technique is easy to implement, it is not suitable for long-term analysis and sensitivity of recordings highly depends on the type of the dye. Alternatively, genetically modified hPSC lines that encode for a calcium indicator overcome the limitations of Ca^{2+} dyes (Huebsch et al., 2016).

As Ca^{2+} flux is induced by changes in cell membrane voltage potential (mV), another relevant measure of CMs functionality is the tracking of the AP profile. The AP starts with depolarization of the membrane by Na^{+} influx and following the peak of the action potential, voltage-gated potassium channels open, allowing K^{+} ions to flow out of the cell. At the

beginning of repolarization, the Ca^{2+} ions flow into the cytoplasm from the sarcoplasmic reticulum and from outside the cell; this causes a plateau phase. Further repolarization caused by continuous K^+ outflow brings the membrane potential back to resting level of −85 mV. At the end of the contraction the Ca^{2+} is pumped back into the sarcoplasmic reticulum. Intracellular recordings of electrophysiological parameters are obtained using sharp electrodes or single cell patch clamp. These techniques are considered the benchmark tools for quantifying the functionality of MHTs and EHTs (Giacomelli, Bellin, Orlova, et al., 2017; Giacomelli et al., 2020; Huebsch et al., 2016; Mills et al., 2018, 2019). OoC and HoC majorly rely on extracellular recordings of field potential, which can be achieved using non-invasive MEAs or voltage sensitive dyes.

Voltage dyes are still suggested for short-term use. While they present the same limitations as Ca^{2+} dyes, contrary to MEAs, they do not require expensive fabrication procedures to be integrated into the chips. Instead, MEAs are suited for long-term continuous recordings of large cell populations and 3D cardiac tissues, and have been widely used for real-time estimation of QT-prolongation (Shinozawa et al., 2017) and conduction velocity (Kehat et al., 2002).

Molecular analysis of expression profiles and pathways, by standard qPCR or -omics approaches, is commonly performed for spheroids and EHTs (Giacomelli et al., 2020; Lee et al., 2019; Leonard et al., 2018; Mills et al., 2019; Richards et al., 2020) but not as often for HoCs (Mastikhina et al., 2020). Microtissues formed in HoC may be too small and provide suboptimal concentration of RNA for standard qPCR, extracting the tissues from chips may be challenging and some chip materials may dissolve with harsh lysis solutions. Techniques such as Spatial transcriptomic and RNAscope, although not yet commonly applied to OoCs offer next generation methodologies for in situ tissue profiling (Bailey et al., 2021; Vickovic et al., 2019; F. Wang et al., 2012). They aim at detecting expressed genes within tissue slices while preserving their spatial information, thus providing insights into the organization and function of cells within complex tissues. Traditional transcriptomic analysis typically involves isolating and sequencing RNA from bulk tissue samples, which provides an average snapshot of gene expression across all the cells in the sample. However, this method overlooks the fact that different cells within a tissue can have distinct gene expression profiles and play diverse roles. Other alternatives include collecting tissue-conditioned media as a source for detection of biomarkers (Jacob & Khan, 2018; McDonaugh & Whyte, 2020) or recent impedimetric immunosensors. These methods are currently being used for quality control of embryos derived from *in vitro* fertilization where invasive cell sampling carries high risk (Abreu et al., 2020; Cortezzi et al., 2013; Iles et al., 2019; Picton et al., 2010).

1.2.3 Metabolic readouts

The adult heart has a low energy reserve. In order to meet its high energy demand, CMs can produce adenosine triphosphate (**ATP**) from several metabolic substrates (e.g., glucose, pyruvate, triglycerides, glycogen, lactate, ketone bodies, FAs, and some amino acids) based on environmental conditions (Evans & Heather, 2016; Taegtmeyer et al., 2016). During early cardiac development, the major energy source for pre-natal CMs is

glucose and lactate and the major metabolic pathways to produce ATP is glycolysis. However, as the CMs mature, mitochondrial oxidative capacity increases and FA beta oxidation becomes the major energy source (Breckenridge et al., 2013; Lopaschuk & Jaswal, 2010). Reproducing this “metabolic switch” from glycolysis to mitochondrial oxidative phosphorylation is an important reflection of maturity in MPS. Several approaches are used to monitor mitochondrial respiration and glycolysis.

Traditional techniques to measure extracellular oxygen, glucose and lactate include: (I) polarography, which is based on the rate of oxygen diffusion to the cathode of a monitoring electrode (Ogneva et al., 2012), (II) spectrophotometric analysis of the mitochondrial respiratory chain enzymes (Hoes et al., 2018) and (III) measuring the activity of limiting glycolytic enzymes (Hexokinase, phosphofructokinase, and PK) by coupling them with nicotinamide adenine dinucleotide (NAD+/NADH) dependent enzymes and measuring change in absorbance (TeSlaa & Teitell, 2014). However, these methods have low sample throughput and are highly invasive since they require cell permeabilization, mitochondrial extraction and cell lysis. Several commercially available kits and instruments (e.g., BioProfile Analyzers and Biochemistry Analyzers) allow quantification of both extracellular glucose, lactate, and FA levels by colorimetric and fluorometric detection in cell culture media and are thus non-invasive. The Seahorse (extracellular flux) XF Analyzer is a fast and comprehensive approach that allows simultaneous recording of mitochondrial respiration and glycolysis by measuring the oxygen consumption rate (**OCR**) and extracellular acidification rate (**ECAR**) of live cells and tissues. The analyser has injection ports for direct addition of compounds in the chamber allowing measurements of drug-induced metabolic changes. Three main metabolic assays can be performed with this technology: (I) Mitochondrial stress test; (II) glycolytic stress test and (III) palmitate oxidation assay (Mdaki et al., 2016).

Although Seahorse-XF is widely used on cell monolayers, spheroids and EHTs (Giacomelli et al., 2020; Mills et al., 2018, 2019; Richards et al., 2020), it has not yet been applied to HoC, possibly due to the difficulty of accessing tissues in HoCs. Most of the microfluidic devices are closed systems where the cells proximity is not easily accessible by instrumentation and the medium is delivered by a continuous flow. One possibility would be to adapt the chip design to fit the instrument reader and to have a top media chamber that can easily be opened/closed and read by the instrument; this would also allow compound delivery by the machine itself instead of through the chip perfusion system. A recent approach to emulate Seahorse-XF readings in OoC platforms has been developed by integrating pH and O_2 sensors within the microfluidic device and perform the assays as done in the machine (Busche et al., 2022). A recent study has confirmed that hiPSC mitochondrial and glycolytic capacity measured on-chip by the integrated sensors was comparable to that of hiPSC in conventional cell culture measured by the analyser (Fuchs et al., 2022). These optical sensors offer integrated measurement of a variety of analytes, such as O_2, pH, and glucose (**Fig. 1.2.1**) (Fuchs et al., 2023; Lladó Maldonado et al., 2019; Mousavi Shaegh et al., 2016). Optical luminescent sensors are fabricated by incorporating the luminescent indicator dye in a polymer matrix and spotting it onto a surface (**Fig. 1.2.1 A**). The dye is sensitive to the specific analyte or coupled with specific enzymes that convert the analyte to

a species that can be detected by the dye (**Fig. 1.2.1 B**). For example, while in oxygen sensors the O_2 binds to the dye quenching its luminescent signal, the glucose sensors rely on the enzyme glucose oxidase which converts glucose to O_2 that can be detected by the dye (Borisov et al., 2008; Grist et al., 2010). This strategy, however, makes glucose measurement sensitive to the intrinsic O_2 concentration in the surrounding environment. When the specie of interest is detected, the dye signal is quenched decreasing the lifetime, resulting in lower intensity and phase-shift (Δφ) (**Fig. 1.2.1 C**). Between intensity and phase-shift measurements the latter was established as most robust (Bambot et al., 1994; Morgan & Mitchell, 1996) and were used in the abovementioned studies.

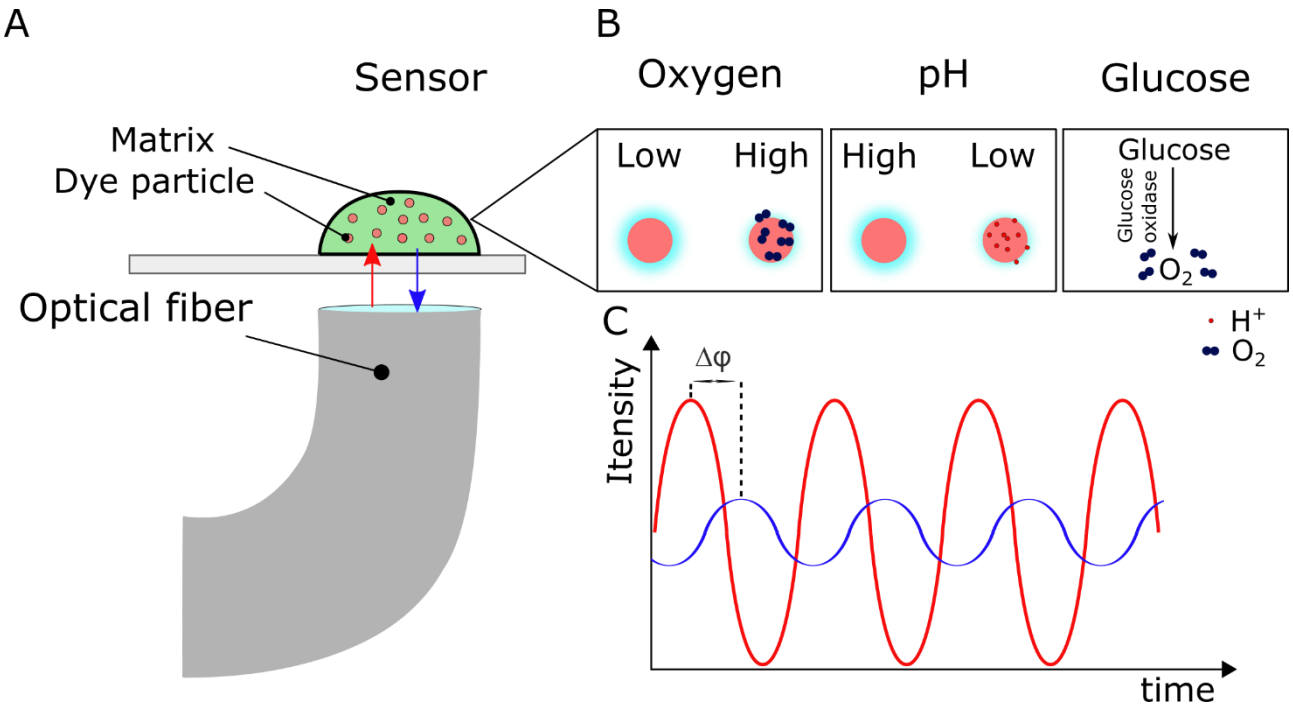

Figure 1.2.1 *Optical sensors schematic.* ***(A)*** *The sensor consists of dye particles embedded in a gel matrix which is deposited on a surface. An optical fibre is placed below the sensor and used to excite the dye and detect emitted signal.* ***(B)*** *Dye particles can be sensitive to O2 (oxygen sensor) or H+ (pH sensor) molecules. When the molecules bind to the dye, they quench the emitted signal. Glucose sensor relies on the Glucose oxidase enzyme to convert glucose to O_2, which is then detected by the dye particles.* ***(C)*** *The emitted wave (blue) has lower intensity and phase shift in respect to the excitation wave. The higher the analyte, the lower the phase shift.*

Lastly, despite being a microscopic technique, fluorescence life-time imaging (FLIM) can be utilized for monitoring NAD(P)H metabolism. Maintaining cellular redox homeostasis and regulating cellular metabolism heavily relies on the NAD+/NADH and NADP+/NADPH redox process. In one study from Berthiaume and colleagues, they quantified the relative levels of NADH and NADPH in different cell types of the mammalian cochlea (Blacker et al., 2014). However, this has not been applied yet to OoCs or HoCs.

An extensive analysis of metabolic changes under different conditions is possible through transcriptomic and proteomic assays such as RNA sequencing (RNA-seq) and liquid chromatography coupled with mass spectrometry (LC-MS). These techniques are used to

investigate expression of metabolic (glycolysis and FA oxidation) related genes and proteins. These high-throughput assays are maximally invasive as mentioned in the functional readout section and mainly used in MHTs for which larger scale production is possible compared to EHT and HoCs. Highly sensitive enzyme linked immunosorbent assays (ELISA) are another quantification approach for metabolic function. Although less widely used, ELISA and LC-MS can also be used non-invasively to analyse the cell secretome by collecting cell culture supernatant. Secretome analysis can be employed to gain insight into disease mechanisms (Kuhn et al., 2020) and microenvironmental changes in the ECM during differentiation of hPSC into CMs (Robert et al., 2020). However, proteome and secretome data acquisition and interpretation are quite challenging, even when applied to simple systems (e.g., monoculture). Low concentration of analytes, serum contaminants in the media, protein splice variants can all result in false negatives and positives; this might be the reason why this technique has not been widely adopted in more complex cardiac systems (e.g., co-culture of different cell types).

Nuclear magnetic resonance spectroscopy (NMR) detects extra-/intra-cellular metabolites in MHTs by the collection of tissue supernatant and lysate. The technique can be used non-invasively and the data gives valuable input in the metabolic state of the tissues (Giacomelli et al., 2020).

Most of the standard techniques (e.g. ELISA, LC-MS, and FX Analyzer) in static culture systems rely on supernatant collection (of a volume of ≥ 50 µL); however, in HoC the miniaturization of the tissue and continuous perfusion allows the use of very small amounts of media during culture, which results in the accumulation of secreted factors and metabolites in very small media volumes (≤ 50 µL), which cannot being handled by standard assays or instruments. It is thus challenging to measure metabolites in these systems. The combination of *in situ* sensors with HoC systems eliminates this challenge and allow for continuous and faster measurements with improved time resolution. Examples of such systems are sensors which can be either integrated in the microfluidic device or used as plug and play component.

Integrated sensors include electrochemical sensors which are commonly used in HoC to measure oxygen and pH analytes as a difference of electrical current or potential (Tanumihardja et al., 2021), but they can also be adapted to measure non-electrically active species such as glucose and lactate. These sensors often require a transducer to detect signals. On the other hand, optical sensors can replace transducers and detect signals from a simple transparent window on top of the sensor. Electrochemical and optical sensors alternatives and their integration in OoC systems have been extensively reviewed in Fuchs *et al*., 2021 (Fuchs et al., 2021).

Modular multi-sensors may contain several physical sensors for monitoring pH, oxygen, temperature, and electrochemical sensors. Skardal and colleagues used modular multisensory systems in combination with a three-tissue liver, heart, and lung organ-on-a-chip. They successfully detected differential secretion of albumin, α-GST, and creatine kinase MB in response to different drugs (Skardal et al., 2017). An important consideration when choosing an integrated or modular sensor is that integrated sensors are single use

while modular sensors can be re-usable. Another difference is that integrated sensors can be positioned close to the tissue allowing real-time measurement; by contrast, modular sensor readings are dependent on the flow rate and some measurements, such as oxygen consumption in PDMS chips, can be impaired (Y. S. Zhang et al., 2017).

1.3 Engineered skeletal muscle tissues

1.3.1 Skeletal muscle physiology

A muscle is formed by several fascicles of muscle fibres, surrounded by a layer of connective tissue called the perimysium. Within one fasciculus, several skeletal muscle fibres are aligned. Each individual muscle fibre is a single cylindrical polynucleated muscle cell (myofiber or myocyte), surrounded by connective tissue called the endomysium. The endomysium consists mainly of collagen fibre types III, IV and V, and a small amount of collagen type I (Passerieux et al., 2007; Trotter & Purslow, 1992). Within the myocyte, the contractile apparatus is comprised of myofibrils (actin, myosin, troponin, and tropomyosin). These constitute 80% of the cell content and are highly organised along the myocyte's length (Hoppeler et al., 1973). The well-developed sarcoplasmic reticulum and the mitochondria surrounding the myofibrils allows for an efficient excitation-contraction coupling.

Muscle tissue undergoes significant wear and tear throughout an individual's lifespan. Therefore, unlike the heart, which has limited regenerative capacity, it maintains its regenerative ability through the presence of satellite stem cells, which are responsible for the lifelong maintenance of muscle tissue. Muscle satellite stem cells lie, quiescent, near the muscle fibres. When certain stimuli, such as physical trauma or the presence of growth signals, are perceived, they get activated. Once activated, they first undergo symmetric divisions to increase their numbers and then asymmetric divisions to produce myogenic progenitor cells. The myogenic progenitors subsequently undergo proliferation and eventually differentiate by fusing with each other or damaged fibres. This process helps restore the integrity and functionality of the muscle fibres (Evano et al., 2020).

Muscle fibres can be classified in 3 types: (I) Type I are slow oxidative fibres, which produce low power slow contraction and rely on aerobic respiration (oxygen and glucose) to produce ATP. They are fatigue-resistant; (II) Type IIA are fast oxidative fibres, which produce fast contractions and can switch their metabolism between aerobic and anaerobic respiration; for this reason, they fatigue faster than type I fibres; (III) Type IIx are the fastest in contraction and rely mainly on glycolysis, therefore are the also the fastest to experience fatigue. The speed of contraction is proportional to the development of the sarcoplasmic reticulum while the mitochondria content correlates to the resistance to fatigue and oxidative capacity (Frontera & Ochala, 2015; Galpin et al., 2012; Lamboley et al., 2014).

The skeletal muscle can use several different substrates to generate ATP. These include creatine phosphate, muscle glycogen, blood-borne glucose, lactate, and free FAs, derived from either adipose tissue or intramuscular triglyceride stores. During high-intensity short-duration exercise, the muscle draw energy from its glycogen and creatine phosphate reserves. While creatine degradation and the breakdown of muscle glycogen to lactate are

the major energy yielding pathways, because the amount of these reserves in muscle fibres is small, oxidative metabolism can also make a significant contribution. If the high-intensity exercise is prolonged (minutes), anaerobic respiration is triggered to quickly to sustain muscle actions; here glycolysis leads to an increase in lactate production and H^+ ions, which is associated with fatigue. Lastly, when physical exercise is carried out for several minutes to hours at a lower intensity (endurance training), the oxidative phosphorylation of carbohydrates and lipids supplies most of the ATP. It is important to note that these pathways overlap and while their relative contribution to ATP production is primarily determined by exercise intensity and duration, this can vary with training status, diet and environmental factors which can modify the metabolic response to exercise (Battey et al., 2023; Smith et al., 2023).

Skeletal muscle plays a critical role in glucose consumption by contributing to over 80% of glucose uptake from blood, storing it as glycogen within the muscle fibres (Ferrannini et al., 1988; Richter & Hargreaves, 2013; Shulman et al., 1990; Thiebaud et al., 1982). Glucose uptake by myocytes is regulated by the insulin responsive glucose transporter 4 (**GLUT4**); which makes skeletal muscle cells highly dependent on insulin for maintaining their metabolic homeostasis. However, in individuals with prediabetes, also known as insulin resistance, the inability to regulate blood glucose concentrations within the normal range arises. As defined by the American Diabetes Association in 2017, when muscles become less responsive to insulin's glucose uptake signals, the fasting blood glucose levels raise from 101 to 125 mg/dL (5.6–6.9 mM) while glucose blood levels two hours after consumption of a 75g oral glucose load reach the range of 140–199 mg/dL (7.8–11.1 mM) (American Diabetes Association, 2017). Interestingly, skeletal muscle's insulin resistance can manifest years before β-cell dysfunction and the onset of symptomatic type 2 diabetes and leads to increased risk of developing various disorders, including cancer, cardio-metabolic complications, neuropathy, and sarcopenia (Centers for Disease Control and Prevention, 2022; Mellbin et al., 2010; Merz & Thurmond, 2020; Warram, 1990).

One of the most prescribed lifestyle interventions for prediabetic and type 2 diabetic patients is physical activity, which has been proven to improve insulin sensitivity in patients (Boulé et al., 2001; Hawley & Lessard, 2007). Several studies have been conducted to determine what training regime is best suited to combat diabetes type 2. Despite all training types (aerobic exercise, resistance training, combined training, and high-intensity interval training) have been reported to improve insulin sensitivity and lower glucose concentration in blood, a consensus on what is the best training regime has not been reached (Kirwan et al., 2017; Praet & van Loon, 2008). Studies showed that various adaptations occur after physical exercise such as a lower percent of body fat, lower inflammatory markers, and a higher metabolic rate at the systemic level, while an increase of skeletal muscle mass, capillarization, mitochondrial content, and respiration have been detected at the muscular levels (Egan & Zierath, 2013). At the molecular level, skeletal muscle cells displayed an increase in GLUT4 expression and consequent glucose uptake during exercise (Richter & Hargreaves, 2013). Based on the exercise type, different metabolic and myogenic transcripts are regulated within the first 4-8 hours but are reported to return at their basal level within 24 hours (Pillon et al., 2020; Y. Yang et al., 2005). Additionally, skeletal muscle

releases myokines and myometabokines, which exert autocrine and paracrine effects on the skeletal muscle and other organs, such as liver, adipose tissue, pancreas, brain, gut, bones, and immune cells (Hoffmann & Weigert, 2017; Severinsen & Pedersen, 2020). However, our knowledge regarding the interaction between muscles and various organs under physical exercise is still limited (Sanford et al., 2020). To explore these biological mechanisms linked to exercise and gain insights into the molecular-level interaction across multiple organs, it is necessary to develop accurate models.

1.3.2 Current approaches for generation of skeletal muscle models

Despite significant progress in identifying the molecular regulation of the expansion and differentiation of satellite cells, understanding their complex cellular and molecular interactions still poses a significant challenge. *In vitro* protocols for differentiating primary human satellite cells into myotubes have been available for several decades (Askanas & Engel, 1975; Bishop et al., 1971; Yasin et al., 1977) and have been refined over the years. While initially they used rat or human brain extract (Benders, 1991; van der Ven et al., 1992) and 2% serum (horse or foetal calf) (Blau & Webster, 1981; Henry et al., 1995), in recent years, serum-free protocols have become available (X. Guo et al., 2014; Hoffmann et al., 2018). Despite these protocols consistently generating long, fused, multinucleated myotubes, they still fall short of fully replicating the physiological functions of myofibers *in vivo*. In particular, they do not exhibit proper muscle contraction during electrical pulse stimulation (Lambernd et al., 2012; Nikolić et al., 2012) as well as essential features of metabolic function, such as mitochondrial respiration and glycemic control (Aas et al., 2013). Such human myotubes predominantly rely on glycolysis for ATP production rather than mitochondrial oxidative phosphorylation (Aas et al., 2011), demonstrate reduced insulin-responsive glucose uptake, and have a low expression ratio of GLUT4 to GLUT1 compared to adult skeletal muscle (Krützfeldt et al., 2000; Sarabia et al., 1992).

Cell lines, such as mouse MM14, rat L6, and mouse C2C12, have been used over the years as an alternative to study the effect of pacing, as they show contraction in response to electrical stimulation. However, compared to adult human skeletal muscle cells, they showed a low glucose uptake upon insulin stimulation due to the deficiency of GLUT4 expression. Rat L6, mouse C2C12, and human primary myotubes exhibit profoundly different transcriptomic profiles and metabolic behaviours, making these cell types non representative of human biology (Abdelmoez et al., 2020). Alternatively, hiPSC-derived myocytes can be used for myofiber generation; several hiPSC lines and differentiation protocols as well as their limitations were extensively reviewed by Iberite *et al*. (Iberite et al., 2022), therefore they will not be summarised here.

To replicate the cellular and structural organization of a 3D bundle of myotubules, also known as a myobundle, several engineering approaches were developed. These make it possible to study skeletal muscle metabolism and drug toxicity. One strategy to generate skeletal muscle myobundles involves creating fibres between two posts, similar to the method described earlier for EHTs (Christensen et al., 2020). The platform described in the study is created using stereolithographic 3D printing of PEGDA (poly(ethylene glycol)

diacrylate), allowing the casting of the cells in a confined hydrogel matrix embedding the anchoring cantilevers. Another strategy was developed by Madden and colleagues, which used a PDMS mould with features for a nylon frame and slits for casting the hydrogel cellular mixture. Upon polymerization of the hydrogel, the hydrogel would keep the tissue anchored to the nylon frame (Madden et al., 2015). After differentiation, the myocytes displayed multinucleated tubular morphology with aligned actin filaments. Their model successfully mimicked key functional aspects of human skeletal muscle, including contractile ability, responsiveness to acetylcholine and β2-adrenergic receptors, and physiological calcium handling. They also evaluated drug responses to statins, chloroquine, and clenbuterol, and demonstrated sensitivity comparable to *in vivo*. Kondash *et al*. used the same model to analyse glucose uptake in response to insulin. Even though the system exhibits relevant drug-mediated perturbations in contractile function and glucose metabolism, the increase in glucose uptake mediated by insulin remains modest (Kondash et al., 2020).

Torres *et al*. conducted a study to examine the musculoskeletal side effects of two chemotherapy drugs, doxorubicin, and docetaxel, using 3D myobundles. They determined that both drugs in a *in vivo*-like drug dosing regimen disrupted cytoskeletal architecture and energy metabolism (Torres et al., 2022). Zhang *et al*., coupled the myobundle to an Ecoflex rubber band with embedded microbeads to measure contraction force through bead displacement and used it for pharmacological assessment of myobundles forces under continuous exposure of cerivastatin (X. Zhang et al., 2018). Davis *et al*., managed to adapt the commercially available O2k system to host the 3D myobundles for non-invasive measurement of mitochondrial respirometry, similarly to the Seahorse XF analyser. The myobundles accurately replicated normal muscle metabolism, even during periods of low and high energy demands. This characteristic allows for the identification of drug-induced mitochondrial toxicity (B. N. J. Davis et al., 2017).

Up to this point, few perfusable skeletal muscle-on-chips have been developed. The skeletal muscle-on-chip developed by Serena *et al*., showed the potential of human mesoangioblasts for restoring dystrophin in myotubes derived from patients with Duchenne muscular dystrophy (Serena et al., 2016). Despite its claim to be a skeletal muscle-on-chip model, there was still no perfusion applied to the tissues. Agarwal took advantage of 3D photopatterning of polyacrylamide by infusing photo-curable polyacrylamide in a bonded microfluidic platform and produced a pillar-based tissue model perfusable with media (Agrawal et al., 2017). In another example, Davis and colleagues achieved prefusion by enchasing a previously generated moybundle (Madden et al., 2015) in an acrylic chamber connected to perfusion tubes through a media inlet and a media outlet (B. N. Davis et al., 2019). This chip also integrated a luminescence quenching optical sensor and electrodes for pacing, so that O_2 consumption of the skeletal muscle tissue could be monitored during electrical stimulation. Wan *et al*., tried to mimic capillary formation within a muscle fibre, using sacrificial layers of thermos-responsive wax to produce a channel within the muscle fibre itself and then seed it with human umbilical vein endothelial cells (HUVEC) to generate a capillary (Wan et al., 2020).

Another aspect of skeletal muscle-on chip research is to investigate the neuromuscular junction since muscle contraction is initiated by motor neurons and is affected by

neurodegenerative diseases (i.e., Amyotrophic lateral sclerosis) (Jongh et al., 2021). However, this will not be covered in this thesis as it is outside its scope. Just like the heart, skeletal muscle plays a crucial role in metabolic and toxicity studies. As a result, it has been incorporated into multi-OoC platforms along with other relevant organs. In Oleaga's platform, four organs (heart, liver, skeletal muscle, and nervous system) were co-cultured over 28 days in serum-free conditions using a pumpless system. Additionally, the platform was provided with non-invasive readouts, such as MEAs for neuronal and cardiac activity recording and mechanical sensors to analyse cardiac and skeletal muscle contraction. These parameters were monitored for chronic toxicity studies *in vitro* (Oleaga et al., 2016; Oleaga, Lavado, et al., 2018).

In the last part of this thesis, the *Spheroflow HoC* platform was repurposed to host a functional skeletal muscle fibre that can be easily paced. This will allow the generated skeletal muscle fibre to undergo long-term stimulation through pacing, while being analysed with the same non-invasive readouts used for the HoC model.

2 Materials and Methods

In this section, a comprehensive overview of the procedures for chip fabrication, cell culture in both 2D and on-chip settings, on-chip experiments, and effluent analysis is provided. Additionally, the approaches employed for data acquisition and subsequent statistical analysis are presented.

The chip fabrication, centrifugal cell injection, and chip perfusion methods of the *Centrifugal HoC*, were already established and published in *User-friendly and paralleled generation of hiPSC-derived µ-tissues in a centrifugal heart-on-a-chip* (O. Schneider et al., 2019), prior to the start of this thesis.

Methods involving the *Spheroflow HoC* (resin-based fabrication of chips which integrate O_2 sensors, cell culture and characterization, spheroid formation, chip injection and culture, immunofluorescence staining, electrical stimulation, and establishment of the O_2 sensor readout) were developed during the current project and have been published in the co-authored paper, *Fusing spheroids to aligned µ-tissues in a heart-on-chip featuring oxygen sensing and electrical pacing capabilities* (O. Schneider et al., 2022).

2.1 Cell culture

All cells were cultured in a humidified atmosphere (95% air, 5% CO_2) at 37° C.

2.1.1 hiPSC culture

Two hiPSC lines were used: Coriell GM25256 (RRID: CVCL_Y803, Gladstone Institute for Cardiovascular Disease) and E1 (RRID: CVCL_RM92, Thermo Fisher Scientific).

Culture vessels were coated with Matrigel® hESC-Qualified Matrix, LDEV-free (Matrigel; 354277, Corning) or Vitronectin Recombinant Human Protein, Truncated (rhVTN-N; A14700, Gibco). hiPSCs are cryopreserved in ibidi Freezing Medium Classic (80022, ibidi). After thawing, hiPSCs were plated on coated 6-well plates at a density of 25,000 cells/cm^2 and cultured in TeSR-E8 (05990, STEMCELL Technologies) medium, supplemented with 10 µM ROCK inhibitor Y-27632 (**RI**; 05990, STEMCELL Technologies) for the first 24 h after thawing or passaging. Cells were media changed daily with 3 mL/well of medium. hiPSCs were passaged with Accumax (SCR006, Sigma-Aldrich) at least once before initiating the differentiation.

2.1.2 Cardiomyocytes differentiation and Lactate purification

Differentiation was achieved using an optimized protocol for the small-molecule manipulation of Wnt signalling adapted from (Lian et al., 2013). Upon reaching ≥ 90% confluence, (day 0) medium was exchanged with RPMI 1640 medium (RPMI; 1185063, Gibco) supplemented with B27 supplement without insulin (B27–I; A1895601, Gibco) and 10 µM of the Wnt agonist CHIR99021 (CHIR; S2924, Selleckchem). Exactly after 24 hrs, medium was changed to RPMI + B27–I. Two days later (day 3), the medium was changed

to RPMI + B27–I with 5 µM Wnt inhibitor IWP-4 (SML1114, Sigma-Aldrich) and incubated for 48 hrs. On day 5, medium was changed to RPMI + B27–I and on day 7 to RPMI 1640 supplemented with B27 complete supplement (B27C; 17504044, Gibco), which was used thereafter for CM culture, and exchanged every second day. Around days 9–12, cells showed spontaneous beating. On day 15, cells were dissociated through incubation with 280 U/mL Collagenase (LS004174, Worthington) and 40 U/mL DNase (LS006331, Worthington) in RPMI + B27C for 1.5 hrs. Detached monolayers were collected in a 50 mL conical centrifuge tube containing 20 mL of phosphate-buffered saline minus (**PBS-**), centrifuged at 200×g for 3 min and resuspended in Accumax solution followed by 25 min of incubation at 37 °C. After singularization, cells were washed and resuspended in RPMI + B27C with 10 µM of RI. Cells were either frozen in RPMI + B27C with 10 µM of RI + 10% foetal calf serum (**FCS**; SH30066.03, Cytiva) +10% Dimethyl sulfoxide (**DMSO**; 472301, Sigma-Aldrich) or replated for lactate purification protocol.

Lactate purification protocol was adapted from Huebsch et al., 2022. Cells were replated at 100,000 cells/cm^2 in RPMI + B27C with 10 µM RI for the first 24 hrs (day 0), then the medium is changed to RPMI + B27C without RI. On day 3, CMs were media changed with Cardiomyocyte selective medium (CSM, see **Table 2.1.1**). CSM medium is exchanged daily for 5 days. On day 8, the medium was exchanged with RPMI + B27C and CMs were left to recover for 3 days. On day 11, the CMs were detached with Accumax and cryopreserved.

CMs purity was checked before and after lactate purification through flow cytometry (either with Guava® easyCyte 8HT, Merck Millipore or BD LSRFortessa™ Cell Analyzer, BD Biosciences) for the cardiac marker Cardiac troponin T conjugated to APC (**cTnT**; 1:50; REA400; 130-120-543, Miltenyi Biotec).

Before loading, CMs were thawed in RPMI + B27C with 10 µM RI and plated at a cell density of 200,000 cells/cm^2 in a 6-well plate coated with Matrigel. After 24 hrs, medium was exchanged with RPMI + B27C and after 3 days of culture, cells were used for experiments. Only hiPSC-derived CMs with purity ≥80% were used for further experiments.

Components	**Final concentration**
RPMI 1640 without glucose or sodium pyruvate (11879020, Gibco)	Basal medium
Sodium bicarbonate (S5761, Sigma-Aldrich)	23mM
Sodium *L*-lacate (L7022, Sigma-Aldrich)	5mM

Table 2.1.1 *Cardiomyocyte selective medium composition from* Huebsch et al., 2022.

2.1.3 Cardiac fibroblasts differentiation protocols

2.1.3.1 Protocol 1

This protocol was adapted from Zhang et al., 2019. Upon reaching ≥ 90% confluence (day 0), hiPSC were media changed with 3mL/well RPMI 1640 + B27–I with 12 µM CHIR. After 24 hrs (day 1), the medium was changed to RPMI + B27-I and cells were cultured in this

medium for 24 hrs. On day 2, the medium was changed to cardiac fibroblasts basal medium (CFBM, see **Table 2.1.2**) with 75 ng/mL Basic fibroblast growth factor (**bFGF**) (130-093-839, Miltenyi Biotec). Cells were fed with CFBM + 75 ng/mL bFGF every other day until day 20. Cells were passaged with 0.05% Trypsin/EDTA (15400054, Gibco) and expanded in FibroGro medium (SCMF001, Sigma-Aldrich) + 2% FCS on cell culture treated vessels. Cells were then cryopreserved in FibroGro + 10% FCS + 10% DMSO. Cells were used for experiments up to passage 9.

Components	**Final concentration**
DMEM, high glucose (4.5 g/L) (P04-04515, Pan-Biotech)	Basal medium
HLL Supplement (LS-1001, Lifeline Cell Technology): HSA (human serum albumin), linolenic acid, lecithin.	HSA: 500 µg/mL Linolenic acid: 0.6 µM Lecithin: 0.6 µg/mL
Ascorbic Acid (A8960-5G, Sigma-Aldrich)	50 µg/mL
GlutaMAX (35050061, Thermo Fisher Scientific)	7.5 mM
Hydrocortisone Hemisuccinate (H2270, Sigma-Aldrich)	1.0 µg/mL
rhInsulin (LS-1004, Lifeline Cell Technology)	5.0 µg/mL

Table 2.1.2 *Cardiac fibroblasts basal medium composition from* J. Zhang et al., 2019.

2.1.3.2 Protocol 2

This protocol was adapted from (H. Zhang et al., 2019). Upon reaching ≥ 90% confluence (day 0), hiPSC were media changed to 3mL/well of RPMI + B27-I with 6 µM CHIR. After 48 hours (day 2), the medium was exchanged with RPMI + B27-I and the cells were cultured in this medium for 24 hrs, followed with a media change to RPMI + B27-I treated with 5 µM IWP-4 and incubation for 48 hrs. On day 5, the hiPSC were differentiated in CPC. After detachment with Accumax, cells were replated on a Matrigel coated 6 wellplate, at a density of 20,000 cells/cm^2 in 3 mL/well advanced DMEM (12634028, Gibco) with 5 µM CHIR and 2 µM Retinoic acid (R2625, Sigma-Aldrich). Cells were media changed the day after to remove dead cells and left in the medium for 2 days. On day 8, the medium was exchange to advanced DMEM for 4 days, refreshing the medium once after 2 days. By day 12, the cells are at the epicardial progenitor cell (**EPC**) stage and were replated on Matrigel in Fibroblasts growth medium (FGM; C-23110, PromoCell) with 10 ng/mL bFGF and 10 µM of TGFβ inhibitor, SB431542 (1614, Tocris). EPC were kept in this medium for 6 days, media changing every other day until day 18. On day 18, the cells were detached with 0.05% Trypsin/EDTA and their purity was assessed through flowcytometry with the marker Discoidin domain-containing receptor 2 (**DDR2**). Cells were cryopreserved in FGM + 10% FCS + 10% DMSO. Cells were used for experiments up to passage 9.

2.1.4 PhDF culture

Primary human dermal fibroblasts (**phDF**) were purchased from PromoCell (C-12300). These cells were isolated from juvenile foreskin. $1 \cdot 10^6$ cells were plated in a cell culture treated T175 flask in DMEM (P04-04515, Pan-Biotech) supplemented with 10% FCS and

1% P/S (DMEM complete). Medium was changed every 3 days. After 7 days, the cells were confluent and were either passaged with 0.05% Trypsin/EDTA and cryopreserved in DMEM +10% FCS +10% DMSO. Cells were passaged at least once before any experiment and only used for experiments up to passage 9.

2.1.5 haCFv culture

Primary human adult cardiac fibroblasts isolated from the ventricle (**haCFv**) were purchased from PromoCell (C-12375). Cells were plated with a cell density of $0.5 \cdot 10^6$ cells in a cell culture treated T75 flask in FGM + 2% FCS. Medium was changed every 3 days. After 7 days, the cells were confluent and were either passaged with 0.05% Trypsin/EDTA and cryopreserved in DMEM +10% FCS +10% DMSO. Cells were passaged at least once before any experiment and only used for experiments up to passage 9.

2.1.6 Skeletal muscle cells culture

Primary myocytes were isolated from patients, sorted for the marker CD56 to exclude non myocytes population, and provided cryopreserved by Dr. rer. nat. Simon Dreher from the Institute for Clinical Chemistry and Pathobiochemistry, University Hospital Tübingen, Germany.

Cells were thawed and cultured in a cell culture treated T175 flask in Cloning medium (see **Table 2.1.3** for composition). Medium was changed every 2 days. Upon reaching > 90% confluency, cells were used for experimental procedures.

Formation of the myotubules was achieved by switching the media to POC medium (see **Table 2.1.3** for composition) with or without the addition of 100 ng/mL of human recombinant Insulin-like growth factor-1 (**IGF-1**; I3769, Sigma-Aldrich). The cells were cultured in such a medium for 10 days and the media was exchanged every 2 days.

Cloning Medium Components	**Final concentration (%)**
MEM α (M4526, Sigma-Aldrich)	38%
Ham's F-12 Nutrient Mix (21765037, Thermo Fisher Scientific)	38%
FBS (S0615, BiochromAG)	20%
L-Glutamine (200 mM) (DE17605, Lonza)	2 mM
Pen/Strep (10,000 U/mL) (DE17602, Lonza)	100 U/mL
Amphotericin B (250 µg/mL) (A2942, Sigma-Aldrich)	0.2%
Chicken extract (MDL-004E-UK, Biotrend/LSP)	1%
Fasting Medium Components	**Final concentration (%)**
MEM α	96%
L-Glutamine (200 mM)	2 mM

Pen/Strep (10,000 U/mL)	100 U/mL
Amphotericin B (250 µg/mL)	0.2%
POC Medium Components	**Final concentration (%)**
Fasting Medium	98%
Palmitate (P0500, Sigma-Aldrich) in fatty acid-free BSA (A1595, Sigma-Aldrich) at 6 mM	50 µM
Oleate (O1008, Sigma-Aldrich) in fatty acid-free BSA at 6 mM	50 µM
Carnitine (C0283, Sigma-Aldrich) in MilliQ at 500 mM	100 µM

Table 2.1.3 *Media composition for myocytes expansion and fusion into myotubules.*

2.2 Spheroids formation

Spheroids were formed following a previous approach established by Hookway et al., 2016. The inverted pyramid pattern of the 6-well microwell culture plate (AggreWell™400, STEMCELL Technologies, USA) was replicated out of Hydrosil (101301, SILADENT) (Dahlmann et al, 2013). The silicone moulds were punched out into circular segment and glued with an epoxy adhesive (UHU PLUS sofortfest, UHU) to a PMMA holder, with cut offs of d = 15.5 mm, h = 2 mm. The structure would represent a 24-wellplate format well, with the silicone inverted pyramid pattern at the bottom. This reusable master mould was sterilized with 70% ethanol before every experiment.

The master mould was filled with 650 µL of sterile 3% agarose solution in DMEM. The agarose would solidify within 10 minutes. Solid agarose moulds were transferred, with the patterned side upwards, into the wells of a 24-well plate. 1 mL/well of medium was added to each well and the plate centrifuged at 1300×g for 3 min to remove any air bubbles trapped at the bottom of the inverted pyramid microstructure.

Previously dissociated CMs and phDFs were mixed with a ratio of 3:1 (CMs: phDFs), and the medium was supplemented with 10 µM RI. A total of 0.5 Mio cells were added to each well and centrifuged at 300 × g for 3 min with a deceleration ramp setting of 3. Cells were incubated (37 °C, 5% CO2) for 24 h. The next day, around 1200 spheroids/well were formed and could be used for chip loading.

2.3 Microfluidic systems fabrication

All fabrication processes share the following common steps:

Substrate cleaning

All substrates went through cleaning before being employed in the fabrication processes. Glass microscopy slides and coverslips were rinsed with acetone followed by isopropyl alcohol (**IPA**), and subsequently blow dried. Thermoplastic substrates, namely polyethylene terephthalate (**PET**) and TPE, were rinsed with IPA and blow dried. PDMS modules, without a bonded membrane, were cleaned with IPA, blow dried, and residual particles removed with sticky tape; when the membrane was bonded no sticky tape was used. Laser cut PET membranes were immersed in Ethanol for 1 min and left to dry before plasma activation.

Laser cutting of PET membranes

The 3 µm pore size PET membrane A4 sheet (030444, SABEU) was placed in the laser cutter R5000 (Universal Systems) and the membrane outline was cut with the following parameters: Power laser 1 = 0%, Power laser 2 = 60%, Total power = 18 W, Speed = 2%, PPI = 100, Air flow = no, Kerf width = 0.0 mm, Number of repetitions = 0.

PDMS modules

Each module of the microfluidic systems was designed using AutoCAD 2019 and CorelDraw 2019 software and a photomask of it was printed and used to fabricate a SU-8 silicon wafer master through UV lithography as previously described (O. Schneider et al., 2019, 2022). PDMS layers were moulded from the silicon wafers. PDMS polymer and linker (Sylgard 184, Dow Corning) were mixed with a ratio of 10:1 (polymer:linker), degassed and poured onto the wafer. The wafer was previously placed in a holder allowing for the PDMS to be confined to the top of the wafer and to have a thickness of 3 mm. After overnight (**O/N**) incubation at 60°C the PDMS was peeled off the wafer and single modules were cut out.

2.3.1 Centrifugal HoC

This protocol was previously published in Schneider et al., 2019.

The *Centrifugal HoC* is composed of two PDMS layers, the tissue and the media layer. The media and tissue ports were punched through the media layer, with a 0.75 mm biopsy puncher (504529, World Precision Instruments). While the media ports were punched perpendicular into the layer, the tissue inlet was either punched on the side at an angle of 15° (relative to the surface of the upper chip) for centrifugal loading or perpendicular for the hydrostatic flow loading of hydrogels. The media PDMS module was plasma activated for 15 s and the side featuring the channel structure was bonded to the PET membrane, which was previously plasma coated as described in Rogal et al., 2020 (Rogal et al., 2020). The tissue PDMS layer was bonded with its unstructured side to a microscopy glass slide after being plasma activated for 15 s. Both modules were incubated at 60°C for 2 h. The last step consisted of bonding the media and tissue layer structured sides together after both sides were plasma activated for 15 s. The full assembly was incubated at 60°C for at least 2 h. Before usage for experiments, the chips were hydrophilized by plasma treatment for 4 min.

Plasma treatment of substrates was performed with the Diner O_2 plasma machine (13.56 MHz, 50W; Zepto, Diener).

2.3.2 Spheroflow HoC

This protocol is published in Schneider et al., 2022.

The *Spheroflow HoC* system features a tissue layer moulded from the NOA81 resin (NOA81, Norland adhesive), a media module made of PDMS and the PET membrane, sandwiched between the two layers.

The PDMS media layer was fabricated as previously described. All media and tissue ports were punched perpendicular to the media layer with the 0.75 mm biopsy puncher.

For the tissue layer, master moulds, with the inverted channel structures, were made of PDMS. Resin injection ports were punched in the four corners of the PDMS master mould with a 2 mm biopsy puncher (504531, World Precision Instruments). The PDMS master mould was positioned on the glass coverslip substrate with the channel structures being in contact with the glass. The NOA81 resin was dispensed from a 10 mL syringe (BD Plastipak, BD) with a 21 GA cannula (21 GA; KDS212P, Kahnetics) in two of the resin injection ports (both on the same side) of the PDMS master. The resin fills the underlying space between the master mould and the substrate by hydrostatic force, until it reaches the opposite two injection ports. When the master mould was completely full, the resin was cured in the ultraviolet chamber (**UV** chamber, UWAVE) at 188 mJ/cm^2. The PDMS master mould was then peeled off, cleaned with IPA, and stored for reuse. In the meantime, the media layer was assembled as stated in the *Centrifugal HoC* protocol. Afterwards, the prepared media-membrane assembly was plasma treated for 60 s and the surface was covered with a solution of 1% (3-Aminopropyl)triethoxysilane (**APTES**) in de-ionized (**DI**) water (A3648, Sigma-Aldrich) for 10 min. The assembly was then thoroughly rinsed with DI water and blow dried. The media assembly was then aligned on top of the tissue layer and the system was further cured in the UV chamber at 21 J/cm^2. The final chip was incubated O/N at 60°C. The tissue and media channels were rinsed with ethanol to remove any remaining residue and to ensure proper flow, and the chip was left to dry at room temperature (**RT**) until use.

Several variations to the standard protocol were applied based on the experimental design:

PDMS tissue layer

A PDMS layer made with the same channel structures was made using SLA-printed master moulds. The same protocol as the *Centrifugal HoC* was carried out for chip assembly.

O_2 sensors integration

In order to integrate O_2 sensors, a PET foil with deposited sensor spots was provided by a collaborator (Stefanie Fuchs, TU Graz). The PET foil was plasma activated for 60 s and treated with 1% APTES solution for 10 min. After treatment, it was thoroughly rinsed with DI water and blow dried. The PDMS master for resin injection was positioned on top of the substrate, carefully aligning the distal knob regions with the sensor's spots.

TPE media layer

750 µm thick TPE sheets were produced by an external service provider (Fraunhofer Institute for Process Engineering and Packaging IVV, Freising, Germany) starting from commercially available TPE pellets (Mediprene OF400M, HEXPOL TPE AB, Åmål, Sweden). It was essential to achieve a TPE top layer of comparable thickness to the PDMS counterpart, and therefore capable of holding the pipette tips in place when inserted in the ports. For this, three sheets of 750 µm TPE were stacked on top of each other and fused together by placing them in the hotpress (LabEcon 100, Fontijne) and applying T = 130°C and F = 6 kN for 20 min. The fused sheets resulted in a triple TPE layer of approximately 2.25 mm in thickness.

To hot emboss the media features into the TPE, an epoxy master was required. To obtain the epoxy master, the silicon wafer with the media layer structures was used for PDMS casting. After the PDMS was cured, it was detached from the silicon wafer.

To cast the epoxy mould, the PDMS was placed within a casting device, which, once closed tightly, presents two upper holes to hold syringes and one side opening for the vacuum pump attachment. The epoxy resin (09400-010-000300, KauPo Plankenhorn e.K.) was prepared following supplier instructions. In addition, 1:10 of Epic Epoxy Thinner (09400-010-000319, KauPo Plankenhorn e.K.) was added to facilitate casting. Before casting, the epoxy mixture is degassed for 5 min. One 50 mL syringe without the piston was attached to one of the top holes in the epoxy mould tool and the epoxy mixture was slowly poured into it from the top, taking care to avoid air bubble formation. On the other side, another 50 mL syringe was attached, and its piston was steadily pulled to suck the epoxy into the tool, taking care to not let the first syringe run out of epoxy. Several cycles of refilling and pulling were required before completely filling the tool.

To avoid any possible air bubbles after resin filling and curing, the vacuum pump was left running for 24 hrs. After that, the syringes and pump were disconnected, and the tool was placed at 60°C for 24 hrs to complete the curing process. After being completely cured, the solid epoxy mould was removed from the tool and tempered at 80°C for 2 hrs, and then at 150°C for 3 hrs. After cooling down, the epoxy mould was cleaned and could be used to hot emboss the media structures on the TPE substrate. A bottom PMMA sheet of 250 µm thickness, the triple TPE layer and the epoxy mould were sandwiched within two aluminium plates with silicon mats. The sandwich was then inserted in the hot press for hot embossing the media features onto the TPE. The hot embossing parameters were optimized to the following setting: T = 130 and F = 2.5 kN for 20 min.

Single media units and ports were cut out from the hot embossed TPE layer by placing the TPE layer between two 250 µm thick PMMA sheets and laser cutting it with the following parameters:
Power laser 1 = 25%, Power laser 2 = 25%, Total power = 16 W, Speed = 2%, PPI = 200, Air flow = high, Kerf width = 0.26 mm, Number of repetitions = 3.

Assembly of the complete chip was performed without plasma treatment of the TPE. After removing the PMMA foils from the TPE media unit and rinsing it thoroughly with IPA, the PET membrane was placed on the media layer and then the media-membrane assembly was aligned to the to the resin tissue layer. Gentle pressure was applied to the assembly and the chip was UV cured at 21 J/cm^2 and incubated O/N at 60°C. To assure flow and wash away potential TPE residues from the channels, the chip was flushed with IPA and left to dry at RT.

2.4 Skeletal muscle fibre in 3D mould

A 3D master was designed in TinkerCAD and printed in UV curable resin (clear resin, Formlabs) with the stereolithography (**SLA**) printer (Form 3, Formlabs). The printed master was post processed to make it suitable for PDMS moulding. First, it was washed in IPA for 10 min to remove any residual non-cured resin and then further cured through UV exposure

(Form Cure, Formlabs) for 15 min. The cured master was washed again with DI water for 1 h and dried at 60°C O/N. To mould PDMS, the polymer was poured onto it, degassed to remove any air bubble trapped the master corners, and then cured at 60°C O/N. The PDMS was peeled off the moulds and sterilized in 70% EtOH before use.

The PDMS mould was used for the generation of skeletal muscle microtissue by Dr. rer. Nat. Simon Dreher from the Institute for Clinical Chemistry and Pathobiochemistry, Department for Diagnostic Laboratory Medicine, University Hospital Tübingen, Germany.

2.5 Chip injection and culture

2.5.1 Centrifugal HoC loading

Different loading procedures were applied, depending on whether only cardiac spheroids or both cardiac spheroids and the hydrogel were injected.

Centrifugal loading of Spheroids

The chip was first equilibrated by plugging the media ports, inserting a pipette tip containing 100 µL of cell culture media, and centrifuging the chip at 200 × g for 3 min. This removes any air bubbles from the chip channels as well as serving as a quality control to detect any chip leakage. Meanwhile, the pre-formed spheroids are collected and filtered through a 150 µm strainer (43-50150-03, pluriSelect) into a 50 mL tube and left to settle at the bottom of the tube. Afterwards, the media was aspirated, and the spheroids were resuspended in 250 µL/well of RPMI + B27C. 50 µL of media was aspirated from the tissue inlet tip and 50 µL of spheroids suspension was added to it. The chip was centrifuged once again at 200 × g for 5 min to load the spheroids into the chip.

Loading of spheroids and hydrogel by hydrostatic flow

Since loading a cardiac spheroid suspension within a hydrogel by centrifugation was found to be unachievable due to the hydrogel solution viscosity, the chip tissue inlet was then punched perpendicular to the chip surface instead so that the chip could be loaded by hydrostatic pressure.

The following procedure was done on ice. In preparation of the experiment, pipette tips, Eppendorf tubes, and 50 mL tubes were all cooled down to 4°C and the spheroids were prepared as previously described. After the chip was equilibrated with media and the media inlet was sealed, a pipette tip containing 50 µL of media and 50 µL of spheroids suspension was inserted into the tissue inlet and an empty pipette tip was inserted into the media outlet. The hydrostatic flow dragged the spheroids into the tissue chambers. In the meantime, the hydrogel solution was prepared with 3mg/mL FibriCol® (#5133, Advanced BioMatrix) in cell culture media following supplier instructions and FluoSpheres™ Carboxylate-modified (diluted in DI water with a dilution factor = 2×10^{-4}; F8811, Thermo Fisher Scientific) were added in a 1:10 dilution. For the injection of hydrogel, the media outlet tip was exchanged with a new empty tip and the tissue inlet tip was exchanged with a new tip containing 100 µL of hydrogel-FluoSpheres mixture. The chip was then incubated for 90 min at 37°C with

5% CO_2. To avoid clogging of the media channels due to hydrogel polymerization, the media channels were flushed with media and tubing was attached for perfusion.

2.5.2 Spheroflow HoC loading

2.5.2.1 Cardiac spheroids

Chips were sterilized by flushing media and tissue layers with 70% ethanol (EtOH) and incubating O/N at RT. Then, chips were thoroughly rinsed with sterile PBS^- (F1141 Sigma-Aldrich) and equilibrated with pre-warmed media. During these steps, pipette tips with 100 µL media were inserted into all tissue and media ports and air bubbles were removed by manual flushing. Spheroids were collected from the well, filtered through the 150 µm strainer and left for sediment to settle on the bottom of the falcon, before aspirating the supernatant. Spheroids were resuspended in 250 µL/well of fresh RPMI + B27C. 100 µL of media were added to the tissue inlet tip while media in the tissue outlet tip was aspirated. The loading procedure was observed using a microscope to ensure that an adequate quantity of spheroids were injected. If needed, additional spheroids could be added to the inlet tip. 30 µL of spheroids suspension was added at the tissue inlet tip and the hydrostatic flow drove the spheroids into the tissue chamber, where they accumulated due to the channel constriction. The chip was incubated O/N at 5% CO2, 37°C, and 95% relative humidity (**RH**) before the tissue ports were sealed with metal plugs and the media ports were attached to the perfusion system.

2.5.2.2 Skeletal muscle cells

Chips were sterilized by flushing media and tissue layers with 70% ethanol (EtOH) and incubating O/N at RT. The chips were then thoroughly rinsed with sterile PBS^- (F1141 Sigma-Aldrich) and equilibrated with pre-warmed media. During these steps, pipette tips with 100 µL media were inserted into all tissue and media ports, and air bubbles were removed by manual flushing. The hydrogel solutions of 1:5 Geltrex® (A1413302, Thermo Fisher Scientific) or 3 mg/mL TeloCol®-6 (#5225, Advanced BioMatrix) in cloning medium, were prepared. Cells were detached and resuspended to obtain $0.5 \cdot 10^6$ cells in 20 µL of hydrogel solution. Tissue inlet and outlet tips were detached and a 100 µL tip containing 20 µL of hydrogel-cell suspension was inserted into the tissue inlet. Gentle active pressure was applied to the tip to load the hydrogel-cell solution, until some hydrogel could be seen exiting from the tissue outlet while making sure to not let air bubbles into the chip. These loaded chips were incubated O/N at 5% CO2, 37°C, and 95% relative humidity (RH) before plugging the tissue ports with metal plugs, and attaching the chip to perfusion.

2.5.3 Chip culture

For both models, the same perfusion system was used. It comprised of a syringe reservoir with media connected by a cannula (21 GA, KDS212P, Kahnetics) to a 50 cm plastic tube (AAD04103, Tygon), which ends in another cannula plugged into the chip media inlet. At the

media outlet, a shorter plastic tube was connected through the cannula to the chip and its opposing end was inserted into a waste reservoir.

2.5.3.1 Cardiac tissues

The HoC devices were connected to an external syringe pump (LA-190 Landgraf HLL), and continuously perfused with RPMI+B27C medium at a constant rate of 50 µL/h through the media channels. The devices were incubated at 5% CO2, 37°C, and 95% RH. The medium outflow was collected in a waste reservoir. The tissues were regularly observed using an inverted light microscope (DMi8, Leica or Observer 7 ApoTom, Zeiss) that had an integrated incubator.

2.5.3.2 Skeletal muscle tissues

For the first 3 days, the chips were perfused with 50 µL/h of cloning medium to allow the cells to adjust to the hydrogel. Afterwards, the media was switched to POC media, with or without IGF, depending on the experimental conditions. They were perfused with this media for 10 days.

A recirculation approach was designed to minimize wasted POC media. A syringe media reservoir with 10 mL of medium was placed in the syringe pump and perfused through the tubing into the media inlet. At the media outlet, another tubing led to a reservoir syringe without the piston, sealed with air permeable membrane, Breathe-Easy® sealing membrane (Z380059, Sigma-Aldrich) and held vertical by a 3D printed holder. Every 5 days the flow was switched from positive pressure to negative pressure for 3 days and reverted to positive pressure for the remaining 2 days.

2.6 On-chip experimental procedures

Based on the experimental design, stimulation and readouts were carried out in under different conditions.

Whenever video recording was carried out to examine tissue functionality (i.e. during electrical stimulation or drug administration), the *Spheroflow HoC* were located under the microscope, within an incubation chamber where a temperature of 37°C and a 5% CO_2 atmosphere were kept. The perfusion system was kept attached and running.

For long-term experiments of several days, the chips were cultured within the incubator (37°C, 5% CO_2, 99% RH), with the electronic devices (i.e. pacer, optical fibres) connected to them by cables going through the incubator door. The pumping system was kept within the incubator to avoid formation of air bubbles within the media due to temperature changes.

The ALS Incubator *FlowBox* allowed for experiments where the set up needed to be easily accessible to the operator without compromising sterility, controlled temperature, RH, and CO_2 levels. For experiments in the ALS Box the following settings were applied: T = 37°C, RH = 65%; CO_2 = 5%.

2.6.1 Electrical Stimulation

Tissues were paced using the in-house built "*Easypace*", as previously described in Schneider et al., 2022. Summarized, crocodile clips were attached to the fluidic connectors and biphasic pulses were delivered for pacing through the media layer; frequency (Hz), pulses duration (ms) and voltages (V) are stated in the results section of each experiment.

2.6.2 O_2 sensor readout

A PMMA platform was built to allow precise alignment of the sensors with the optical fibres (d = 1 mm, l = 1 m). The platform had cut-outs in which the optical fibres would fit in, which would match the positions of the sensor spots of four *Spheroflow HoC* chips, allowing the reading of up to eight sensors spot simultaneously. Chips were kept in place with magnets. The optical fibres were connected to the phase fluorimeter and the FirePlate (a prototype platform similar to the FireSting pro (Pyroscience) but with 48 channels available instead of four). Using the software Pyro SimplePlateReader v1.42, the phase fluorimeter was set to an illumination intensity of 100% and detection amplification of 400x. Correctly aligned sensors spots must yield a signal intensity above U = 100 mV for every measurement. To calibrate the sensors, a lower calibration point (defined as, $p_{O_2} = 0\%$) and an upper calibration point (defined as $p_{O_2} = 100\%$) were used. For the calibration of $p_{O_2} = 0\%$, a fully deoxygenated solution was perfused at 50 µL/h for at least 1 hour in a cell culture incubator (37°C, 5% CO_2, 99% RH) through two chips. The deoxygenated solution was obtained by dissolving 100g/L of Na_2SO_3 in ultrapure water, which quenches the O_2 dissolved in the water. The average phase shift ($\Delta\varphi$) measured by the four sensors ($\Delta\varphi = 50.5°$) was used for all the following experiments. As the complete rinsing out of the Na_2SO_3 cannot be guaranteed, the chips used for the $p_{O_2} = 0\%$ calibration point could not be used for cell seeding. For the $p_{O_2} = 100\%$ calibration point, each HoC was calibrated before cell seeding. For this, chips were perfused with cell culture media for 1 hour and the $\Delta\varphi$ recorded by each sensor was set as the upper calibration point ($p_{O_2} = 100\%$) for that sensor. When reading O_2 levels, it is important to set the temperature (°C), atmospheric pressure (mbar), humidity (100% in liquid), and salinity of the media (g/L) used. Acceptable values are $50° < \Delta\varphi \leq 53°$ for the $p_{O_2} = 0\%$ calibration point, and $20° \leq \Delta\varphi < 23°$ for the $p_{O_2} = 100\%$.

Regarding data acquisition and graphical representation: for short-term assays (a few hours long), the phase shift was read 1 / s and then averaged to obtain one data point / minute which was then plotted; for long-term assays, the phase shift was read 1 / 10 s and then averaged to obtain one data point / 30 minutes which was then plotted.

2.6.3 Drug injection automation

The uProcess™ (LabSmith) hardware suite included the following: breadboard (uPB-05), EIB200 (USB) uProcess Interface, uProcess software (EIB200), one-piece fitting, interfaces valve with capillary tubing (T132-100), uProcess Manifold for Valve Control 4VM02 (4VM02), uProcess Automated 4-port Selector Valve AV202 (AV202-T132), and tools for component & breadboard installation (LS-HEX, LS-TORX, LS-Screws.25).

The hardware was assembled in the ALS box and the tubings (Tubing, Medical Grade, Tygon® ND 100-80, AAD04091, avantor) were connected to the perfusion system and pre-filled with cell culture media. The valve outlet that would be connected to the chip had a short tube hosting a metal cannula 27G (783-TE727050, AAT Aston) for chip connection. This tube was made as short as possible to minimize the delay between the solution being switched and the new solution reaching the chip. The set up (**Supplementary Fig. 1**) required two pumps, one (pump A) would deliver flow to the valve inlet A and the other (pump B) would deliver flow to the valve inlet B. The perfusion was set to 50 µL/h and the chip was connected to the 4-port valves. The first solution being delivered to the chip, with the valve set to position A, was culture media, while pump B would perfuse a 7.5 µM Oligomycin A (75351, Sigma Aldrich) solution (or just culture media for the control chips) to the waste outlet. Once the chip oxygen level reached an equilibrium, the valve position was switched to B, to deliver the Oligomycin solution. Perfusion of Oligomycin lasted for 40 minutes, during which the syringes in Pump A were exchanged with syringes containing a solution of 2.4 µM Carbonyl cyanide 4-(trifluoromethoxy)phenylhydrazone (FCCP; C2920, Sigma Aldrich) in media and the tubings were equilibrated with this solution. At 40 minutes, the valves were switched back to position A, to perfuse the chip with FCCP for 90 minutes. During this time, the syringes with Oligomycin A in pump B were changed to 3 / 6 µM Rotenone / Antimycin A (R8875 and A8674 Sigma Aldrich) and tubings were equilibrated. After 90 minutes, the valves were switched to position B once again and the solution of Rotenone / Antimycin A was perfused for 40 minutes before stopping the recording. All valve switching steps were scripted for automation with the uProcess™ Software.

2.7 Staining and imaging

2.7.1 Flow cytometry

For flowcytometry analysis, cells were stained first with surface markers in PBS with 1% Bovine Serum Albumin (BSA; A9647-50G, Sigma-Aldrich), and then fixed with 4% Roti®Histofix (P087, Carl Roth). After fixation, cells were permeabilized and blocked with a solution of 0.2% Saponin (8047-15-2, Sigma-Aldrich) + 1% BSA in PBS and stained with intracellular markers in the same solution. In **Table 2.7.1**, a list of all the antibodies used for flow cytometry is reported.

For primary conjugated antibodies, cells were incubated for 10 minutes at RT in the dark. For markers that required primary and secondary antibody staining, the cells were incubated for 30 minutes at RT, washed with 0.2% Saponin + 1% BSA in PBS and stained with the secondary antibody in the same solution for 20 minutes at RT. After each step cells were centrifuged at 200× for 3 min and washed with 0.2% Saponin + 1% BSA in PBS.

For all analyses the following controls were included: unstained control, isotype control for primary conjugated antibodies and secondary antibody only for primary un-conjugated antibodies and FMO controls. Sample acquisition was performed using Guava® easyCyte 8HT, Merck Millipore or BD LSRFortessa™ Cell Analyzer (BD Biosciences) and results

analysis and graphs generation was done with the built-in Guava® easyCyte 8HT software or using FlowJo (ver. 10).

Antibody	Dilution
CD90-APC-Vio770 (REA897; 130-114-905, Miltenyi Biotec)	1:50
cTnT-APC (REA400; 130-120-543, Miltenyi Biotec)	1:50
Vimentin-FITC (REA409; 130-116-663, Miltenyi Biotec)	1:50
Fibroblast Antibody-PE (REA165; 130-126-007, Miltenyi Biotec)	1:11
Anti-NKX2.5 in mouse (259416; MAB2444, R&D systems)	1:100
Anti-WT-1 in rabbit (CAN-R9(IHC)-56-2; ab89901, abcam)	1:100
Anti-ZO1 in rabbit (40-2200, Invitrogen)	1:100
Anti-DDR2 in mouse (3B11E4; ab63337, abcam)	1:100
Goat anti-mouse Alexa Fluor™ 488 (A-11001, Invitrogen)	1:100
Goat anti-rabbit Alexa Fluor™ 488 (A-11008, Invitrogen)	1:100

Table 2.7.1 *Antibodies and respective dilutions used for flowcytometry analyses.*

2.7.2 Immunocytochemistry

2.7.2.1 2D

Cells cultured on Matrigel-coated wells were washed with PBS and fixed using 4% Roti®Histofix for 10 min. For permeabilization and blocking, a solution of 3% BSA + 0.1% Saponin in PBS was used for 30 min. Saponin maintains the integrity of protein surface antigens, however it does not permeate the nuclear membrane making the use of the permeable nuclear dye Hoechst necessary. All the antibodies and the nuclear dye used are reported in **Table 2.7.2**.

The cells were then incubated O/N at 4°C with the primary antibodies in a 1:10 diluted blocking and permeabilization solution in PBS. After incubation with primary antibodies, cells were washed with a 1:10 diluted blocking and permeabilization solution and incubated with secondary antibodies and Hoechst, or for conjugated primary antibodies, just with Hoechst, at 4°C O/N. Cells were finally washed and imaged with the Leica DMi8 microscope for Cardiomyocyes, hiPSC-CF protocol 1 and haCFv; and with Zeiss Observer 7 ApoTome microscope for the hiPSC-CPC, EPC and CF in protocol 2. Negative controls stained with only the respective secondary antibody, or the isotype were acquired.

Images were processed in ImageJ, by removing the background noise of the negative controls from the stained samples.

Primary Antibody	Dilution
Anti-Vimentin in goat (ab11256, abcam)	1:200 for cardiomyocytes
cTnT-APC (REA400; 130-120-543, Miltenyi Biotec)	1:50

Vimentin-FITC (REA409; 130-116-663, Miltenyi Biotec)	1:50 for hiPSC-CF protocol 1 and haCFv.
Fibroblast Antiboy-PE (REA165; 130-126-007, Miltenyi Biotec)	1:50
Collagen I Antibody-APC, anti-human, REAdye_lease™ (REAL958; 130-127-017, Miltenyi Biotec)	1:50
Anti-ZO1 in rabbit (40-2200, Invitrogen)	1:100 for hiPSC-CF protocol 1 and haCFv; 1:200 for hiPSC-EPC protocol 2
Anti-Connexin 43 in rabbit (ab11370, abcam)	1:1000
Anti-NKX2.5 in mouse (259416; MAB2444, R&D systems)	1:500
Anti-WT-1 in rabbit (CAN-R9(IHC)-56-2; ab89901, abcam)	1:50
Anti-DDR2 in mouse (3B11E4; ab63337, abcam)	1:200
Secondary Antibody	
Donkey anti-goat Alexa Fluor™ 546 (A11056, Invitrogen)	1:500
Goat anti-rabbit Alexa Fluor™ 488 (A-11008, Invitrogen)	1:100 for hiPSC-CF protocol 1 and haCFv; 1:500 for hiPSC-EPC protocol 2
Goat anti-mouse Alexa Fluor™ 488 (A-11001, Invitrogen)	1:500
Hoechst 33342 (62249, Thermo Fisher Scientific)	1:500

Table 2.7.2 *Antibodies and dyes with respective dilutions used for 2D staining procedures.*

2.7.2.2 On-chip immunocytochemistry

Spheroflow HoC Cardiac tissue

Using 100 µL pipette tips, tissues were fixed inside the chips at RT for 15 min with 4% Roti®Histofix, and then permeabilized for 15 min with 0.1% Triton X-100 (28314, Thermo Fisher Scientific). The medium layer was removed and blocking solution of 3% BSA was applied on top of the tissue. After incubation of 1 h at RT, the drop was aspirated and the staining solution of 1:50 cTnT-APC, 1:250 4',6-Diamidino-2-phenylindole dihydrochloride (**DAPI;** 1 mg/mL; D9542, Sigma-Aldrich) in 0.1% Saponin, and 0.1% BSA in PBS^- was applied O/N at 4°C. After staining the tissue was washed with PBS^- and flipped onto a glass coverslip for imaging with the laser scanning microscope (**LSM**) 710, Zeiss.

Spheroflow HoC Skeletal muscle tissue

Using 100 µL pipette tips, tissues were fixed inside the chips at RT for 15 min with 4% Roti®Histofix, and then blocked and permeabilized for 30 min with 3% BSA + 0.2% Saponin. A tip containing 100 µL of 1:500 Hoechst and 1:100 Alexa Fluor™ 546 Phalloidin (A22283, Invitrogen) in 0.3% BSA + 0.2% Saponin solution. An empty tip was inserted in the media

outlet to allow for equilibration. The chips were incubated in a humid environment at RT O/N. Chips were then flushed 5 times with a 0.3% BSA + 0.2% Saponin solution before being imaged in the Cell Observer Spinning Disk (Axio Observer.Z1, Zeiss).

2.7.3 Live/Dead staining

2.7.3.1 2D

Wells were media changed with media containing 135 µg/mL propidium iodide (PI; P4170 Sigma-Aldrich), 27 µg/mL fluorescein diacetate (FDA; F7378 Sigma-Aldrich) and 1:1000 Hoechst. After 5 minutes of incubation at 37°C, the wells were washed with PBS and imaged by fluorescence microscopy (DMi8, Leica).

2.7.3.2 On-chip

For cardiac chips cultured under pacing, media containing 1:5000 CellTox™ Green Cytotoxicity Assay (G8731, Promega) was perfused O/N and the chip was imaged by fluorescence microscopy (Observer 7 ApoTom, Zeiss).

Live/dead staining of skeletal muscle tissues was performed under static conditions by incubating the chip in media with 1:5000 CellTox™ Green Cytotoxicity Assay (G8731, Promega) and 1:500 Hoechst, for 15 min. The chip was flushed with fresh pre-warmed media and imaged by fluorescence microscopy (Observer 7 ApoTom, Zeiss).

2.7.4 Raman imaging

Raman imaging and data analysis was performed by our collaborator, Daniel Carvajal Berrio from the Schenke-Layland Lab, Universitätsklinikum Tübingen, Germany.

Raman imaging was performed with a WiTec alpha 300R upright microscope (WiTec GmbH, Ulm, Germany). Spontaneous Raman was excited through a 63x water dipping objective (Zeiss GmbH, Jena, Germany) and a 532 nm laser. Spectral detection was done with a spectrograph with a 600g/mm grating and a charge-coupled device (CCD) camera (WiTec GmbH, Ulm, Germany). Raman spectra were scanned with a 1 x 1 µm resolution, a laser power of 50mW and an integration time of 0.5 seconds. Raman scans were analysed via true component analysis (**TCA**) to detect the main components of the sample. Principal component analysis (**PCA**) analysis was performed to evaluate differences in lipids and protein composition between non electrically stimulated tissue at day 5 and electrically stimulated tissues ad day 14 of culture.

2.8 Effluent assays

2.8.1 LDH-Glo

Cells were seeded in a 96 wellplate format at density of 5,000 cells/well for fibroblasts (phDF, hiPSC-CF, haCFv) and 30,000 cells/well for CMs with 100 µL/well of media. For each media condition and time point, cells were seeded at least in duplicates. Media formulations comprise of: RPMI + B27C, RPMI + B27C + 5 ng/mL bFGF, RPMI + B27C : FGM in ratio 3 to 1, FGM, FibroGro. Wells with media only were included as blanks; and no FCS was added to the fibroblast's media: FibroGro, FGM and DMEM. Samples were collected on different

days. Cells that were not used for sample collection at a specific time point were media changed instead. The samples were collected and analysed following the LDH-Glo (J2380, Promega) instructions. To summarize, 5 µL of media were collected from each well, diluted in 95 µL of LDH Storage Buffer pH 7.3 (200 mM Tris-HCl, 10% Glycerol, 1% BSA in MilliQ) and frozen at −20 °C until analysis. After sample collection, the total release LDH controls from the same wells were generated by adding 2 µL/well of 10% Triton X-100 for 15 min; and another 5 µL were collected and stored. After collection of all the samples, they were thawed at RT and mixed in a white 384-wellplate (781075, greiner Bio-One) at a 1:1 ratio with the LDH Detection Reagent. The samples were pipetted in technical triplicates and the plate was left to rest at RT in the dark for 30 min for fibroblasts and 60 minutes for CMs. The luminescence measurement was acquired with the TECAN Spark plate reader. Data was analysed by removing the media blank signal from the respective samples and total release LDH controls. The sample values were then divided by their total release LDH controls. Finally, for data analysis, the fibroblasts data was normalized over their respective medium (DMEM for phDF and FibroGro or FGM for cardiac fibroblasts) and for CMs over the RPMI + B27C medium.

2.8.2 MTS

Cells were seeded in a 96-wellplate format at density 5,000 cells/well for fibroblasts (phDF, hiPSC-CF, haCFv) and 30,000 cells/well for CMs with 100 µL/well of media. For each media condition and time point, cells were seeded at least in duplicates. Media formulations comprised of: RPMI + B27C, RPMI + B27C + 5 ng/mL bFGF, RPMI + B27C : FGM at a ratio of 3 to 1, FGM, and FibroGro. Wells containing only media were included as blanks; and no FCS was supplemented to the fibroblast media: FibroGro, FGM and DMEM.

Samples were collected on different days. Cells that were not used for sample collection at a specific time point had their media changed instead. The samples were prepared and analysed following the CellTiter 96® AQueous One Solution Cell Proliferation Assay (MTS; G3580, Promega) instructions. To summarize, at each timepoint, 20 µL of CellTiter 96® AQueous One Solution Reagent was added to each well of the 96-well assay plate containing the samples or media controls intended for the respective day. The plates were incubated at 37 °C, 5% CO2 for 2 h for the fibroblasts and for 4 h for the CMs; then the absorbance at 490 nm was measured by the TECAN Spark plate reader. Data was analysed by removing the media blank signal from the respective samples. Then the sample values were normalized over their respective medium (DMEM for phDF and FibroGro or FGM for cardiac fibrobalsts) and for CMs over the RPMI + B27C medium.

2.8.3 Glucose QuantiChrom

The QuantiChrom™ Glucose Assay Kit (DIGL-100, BioAssay Systems) was used for the detection of lactate HoC effluent.

The same effluents of the Lactate-Glo were used to determine the consumption of glucose from the media. Samples were thawed at RT and mixed in 1 mL tubes with the reagent at a ratio of 1:100. Following the kit supplier instructions, the tubes were placed in the pre-heated

(100°C) heat block for 8 min and then cooled down in ice for 4 min. 200 µL of each tube solution was transferred into 3 wells of a clear bottom 96-wellplate and absorbance at 630 nm was acquired with the TECAN Spark plate reader.

A calibration curve was extrapolated out of the absorbance from 6 concentrations points (16.6, 14, 10.5, 7, 3.5, 0 µM) and used to calculate glucose concentration of the samples. Resolution, limit of detection (**LOD**) and limit of quantification (**LOQ**) were calculated as following:

$$Resolution = \frac{Standard\ Error\ of\ the\ Slope}{Slope}$$

$$LOD = 3.3 \cdot Resolution$$

$$LOQ = 10 \cdot Resolution$$

2.8.4 Lactate-Glo

The kit Lactate-Glo™ Assay (J5022, Promega) was used for the detection of lactate HoC effluent.

Chips were perfused for 14 days, and effluent samples were collected at day 3, 5, 7, and 14. To collect effluents, the outlet tubes of the chip perfusion systems were inserted into 2 mL collection tubes, 24 hrs prior to effluent collection. At each time point the effluent samples were frozen at −80°C until analysis. For lactate detection, samples were thawed at RT and mixed in a white 384-wellplate (781075, greiner Bio-One) at a 1:1 ratio with the Lactate Detection Reagent (prepared as per kit supplier protocol). The samples were pipetted in technical triplicates and the plate was left to rest at RT in the dark for 60 minutes. The luminescence measurement was acquired with the TECAN Spark plate reader.

To measure lactate, a calibration curve was extrapolated out of the luminescence signal from 7 concentrations points (200, 50, 12.5, 3.13, 0.78, 0.20, 0 µM); and concentrations of the effluents were then calculated. Resolution, LOD and LOQ were calculated as described in the previous method section (2.8.3 Glucose QuantiChrom).

2.8.5 Drug retention analysis by HPLC-UV

For High-Performance Liquid Chromatography (**HPLC),** an EC-C18 column (695975-902T) with a particle size of 2.7 µm was used. Solute separation was carried out with an isocratic elution for 8 minutes at 1 mL/min using as Eluent A, 20 mM KH2PO4 in water, pH 3.0 (by adding 1M H3PO4) and Eluent B, Acetonitril LC-MS grade.

To collect the chips' effluents, the chips' tissue inlets and outlets were sealed with metal plugs, the drug solutions were loaded into syringes and then connected to the chips with 50 cm long plastic tubings. The tubings were prefilled with the drug solution before starting perfusion, as per standard experimental procedure. Tubings of the same length leading to a tube reservoir were used as a negative control. The system was perfused at the standard

flow rate of 50 µL/h in an incubator (37°C, 5% CO2, 99% RH) for 2 hrs and the chip effluent was collected in a 200 µL tip inserted in the media outlet.

Calibration curves were obtained by measuring the area under the curve of 6 different concentrations points (1, 2.50, 5, 10, 25, 50 µM). The drugs used for this assays were isoproterenol (I5627, Sigma Aldrich) and verapamil (329330010, Thermo Fisher Scientific).

2.9 ImageJ analyses

ImageJ was used for image processing.

2D staining

ImageJ was used to subtract the background signal of the negative controls (secondary antibody only) from the stained samples.

Spheroids diameter analysis

To determine the spheroids diameter, bright field images of the spheroids at day 1 were acquired at 10x with the Leica DMi8 microscope. Using an ImageJ macro, the images were converted to binary and then to masks. The analyse particle option was then used with the following settings: *size = 5000-Infinity µm²*, *include holes* and *exclude on the edges*. The diameter of the spheroids was calculated, approximating their shape to a circle, using the formula: $d = 2\sqrt{A/\pi}$.

2.10 OpenHeartWare analyses

Brightfield videos of beating cardiac tissues were recorded with a frame rate of at least 30 fps. The previously developed software OpenHeartWare (**OHW**; https://github.com/loslab/ohw) was used for the analysis of beating parameters, with a block width of 16 pixels, delay of 2 frames and maximum shift of 7 px. Beating rate (beat/min), maximum contraction and relaxation (µm/s) and mean intervals between contraction-contraction peaks, relaxation-relaxation peaks and between contraction-relaxation peaks (s) were extrapolated. Additionally, the software displayed motion vectors which indicated the direction and amplitude of the tissue displacement.

2.11 Statistical analysis

Statistics and reproducibility of chip study design: Each *Spheroflow HoC* contains two independent tissues, which were considered technical duplicates during one experimental run. Every experiment was repeated 3 times, where each chip/condition was considered a biological replicate. For all graphs with a statistical analysis, the minimum sample size of independent replicates is 3.

The graphical representation of data and whether the error is represented by standard error of the mean (**SEM**) or standard deviation (**SD**) are described in each Figure caption. The number of independent experiments and biological replicates are detailed in each Figure caption. Whenever statistical analysis was performed, the statistical test used is reported in

the Figure caption. In general, data was always tested for normality and Student t-test, One-way, or Two-way ANOVA were performed for comparison between two or more groups respectively. If the data did not follow normality distribution, non-parametric tests were performed. Graphpad Prism software (version 9.3.1), with the threshold for significance set at $p < 0.05$ was used for data analysis.

3 Results

In this section, scientific findings regarding i) the differentiation and characterization of hiPSC-CMs and CFs, ii) the validation of the heart tissue culture on two HoC platforms and iii) the establishment of compatible readout technologies will be reported. Lastly, the suitability of one of the developed platforms for the generation of skeletal muscle tissues on-chip is demonstrated.

3.1 Differentiation and characterization of cardiomyocytes and cardiac fibroblasts

To provide a robust basis for the on-chip experiments, first hiPSC maintenance and differentiation protocols for CMs and CFs had to be established. Here, I explored the possibility to avoid use of undefined media and plate-coating for hiPSC maintenance and tested two different protocols for CFs generation. I benchmarked them by comparing protein expression of relevant markers with haCFv and phDF. Finally, I optimised a common media for co-culture of CMs and fibroblasts, and defined their aggregation capability.

3.1.1 hiPSC maintenance and cardiomyocytes differentiation

Although hiPSCs were cultured in TeSR-E8, an animal component-free medium, the previously established protocol for hiPSC maintenance and differentiation still included plating on Matrigel and freezing cells in culture medium with the addition of 10% FCS, which are both animal derived components of undefined composition and batch-to-batch variability. Therefore, suitable alternatives for coating and freezing hiPSC without affecting their viability and morphology were explored. rhVTN-N was chosen for coating because it is chemically defined and xeno-free, while ibidi Freezing Medium Classic was selected as a chemically defined freezing medium.

From the same batch, the same number of cells were frozen in either TeSR-E8+10% FCS+10% DMSO+10 µM RI or ibidi Freezing Medium Classic+10 µM RI. After 3 weeks of cryopreservation, hiPSC were thawed and seeded as single cells at 25 000 cells/cm^2 on Matrigel or rhVTN-N in the presence of 10 µM of apoptosis inhibitor RI. After 24 hrs, cells frozen in ibidi Freezing Medium Classic showed higher recovery compared to cells frozen in TeSR-E8+10% FCS+10% DMSO. Cell adhesion and survival were comparable between Matrigel and rhVTN-N substrates (**Fig. 3.1.1 A**). In all conditions, the single cells retained the same morphology. On day 3, it is possible to see that cells frozen in ibidi Freezing Medium Classic retain the ability to form tightly packed colonies with defined borders. The colonies' morphology and growth rate are comparable on both substrates (**Fig. 3.1.1 B**). Therefore, both the ibidi Freezing Medium Classic and the use of rh-VTN are suitable for expansion of hiPSC in chemically defined conditions.

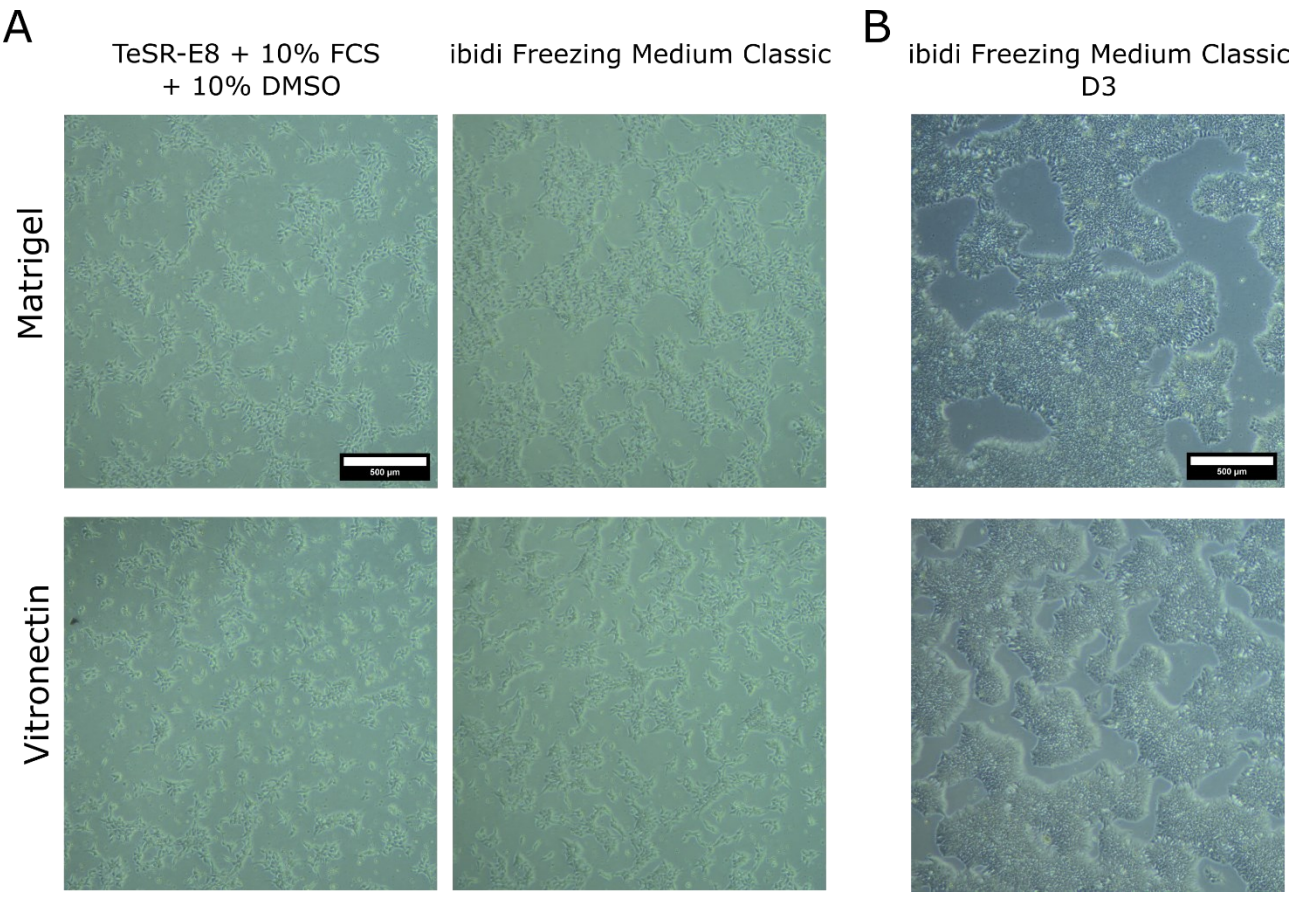

Figure 3.1.1 *hiPSC culture under chemically defined culture conditions.* ***(A)*** *Day 1 of hiPSC, previously frozen in TeSRE8 medium + 10% FCS + 10% DMSO or ibidi freezing medium classic, plated on Matrigel or Vitronectin (rhVTN-N).* ***(B)*** *Day 3 of hiPSC colonies previously frozen in ibidi Freezing Medium Classic on Matrigel and hr-Vitronectin. Scale bar = 500 µm.*

The differentiation protocol is based on the modulation of the Wnt/β-catenin signalling pathway by small-molecule manipulation. The first step consists of the activation of the pathway by the GSK-3α/β inhibitor, CHIR99021, followed by the inhibition of the pathway by the porcupine inhibitor, IWP-4. The medium was then switched to the maintenance medium which contained insulin (**Fig. 3.1.2 A**).

On day 15, the differentiated CMs were detached from the well. CMs were replated and stained for the cardiac troponin T marker (cTnT), and the Vimentin marker, a commonly used fibroblasts marker. Even though most of the cells expressed cTnT, they also showed a low expression of the vimentin marker (**Fig. 3.1.2 B**). This was confirmed by the additional flow cytometry analysis of CMs co-stained with cTnT and Vimentin or CD90 (**Fig. 3.1.2 C**). Differentiated CMs showed a high percentage of cTnT+ cells, with a part of the population also positive to vimentin (18.3%). On the contrary, almost no cTnT+ cells co-express CD90 (1.09%), another commonly used marker for the detection of fibroblasts. This protocol has also been successfully transferred to the E1 hiPSC-cell line.

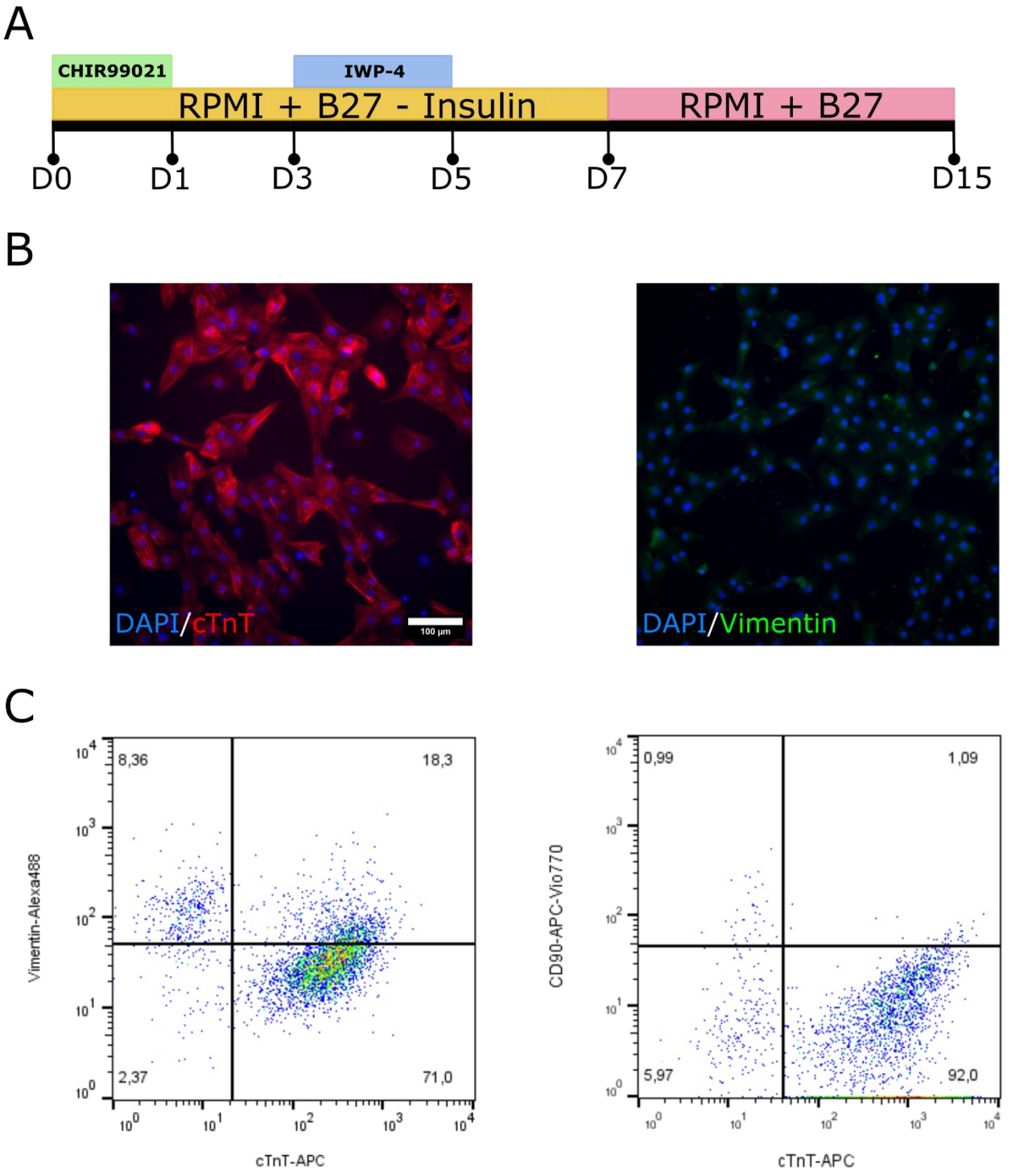

Figure 3.1.2 *Cardiomyocyte differentiation, GM25256 hiPSC-line.* ***(A)*** *hiPSC differentiation protocols adapted from* Lian et al., 2013. ***(B)*** *Representative images of hiPSC-CMs, fixed and stained for DAPI, cTnT (red) and Vimentin (green) (scale bar = 100 µm).* ***(C)*** *Representative flow cytometry graphs of CMs on day 15 of differentiation, stained for cTnT, CD90 and Vimentin.*

After differentiation, CMs could be either replated or cryopreserved. To assess whether replating or cryopreservation could affect the CMs purity, they were dissociated on day 15 of differentiation. One part of the cells was directly evaluated by flowcytometry for cTnT, one

part was replated, and one part was cryopreserved. After being replated, the CMs were kept in culture for 3 days before their cTnT+ cell content was determined by flowcytometry. The cryopreserved fraction was also thawed and kept in culture for 3 days before flowcytometry.

In **Fig. 3.1.3 A**, the purity of three independent differentiation is shown at day 15, after replating and after cryopreservation. In all three replicates, their purity is not compromised by replating and freezing procedures. The average purity had been shown to slightly increase during replating (from 67% to 73%) and cryopreservation (78%). Additionally, lactate treatment of the differentiated CMs can further enhance their purity.

The protocol consists of using medium without of glucose, the main energy source for cells, supplemented with Na-lactate instead. While most of the contaminant cell types would die of starvation, the CMs, which are able to metabolize lactate, will switch their metabolism from glucose to lactate, surviving the treatment. With this method, the purity of CMs derived from both cell lines can be significantly enriched, resulting in an approximately 26% cTnT+ cells increase (**Fig. 3.1.3 B**).

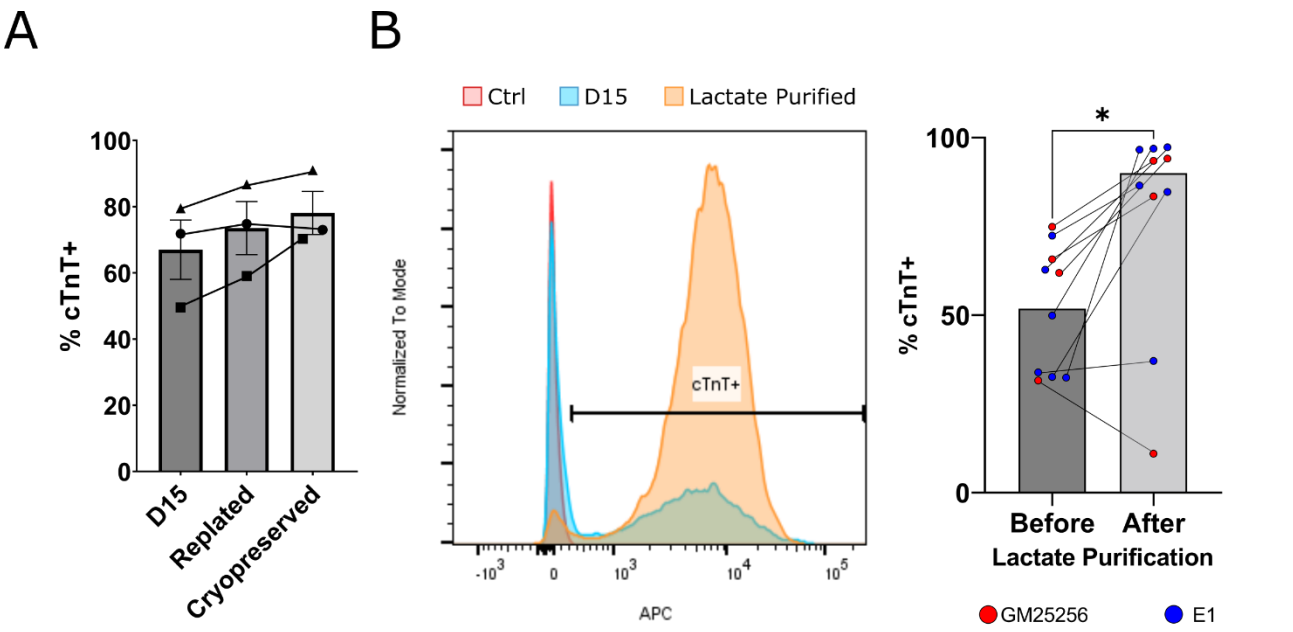

Figure 3.1.3 *Cardiomyocytes purity characterization.* ***(A)*** *hiPSC-CMs purity (% cTnT+) at day 15 (D15), 3 days after replating (Replated) and 3 days after thawing from cryopreservation (Cryopreserved). hiPSC-line used GM25256 (N=3). Bar plot of the average purity ± SEM.* ***(B)*** *Flow cytometry analysis of CMs at day 15 of the differentiation before and after lactate purification protocol. On the left, a representative histogram showing cTnT+ cells at D15 (blue) and after lactate purification (orange), compared to the negative unstained control (red). On the right, a bar plot of the average percentage of cTnT+ cells before and after the lactate purification protocol. Each line connects data points of the same differentiation (N) before and after lactate purification. Data from hiPSC-line GM25256 (N=4) and hiPSC-line E1 (N=6). Data was analysed by Wilcoxon test. * p ≤ 0.05.*

3.1.2 Differentiation of cardiac fibroblasts

As CFs are interspersed within the cardiac tissue and support CMs functionality, it was important to develop isogenic CFs to be added to the hiPSC-CMs. Therefore, hiPSC derived CFs were differentiated following two different protocols (**Fig. 3.1.4** and **Fig. 3.1.5**). The first protocol (**Fig. 3.1.4 A**) consists of an initial treatment of 24 hrs with CHIR followed by induction of CF differentiation through the addition of bFGF for 18 days in CFBM (high glucose DMEM containing HLL, Ascorbic acid, GlutaMAX, Hydrocortisone Hemisuccinate and rh Insulin). The differentiated CFs were stained for different fibroblasts markers and compared to the haCFv which were stained in the same way (**Fig. 3.1.4 B**). Both hiPSC-CF and haCFv were positive for the commonly used intracellular marker Vimentin (**Fig. 3.1.4 B-C**). However, they present differing expressions of the surface fibroblast marker (FSP-1), with haCFv cells presenting a higher expression compared to both hiPSC-CF and phDF in the flow cytometry analysis (**Fig. 3.1.4 B-C**). Even though, both hiPSC-CF and haCFv show almost no expression of Zonula occludens-1 (**ZO1**); the hiPSC-CF have a higher expression level of Cx43, which is involved with ZO1 in the gap junction formation. Additionally, hiPSC-CF seems to produce more collagen (**Col1A1**) compared to their primary adult counterpart. The flow cytometry analysis of the different fibroblast populations (phDF, hiPSC-CF and haCFv), confirmed the expression of Vimentin and the Fibroblast Marker in the CF populations, while the expression of CD90, which has been used as a cell surface marker for some fibroblast populations, was uniform in phDFs and haCFv while being completely absent in hiPSC-CF (**Fig 3.1.4 C**).

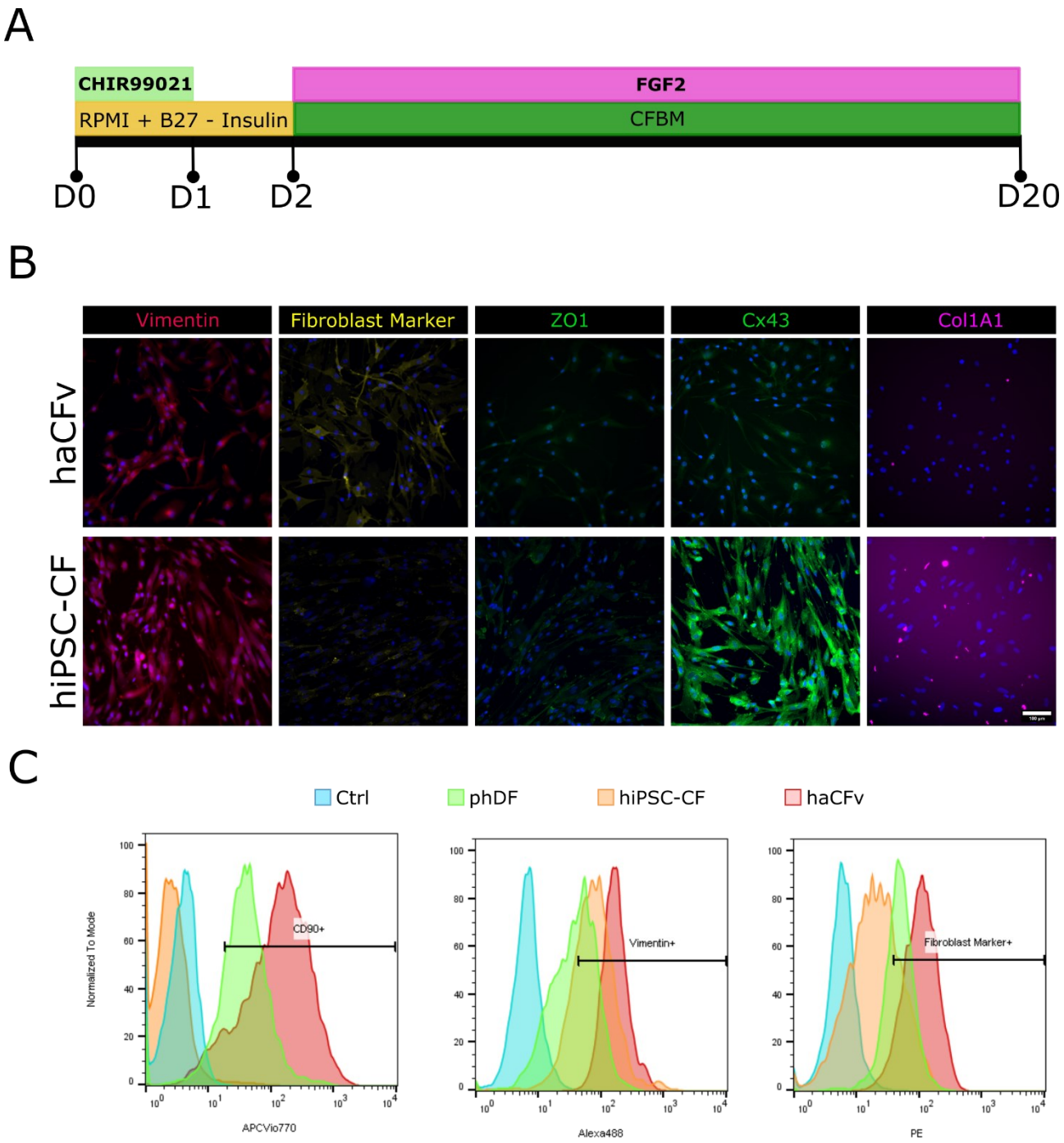

Figure 3.1.4 *Cardiac fibroblasts differentiation protocol 1.* ***(A)*** *Schematic of the differentiation protocol derived from* J. Zhang et al., 2019*.* ***(B)*** *Immunocytochemistry comparison of hiPSC-derived CF and haCFv. Nuclear stain DAPI (blue); (scale bar = 100 µm).* ***(C)*** *Flowcytometry analysis of phDF (green), haCFv (red) and hiPSC-CF (orange) using different fibroblasts markers (CD90, Vimentin, Fibroblast marker). In blue the negative control of unstained phDF.*

In the second CF differentiation protocol tested (**Fig. 3.1.5 A**), hiPSC are driven through the cardiac developmental pathway. Starting with the modulation of the Wnt/β-catenin signalling pathway by small-molecule manipulation, cells reach the CPC stage at day 5. CPCs were confirmed by immunocytochemistry for the cardiac mesodermal gene, NKX2.5. From day 5 to day 12, CPCs undergo differentiation through the addition of CHIR and Retinoic Acid

between day 6 and 8. On day 12, they reach the EPC stage, characterized by the expression of WT-1 and ZO1. In the last 6 days of differentiation, the commercial medium (FGM) was supplemented with bFGF and TGFβ to direct the EPCs towards the CF fate. At day 18 the cells express the fibroblasts marker DDR2. For all the differentiation stages, cells were also characterized by flowcytometry using the stage-specific markers (**Fig. 3.1.5 B**). Throughout the distinct stages of cellular development, the majority of cells expressed stage-specific markers, with 88% of the CPC being NKX2-5+ and 96% and 90% of EPC being WT+ and ZO1+ respectively. Again, the final hiPSC-CF were positive for the DDR2 (97%), however only a small fraction (13%) of DDR2+ cells also expressed the fibroblast marker CD90.

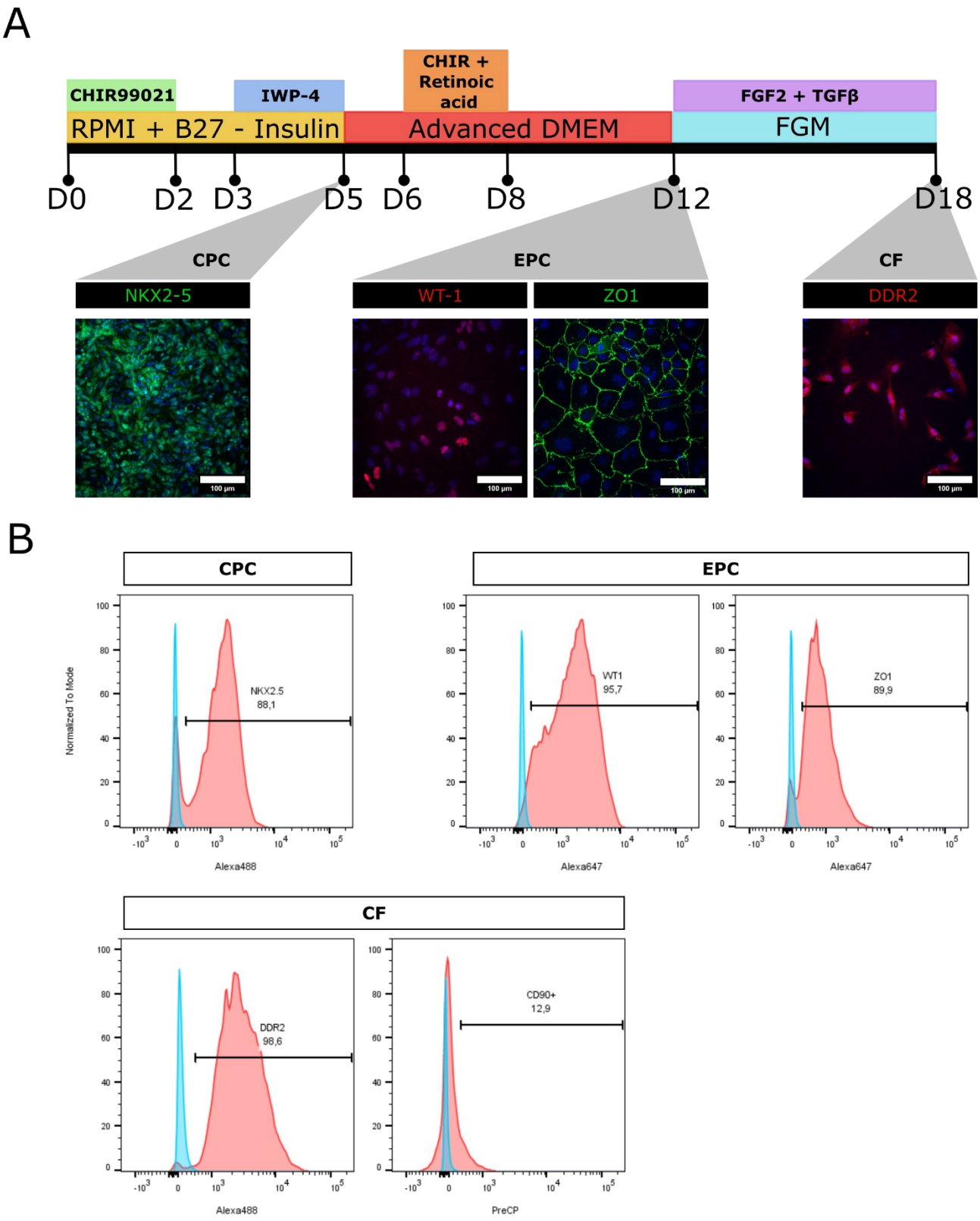

Figure 3.1.5 *Cardiac fibroblasts differentiation protocol 2.* ***(A)*** *Schematic of the differentiation protocol derived from* H. Zhang et al., 2019*, and immunocytochemistry of stage-specific progenitors (CPC = cardiac progenitor cells; EPC = epicardial progenitor cells, CF = cardiac fibroblasts). Nuclear stain Hoechst (scale bar = 100 µm).* ***(B)*** *Flowcytometry analysis of the differentiation stage-specific progenitors with specific markers (NKX2-5, WT-1, ZO1) and of resulting hiPSC-CF using the fibroblasts markers CF90 and DDR2. In blue the negative control of unstained hiPSC-CF.*

3.1.3 Media optimization for co-culture of cardiomyocytes and fibroblasts

CMs and CFs have different nutritional requirements and therefore are typically maintained in different media. CMs were cultured in RPMI+B27C, phDF in DMEM (high glucose, stable glutamine) and CFs (both hiPSC-CF and haCFv) can be cultured in either FibroGRO™ or Fibroblast Growth Medium (FGM). Therefore, the different types of fibroblasts were plated and cultured either in RPMI+B27C or their respective medium, as control condition, for 3 days. Lactate dehydrogenase (**LDH**) release and their metabolic activity (**MTS**) (**Fig. 3.1.6 B**) in RPMI+B27C were measured each day and normalized on the values of the control condition (**Fig. 3.1.6**).

The release of lactate dehydrogenase into the cell culture medium happens upon disruption of the cellular plasma membrane and is a widely used marker of cytotoxicity. In **Fig. 3.1.7 A**, phDF shows low levels of LDH, during the 3 days of culture; contrary to this, both hiPSC-CF and haCFv present levels of LDH far above their baseline, 7±2 and 17±5-folds higher than the control condition at day 3. This suggest that, while the RPMI+B27C do not exert a cytotoxic effect on phDF, it does on CFs. These results are supported by the MTS assay data (**Fig. 3.1.6 B**). The metabolic activity of phDF measured in RPMI+B27C remains close to the baseline over the three days (0.92±0.02 on day 1, 0.91±0.05 on day 2 and 0.86±0.05 on day 3). Both hiPSC-CF and haCFv cells shows a decreased metabolic activity compared to their native medium over the 3 days, with an average metabolic activity on day 3 of only 0.567±0.006 and 0.18±0.01-folds the control condition, respectively.

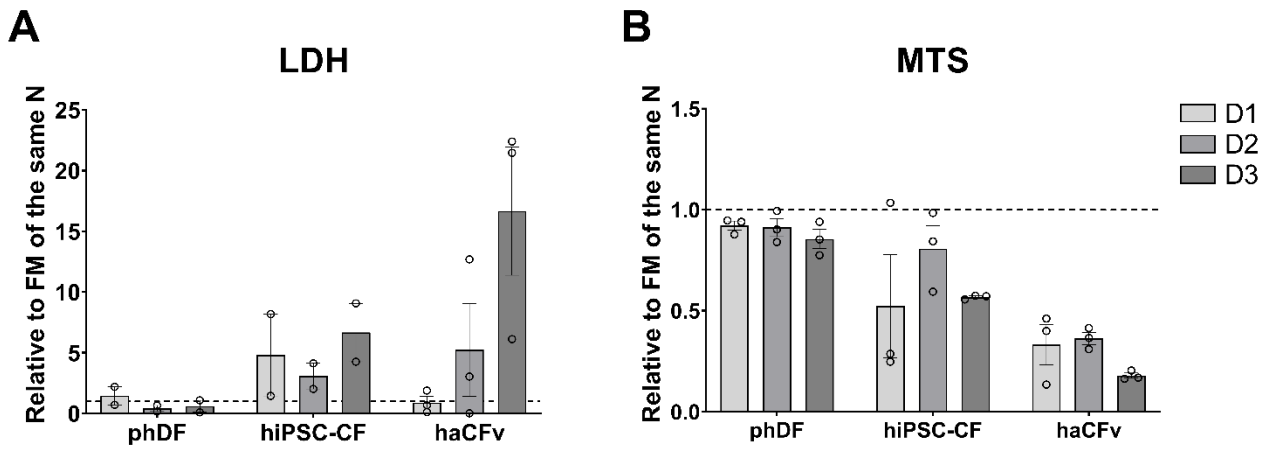

Figure 3.1.6 *Assessment of media compatibility of cardiomyocyte medium with fibroblast types: primary dermal fibroblasts (phDF), hiPSC-derived cardiac fibroblasts (hiPSC-CF), human adult ventricular cardiac fibroblasts (haCFv). Fibroblasts were plated and cultured for 3 days (D1, D2, D3) in RPMI+B27C. The levels are normalized onto the corresponding fibroblasts medium.* ***(A)*** *Lactate-dehydrogenase fluorometric assay (LDH).* ***(B)*** *MTS absorbance levels. The dotted line represents the fibroblast medium level of y = 1. Bar plots represent the average ± SEM.*

As the CMs medium does not support CFs viability, two alternative formulations of co-culture medium were tested. The formulations are based on the CMs medium, called “RPMI”, as CMs are the main cell type of interest in this study. The formulation called “bFGF” includes the addition of 5ng/mL bFGF to the RPMI+B27C medium. bFGF binds to fibroblast growth factor receptor proteins and promotes cell survival and proliferation. The other formulation, named “3to1”, included mixing the RPMI+B27C with the FGM in a ratio of 3 parts to 1 part, to provide, in addition of bFGF, other nutrients present in the FGM basal medium. I opted for this specific media ratio as it matches the ratio of CMs to fibroblasts that I intend to combine for co-culture. The LDH and MTS assays were performed on haCFv cultured in these media again. RPMIwas used as a negative control condition while Fibroblasts Growth Media, named “FGM”, was used as a positive control condition and as baseline.

Over 7 days of culture, haCFv showed higher LDH release compared to the base line, starting at day 3 for both RPMI+B27C and bFGF supplemented media. Only the “3to1” mix medium, showed reduced release of LDH by the haCFv, with an average level comparable to the baseline on day 7 (1.1±0.5-folds) (**Fig. 3.1.7 A**). These results were supported by the metabolic activity assay (**Fig. 3.1.7 B**) where, after the first day of culture, the RPMI and bFGF samples showed already a decreased metabolic activity relative to the baseline. Also, in this assay the mixed medium “3to1” performed similarly to the FGM control (1.0±0.3-folds), presenting therefore the best alternative medium for haCFv in co-culture.

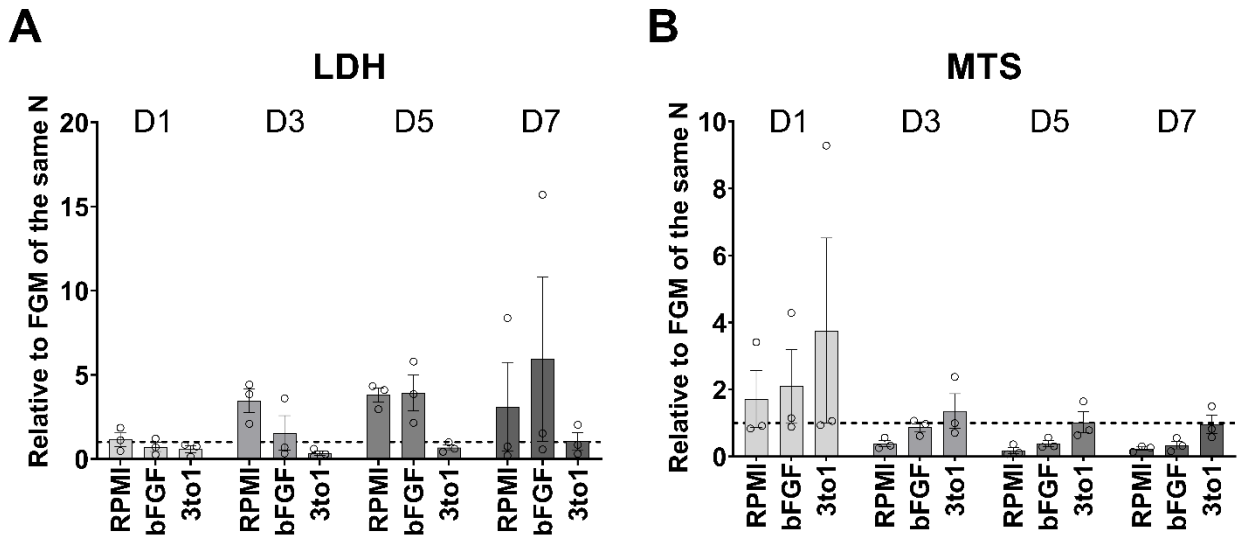

Figure 3.1.7 *Assessment of co-culture medium compositions on haCFv. Media compositions: RPMI = RPMI+B27C, bFGF = RPMI+B27C + 5ng/mL bFGF, “3to1” = RPMI+B27C mixed with FGM in 3 to 1 ratio, FGM = fibroblasts growth medium. Fibroblasts were plated and cultured for 7 days and readings were performed on days 1, 3, 5 and 7 (D1, D3, D5, D7). The levels are normalized onto FGM.* ***(A)*** *Lactate-dehydrogenase fluorometric assay (LDH).* ***(B)*** *MTS absorbance levels. The dotted line represents the fibroblast media level of y = 1. Bar plots represent the average ± SEM.*

The same assays were performed on a monoculture of hiPSC-CMs (**Fig. 3.1.8**). For the CMs the RPMI medium was used as baseline control. The release of LDH (**Fig. 3.1.8 A**) was comparable between all the media and the baseline on the first 5 days. On day 7, there was a spike in LDH release for the FGM medium in one of the replicates. The bFGF and "3to1" media have comparable average LDH levels of 1.9±0.2 and 1.8±0.1-folds the baseline. Regarding the metabolic activity of CMs in the different media (**Fig. 3.1.8 B**), the media alternatives "3to1" and FGM showed metabolic activity after day 1 several folds above the baseline and the RPMI medium supplemented with bFGF only. Additionally, the "3to1" medium showed metabolic levels similar to the FGM medium from day 3 to day 7. At day 7, CMs in "3to1" medium and FGM medium showed 9.4±0.3-folds and 10±1-folds higher metabolic activity compared to RPMI medium. This suggests that, even diluted, some components of the FGM medium affects the metabolic activity of the CMs.

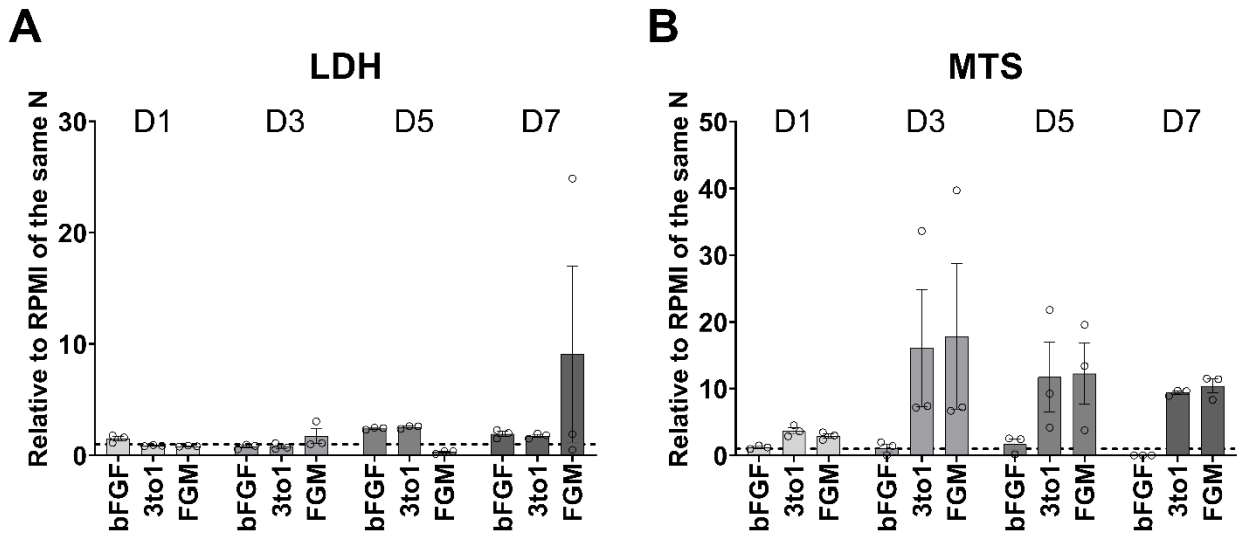

Figure 3.1.8 *Assessment of co-culture media compositions on hiPSC-CM. Media compositions: RPMI = RPMI+B27C, bFGF = RPMI+B27C + 5ng bFGF, "3to1" = RPMI+B27C mixed with FGM in 3 to 1 ratio, FGM = fibroblasts growth medium. CMs were plated and cultured for 7 days and readings were performed on days 1, 3, 5 and 7 (D1, D3, D5, D7). The levels are normalized onto RPMI.* ***(A)*** *Lactate-dehydrogenase fluorometric assay (LDH).* ***(B)*** *MTS absorbance levels. The dotted line represents the RPMI medium level of y = 1. Bar plots represent the average ± SEM.*

3.1.4 Cardiac spheroid formation

One of the main goals of the project is to obtain a cardiac model within a microfluidic device. The tissue generation concept, using spheroids as building blocks, was designed to achieve three key points: (I) achieving physiological densities and cell-cell contacts; (II) obtain a 3D tissue with the structural organization of the heart tissue; (III) possibility to integrate other relevant cell types (i.e., fibroblasts) within the tissue.

The tissue formation (**Fig. 3.1.9 A**) consists of pre-generating cardiac spheroids as 3D building-blocks from differentiated CMs and fibroblasts, which subsequently fuse into a

uniaxially aligned cardiac muscle fibre. The aggregation protocol was tested first with single cell type (CMs, phDF, haCFv) in their own media to verify their aggregation capabilities (**Fig. 3.1.9 B**). Spheroids were obtained by seeding 0.5 10^6 cells into an AggreWell™400 (STEMCELL Technologies) format, resulting in around 1200 spheroids with a diameter ≤ 150 µm, which are suitable for seeding in the microfluidic devices. Differentiated CMs of high purity (≥ 90%) could not form compact and spherical aggregates but resulted in irregular-shaped clumps of few cells, while the majority of the cells remained as singles cells. The phDF alone formed compacted, round-shaped, cell spheroids with smooth edges; these spheroids were able to withstand shear stress without falling apart. HaCFv formed loosely packed cell spheroids without a defined smooth edge, which easily fell apart upon shear stress. Mixing fibroblasts with the CMs (**Fig. 3.1.9 C**) improved aggregation. Again, while the addition of 25-30% of phDF was enough to achieve compact round spheroids in RPMI+B27C, adding haCFv to the CMs in "3to1" medium produced loose cardiac spheroids similar to the haCFv monoculture, which did not withstand shear stress. Analysis of the spheroids' diameters (**Fig. 3.1.9 D**) showed a significant difference in the compaction of phDF and haCFv with an average diameter of 112 ± 8 µm (standard deviation) and 139 ± 5 µm respectively. When mixed with CMs, the phDF allows the formation of cardiac spheroids (CM+phDF) of 120 ± 7 µm diameter on average, significantly smaller than the cardiac spheroids with haCFv (138 ± 8 µm), which have comparable diameter to the haCFv monoculture.

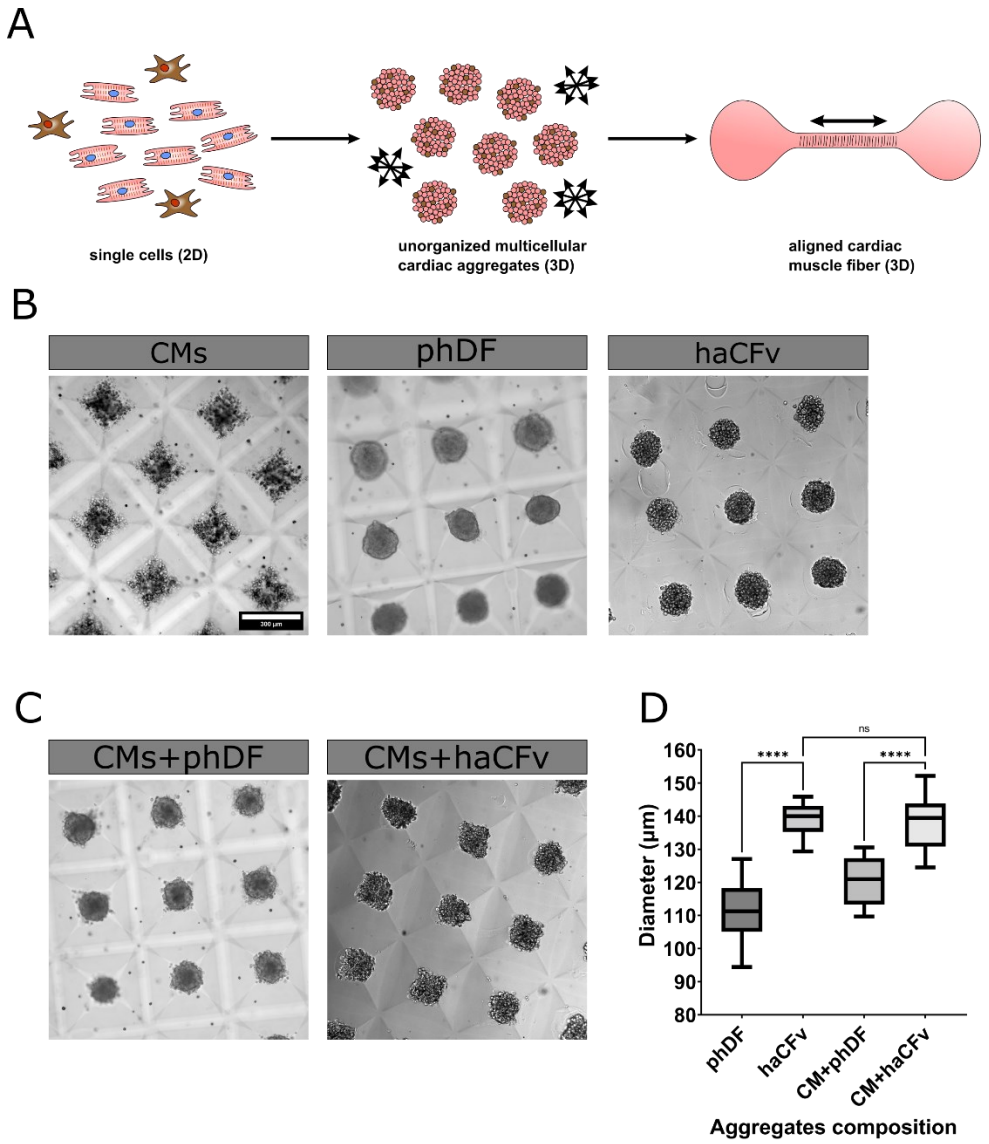

Figure 3.1.9 *Cardiac aggregation concept and performance.* ***(A)*** *Schematic of generation of aligned cardiac fibres, taken from* Schneider et al., 2022 *(available under the CC BY 4.0 license). Starting by mixing single cell populations of CMs with fibroblasts in a defined ratio, which will form spherical 3D spheroids of a homogenous size. Spheroids are used as 3D building blocks to fuse into an aligned tissue fibre, guided by the provided chamber shape. Double headed arrows indicate alignment direction.* ***(B)*** *Spheroids made of a single cell type. CMs = hiPSC- CMs of purity ≥ 90%, primary dermal fibroblasts (phDF), human adult ventricular cardiac fibroblasts (haCFv). Scale bar = 300 µm* ***(C)*** *Spheroids containing 2 different cell types: CMs+phDF = 70% CMs + 30% phDF, CMs+haCFv = 75% CMs + 25% haCFv.* ***(D)*** *Box and whiskers plot of the diameter of spheroids with different cell composition, obtained by seeding 0.5 · 10^6 cells into a 24-wellplate format AggreWell™. phDF (N=36), haCFv (N=9), CM+phDF (N=8), CM+haCFv (N=9). Whiskers extends from min to max values. Data was analysed by One-way ANOVA. * p ≤ 0.05; ** p ≤ 0.01; *** p ≤ 0.001; **** p ≤ 0.0001, ns = non significative.*

Based on the media optimization results and the spheroids experiments, a mixture of 25% phDF and 75% hiPSC-CMs with a purity ≥ 80% was chosen for all further experiments.

3.2 Cardiac tissue formation in HoC systems

In the framework of this project, two HoC platforms have been established featuring different cell loading concepts, centrifugal loading of single cell suspensions and convective flow loading of spheroids. I then describe different loading approaches of cardiac aggregates with or without hydrogel within the platforms and validate them for tissue formation and culture.

3.2.1 Spheroids and hydrogel integration within the Centrifugal HoC platform

The first HoC system tested was the previously developed *Centrifugal HoC* (O. Schneider et al., 2019), with the aim of introducing spheroids instead of single cells and integrating ECM components in the tissue.

The *Centrifugal HoC* consists of two PDMS layers, called tissue layer and media layer, separated by an isoporous membrane that allows the diffusion of dissolved medium components between them. The tissue layer features a main channel tilted at 45° with respect to the long side of the rectangular chip (**Fig. 3.2.1 A**); this channel branches into eight tissue chambers with the shape of a dog-bone. The knob regions of the dog bone shape offer two adhesion areas at the ends of the shaft region, where the cells self-organize in a cardiac aligned fibre. Compared to the original design the dimensions of the tissue chambers had to be adjusted to accommodate the cardiac spheroids. The height of the chamber was changed from 100 µm to 150 µm and the width of the shaft region from 150 µm to 200 µm, while the length of the chamber was kept 1 mm long.

The media layer comprises of a media channel that splits in eight independent channels providing media to each tissue before joining back together to exit in the media outlet. An isoporous membrane is placed at the interface of the tissue and media layer (**Fig. 3.2.1 B**), acting as an endothelial-like barrier, by protecting the tissue from shear stress while enabling diffusion of nutrients and waste metabolites between the layers, while the convective media flow remains confined to the media layer. For easy handling, the chip was mounted on a microscope glass slide.

The loading procedure consists of inserting a pipette tip with the cell suspension in the chip tissue inlet, sealing the media in- and outlet to avoid convective flow, and placing the platform in a falcon tube for centrifugation (**Fig. 3.2.1 C**). During centrifugation, the cells travel through the main tissue channel and start filling each chamber consecutively (**Fig. 3.2.1 D**). As the cells reach the first tissue chamber, they are trapped in the dead-end tissue chamber and start filling it. Once the first chamber is completely full, the following chamber will start filling. This ensure that during loading each chamber is densely packed; and if the proper number of cells (100,000 cells/chip) is loaded, all 8 tissue chambers will be completely filled, generating eight non-connected, cardiac tissue replicates. Reducing the number of cells will result in fewer chambers being filled and therefore fewer replicates. However, if an excessive number of cells is introduced, the additional cells will start filling the main channel connecting the neighbouring tissues, which cannot be considered anymore as independent replicates.

.

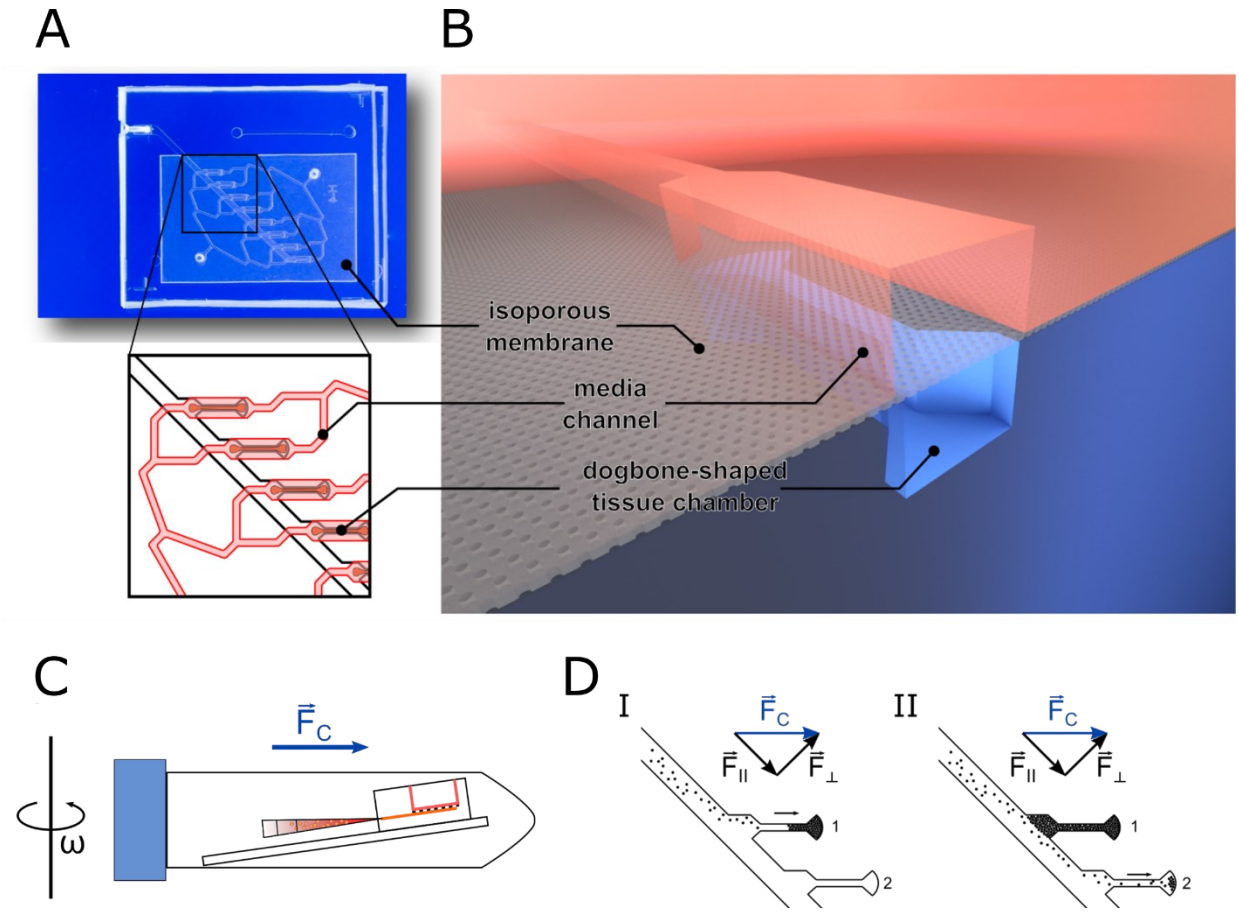

Figure 3.2.1 *Centrifugal HoC design adapted from* Schneider et al., 2019 *(available under the CC BY 4.0 license).* ***(A)*** *Photo of the HoC platform. The main channel, tilted by 45° with respect to the central axis, splits in eight parallel, dog bone-shaped tissue chambers. The zoomed-in schematic shows the parallelized medium supply of individual chambers.* ***(B)*** *Chamber side view highlighting the 3 layers forming the chip platform. The tissue layer (blue) is separated from the top media layer (red) by an isoporous membrane (grey).* ***(C)*** *Schematic of the system during centrifugal cell injection. A pipette tip containing cell suspension is inserted in the chip tissue inlet. The chip is then inserted into a falcon tube and centrifuged at rotational speed (ω) = 200 × g.* ***(D)*** *Illustration of the sequential loading of the chambers. Due to the 45° inclination of the main channel, the individual tissue chambers are filled subsequently.*

The same loading concept used to load single cells was applied to load cardiac spheroids (**Fig. 3.2.2 A**). To introduce physiologically relevant ECM, a collagen I hydrogel (FibriCol®), which is the most abundant ECM component in the cardiac interstitial matrix, was tested for loading into the platform.

While hydrogels could be loaded in an empty chip by centrifugation, centrifugation was not a viable solution when injecting both spheroids and hydrogel. Firstly, in a sealed chip, the hydrogel could not displace the media that had already filled the chip during the equilibration step. Secondly, due to the high viscosity of the hydrogel, the spheroids were unable to settle within the chambers during centrifugation. Therefore, using the same chip design, the loading process was carried out taking advantage of hydrostatic pressure instead. A perpendicular tissue inlet was punched through the media layer and the hydrogel was

loaded by a tip in the tissue inlet, while an empty pipette tip was placed in the tissue outlet. In this way the hydrostatic flow through the membrane allowed the displacement of the liquid media towards the media outlet while the hydrogel slowly filled the tissue channels. However, this procedure was possible only with hydrogels of low viscosity. After 90 min of incubation at 37 °C, 3 mg/mL FibriCol® polymerized in a 3D hydrogel completely filling the tissue chamber. To avoid clogging of the media channels, after hydrogel injection, the media channels are flushed with media to remove any hydrogel that may have passed through the membrane pores. The hydrogel can be visualized by the addition of fluorescent beads to the hydrogel solution prior to loading (**Fig. 3.2.2 B**).

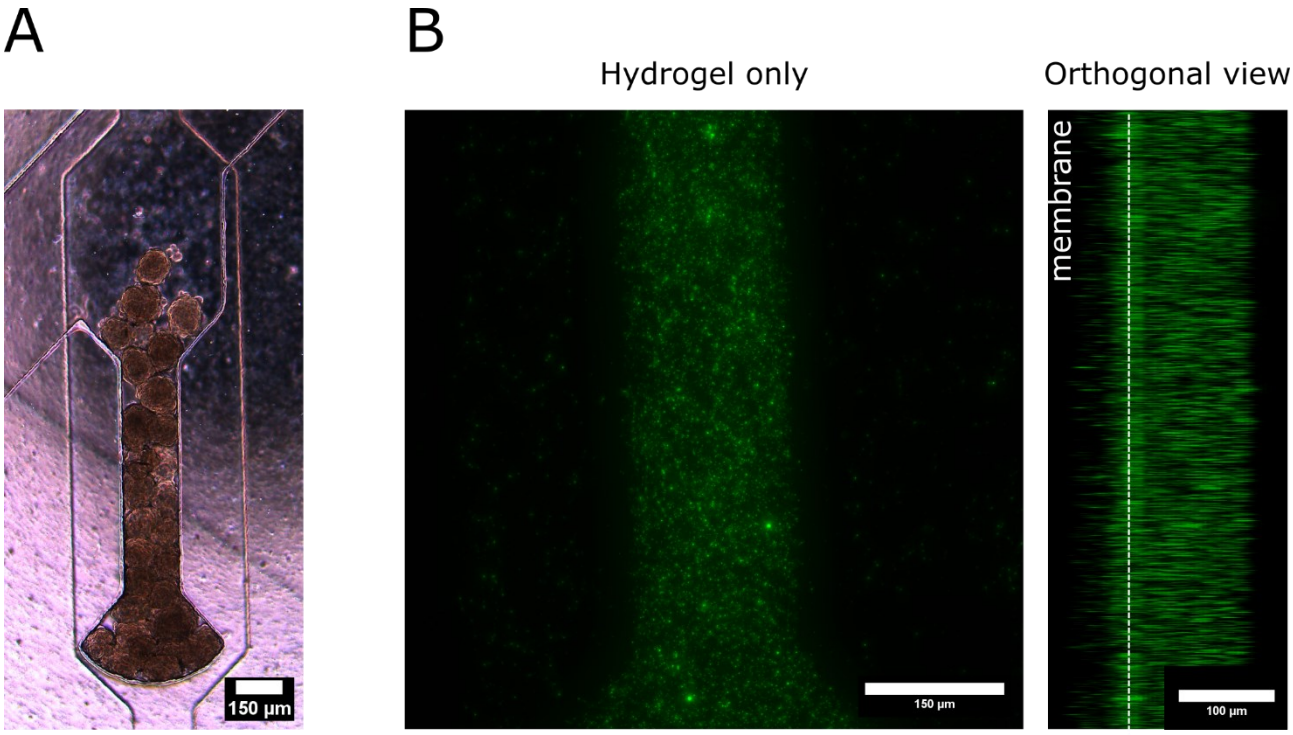

Figure 3.2.2 *Representative pictures of Centrifugal HoC chambers loaded with:* ***(A)*** *phDF spheroids.* ***(B)*** *3 mg/mL FibriCol® hydrogel with FITC-conjugated beads (left = max intensity projection of front view, right = orthogonal view).*

To achieve the loading of cardiac spheroids and hydrogel, the optimal approach consisted of pre-loading the cardiac spheroids into the chip before injecting the hydrogel. As shown in **Fig. 3.2.3**, the spheroids completely fill the shaft region upon loading (**Fig. 3.2.3 A**), while the subsequent hydrogel injection filled the gaps between the cardiac spheroids, revealing again the three-dimensionality of the tissue (**Fig. 3.2.3 B**). After 90 min of incubation the chip can be attached to the perfusion system.

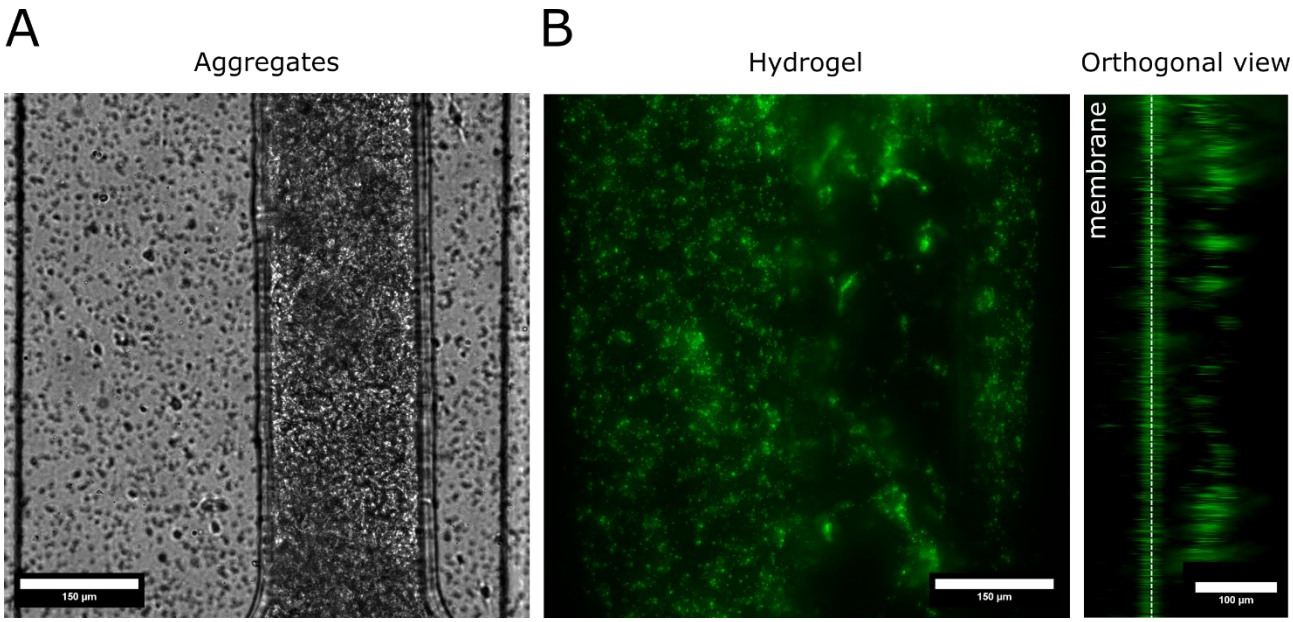

Figure 3.2.3 *Representative images of a Centrifugal HoC chamber loaded with spheroids and hydrogel.* ***(A)*** *Bright field image of spheroids in the shaft region.* ***(B)*** *FITC-conjugated beads in the 3 mg/mL FibriCol® hydrogel surrounding the spheroids (left = max intensity projection of the front view, right = orthogonal view).*

After 3 days of culture, the spheroids fused together, and the tissue compacted (**Fig. 3.2.4 A**). The shrinkage of the tissue leaves the lower knob region partially empty, and the tissue starts detaching from the edges of the chamber. The tissue showed spontaneous beating, and the motion vectors showed collective displacement on the y-axis (**Fig. 3.2.4 B**). Optical analysis of the bright field video of the beating tissue was performed with the in-house developed *OpenHeartWare* software. The beating motion revealed higher contraction (47.3 ± 0.2 µm/s) peaks followed by lower relaxation peaks (5.5 ± 0.8 µm/s) with an average beating rate of 7.0 ± 0.5 beats/min (**Fig. 3.2.4 C**).

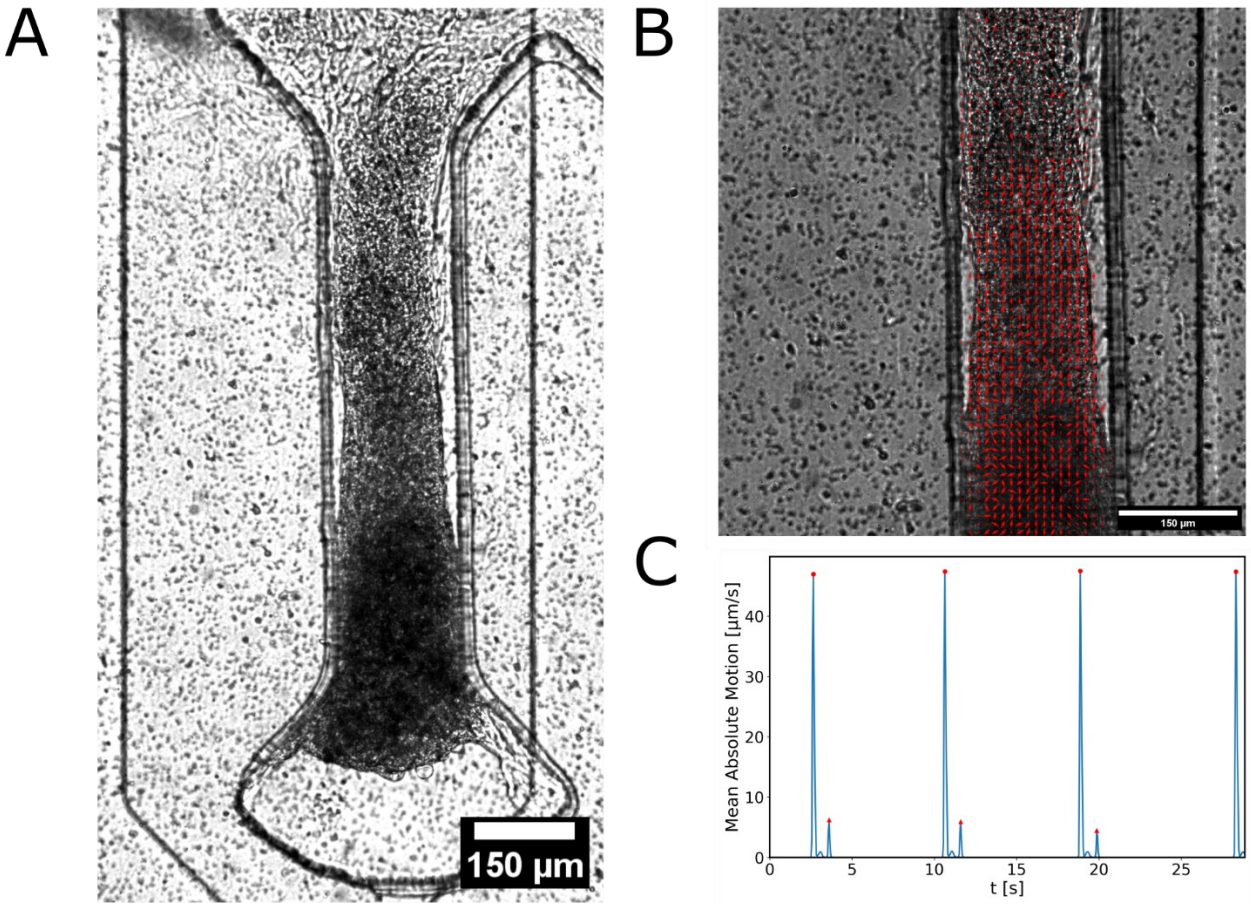

Figure 3.2.4 *Representative images of the Centrifugal HoC chamber loaded with spheroids and hydrogel at day 3.* ***(A)*** *Bright field image of the spheroids fused into a cardiac fibre.* ***(B)*** *Motion vectors of the beating tissue.* ***(C)*** *Optical analysis of the beating kinetics displays contraction (red circles) and relaxation (red triangles) peaks, which can be used to extrapolate the beating frequency.*

After 6 days of culture, the tissue collapsed from the lower knob to the shaft region, probably due to the collagen shrinkage (**Fig. 3.2.5 A**). The tissue, however, still retained the spontaneous beating capability, even though the motion vectors showed a more disorganised displacement compared to day 3 (**Fig. 3.2.5 B**). The optical analysis of the beating motion (**Fig. 3.2.5 C**) revealed irregular contraction peaks, with an average of 44 ± 3 µm/s followed by very low relaxation peaks (0.7 ± 0.1 µm/s). Even though the tissue presented a higher beating rate (12 ± 1 beats/min) compared to day 3, the tissue embedded within a hydrogel showed much lower beating rate compared to non-embedded tissues (45 ± 1.8 beats/min in Schneider et al., 2019), which exhibit beating rates close to the physiological range.

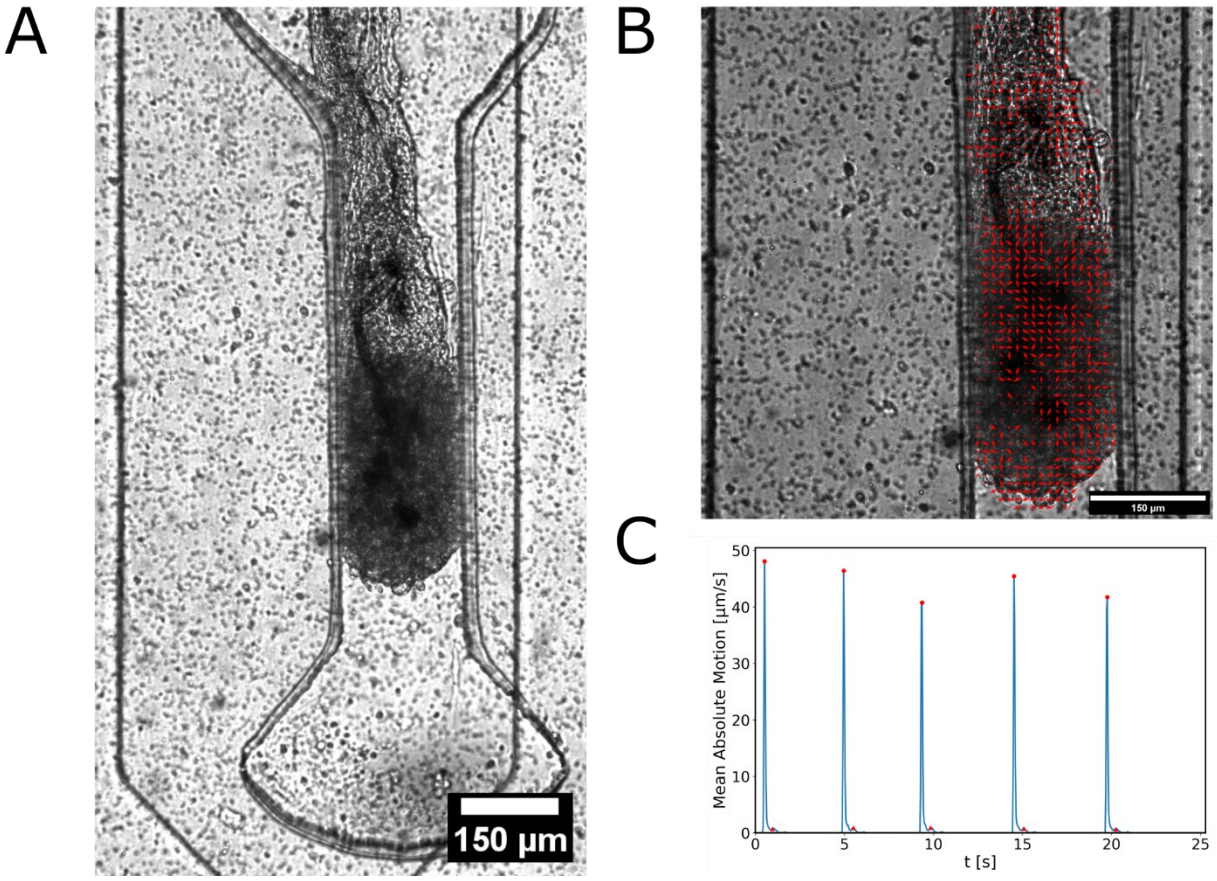

Figure 3.2.5 *Representative images of the Centrifugal HoC chamber loaded with spheroids and hydrogel at day 6.* ***(A)*** *Bright field image of the spheroids fused into a cardiac fibre.* ***(B)*** *Motion vectors of the beating tissue.* ***(C)*** *Optical analysis of the beating kinetics displays contraction (red circles) and relaxation (red triangles) peaks, which can be used to extrapolate the beating frequency.*

3.2.2 Establishment of the Spheroflow HoC platform

The second HoC design was developed to enable the injection of spheroids by hydrostatic pressure driven flow. The advantage of using spheroids as building blocks is the precise control over size and cellular composition as well as the possibility to trap them in microfluidic channels while still allowing media flow through the gaps between spheroids. The *Spheroflow HoC* platform comprises of a media layer and tissue layer sandwiching a porous membrane. The tissue layer features two structures of different heights, namely a channel of 150 µm, ending in the typical dog bone-shaped tissue chamber (blue in **Fig. 3.2.6 A**) and an overlapping channel of 30 µm in height (light blue in **Fig. 3.2.6 A**), that spans around the main channel of about 100 µm each side and continues towards the tissue outlet. The tissue chamber's shaft region is 270 µm wide while the knob regions are 700 µm in diameter.

During loading, a pipette tip containing the spheroids suspension is inserted in the tissue inlet and an empty pipette tip is inserted in the tissue outlet. The difference in liquid column height between the inlet and outlet tip induces a hydrostatic flow, dragging spheroids into the channel (**Fig. 3.2.6 A i**). The channel constriction of 30 µm around the tissue chamber prevents the spheroids from being flushed out to the outlet port. They therefore accumulate within the tissue chamber (**Fig. 3.2.6 A ii**), while the clogging of the channel is avoided by

the flanking 30 µm side channel which the spheroids cannot fill. This allows for a constant flow of media from the inlet to the outlet during spheroids loading.

After completely filling of the tissue chamber, the spheroids merge within 24 hours to an aligned tissue in the shape of the tissue chamber (**Fig. 3.2.6 A iii**). 24 hrs after loading, the tissue ports are sealed with metal plugs. The media layer on top comprises of a channel structure of 150 µm in height and 200 µm wide which enlarges to a width of 900 µm directly above the tissue chamber. Continuous perfusion at 50 µL/h is achieved via a syringe pump connected to the chip media inlets (**Fig. 3.2.6 B**), while tubings leading to the waste reservoir are connected to the media outlets. The perfused media can be sampled as effluent at the media outlet. In this concept, electrical stimulation can be directly provided though the metal cannulas used for media perfusion (**Fig. 3.2.6 B**) while, at the same time, a sensor spot, integrated below the tissue (**Fig. 3.2.6 A iii**), provides real-time measurements of O_2 concentrations at tissue level (**Fig. 3.2.6 B**).

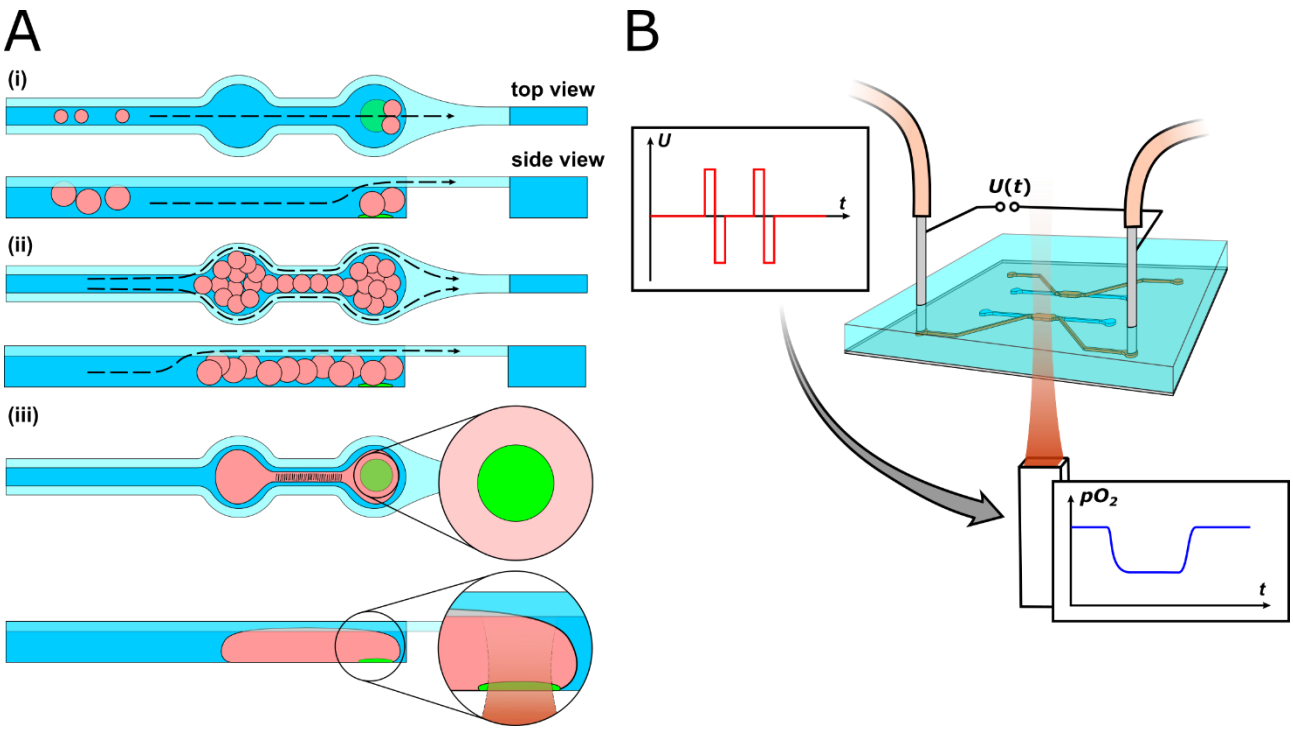

Figure 3.2.6 *Concept of the Spheroflow HoC, taken from* O. Schneider et al., 2022 *(available under the CC BY 4.0 license).* ***(A)*** *Chip loading mechanism: (i) Hydrostatic flow guides the spheroids into the dog bone-shaped tissue chamber, where a channel constriction traps them. (ii) With gradual filling, the loading flow is maintained by the flanking constriction channel. (iii) Within 24 hours, spheroids fuse into a single aligned cardiac fibre. An O_2 sensor embedded in the knob region enables the real-time readout of O_2 levels.* ***(B)*** *Online monitoring of tissue metabolic activity under electrical stimulation.*

3.2.2.1 Platform fabrication approach

The *Spheroflow HoC* was implemented to hold two independent tissues, separated from the respective media channels by a porous membrane. Each tissue chamber's rear knob has

an integrated O_2 sensor, that will lie beneath the tissue (**Fig. 3.2.7 A**). The completed chip has a thin bottom layer (tissue layer), made of NOA81 resin, which lies on a PET substrate where the integrated sensors are located, provided by my collaborator, Stefanie Fuchs, from the Institute of Analytical Chemistry and Food Chemistry, Graz University of Technology, Austria. On top of the tissue layer, the PDMS media layer allows for fluidic connections via media inlets and outlets (**Fig. 3.2.7 B**). Alternatively, the whole system can be built on a glass coverslip (25 × 75 mm, 0.13-0.16 mm). This allows for high-resolution microscopy and compatibility with other microscopic techniques such as Raman Spectroscopy; however, it does not allow the inclusion of sensors spot due to the lack of adherence of the sensor mixture to the glass substrate.

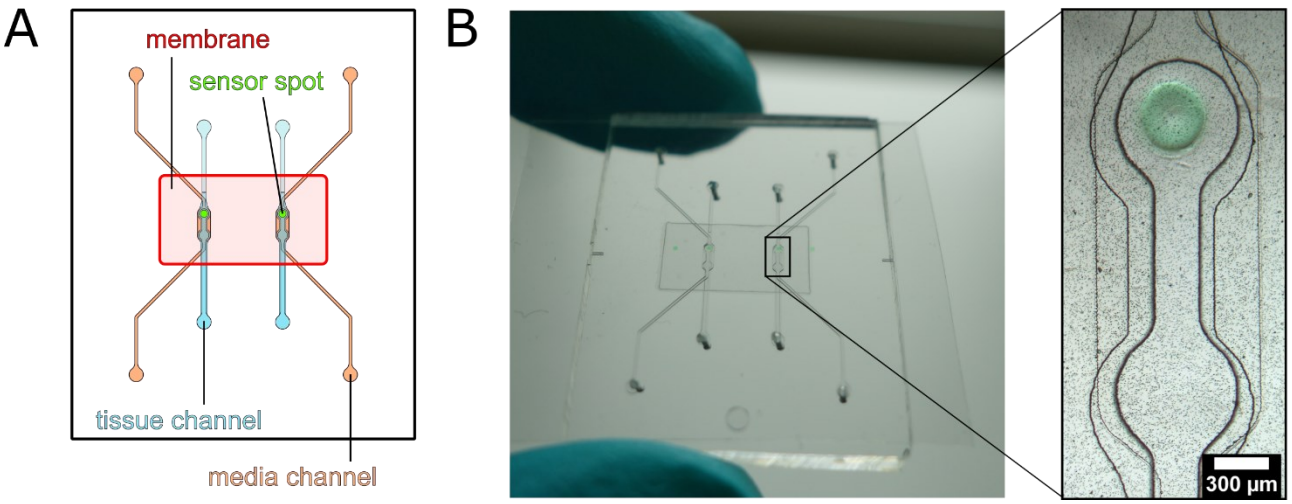

Figure 3.2.7 *Design of the Spheroflow HoC, taken from* Schneider et al., 2022 *(available under the CC BY 4.0 license).* ***(A)*** *Schematic: Each chip comprises of two individual systems consisting of a tissue and a media channel, separated by a porous membrane. Sensor spots can be integrated into the knob region of the tissue chamber.* ***(B)*** *Photo of an assembled chip with integrated sensors. On the left the magnified view shows the dog bone-shaped tissue chamber with the O_2 sensor spot.*

3.2.2.2 Biocompatibility of chip materials

Two different resins, which are claimed to be biocompatible (R. Li et al., 2016; Yoon et al., 2016), namely NOA81 and NOA86, were tested to ensure biocompatibility with CMs. The two resins were deposited and cured in wells of a 24 well plate. The cured resins were then coated with Matrigel to allow for CM adhesion, and cells were plated. Control condition consisted of cells plated in wells without resin coated with Matrigel. A clear difference was already visible between cells plated on NOA86 and the control condition on day 1 after plating (**Fig. 3.2.8 A**). While in the control condition and on NOA81 resin the cells appeared to have adhered and spread over the substrate, the NOA86 condition shows few cells with round morphology. Viability staining at day 3 (**Fig. 3.2.8 B**) confirmed viable cells in the control and NOA81 conditions, while no viable cells was present in the NOA86 condition. Therefore, the NOA81 resin was chosen for the tissue layer fabrication of the *Spheroflow HoC* platform.

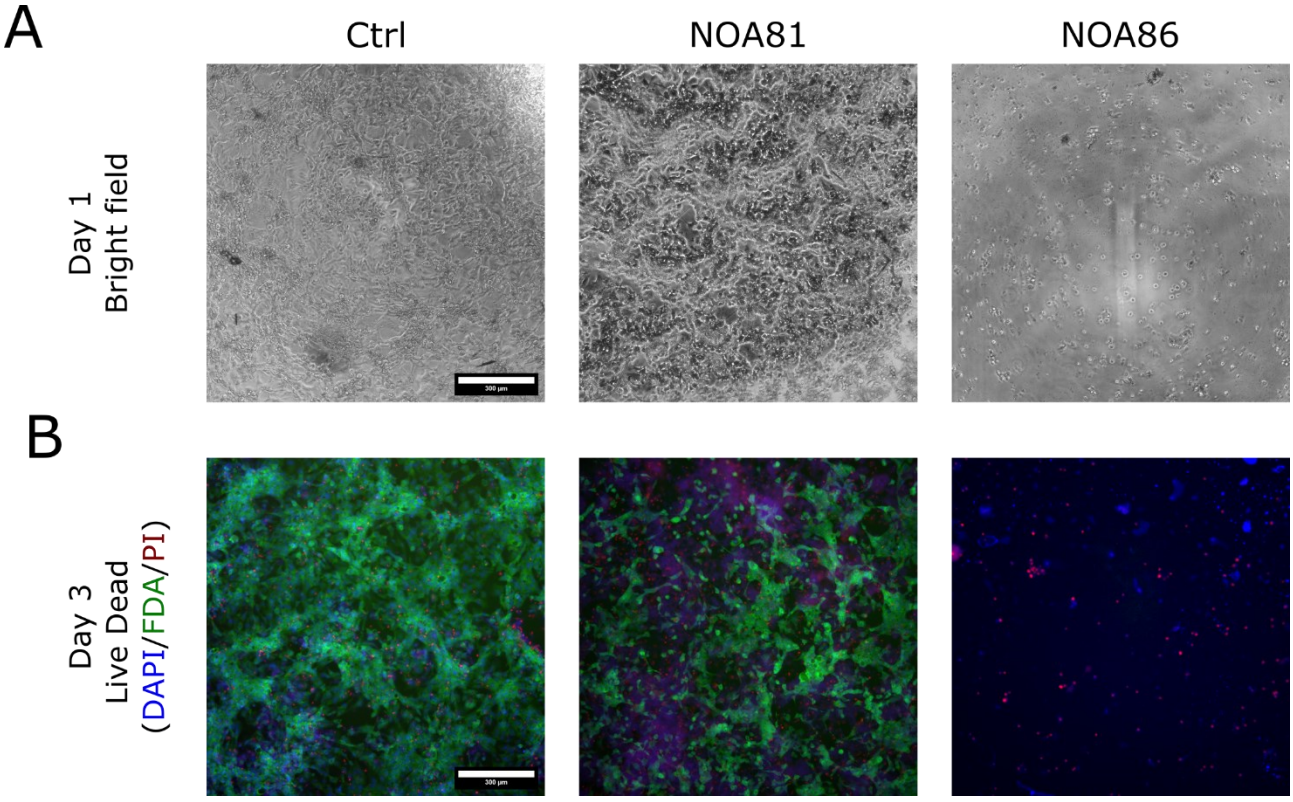

Figure 3.2.8 *Resin compatibility testing.* ***(A)*** *Bright field images of CMs plated on resin substrates coated with Matrigel at day 1 after plating.* ***(B)*** *Live dead staining of CMs plated on resin substrates after 3 days.*

3.2.2.3 Small molecule absorption

Another important aspect to consider when building an OoC device is the adsorption and absorption properties of its material components. Understanding the extent of retention of the drug of interest within the system enables us to make necessary adjustments to either the design and material composition of the OoC to prevent or reduce drug absorption. Additionally, it allows us to fine-tune the initial concentration to achieve the desired level at the tissue interface.

To examine if different chip material compositions absorb drug compounds, the drug concentration needs to be quantified after flowing through the chip platform, for instance via HPLC. To obtain an absorption profile which is as accurate as possible, several parameters must be considered. First, each compound may be retained differently by each material, based on their chemical properties (i.e., Molecular Weight, logP, and functional groups), therefore each different compound should be tested beforehand. Secondly, the set-up for the analysis must correspond as closely as possible to the set-up of the experiment; this ideally comprises the same perfusion methods, flow-rate, time and temperature, and if possible, the same medium solution in which the drugs are dissolved during experimental procedure.

For these reasons, I chose to test Isoproterenol and Verapamil as the two main drugs used for the validation of heart tissue models. However, the drug compounds were diluted in MilliQ water as the media components might interfere with the spectroscopic absorption of the drugs at 278 nm. As for the chip materials, the chips were built with the following combinations of materials: 1. both tissue and media layer were made of PDMS (PDMS-PDMS); 2. NOA81 resin for the tissue layer and PDMS for the media layer; 3. NOA81 resin for the tissue layer and TPE for the media layer. Syringes containing drug solutions were connected to 50 cm tubings. These were either attached to the chips (samples) or directly ended in 0.5 mL collection tubes (negative controls). The system was perfused at the standard flow rate of 50 µL/h in an incubator (37°C, 5% CO_2, 99% RH) for 2 hrs and the chip effluent was collected in a 200 µL tip inserted in the media outlet.

The HPLC-UV method and samples analysis was carried out by the HPLC technical employee, Marina Shirokikh (**Fig. 3.2.9**). From the calibration curves the limit of detection (LOD) and limit of quantification (LOQ) were calculated. Verapamil (**Fig. 3.2.9 A**) had LOD = 1.18 µM and LOQ = 3.35 µM while Isoproterenol (**Fig. 3.2.9 B**) had LOD = 1.78 µM and LOQ = 5.35 µM. Taking into consideration the LOD and LOQ values and the highest concentration of verapamil and isoproterenol delivered in a similar model (Mathur et al., 2015), concentrations in the range of 10 µM were tested.

Both drugs were mainly retained by the tubings, with a significative difference compared to the stock solution of 2.1 µM for the Verapamil (**Fig. 3.2.9 A**) and 1.6 µM for the Isoproterenol (**Fig. 3.2.9 B**). The drug retention by the chips of different materials was negligible compared to the tubings. These results proves that most of the drug retention happens even before the compounds reach the chip. Optimized HPLC protocols for each drug needs to be implemented to further examine, at a higher resolution, the differences in retention between chips of different material as well as their absorption and adsorption kinetics. However, this was outside the scope of this thesis.

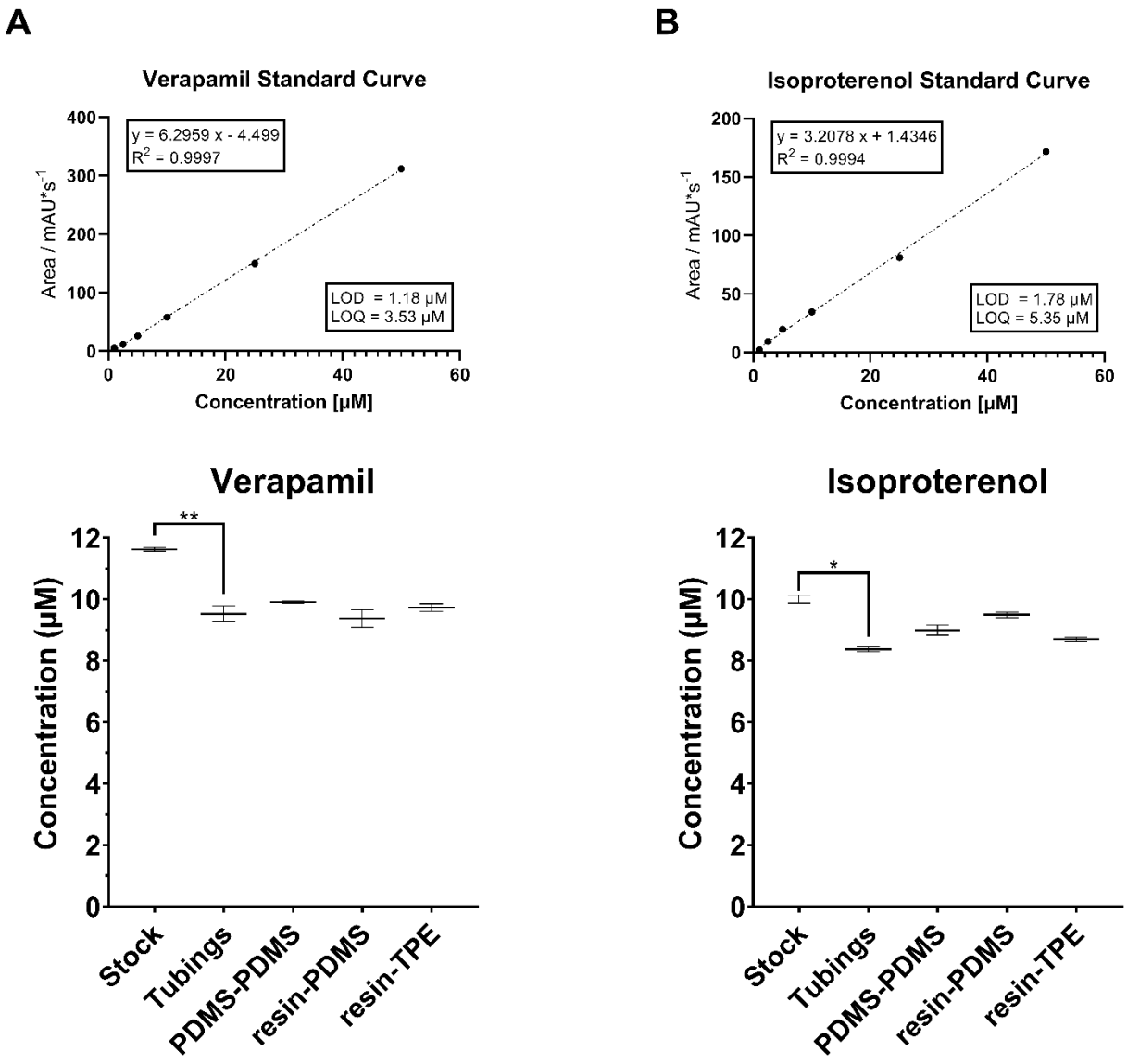

Figure 3.2.9 *Drug absorption during perfusion by Spheroflow platforms made of different materials. Different chip assemblies are as follow: PDMS tissue layer – PDMS media layer (PDMS-PDMS), NOA81 resin tissue layer – PDMS media layer (resin-PDMS), PDMS tissue layer – TPE media layer (PDMS-TPE).* ***(A)*** *Verapamil: at the top, calibration curve (equation, R^2, LOD and LOQ); at the bottom, Verapamil concentrations after 2 hours perfusion at 37°C, 99% RH, 5% CO_2, compared to stock solution. (Stock N = 2; Tubings N = 2; PDMS-PDMS N = 2; NOA81-PDMS N = 4; NOA81-TPE N =3).* ***(B)*** *Isoproterenol: at the top, calibration curve (equation, R^2, LOD and LOQ); at the bottom, Isoproterenol concentrations after 2 hours perfusion at 37°C, 99% RH, 5% CO_2, compared to stock solution. (Stock N = 1; Tubings N = 2; PDMS-PDMS N = 4; NOA81-PDMS N = 4; NOA81-TPE N = 3). Data is represented as average ± SEM in a Scatter dot plot. The Mann-Whitney test was used for comparison between the Stock and the Tubings samples. * $p \leq 0.05$; ** $p \leq 0.01$.*

3.2.3 Cardiac tissue formation and characterization within the Spheroflow HoC

Upon adding the spheroids from the pipette tip into the inlet port, within one minute the tissue chamber is completely filled with spheroids (**Fig. 3.2.10 A**). During this loading process, a number important aspects need to be considered, i.e.: (I) The optimal spheroid size is 150

µm; larger spheroids increase the risk of clogging the loading channel, while too small spheroids may squeeze through the channel, constricting, reducing or even stopping liquid flow; (II) when the tips at the tissue inlet and outlet are equilibrated, the flow ceases, requiring the top up of the tissue inlet tip to restore flow. (III) Backflow from the tissue outlet to the inlet can displace the spheroids loaded in the chamber; therefore, it is important to avoid causing backflow by tilting the chip or having a higher fluid volume in the outlet tip.

After loading, the chip is incubated at 37°C, 5% CO_2 with media provided only by the tips placed in the tissue and media inlets and outlets. After 24 hours, the spheroids merge into a single cardiac fibre instead of spreading on the substrate (**Fig. 3.2.10 B**). In fact, the lack of any coating promotes cell to cell adhesion. Compared to t = 1 hr, where individual spheroids could be distinguished, at t = 24 hr the spheroids edges are not visible anymore (**Fig. 3.2.10 B**).

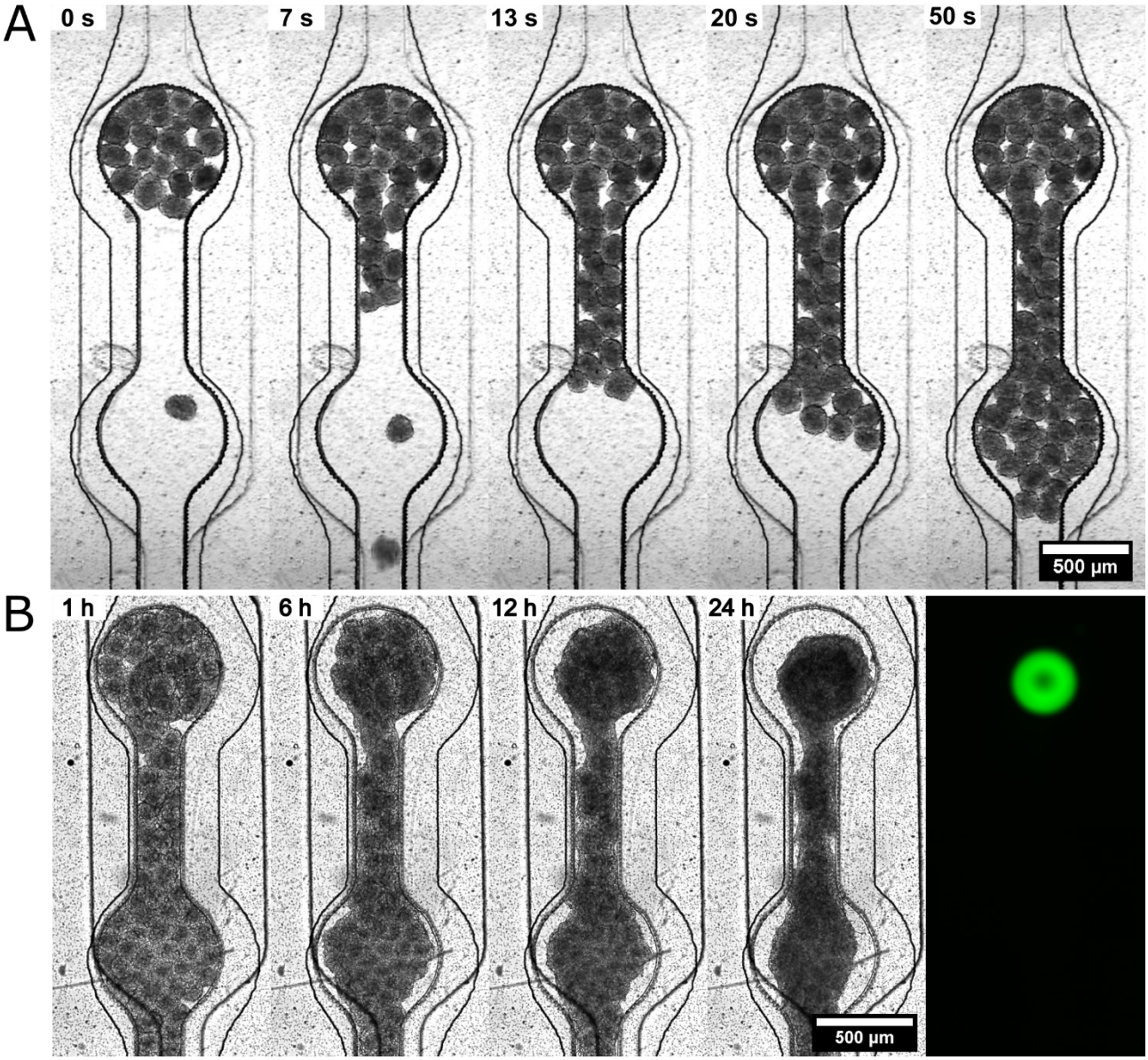

Figure 3.2.10 *Spheroflow HoC loading and tissue formation.* ***(A)*** *Time-lapse of the chip loading by hydrostatic spheroid injection.* ***(B)*** *Adapted from* Schneider et al., 2022*. Time-lapse of the cardiac*

spheroid fusion to an aligned tissue over the timespan of 24 h after loading. On the right the underlying integrated O_2 sensor spot is imaged by fluorescence microscopy (green, Cy5).

Cell re-organization from single spheroids to a connected cardiac fibre was confirmed via immunofluorescence microscopy and cTnT and nuclei staining (**Fig. 3.2.11 A**), showing the uniaxial alignment of the filaments in the shaft region (**Fig. 3.2.11 A-B**). Additionally, z-stack imaging of the tissue demonstrates that three-dimensionality of the spheroids is maintained. Three days after loading, the generated tissues display spontaneous beating, with collective uniaxial motion (**Fig. 3.2.11 C**) and pronounced contraction and relaxation peaks (**Fig. 3.2.11 D**).

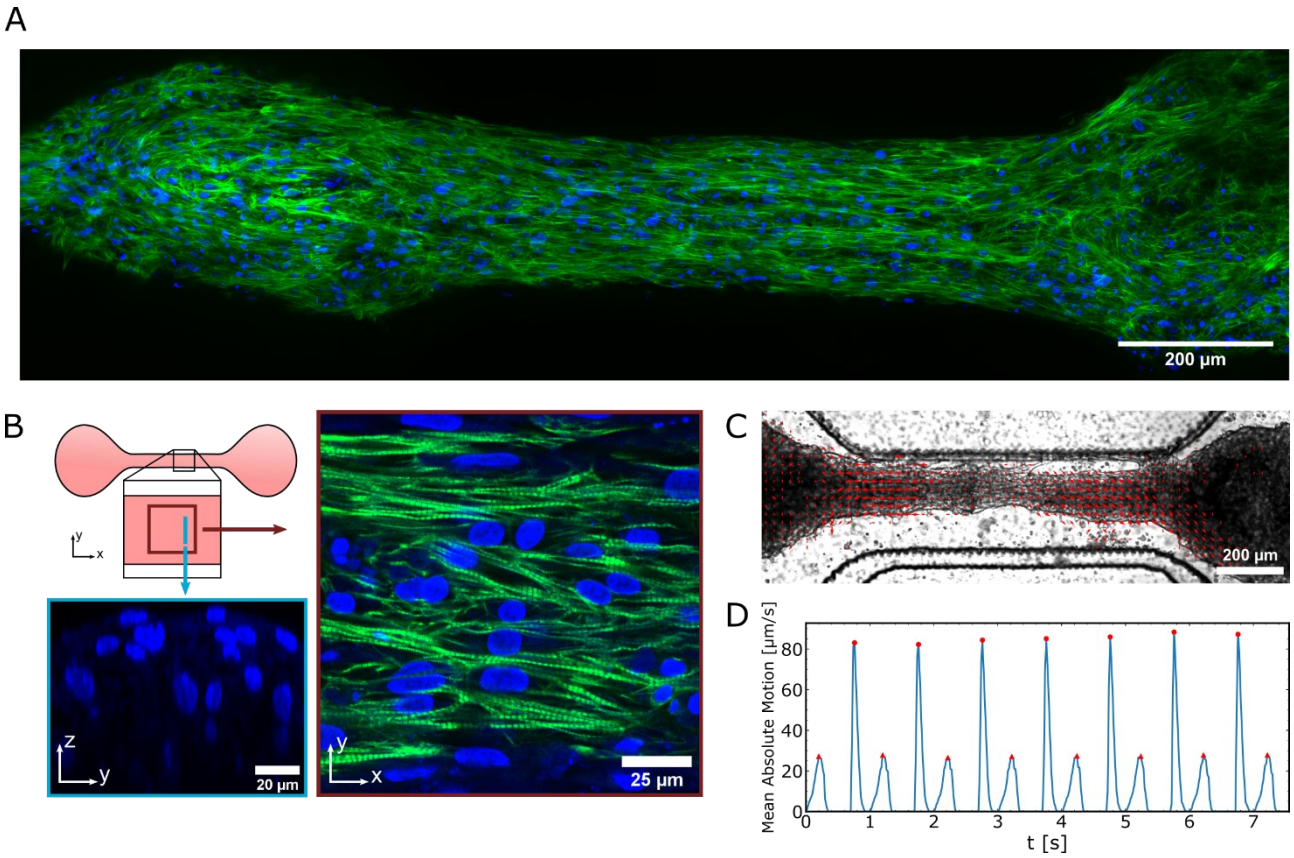

Figure 3.2.11 *Spheroflow HoC tissue characterization adapted from* Schneider et al., 2022 *(available under the CC BY 4.0 license).* ***(A)*** *Immunostaining with cTnT (green) and DAPI (blue) of the whole tissue (20x, tiled).* ***(B)*** *Immunostaining with cTnT (green) and DAPI (blue) shows aligned cardiac fibres (xy slice) within the shaft region. The orthogonal view (yz slice) of the nuclei confirms the generation of a multilayered 3D tissue.* ***(C)*** *Analysis of the beating motion of the fibre. The motion vectors reveal collective displacement.* ***(D)*** *Optical analysis of the beating kinetics displays pronounced contraction (red circles) and relaxation (red triangles) peaks.*

3.2.4 Tissue responsiveness to electrical impulses

To assess tissue responsiveness to external stimuli, electrical stimulation was provided by an in-house built pacer, named “Easypace” (**Fig. 3.2.12 A**) (see building instruction at https://github.com/loslab/easypace/). The stainless-steel cannulas used for tubing

connections for the media supply were used as pacing electrodes. A fit-for-purpose platform (**Fig. 3.2.12 B**) was made of PMMA to hold the *Spheroflow HoC* in place during pacing and O_2 readout procedures. The HoC was held in place by magnets while crocodile clips were attached to the metal cannulas and connected to the pacer. The cut outs at the bottoms of the PMMA platform were designed to match the sensors' positions within the HoC and host the optical fibres for the readout. The platform could hold up to 4 chips. A COMSOL simulation (**Fig. 3.2.12 C**) of the distribution of the electrical field within the channels was performed by Dr. Oliver Schneider (Fraunhofer IGB). The theoretical electrical field distribution within the tissue shaft region was estimated to be uniform with an average of |E| = 0.8 V/cm under a voltage of U_0 = +10 V applied to the inlet and outlet media connectors.

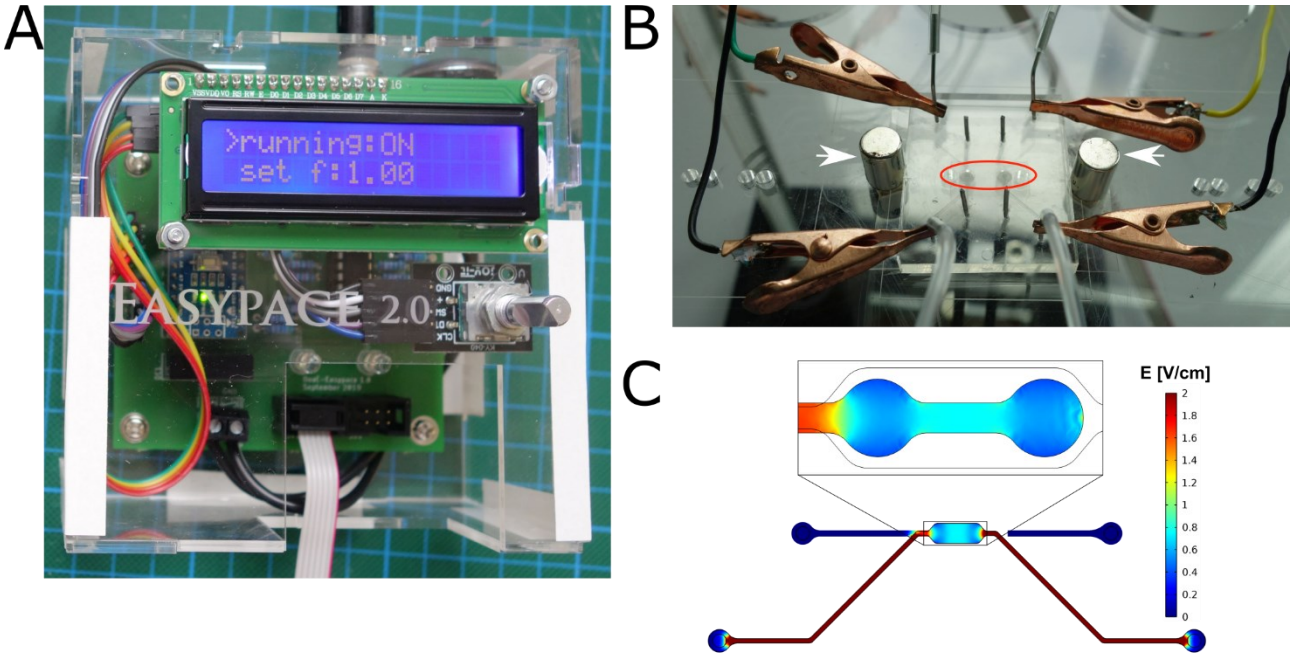

Figure 3.2.12 *Electrical stimulation set up, adapted from* Schneider et al., 2022 *(available under the CC BY 4.0 license).* ***(A)*** *Picture of the in-house build pacer "Easypace".* ***(B)*** *The "Easypace" is connected via crocodile clips to the stainless-steel media fluidic connectors, which act as electrodes and deliver the electrical impulses through the media to the tissue. White arrows highlight the magnets holding the chip in place. The red circle indicates the two optical fibre sockets.* ***(C)*** *Simulation in COMSOL of the electrical field intensity withing the media and the tissue channels, when a current of 10 V is applied.*

At day 5 of culture in the *Spheroflow HoC*, tissues were electrically stimulated. Frequencies in the range of 0.3–2.0 Hz, with a stepwise increase of Δf = 0.1 Hz, were applied for 10 s per frequency, videos of the tissues beating were recorded and beating kinetics extrapolated. For each frequency tested, the recorded beating frequency was plotted, showing a linear relation between pacing frequency and the beating frequency up to 2 Hz (**Fig. 3.2.13**). Tissues could not match their beating frequency to frequencies above 2 Hz,

showing beating rates of half of the applied frequency. Nevertheless, integrated tissues could be electrically stimulated, and their beating frequency could be precisely adjusted within a physiological range.

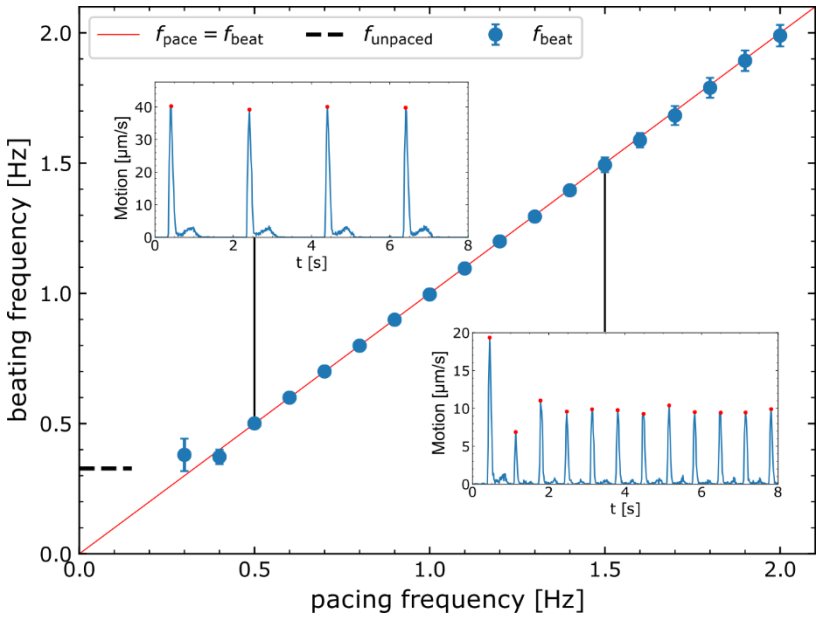

Figure 3.2.13 *Beating analysis of electrically stimulated tissues, adapted from* Schneider et al., 2022 *(available under the CC BY 4.0 license). Tissue beating frequency in function of the pacing frequency. Red line indicates beating frequency equal to pacing frequency. Insets show the beating kinetics from which the beating frequency of the tissue is calculated from. Scatter XY plot with average ± SEM. (N = 3).*

To explore whether continuous pacing at a physiological frequency of 1Hz would affect tissue functionality and metabolism, cardiac tissues were cultured in the *Spheroflow HoC* for 14 days and continuously paced from day 5, were compared to control tissues, which were cultured in parallel without undergoing the pacing regime. Pacing was carried out at 1 Hz, 50 ms, 10 V. The only times where electrical stimulation was paused was during media change procedures and effluent collection.

A cell death dye was used to compare tissue viability between paced and control tissues at day 14. As shown in **Fig. 3.2.14**, both conditions show low level of cell death. This result indicates not only that continuous pacing does not exert cytotoxicity but also that the *Spheroflow HoC* provides adequate conditions for long-term culture of cardiac tissues. I arbitrarily chose day 14 as the end timepoint but theoretically the tissues could be cultured for longer periods.

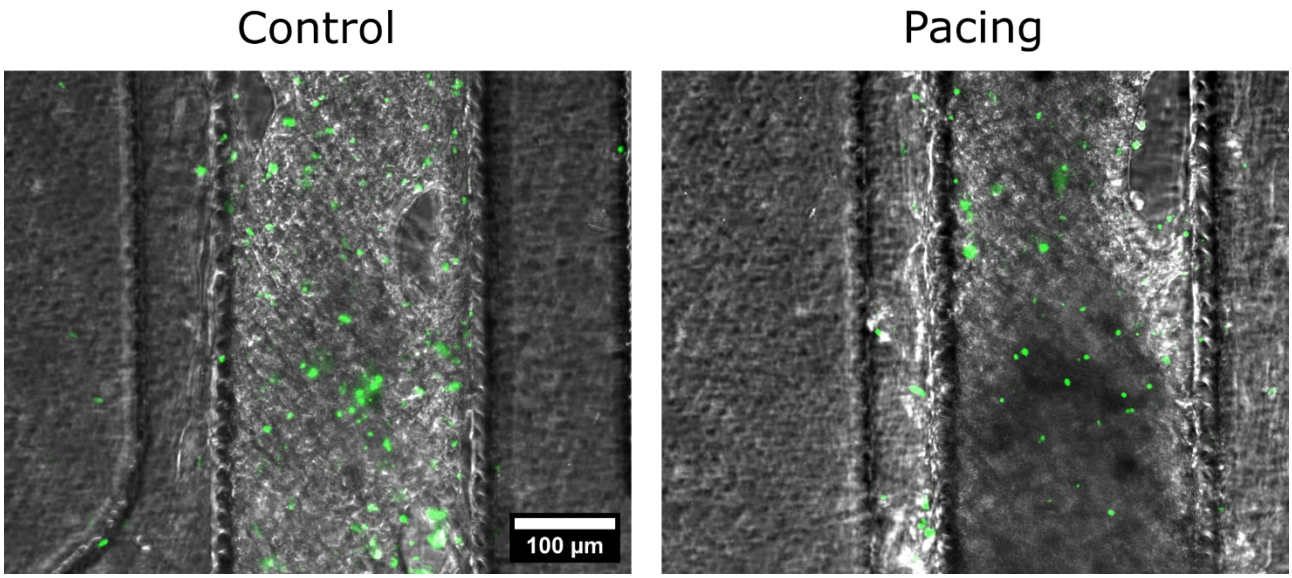

Figure 3.2.14 *Tissue viability after prolonged continuous pacing. Assessment of cell death by CellTox™ Green (green) staining. On the left, a control tissue after 14 days of culture, while on the right a tissue continuously paced from day 5 to day 14 of culture at 1 Hz, 10 V, 50 ms pulses. Scale = 100µm.*

Tissues in both conditions are responsive to pacing at 1 Hz at day 5 and day 14 (**Fig. 3.2.15 A**). Control tissue exhibited a reduced spontaneous beating rate at day 14 compared to day 5, albeit not significant. Tissues under constant pacing exhibited spontaneous beating at day 14 comparable to their spontaneous beating at day 5. However, paced tissues exhibited significant higher spontaneous frequency ($p = 0.02$), compared to control tissues. The average *maximum contraction velocity* (**Fig. 3.2.15. B**) decrease slightly but not significatively when tissues in both conditions are paced. Moreover, an overall, but not significant, decrease in the spontaneous maximum contraction velocity is observed during culture (comparing day 5 and day 14) in both control and paced conditions.

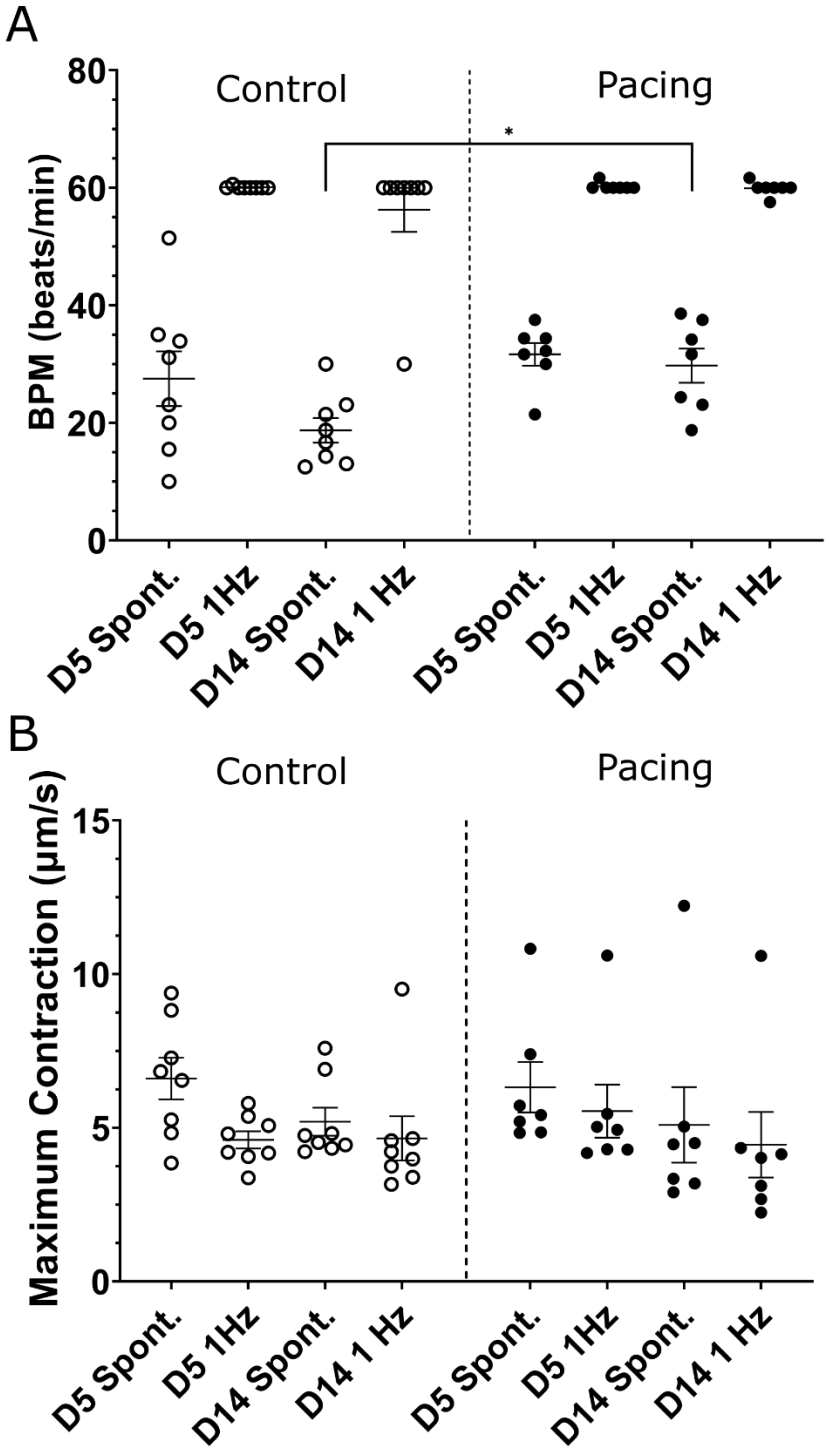

Figure 3.2.15 *Tissue functionality at day 5 and day 14 after prolonged continuous pacing.* ***(A)*** *Beating frequency during spontaneous beating (Spont.) and under pacing at 1Hz.* ***(B)*** *Maximum contraction velocity during spontaneous beating and under pacing at 1Hz. Data is represented as a Scatter dot plots, with average ± SEM. Control condition = tissues cultured for 14 days without electrical stimulation (N = 9); Pacing = tissues continuously paced from day 5 to day 14 of culture at 1 Hz, 10 V, 50 ms pulses (N = 7). Statistical analysis of the spontaneous beating frequencies of control and paced tissues at day 5 and day 14 was conducted by One-way ANOVA. The following pairs were compared: Control D5 Spont. Vs Control D14 Spont.; Control D5 Spont. Vs Pacing D5 Spont.; Pacing D5 Spont. Vs Pacing D14 Spont. and Control D14 Spont. Vs Pacing D14 Spont. * p ≤ 0.05.*

3.3 Readouts

In the scope of this thesis, I aimed at integrating electrical stimulation of the tissue and coupled it with non-invasive readouts. Non-invasive measurements can be performed repeatedly over time without affecting tissue functionality and viability, therefore allowing for long-term monitoring of tissues changes. In medical research, this is crucial for understanding disease progression, evaluating treatment effects, and developing new therapies. As they do not require the sacrifice of the sample for data acquisition, non-invasive readouts maximize data yield while minimizing the need of additional resources. This is more efficient and cost-effective compared to terminal assays. Here, a broad toolbox of non-invasive readouts for the *Spheroflow HoC* was developed, namely video recording, O_2 sensors, Raman spectroscopy, and analysis of effluents. This toolbox enables the investigation of changes in tissue function and metabolism upon electrical stimulation or drug injection.

3.3.1 Establishment of O_2 sensors readouts

For real-time recording of oxygen levels, optical fibres were connected to either the phase fluorimeter (FireSting pro or the FirePlate prototype), which was set to have an illumination intensity of 100% and detection amplification of 400x. The *Spheroflow HoC* sensors were manually aligned to the optical fibres, until an acceptable intensity above U = 100 mV was achieved for every measurement. While for the $p_{O_2} = 0\%$ calibration point the average phase shift ($\Delta\varphi$) of 4 sensors spots was used, for the $p_{O_2} = 100\%$ calibration point each sensor was calibrated in cell culture media before cell seeding. To verify sensors stability under culture conditions, empty *Spheroflow HoC* were perfused at 50 µL/h in culture media at 37°C while recording O_2 levels every second for 12 hours (**Fig. 3.3.1 A**). The signal did not shift significantly over time (≤ 1 hPa/h), excluding any scavenging of the O_2 from the media by the NOA81 resin. Additionally, it is possible to detect in real time the passing through of potential air bubbles, as shown by the temporary spike in chamber D.

As one of the main goals was to couple the electrical stimulation with the O_2 sensing to understand if pacing might affect O_2 metabolism, it was important to investigate if the application of an electrical current would skew the O_2 readouts due to electrolysis. Therefore, O_2 levels were recorded in empty chips perfused with media, while electrical stimulation at 12.5 V and 50 ms with 1Hz and 3 Hz frequency was applied. In **Fig 3.3.1 B** it is possible to observe that chambers C and D maintained constant O_2 level during both pacing regimes, comparable to non-paced controls (chambers A and B). This excludes possible O_2 changes induced by electrolysis, allowing O_2 measurement during electrical stimulation.

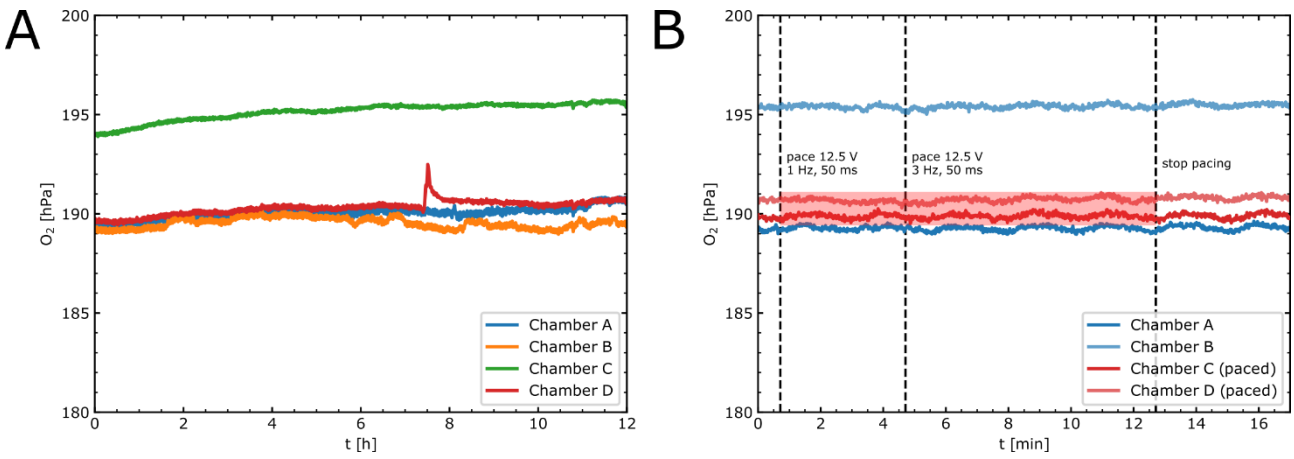

Figure 3.3.1 *Assessment of O_2 sensors stability under experimental conditions, adapted from* Schneider et al., 2022 *(available under the CC BY 4.0 license).* ***(A)*** *Stability of the O_2 sensors over 12 hours of media perfusion in empty Spheroflow HoC.* ***(B)*** *Effect of pacing (red area) onto O_2 level and sensor readout in media-perfused empty Spheroflow HoC. Chambers C and D were paced first at 1 Hz, 12.5 V, 50 ms pulses, followed by pacing at 3 Hz, 12.5 V, 50 ms. Chambers A and B were used as negative controls.*

Following this, pacing and O_2 readout were combined to assess whether increased beating frequency would result in a higher O_2 consumption. Two cultured tissues within the same chip, were alternatively paced at increasing frequencies of 0.7, 1.0, 1.2, and 1.5 Hz for 10 minutes, followed by 30 minutes at rest before the next pacing cycle was applied (**Fig. 3.3.2 A**). Each frequency cycle was repeated three times. The choice of pacing one tissue while keeping the other at rest was made to have an internal control, excluding external influences on O_2 levels but also to exclude any crosstalk between tissues residing within the same *Spheroflow HoC* platform. This proves that each *Spheroflow HoC* hosts two completely independent tissues. Coincident to the starting of the pacing, a noticeable decrease in measured O_2 occurred (as indicated by the reference line), which returned to the basal level upon termination of the electrical stimulus. For each iteration, no O_2 level change was detected in the respective non-paced chamber. Additionally, higher pacing frequencies showed larger decreases in O_2 levels.

In **Fig. 3.3.2 B**, the differences in O_2 levels between onset of pacing and pacing termination were normalized to the difference of O_2 partial pressure between the non-paced state and the fully oxygenated state, yielding relative differences in O_2 consumption. Relative differences consistently increased with higher pacing frequencies in each pacing cycle for both investigated systems. These results indicate that the drops in O_2 levels correlate to a higher O_2 consumption rate of the tissues. The difference in O_2 consumption appears to be proportional to the beating frequency of the tissue. My theory is that the electrical stimulation triggers an increase in the metabolic activity of the cardiac tissues.

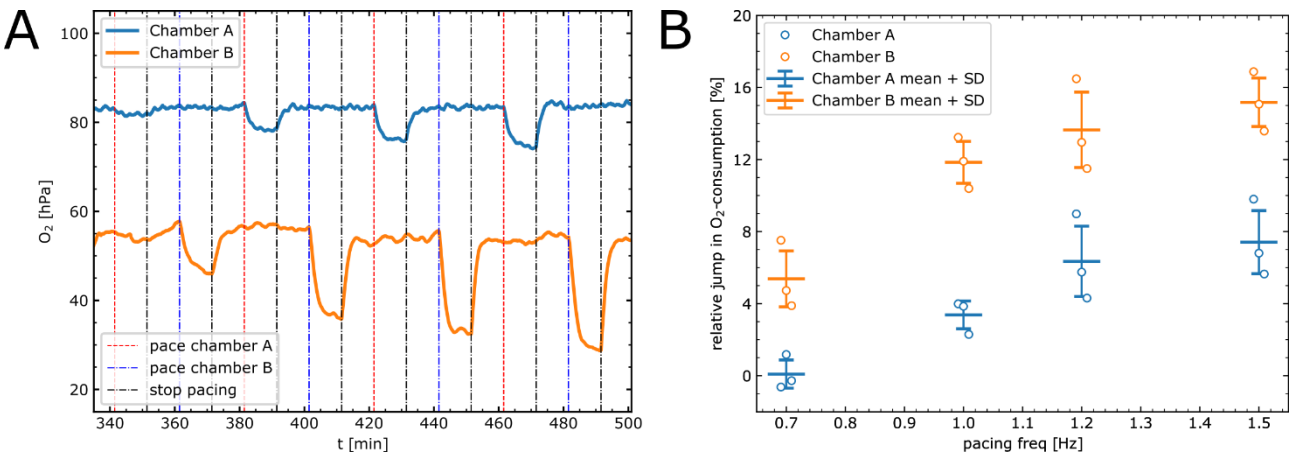

Figure 3.3.2 *O_2 levels recording by integrated optical sensors, adapted from* Schneider et al., 2022 *(available under the CC BY 4.0 license).* ***(A)*** *Alternate pacing of two tissues (blue and red dashed lines) coupled to simultaneous recording of O_2 partial pressures (hPa). Increasing frequencies of 0.7, 1.0, 1.2, 1.5 Hz.* ***(B)*** *Analysis of the relative difference in O2 consumption (%) dependent on the pacing frequency (0.7, 1.0, 1.2, 1.5 Hz). Data is expressed as average ± SD. Data points are technical triplicates of 2 independent tissues (orange and blue).*

In the next step I wanted to monitor the O_2 levels from the start of the pacing procedure to the endpoint at day 14. In **Figure 3.3.3**, it is possible to see two tissues being monitored for several days. As observed in the previous experiments, as soon as electrical stimulation was started, the paced tissue (blue line) presented a steep drop in O_2 level (from 101 hPa to 71 hPa in 2 hours), while the control level remained unchanged (61 hPa at both time points). However, it is possible to see after 24 hours a high spike, of the same magnitude, in O_2 levels for both systems (red highlighted area). This was caused by a partial dealignment of the sensor spots from the optical fibre during acquisition, confirmed by the concurrent drop of signal intensity below the 100 mV. Chips were re-aligned on top of the optical fibres after media change, bringing back the measured O_2 levels at the previous values. It is also possible to notice a gradual increase in O_2 levels over the days in both systems, with an increase of 26 hPa for the control at day 14 and an increase of 22 hPa for the paced tissue from the O_2 levels detected after pacing. This underlines changes in O_2 dependent metabolism over time in both tissues.

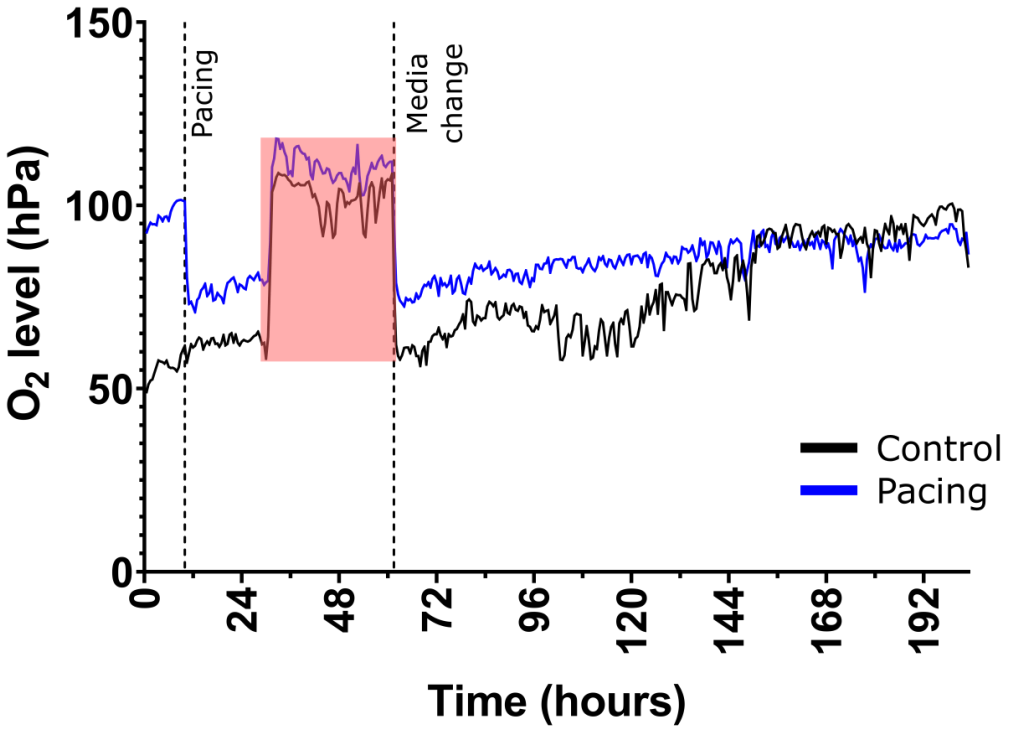

Figure 3.3.3 *Recording of O_2 partial pressures (hPa) of 2 tissues over 8 days. Dashed lines illustrate the times of the start of the pacing regime and the time of media change. Blue line indicates O_2 level of the tissue under pacing, while black line illustrates the O_2 level of the control tissue.*

This experiment was overall difficult to perform due to the complex set up, which included a several electronical devices outside of the incubator being connected to the chip within the incubator by cables, which could be accidentally pulled by the lab staff and the operator themselves. It is also possible to see much higher fluctuations (> 1 hPa) in the O_2 level compared to previous graphs. This was due to the fact that bigger volume syringe (10 mL) as well as a lower acquisition rate of the shift phase (1 / 10 seconds) were used. Using higher volume syringes was necessary to assure continuous perfusion of media over several days without the operator touching the set up; however, as previously demonstrated this translates into high oscillations of amplitude ≈ 10 hPa (data not shown – (O. Schneider, 2022)).

3.3.2 On-chip mitochondrial respiration assay

To verify that the current readout method could be used to detect drug-induced metabolic changes in O_2 consumption, I tested different compounds known to affect the cellular respiratory chain (or Electron transport chain) (**Fig. 3.3.4**). These drugs, nominally, Oligomycin A, FCCP, Rotenone and Antimycin A, are also used for the analysis of mitochondrial respiration in the Seahorse XF Analyzer (Agilent).

In order to administer several drugs within each chip in an automated and timely manner, the uProcess Microfluidic Automation switches (LabSmith) were used and a script was written in the uProcess software to control each switch. In this way drugs were automatically

injected without stopping the perfusion system and manually switching syringes, decreasing chances of air bubble formation and perturbation of the readout.

In **Fig. 3.3.4 A**, it is possible to observe how the addition of each drug influences O_2 consumption by the tissues. Oligomycin A is an ATP synthase (complex V) inhibitor, it blocks the intake of H^+ ions required for ATP synthesis as well as leading to reduced levels of intracellular H^+ ions which are used by the previous protein complexes of the respiration chain. Therefore, after the addition of Oligomycin A, the tissues consumed less O_2 and the O_2 level rose. Conversely, FCCP disrupts the H^+ gradients and mitochondrial membrane potential, uncoupling the intake of H^+ ions from the ATP synthase, allowing higher H^+ intracellular concentration and increased oxygen consumption by the complex IV. During incubation of the tissues with FCCP, it was possible see a gradual decrease in O_2 levels until a plateau was reached. Lastly, Rotenone and Antimycin A (R / A) blocks the complex I and III of the electron transportation chain respectively. This completely shuts down mitochondrial respiration, leading to a spike in O_2 levels.

As different chambers present different basal O_2 levels due to different cell number, before analysis, the data from each tissue was normalized over the average O_2 level before the addition of Oligomycin A (**Fig. 3.3.4 B**). To calculate the mitochondrial respiration parameters, the following variable were defined: $pOligo$ refers to the last measured O_2 value (hPa) prior to the injection of Oligomycin A; $pFCCP$ refers to the last measured O_2 value (hPa) prior to the injection of FCCP; pRA refers to the last measured O_2 value (hPa) prior to the injection of Rotenone / Antimycin A; aRA refers to the last measured O_2 value (hPa) after the injection of Rotenone / Antimycin A. The mitochondrial respiration parameters (**Fig. 3.3.4 C**) were then calculated as described in Busche et al. (2022):

$$Basal\ respiration = pOligo - aRA$$

$$Proton\ leak = pFCCP - aRA$$

$$ATP\ production = Basal\ respiration - Proton\ leak$$

$$Maximal\ respiration = pRA - aRA$$

$$Spare\ capacity = Maximal\ respiration - Basal\ respiration$$

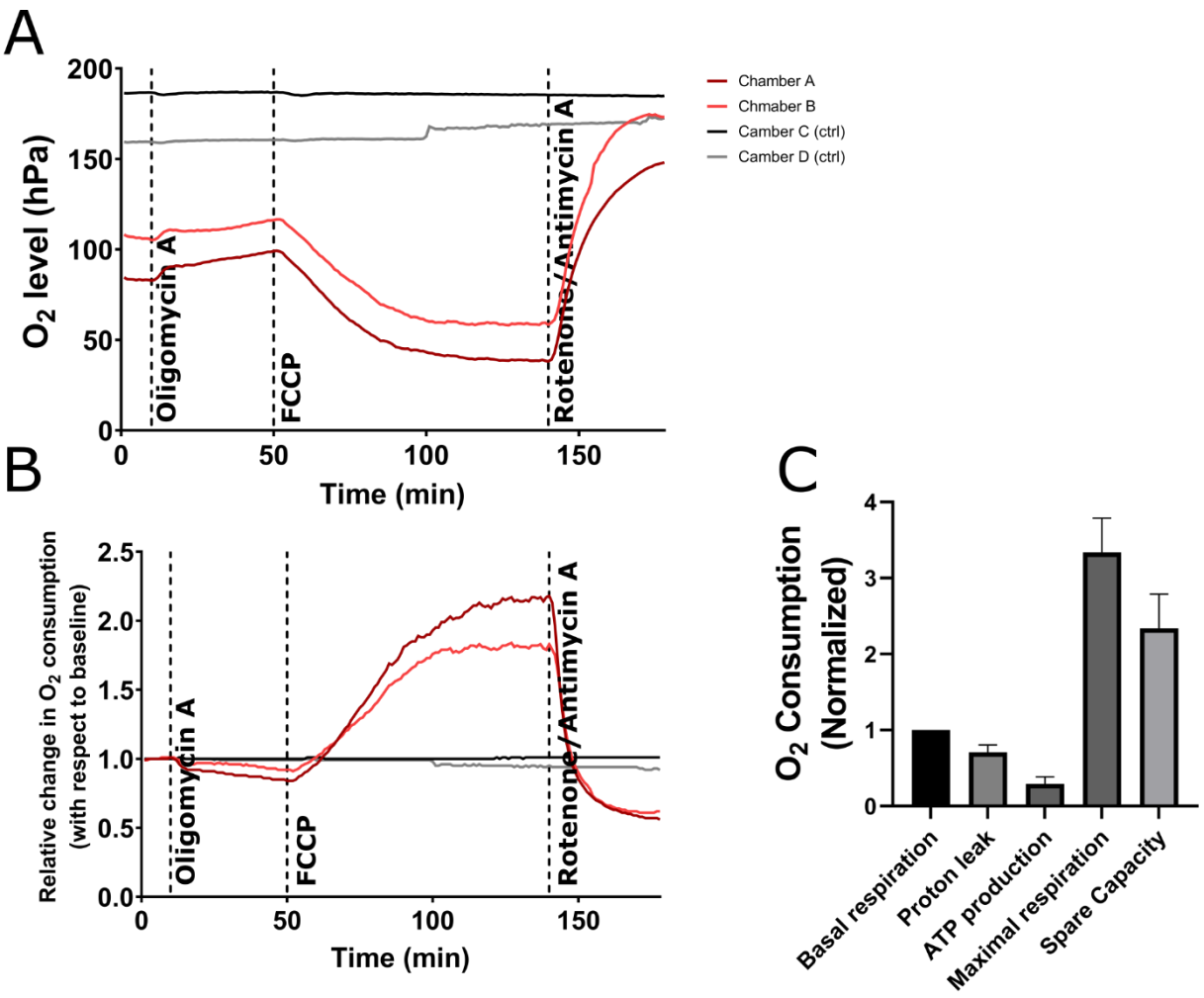

Figure 3.3.4 *On-chip mitochondrial respiration assay.* ***(A)*** *O_2 levels (hPa) of cardiac tissues treated in sequence with Oligomycin A (7.5 µM), FCCP (2.4 µM) and Rotenone / Antimycin A (3 µM / 6 µM) (Chambers A and B - red lines). Controls were provided with equivalent dilution of DMSO in media (Chambers C and D – black/grey lines)* ***(B)*** *O_2 consumption normalised on baseline (average of O_2 consumption before Oligomycin A injection). Dashed lines highlight timepoints of the drug injections. Negative controls (grey scale) were treated with media containing DMSO.* ***(C)*** *Analysis of cellular respiration from the O_2 levels measured by integrated sensors. Values are normalized on Basal respiration. Data is represented in a Bar plot as average ± SD (N=2).*

3.3.3 Drug response – Optical and O_2 sensors readouts

After successfully demonstrating that the induction of higher beating frequencies via electrical stimulation leads to changes in O_2 consumption, which can be measured non-invasively via the integrated sensors, the next question was whether drugs affecting cardiac function would also affect O_2 consumption. Therefore, the HoC with integrated sensors was exposed to two commonly used drugs, Verapamil and Isoproterenol, with opposing effects on cardiac beating.

Verapamil is a calcium channel blocker, which causes a decrease in beat frequency (negative chronotropic response) and cardiac contraction force (negative inotropic

response). On the contrary, administration of Isoproterenol, a beta-adrenergic agonist, results in a positive chronotropic and inotropic effect.

As previously showed, during perfusion, these compounds were retained by the plastic tubings. To avoid this in the following experiments, the compounds were supplied by a 100 µL tip inserted in the media outlet and the perfusion was performed by withdrawing the media from the tip through the chip and then into the syringes (**Supplementary Fig. 2**).

To test the effects of these compounds on tissue functionality, increasing concentration of the drugs (0 – 10'000 nM) was administered to the tissue and videos of the tissue beating were acquired. For each concentration, the drug was delivered under a constant flow rate for 20 minutes before video recording, after recording the tissues were left to recover in normal media for another 20 minutes before the injection of the next dose. Beating kinetics calculated from the videos showed a sharp increase in beats per minute already at 10 nM of Isoproterenol, while for Verapamil, higher concentrations were needed to lower the beat rate, with 10'000 nM stopping completely the beating of both tissues (**Fig. 3.3.5 A**). The average relative contraction also showed a similar trend (**Fig. 3.3.5 B**), presenting a progressive increase from 100 nM of Isoproterenol and complete ceasing at 10'000 nM of Isoproterenol.

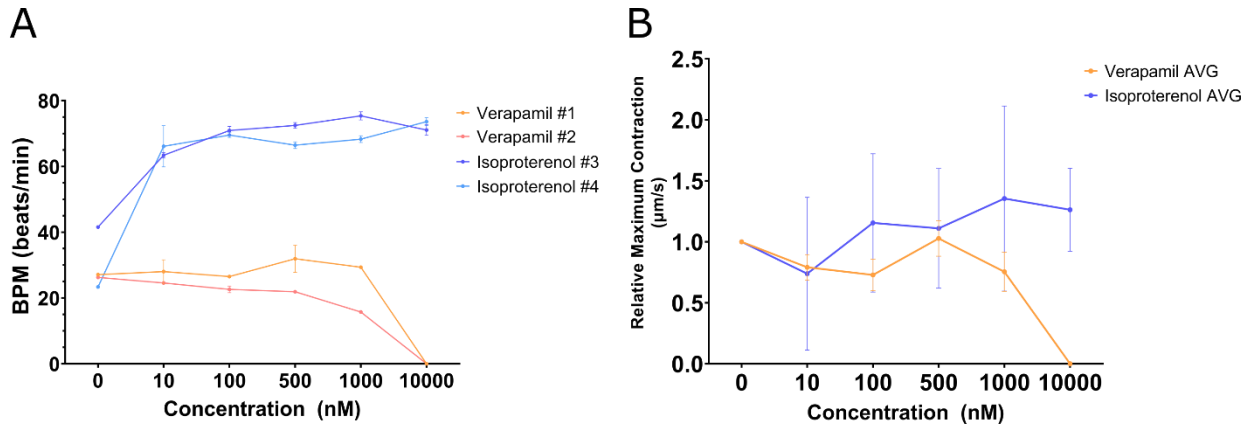

Figure 3.3.5 *Functional response to Verapamil and Isoproterenol drugs.* ***(A)*** *Beating frequency in response to increasing concentrations (0 – 10'000 nM) of Verapamil (orange, N = 2) and Isoproterenol (blue, N = 2).* ***(B)*** *Relative Maximum Contraction velocity in response to increasing concentrations (0 – 10'000 nM) of Verapamil (orange, N =2) and Isoproterenol (blue, N = 2). Line plot with standard deviations.*

To understand if the changes in functionality previously observed are reflected by a change in O_2 metabolism, I measured O_2 consumption before and during treatment with 10 µM of Verapamil or 100 nM of Isoproterenol (**Fig. 3.3.6 A**). The data from each chip was normalized by the average O_2 level before the start of the treatment; then relative O_2 levels were averaged for samples and controls. As **Fig. 3.3.6 B** illustrates, there is no significant difference in O_2 levels between the samples and the respective controls in the trend. This hints that both drugs, despite affecting the tissues functionality, do not induce a change in the cellular metabolism; at least in the short-term. From the drug response curves, I

calculated the Isoproterenol half-maximal effective concentration (EC_{50} = 250 nM) and the Verapamil half-maximal inhibitory concentration (IC_{50} = 1155 nM).

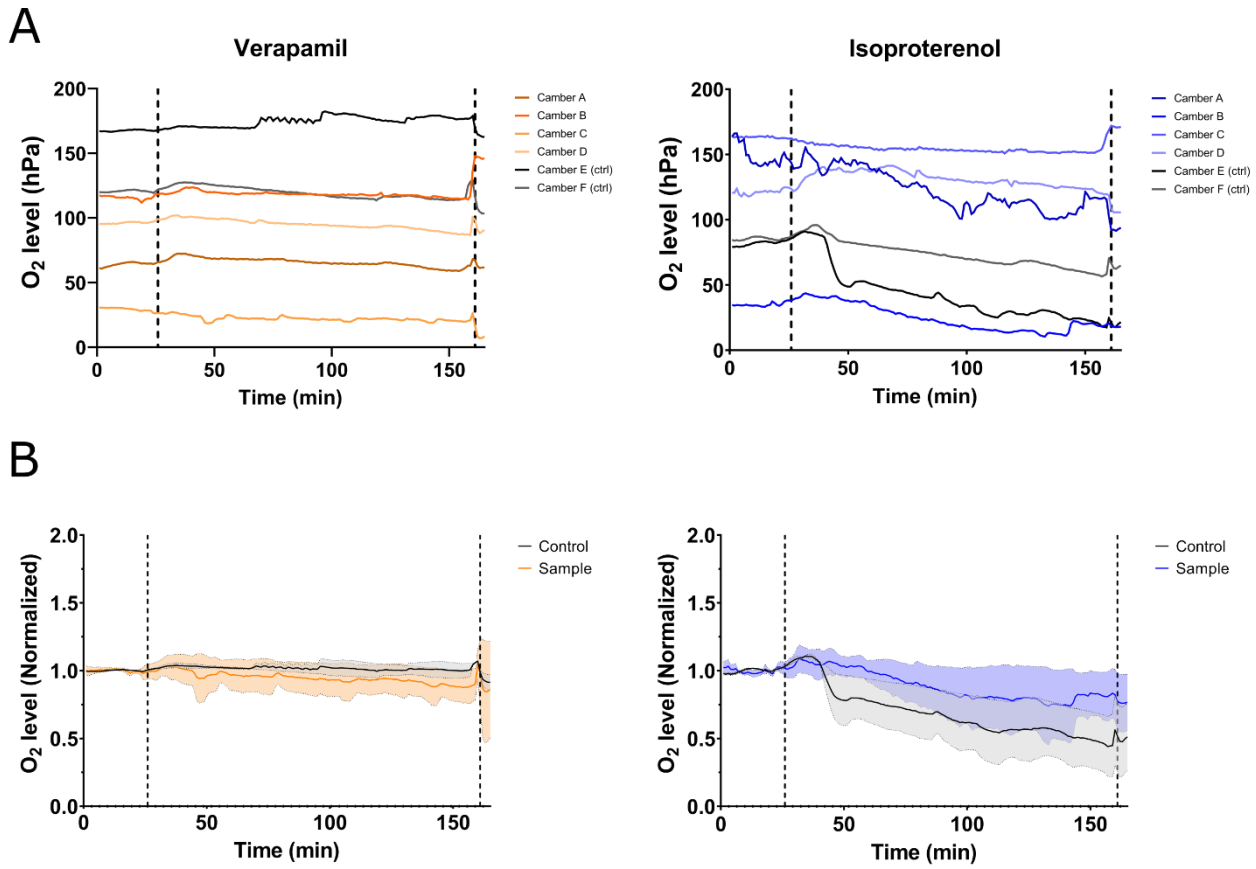

Figure 3.3.6 *Consumption of O_2 in cardiac tissues treated with 10 µM of Verapamil or 100 nM Isoproterenol.* ***(A)*** *O_2 levels (hPa) under drug treatment with either Verapamil (orange scale) or Isoproterenol (blue scale).* ***(B)*** *Average O_2 levels normalised on baseline (average O_2 value before treatment start) ± SD (area around the curve). Negative controls (grey scale) were treated with media containing DMSO 1:1000. Vertical dashed lines highlight the start and end of the treatment.*

3.3.4 Effluent Analysis

While the use of integrated sensors for detection and real-time measurement of biomolecules such as glucose and lactate are still a challenge, it is still possible to assess a tissues metabolism over-time by using commercial kits for effluent analysis. In particular, I investigated glucose consumption and lactate production to understand the metabolism of tissues cultured in the *Spheroflow HoC* over 14 days with and without pacing.

Chips were perfused in RPMI media (11.1 mM Glucose) + 2% B27 supplement at a constant rate of 50 µL/h. 24 hours before effluent collection, the outlet tube was moved from the waste reservoir to a 2 mL tube and after 24 hours the tube was collected and stored at −80°C until analysis. The effluent was collected at several time points (days 3, 5, 7, and 14). Pacing of the chip always started at day 5 after effluent collection.

The glucose concentration was measured using the QuantiChrom™ Glucose Assay Kit (DIGL-100, BioAssay Systems). The standard curve was obtained using 6 concentration points of glucose dissolved in water. The kit had a resolution of 0.3 mM, LOD = 0.9 mM and LOQ = 2.7 mM. The nominal medium Glucose concentration is 11.11 mM, however as it is possible to see in **Fig. 3.3.7**, most of the measured samples presented a higher glucose concentration. This could be due to partial water evaporation of the effluent during collection as a volume of only 50 µL/hr was perfused and collected over 24 hrs. Assuming the evaporation rate would remain constant for each chip for the duration of the experiment, to attempt to assess changes in glucose consumption over 14 days of culture, I normalised the concentration measured at each timepoint on the concentration at day 3 for each chip. At all timepoints, the concentration remained constant with differences below the resolution of the method (**Fig. 3.3.7 A**). The same could be observed for the comparison between paced and non-paced groups (**Fig. 3.3.7 B**). These results highlight that the QuantiChrom™ Glucose Assay Kit for detection of glucose in blood samples may not be suited for in-chip experiments.

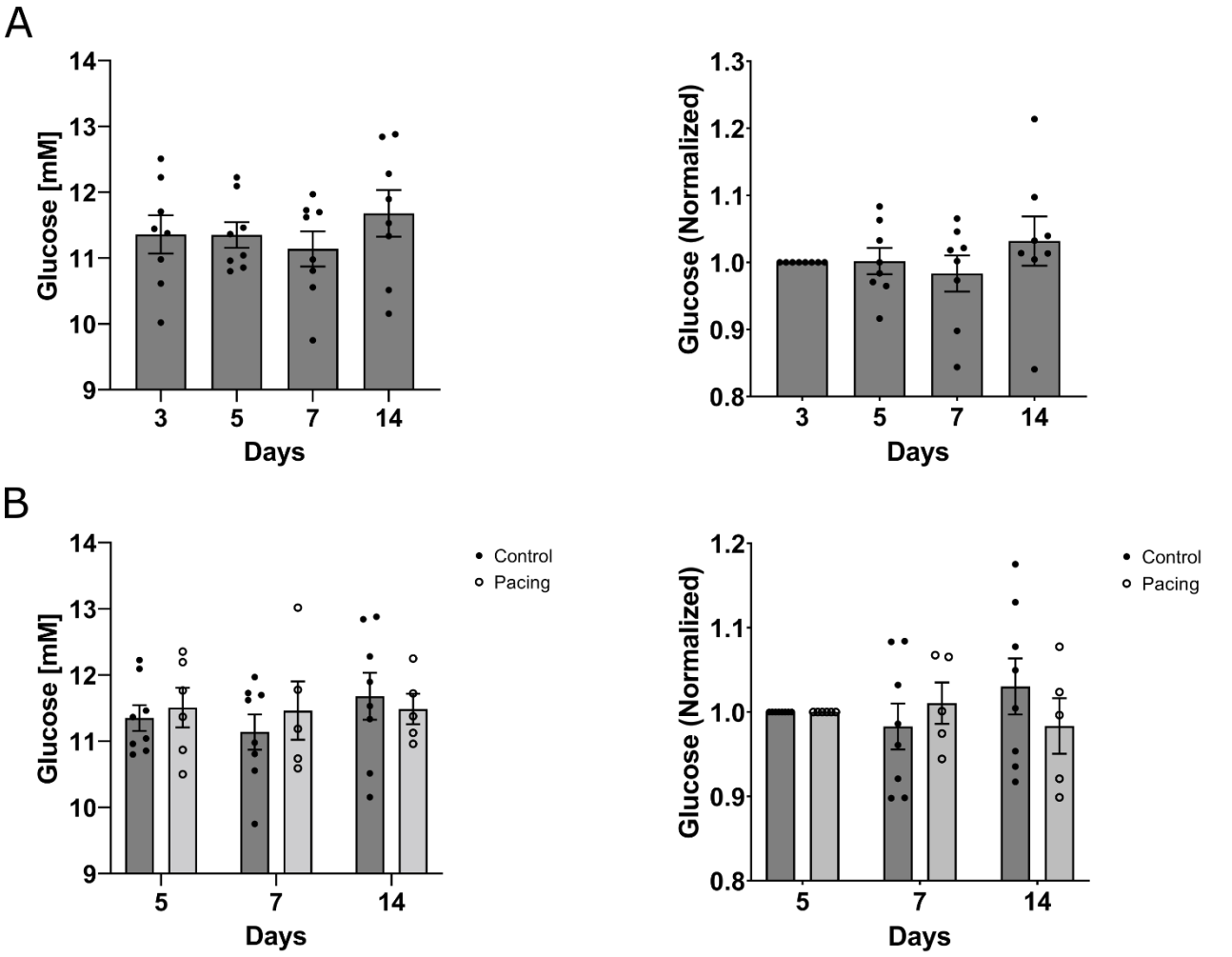

Figure 3.3.7 *Analysis of glucose consumption in chip effluent. Effluent samples are collected at day 3, 5, 7, 14 after 24 hours of perfusion.* ***(A)*** *On the left, Glucose concentration in chips' effluent over 14 days of culture; on the right, glucose concentrations of each chip were normalized over the*

respective glucose value at day 3. Statistical analysis by Two-way ANOVA of the normalized data showed no significative difference in glucose concentration between different timepoints. ***(B)*** *Comparison in glucose levels between Control condition and Pacing condition, where pacing started at D5 after effluent collection. On the left, Glucose concentration in chips' effluent over 14 days of culture; on the right, glucose concentrations of each chip were normalized over the respective glucose value at day 3. Data is represented in a Scatter dot plot with average ± SEM. Control condition (N = 8); Pacing condition (N=6, data points for tissue 2 on day 14 and tissue 5 on day 7 are missing). Statistical analysis by Two-way ANOVA of the normalized data showed no significant difference in glucose concentration between control and pacing condition at day 7 and day 14.*

While detection of glucose consumption could not be achieved, the Lactate-Glo™ Assay kit (J5022, Promega) worked in the µM range (up to 200 µM) and could detect secreted lactate in the media. From a 7-point calibration curve, a resolution of 0.2 µM, LOD = 0.7 µM and LOQ = 2.1 µM were calculated. Measured lactate concentrations fit within the range of the assay (**Fig. 3.3.8**), and differences in lactate secretion over time could be determined (**Fig. 3.3.8 A**). Over 14 days of culture, non-paced tissues show a progressive decrease in lactate secretion, from an average of 87 µM to an average of 57 µM at day 14. By normalizing the data for each chip over their baseline at day 3, a significant decrease in lactate concentration at day 14 by an average of 35% compared to the baseline is observed. Comparison between non-paced and paced tissues during the 14 days culture (**Fig 3.3.8 B**) showed constant higher levels of lactate secreted by paced tissues compared to non-paced controls, although not statistically significant.

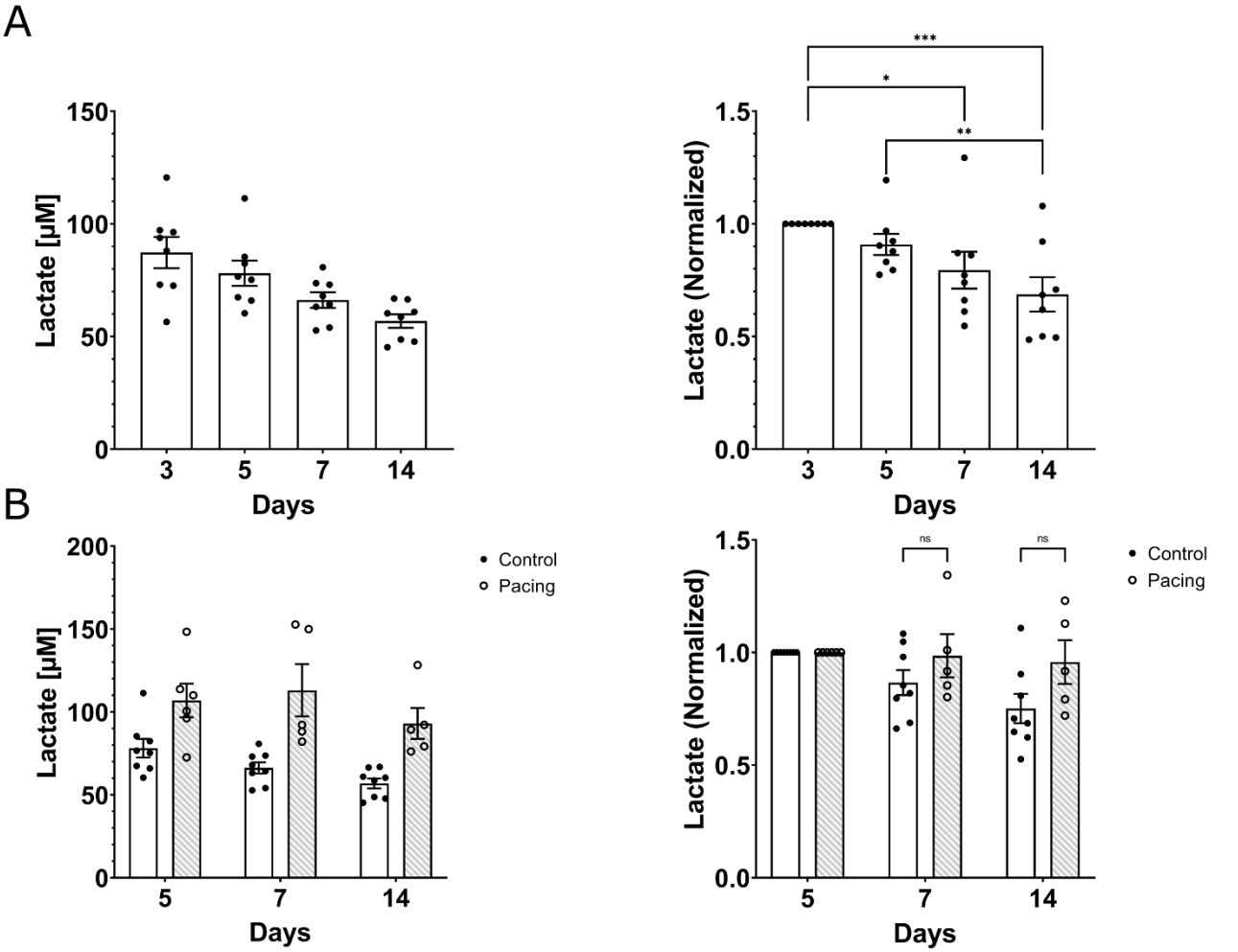

Figure 3.3.8 *Analysis of lactate secretion in chip effluent. Effluent samples are collected at day 3, 5, 7, 14 after 24 hours of perfusion.* ***(A)*** *On the left, lactate secretion in chips' effluent over 14 days of culture; on the right, lactate secretion of each chip was normalized over the respective glucose value at day 3. Statistical analysis by Two-way ANOVA of the normalized data showed significance in lactate secretions between different timepoints.* ***(B)*** *Comparison in lactate secretion between Control condition and Pacing condition, where pacing started at D5 after effluent collection. On the left, lactate secretion in chips' effluent over 14 days of culture; on the right, lactate secretion of each chip was normalized over the respective lactate value at day 3. Data is represented in a Scatter dot plot with average ± SEM. Control condition (N = 8); Pacing condition (N=6, data points for replicate 2 day 14 and replicate 5 day 7 are missing). Statistical analysis by Two-way ANOVA of the normalized data showed no significative difference in lactate secretion between control and pacing condition at day 7 and day 14. * p ≤ 0.05; ** p ≤ 0.01; *** p ≤ 0.001; ns = non significative.*

3.3.5 Raman Spectroscopy

While sensors and effluent analysis provide a non-invasive approach for monitoring tissue metabolites uptake or secretion in media, Raman microspectroscopy provides a non-invasive imaging approach for live-tissue characterization without the use of dyes or cell-reporter lines. The Raman imaging, spectra fingerprints detection, TCA and PCA were carried out together with Daniel Carvajal Berrio, from the Schenke-Layland Lab, Universitätsklinikum Tübingen, Germany.

Thanks to the *Spheroflow HoC* design, where the tissue is directly in contact with the bottom glass coverslip, it was possible to perform Raman spectra analysis through the glass substrate without the interference of the PDMS material.

Raman spectra were scanned with a 1 x 1 µm resolution and the resulting scans were analysed via TCA. TCA allows for the generation of true components that explain the spectral variability of the analysed sample. Moreover, heatmaps displaying the spatial distribution of the extracted true components, can be generated allowing the evaluation of changes within samples. Marker-independent imaging could be achieved within the platform and different cellular components (i.e., single cell nucleus) could be distinguished (**Fig. 3.3.9**).

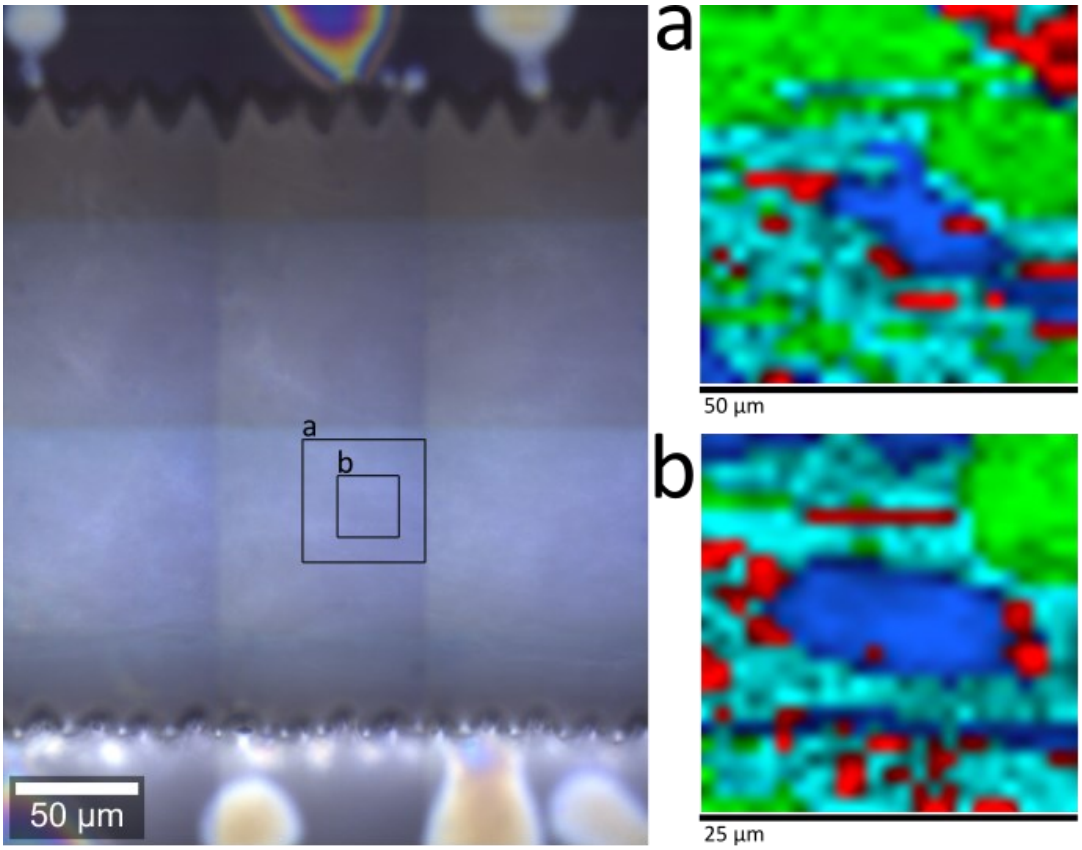

Figure 3.3.9 *TCA results of Raman imaging of fixed sample of fibroblasts in Spheroflow HoC. On the left, bright-field image of the tissue (scan tile) with highlighted 2 areas (a and b) for Raman scanning. On the right, TCA of Raman spectra of 2 areas (a, b). Different spectra are color-coded (lipids in red, background in-green,proteins in light blue and DNA in dark blue).*

Additionally, Raman depth-scans were performed to assess the Raman spectra signal characteristics and distribution in the z plane. The scans were done to a depth of 200 µm starting from the bottom of the chip, which was characterized by the dominant contribution of glass to the Raman signal. Within the *Spheroflow HoC* chip, the spectra from the chip materials could be identified and discerned from biological fingerprints (**Fig. 3.3.10**),

ensuring that the chip materials do not interfere with detection of cellular components within the tissue.

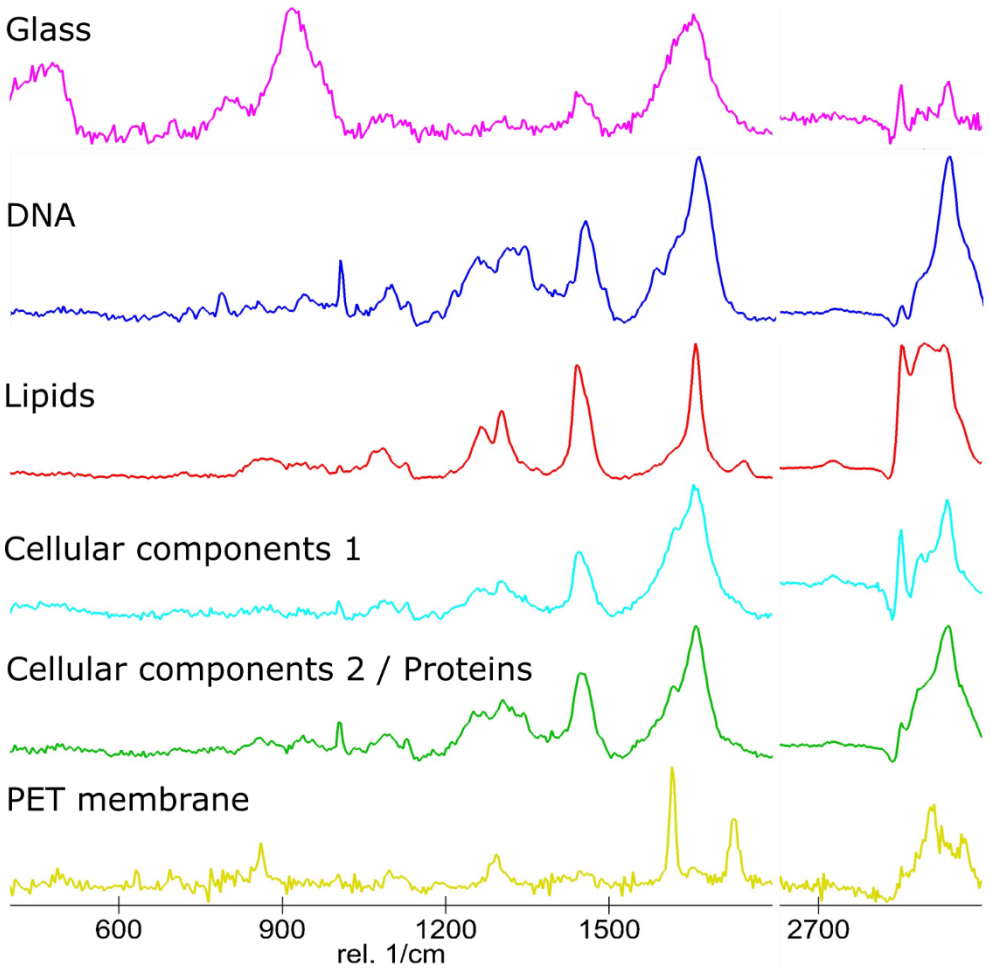

Figure 3.3.10 *Raman spectra detected in Spheroflow HoC tissue. Known spectra fingerprints are glass (magenta), DNA (blue), Lipids (red), PET membrane (yellow). Light blue and green spectra belong to cellular components that are not fully characterized.*

When phDFs were seeded in the *Spheroflow HoC*, these cells spread from the aggregates adhering mainly to the chip material. These resulted in a less compacted tissue compared to the cardiac fibre, where CMs form tighter cell-cell junctions and do not adhere to the chip material. In this scenario, it was possible to image along the Z axis and observe the distribution of different cellular components, such as lipids and proteins (**Fig. 3.3.11**). This, however, was not possible in highly compacted tissues such as cardiac fibres. Therefore, further tissue analyses were performed solely by imaging the tissue on the XY plane.

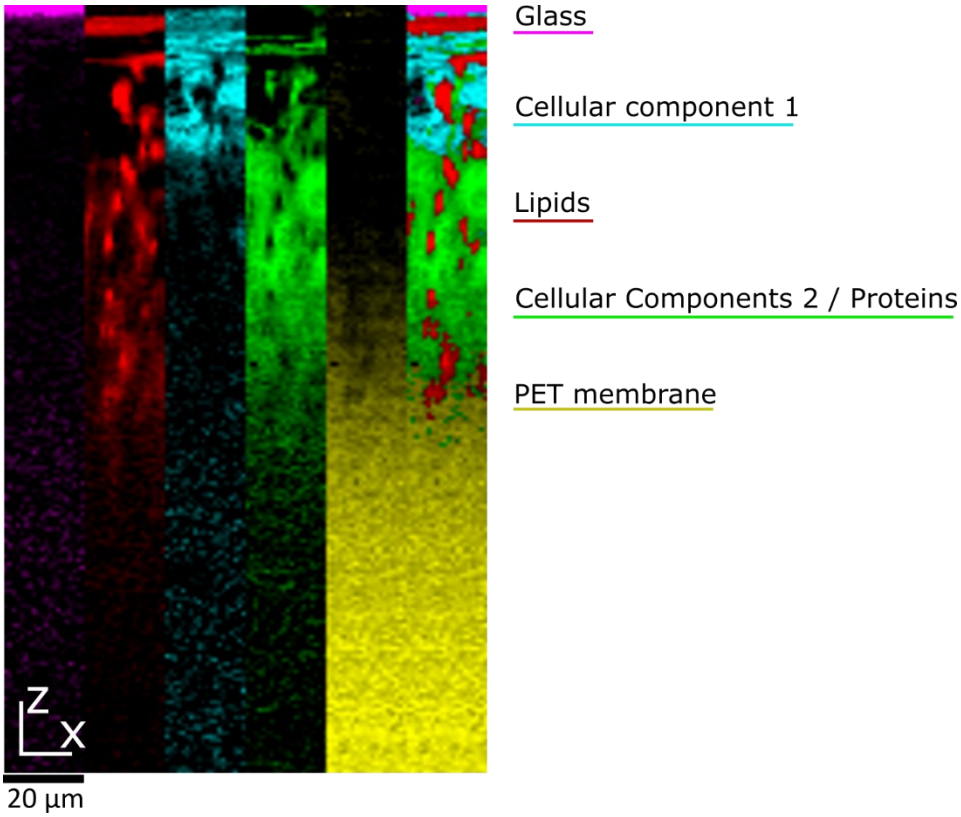

Figure 3.3.11 *Raman Imaging in fixed Spheroflow HoC fibroblasts tissue sample on the Z-axis. Scan of the tissue spectra from the glass surface (top, magenta) to the PET membrane (bottom, yellow). Color-coded single components distribution over the whole tissue thickness, in the following order from left to right: Glass, Lipids, Cellular components 1, Cellular components 2, PET membrane. The last panel on the right is the merged image.*

For a preliminary characterization of cardiac tissues on-chip, tissues were fixed and imaged at day 5. Five different cellular components were detected, and colour coded in **Fig. 3.3.12 A**, with the most abundant ones being proteins and Component #1. It was also possible to detect DNA within the tissue, showing high nuclei content (**Fig. 3.3.12** B). While some of the spectra fingerprints could be identified (**Fig. 3.3.12 C**), as lipid (yellow), DNA (blue) and proteins (green), some others were difficult to interpret. Component #1 may be Glycogen as it presents prominent peaks around 488, 854, 940 cm^{-1} as reported in literature (Konorov et al., 2011; Zbinden et al., 2020), while Component #2 present a spectrum similar to the mitochondria fingerprint (Tang et al., 2007; Zbinden et al., 2020). Component #3 was not properly identified.

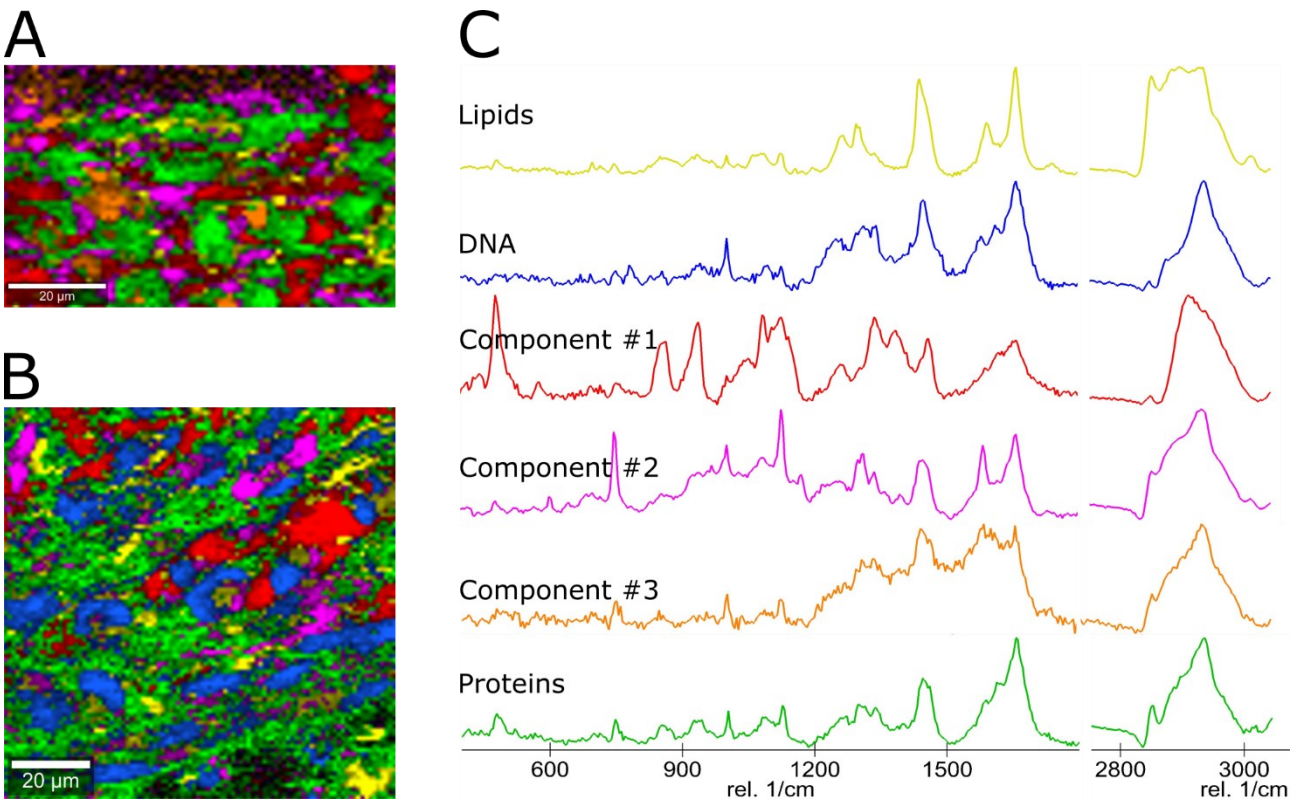

Figure 3.3.12 *Raman imaging of a cardiac tissue at day 5 in the Spheroflow HoC.* ***(A)*** *Raman image, showing presence of lipids, proteins, and 3 different cellular components (#1, #2, #3).* ***(B)*** *Raman image, highlighting the presence of lipids, DNA, cellular components #1 and #2 and proteins.* ***(C)*** *Spectra from of each component identified within the tissue.*

To compare cardiac tissues at day 5 to paced cardiac tissues at day 14, wavenumbers in the fingerprint region, from 397 to 1800 cm^{-1}, were further analysed via PCA. PCA of the protein content (**Fig. 3.3.13**) revealed differential distribution of the scores on the PC-2 axis between the two conditions (**Fig. 3.3.13 A**). The loadings of PC-2 show at what wavenumbers the paced tissues presented higher differences to the unpaced tissue at day 5, with positive values meaning that the paced tissues presented higher intensities at those wavenumbers, while negative values stand for lower intensities compared to the unpaced tissue at day 5 (**Fig. 3.3.13 B**). Statistical comparison of the average protein scores for PC-1 and PC-2 (**Fig. 3.3.13 C**), reveals a significative difference between unpaced and paced samples for PC-2 ($p = 0.0001$).

A

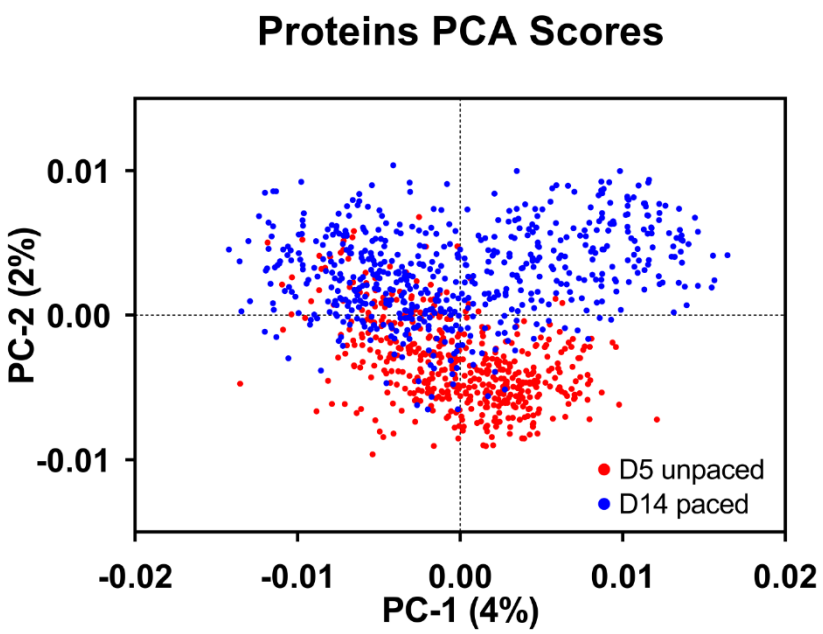
Proteins PCA Scores
0.01
0.00
-0.01
PC-2 (2%)
D5 unpaced
D14 paced
-0.02
-0.01
0.00
0.01
0.02
PC-1 (4%)

B

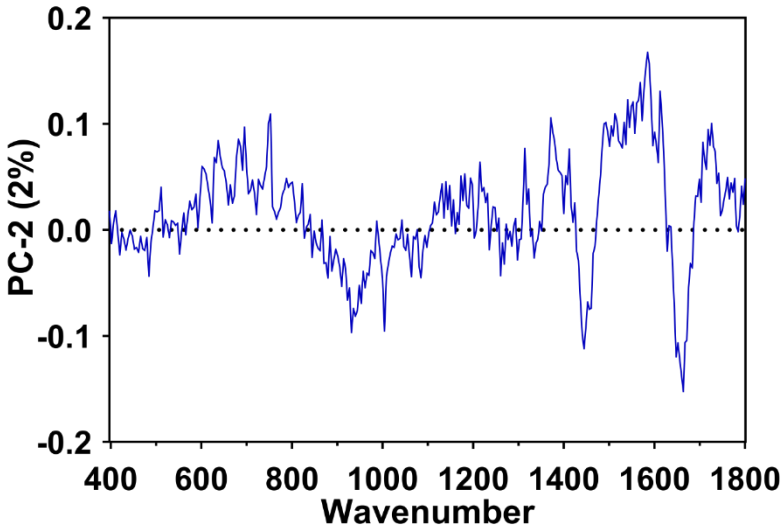
Proteins PCA Loadings
0.2
0.1
0.0
-0.1
-0.2
PC-2 (2%)
400
600
800
1000
1200
1400
1600
1800
Wavenumber

C

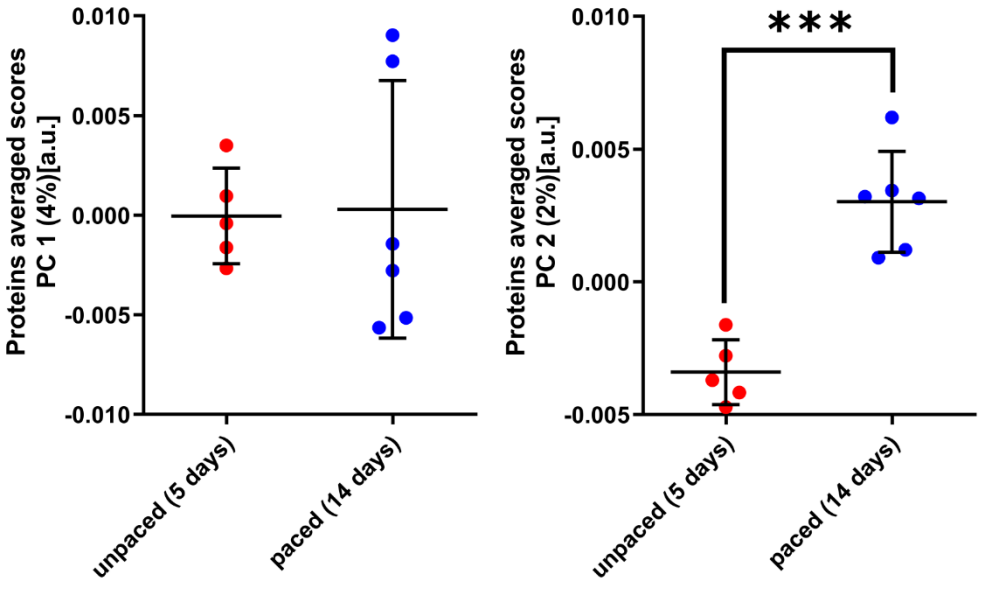
Proteins averaged scores
PC 1 (4%)[a.u.]
0.010
0.005
0.000
-0.005
-0.010
unpaced (5 days)
paced (14 days)
Proteins averaged scores
PC 2 (2%)[a.u.]
***
0.010
0.005
0.000
-0.005
unpaced (5 days)
paced (14 days)

Figure 3.3.13 *PCA of the Raman proteins spectrum.* ***(A)*** *Scores for the PC-1 (x-axis) and PC-2 (y-axis) of cardiac tissue at day 5 before pacing (unpaced - 5 days, red) and at day 14 after pacing regime (paced – 14 days, blue).* ***(B)*** *Loadings graph for the PC-2 displays the difference at each wavenumber in the fingerprint region (397 – 1800 cm^{-1}) of the paced tissue compared to the unpaced tissue.* ***(C)*** *Scatter dot plot of the average ± SD, PC-1 and PC-2 and comparison between unpaced and paced tissues. Data points represent 5 different images acquired randomly within the sample. Data was analysed by Unpaired t-test. *** p = 0.0001.*

In the same way, lipid content was also analysed and compared in cardiac tissues at day 5 and day 14 after pacing (**Fig. 3.3.14**). Scores between day 5 and day 14 samples were shifted on the PC-1 axis (**Fig. 3.3.14 A**). The loadings of PC-1 show bigger shifts in the paced tissue compared to the unpaced tissue in the 1300 – 1800 cm^{-1} range (**Fig. 3.3.14 B**). Statistical comparison of the average lipid scores for PC-1 and PC-2 (**Fig. 3.3.14 C**), reveals a significative difference between unpaced and paced samples for PC-1 ($p = 0.02$).

A

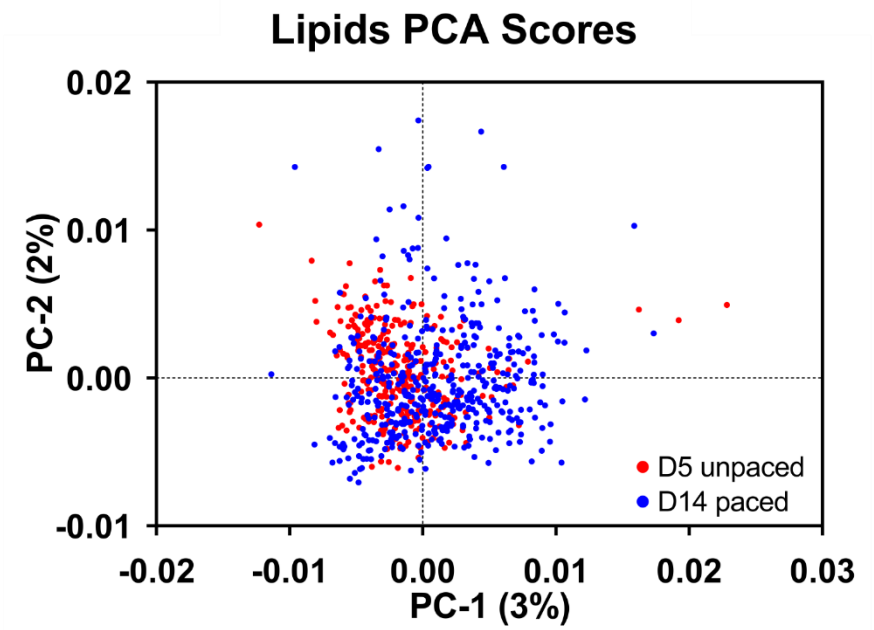
Lipids PCA Scores
0.02
0.01
0.00
-0.01
PC-2 (2%)
-0.02
-0.01
0.00
0.01
0.02
0.03
PC-1 (3%)
D5 unpaced
D14 paced

B

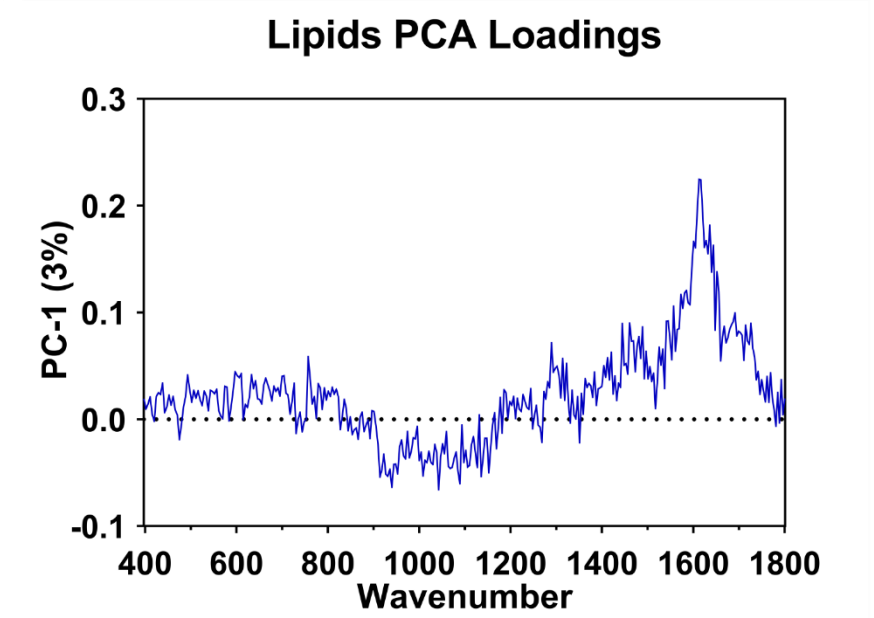
Lipids PCA Loadings
0.3
0.2
0.1
0.0
-0.1
PC-1 (3%)
400
600
800
1000
1200
1400
1600
1800
Wavenumber

C

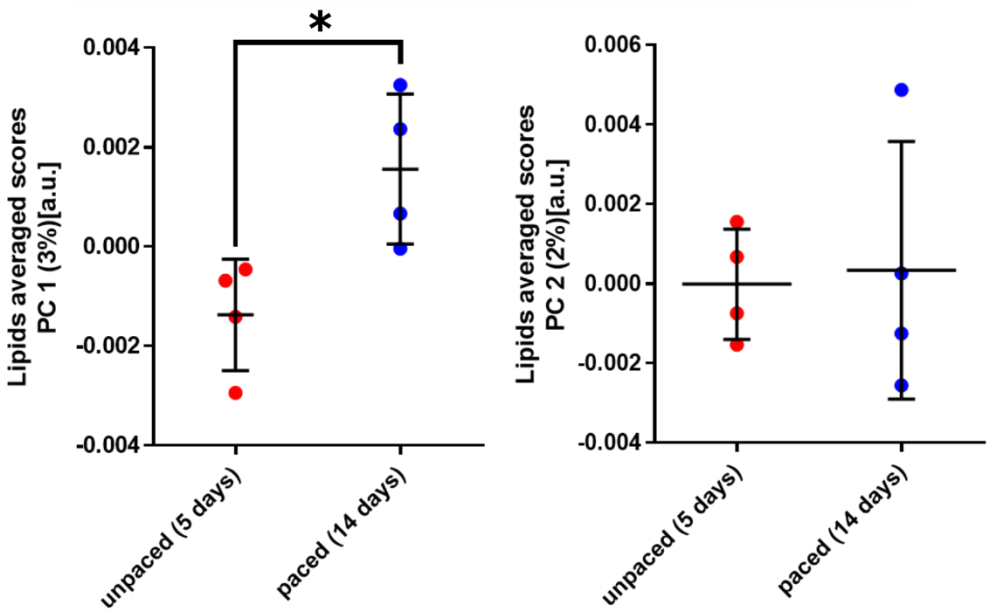
*
Lipids averaged scores
PC 1 (3%)[a.u.]
0.004
0.002
0.000
-0.002
-0.004
unpaced (5 days)
paced (14 days)
Lipids averaged scores
PC 2 (2%)[a.u.]
0.006
0.004
0.002
0.000
-0.002
-0.004
unpaced (5 days)
paced (14 days)

Figure 3.3.14 *PCA of the Raman lipids spectrum.* ***(A)*** *Scores for the PC-1 (x-axis) and PC-2 (y-axis) of cardiac tissue at day 5 before pacing (unpaced - 5 days, red) and at day 14 after pacing regime (paced – 14 days, blue).* ***(B)*** *Loadings graph for the PC-1 displays the difference at each wavenumber of the paced tissue compared to the unpaced tissue.* ***(C)*** *Scatter dot plot of the average ± SD, PC-1 and PC-2 and comparison between unpaced and paced tissues. Data points represent 4 different images acquired randomly within the sample. Data was analysed by Unpaired t-test. * p = 0.02.*

Overall, these results demonstrate the suitability of the platform for tissues investigation through Raman spectroscopy and the possibility to detect biological changes within tissues that underwent electrical stimulation.

3.4 Skeletal muscle-on-chip

The *Spheroflow HoC* platform and the readouts were established mainly focusing on cardiac tissues. However, the platform is also suitable for generation of skeletal muscle models. The aim is to generate functional skeletal muscle tissue out of primary myocytes isolated from either healthy or diabetic patients in order to study how physical exercise, modelled by electrical stimulation, can influence skeletal muscle functionality and metabolism.

Skeletal muscle cells were isolated from patients' biopsies and cryopreserved. For the experiment, the cells were thawed and expanded in "*Cloning medium*" (for medium composition see **Table 2.1.3**) until confluency. During expansion, the skeletal muscle cells mainly remain as elongated mononucleated cells. To induce cellular fusion into myotubules, the media was switched to "*POC medium*" (for medium composition see **Table 2.1.3**), which contained important FAs (palmitate, oleate and carnitine) for cellular maturation. Cells were cultured in POC medium for 10 days (**Fig. 3.4.1 A**). However, such medium was not generating functional myotubules. Even though cellular fusion was prompted, the cells were not responsive to electrical stimulation. It was determined that addition of IGF-1 to the POC medium was essential for generation of functional myotubules. Myocytes treated with POC media supplemented with IGF-1 not only showed higher cell fusion into bigger myotubules compared to the control condition without IGF-1 (**Fig. 3.4.1**), but also produced myotubules responsive to pacing. However, a frequent occurrence during pacing in adherent cells was the detachment and cell death of such formed myotubules during contraction.

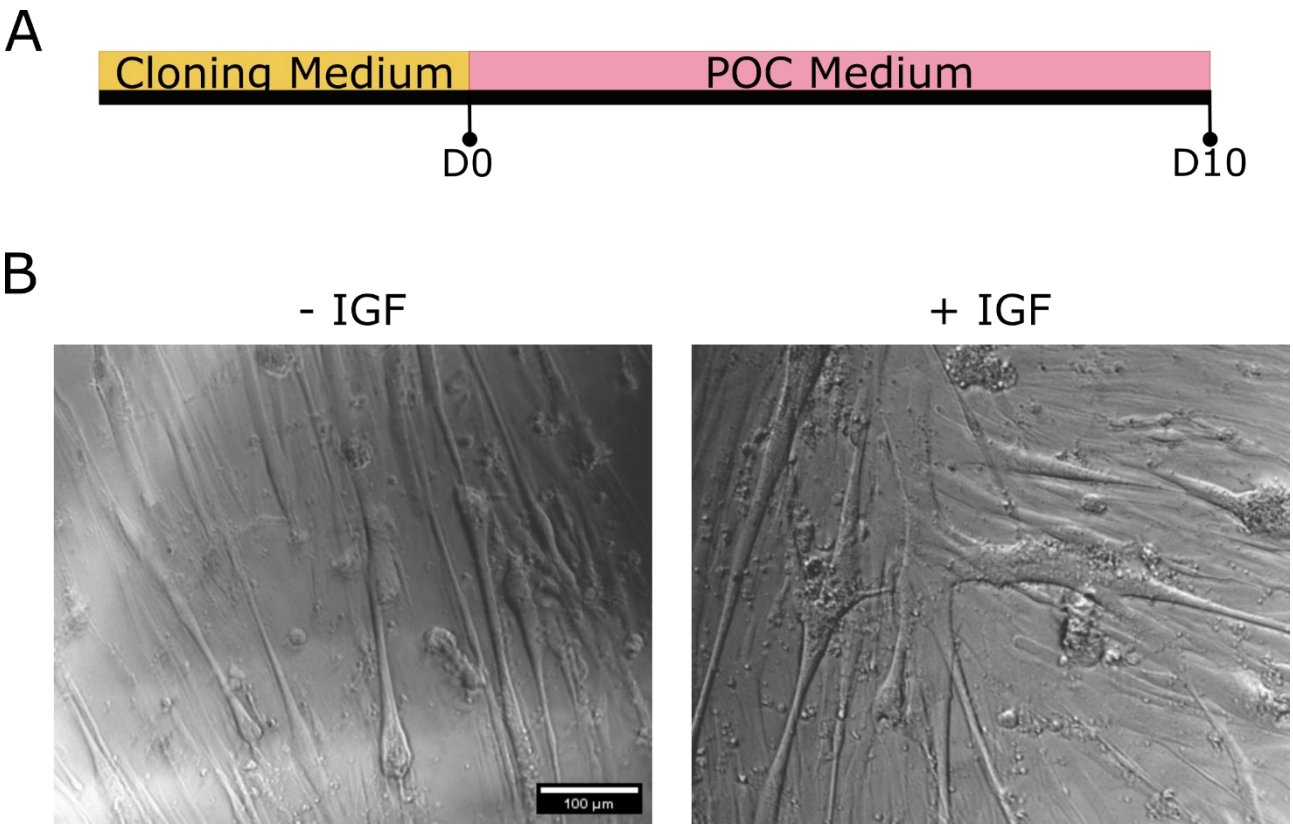

Figure 3.4.1 *Myotubule formation and functionality in 2D culture.* ***(A)*** *Timeline of the protocol: myocytes are cultured in cloning media until confluency is reached. The media is then switched to the POC media to allow for cell fusion in myotubules.* ***(B)*** *Differences in myotubules' morphology formed in POC media with and without IGF.*

Before establishing the protocol within a microfluidic device, the generation of 3D tissues following the 2D protocol was tested. To produce 3D skeletal muscle fibres, a 3D printed master mould for PDMS casting was designed (**Fig 3.4.2 A**). The PDMS mould featured an outer frame to hold a polyester frame and 2 channels to host the muscle fibres. The PDMS mould was provided to Dr. rer. nat. Simon Dreher from the Institute for Clinical Chemistry and Pathobiochemistry, University Hospital Tübingen. The mould allowed for the generation of primary human myobundles in a Fibrin/Matrigel® hydrogel, with the tissue extremities anchored to a polyester frame (**Fig 3.4.2 B**). The tissues were cultured following the same protocol applied for myocytes in 2D, and at day 10 the 3D myobundles displayed the same functionality (**Fig 3.4.2 C**). The flexibility of the polyester frame allowed the myobundles to contract during pacing while remaining anchored to it.

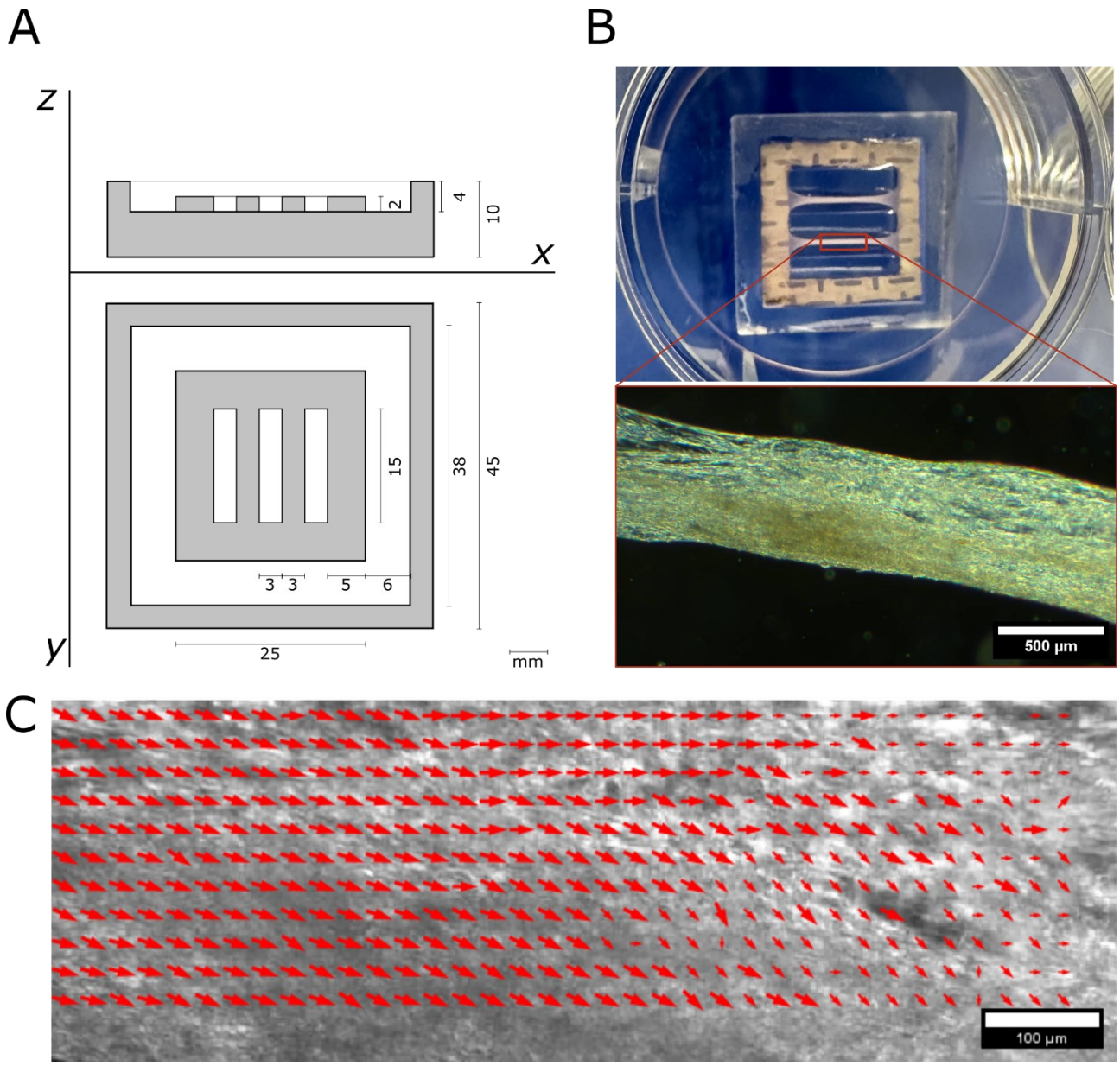

Figure 3.4.2 *Myobundle formation in 3D.* ***(A)*** *Design of the 3D printed master for generation of the myobundle PDMS moulds. Top view on the XY axes and view of the sidecut on the XZ axes. (units = mm)* ***(B)*** *Myobundles formed in the PDMS mold with a polyester frame, generated by Dr. Simon Dreher.* ***(C)*** *Motion vectors of the beating myobundle.*

Having successfully formed 3D myobundles in a Fibrin/Matrigel® hydrogel, the next step involved testing a similar approach within a microfluidic device. The protocol was chosen to be implemented in the *Spheroflow HoC* based on the hypothesis that the chamber geometry would facilitate the formation of aligned myotubules. Primary human satellite cells were mixed with either 4 mg/mL Fibrin/Geltrex® hydrogel, 1:5 Geltrex®, or 3 mg/mL TeloCol®-6, and 500,000 cells were injected per chamber into the *Spheroflow HoC* by pipetting. However, introduction of fibrin hydrogels within the tissue posed a challenge due to their high viscosity and the fast polymerization time of the hydrogel, which met high flow resistance due to the narrow chip channels. Therefore, further experiments were carried out in 1:5 dilution of Geltrex® or 3 mg/mL TeloCol®-6. The same culture protocol was

reproduced in 2D with and without the addition of IGF-1; as shown in **Fig 3.4.3**, the addition of IGF-1 led to the formation of bigger myotubules in the shaft region, spanning from one knob region to the other.

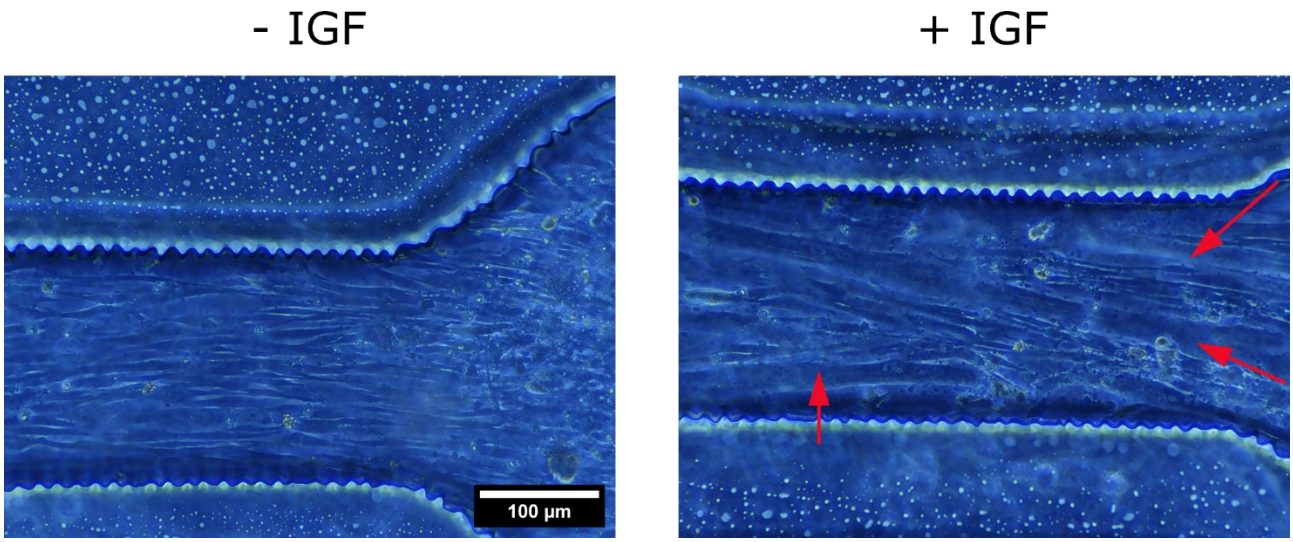

Figure 3.4.3 *Generation of the skeletal muscle tissue into the Spheroflow chip. Myocytes were seeded in Geltrex® hydrogel and the same protocol for myobundle formation in 2D was carried out with or without the addition of IGF. Red arrows indicate the myotubules formed.*

After 10 days, the skeletal muscle myobundles formed in Geltrex® hydrogel within the *Spheroflow HoC*. The myobundles showed responsiveness to electrical stimulation and collective movement during contraction at 1Hz (**Fig 3.4.4**). However, in both the 3D generated myobundles and on chip, Matrigel® and Geltrex® derived hydrogels were used. To move away from non-chemically defined product a bovine derived collagen hydrogel was tested, 3 mg/mL TeloCol®-6, which is, however, still of animal origin. The TeloCol®-6 hydrogel supported the tissue formation in the same way and resulted in a more ordered motion of the tissue during contraction, as displayed by the red arrows in **Fig 3.4.4 B**.

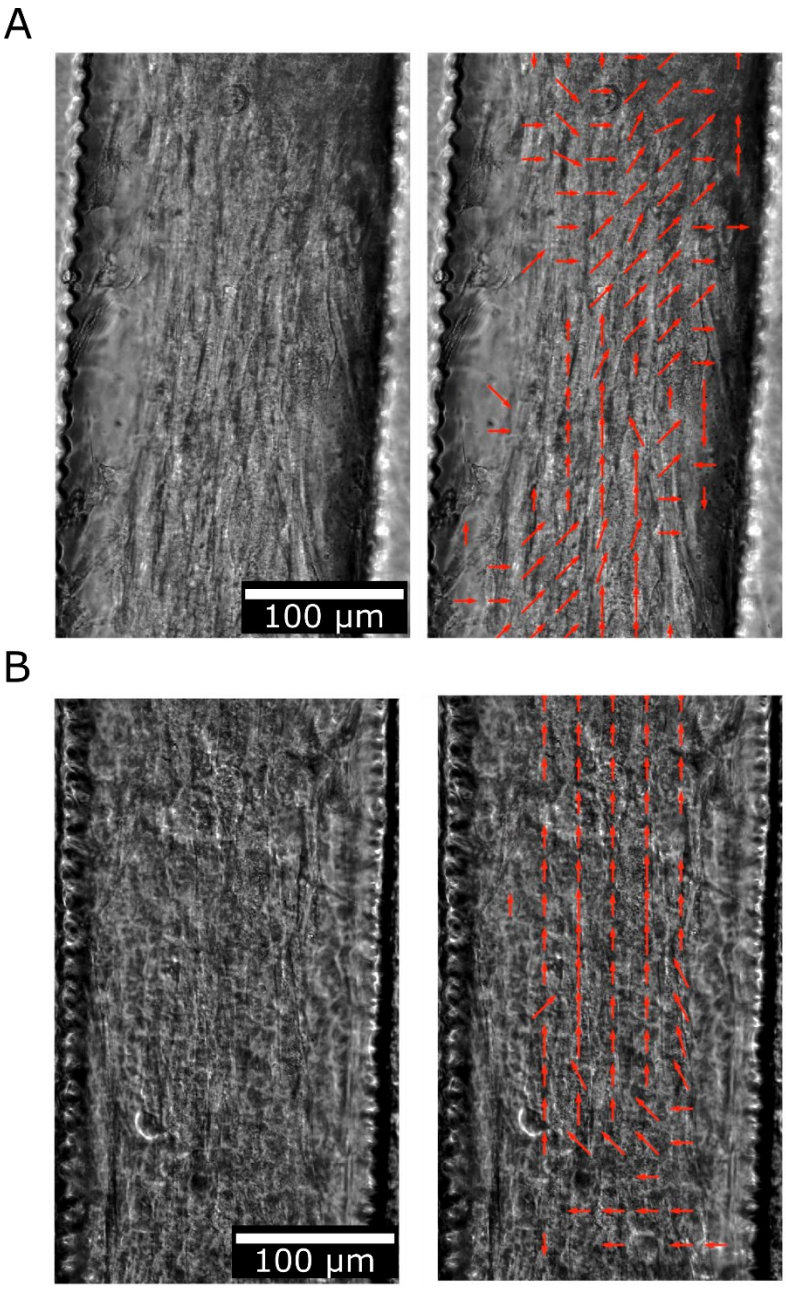

Figure 3.4.4 *Tissue formation and functionality in hydrogels.* ***(A)*** *Beating skeletal muscle fibre in Geltrex® (1:5).* ***(B)*** *Beating skeletal muscle fibre in TeloCol® (3 mg/mL). Red arrows show collective movement of the tissue within the chip shaft region.*

Tissue characterization showed good tissue viability at day 10 (**Fig 3.4.5 A**), under continuous perfusion of 50 µL/h with the media recirculation approach described in the method section 2.5.3.2. This approached allowed the use of a total of 6 mL of media/tissue over the 10 days of culture in POC media; compared to the standard approach without recirculation, which required 12 mL of media/tissue. The orthogonal view of the tissue revealed a 3D distribution of the nuclei within the height of the channel; however, a higher density of cells can be detected closer to the membrane side compared to the chip bottom (**Fig 3.4.5 B**). This could be due to the hydrogel slowing down nutrient diffusion from the membrane to the bottom of the chip. The staining of the tissues for F-actin and nuclei

revealed multinucleated myotubules and aligned actin filaments in the shaft region of the chip (**Fig 3.4.5 C**).

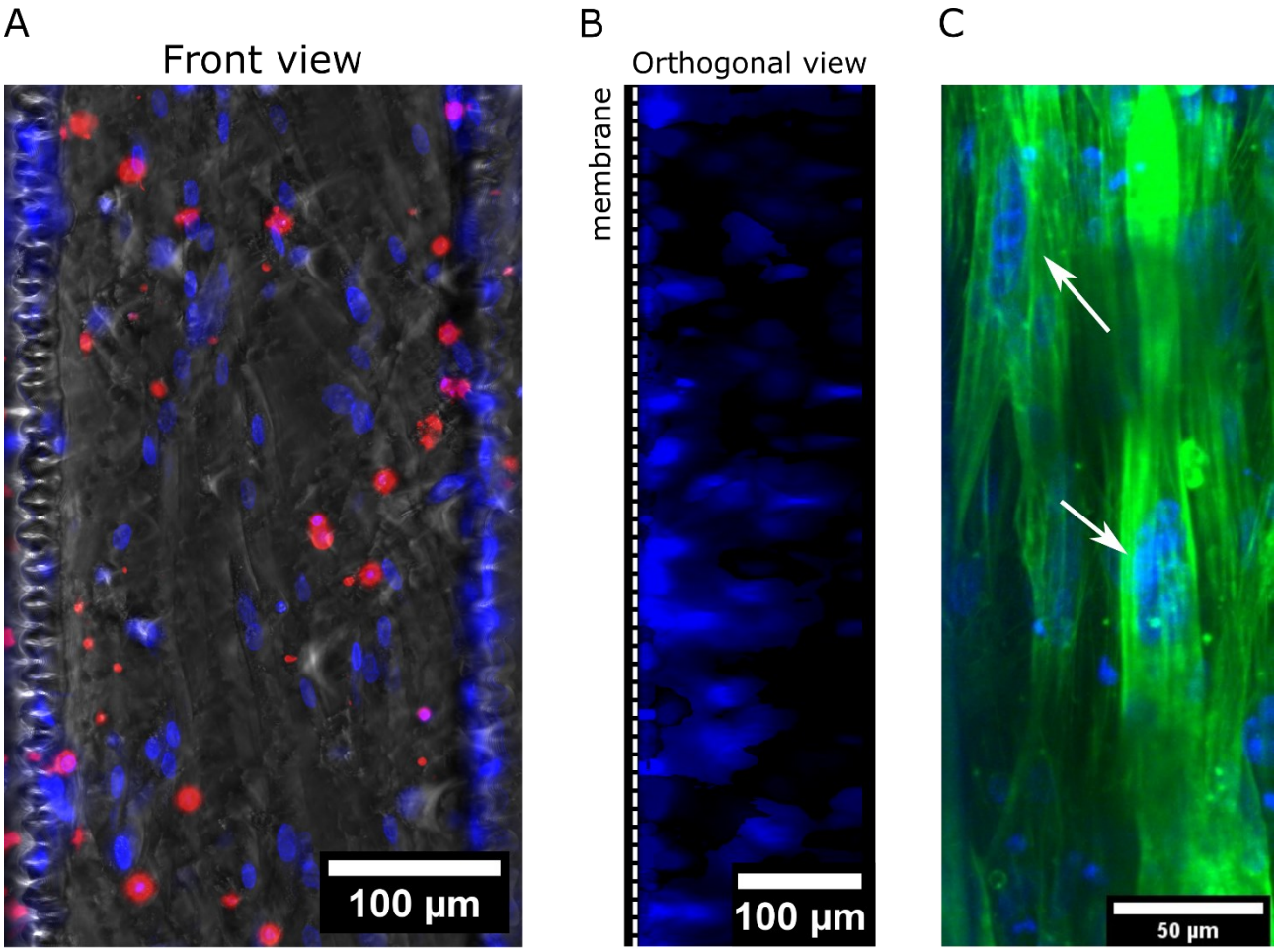

Figure 3.4.5 *Tissue viability and myotubules structure.* ***(A)*** *Front view: cell nuclei stained with Hoechst (blue) and dead cells stained with CellTox™ Green (red). Side view of nuclei reveals 3D distribution of cells.* ***(B)*** *Staining of the skeletal muscle fibre nuclei (blue) and actin filaments (green) displays multinucleated myotubules (white arrows) and aligned actin filaments on the y-axis in the shaft region.*

4 Discussion

The aim of this project was to establish and characterise a novel OoC platform for the robust generation of 3D cardiac tissues. The first milestone involved hiPSC differentiation and characterization of cardiac cell types such as CMs and CFs, followed by media screening for co-culture of CMs and fibroblasts. In parallel, the second milestone consisted of the development and validation of a microfluidic platform with a thin glass bottom layer and incorporation of electrodes for electrical stimulation and optical O_2 sensors. The third milestone consisted of achieving 3D tissue formation by loading pre-generated cardiac spheroids and characterising tissue morphology and functionality. The last milestone was to develop and apply non-invasive readout technologies to monitor tissue functionality and metabolic changes during electrical stimulation or drug treatment.

An additional part of this thesis included the repurposing of the OoC platform for generation of skeletal muscle fibres with the future aim of utilizing the platform for investigation of the effects of physical exercise on diabetic patients' skeletal muscles as well as to combine the skeletal muscle-on-chip model with other metabolic relevant OoCs (i.e. pancreas, fat and liver) to investigate metabolic interactions between the tissues in patho-/physio-logical conditions.

4.1 Validation of cell types used in this study

In the initial phase of the study, I developed protocols for maintaining and differentiating hiPSCs into CMs and CFs. The aim was to investigate alternatives to the use of undefined media composition and plate-coating for hiPSC maintenance. Despite their attempt to use chemically defined media, commonly used protocols for hiPSCs culture in monolayer rely on Matrigel coating and FBS for cryopreservation, which are chemically undefined due to their complex composition and isolation method (Y. Y. Kim et al., 2011; Laflamme et al., 2007; Lian et al., 2013; Passier et al., 2005; van den Berg et al., 2014). From the previously established protocol (O. Schneider et al., 2019), I substituted Matrigel with human recombinant vitronectin and used the chemically defined ibidi Freezing Medium Classic as freezing medium. Comparing different conditions, cells frozen in ibidi medium showed higher recovery rate and retained their morphology when thawed and seeded on vitronectin (**Fig. 3.1.1**). Despite being suitable for hiPSC maintenance, neither vitronectin nor laminin were able to support consistent differentiation of hiPSC into CMs (data not shown). Few papers, reviewed in Barnes *et al*., investigated the possibility of using human recombinant proteins as substrates for hiPSC differentiation into CMs (Barnes et al., 2022). Similar to my experience, Burridge *et al*., showed that vitronectin does not allow for adhesion of terminally differentiated CMs, resulting in the detachment and cell death of differentiated CMs; but contrary to my observations they estimated that laminin-521 substrate would be a suitable substrate for efficient CM generation, while fibronectin substrate despite being able to support terminally differentiated CM adhesion (O. Schneider et al., 2019) did not support pluripotent growth (Burridge et al., 2014). Therefore, hiPSC differentiation procedures in this thesis still rely on Matrigel coating.

Despite being suitable for hiPSCs and hiPSC-CMs cryopreservation, ibidi Freezing Medium Classic still contains BSA as a component; to further move away from animal components, alternative xeno-free freezing media (i.e., StemMACS™ Cryo-Brew and CryoStor® CS10) should be used. Additionally, B27 supplements, used in the described protocols, should also be switched with their commercially available xeno-free variants.

hiPSC-CMs differentiation protocol is based on the modulation of the Wnt/β-catenin signalling pathway by small-molecule manipulation. Differentiated CMs showed high expression of cTnT, indicating their CMs identity, but they also faintly expressed vimentin (**Fig. 3.1.2**), which has been reported to be a marker of foetal and hiPSC-CMs and to disappear postnatally (Dewing et al., 2022; H.-D. Kim, 1996; Zuppinger et al., 2017). This reveals that the hiPSC-CMs still lack proper maturation to a more adult phenotype. Cryopreservation or replating of the CMs does not compromise their purity, and lactate treatment further enhances their purity by selectively promoting the survival of CMs (**Fig 3.1.3**).

I then tested two protocols for isogenic CFs generation to support the functionality of hiPSC-CMs and compared protein expression of relevant markers with haCFv isolated from adult heart tissue and phDF.

In the first protocol, fibroblasts were differentiated by treating the cells with CHIR and bFGF for 18 days (**Fig 3.1.4**). The differentiated fibroblasts showed positive staining for vimentin but differences in the protein expression of the surface fibroblast marker, Cx43 and Collagen I compared to haCFv. In the second protocol, hiPSCs were driven through the cardiac developmental pathway, reaching CPCs stage at day 5 and EPCs stage at day 12. By day 18, the cells expressed the fibroblast marker DDR2 (**Fig 3.1.5**). In both protocols only a small fraction of hiPSC-CFs expressed the fibroblast marker CD90, for which the haCFv were positive. In accordance with Zhang *et al*., haCFv contrary to phDF do not express CD90 marker (J. Zhang et al., 2019). However, the haCFv bought by us from another company displayed high expression of CD90. These discrepancies in commonly used CF markers expression (fibroblast marker, CD90, Vimentin) and the lack of a CF unique marker make it hard to identify proper fibroblasts population and verify proper hiPSC differentiation into the fibroblast cell type. The lack of well-defined and specific markers hinders precise characterization and understanding of CF populations, emphasizing the need for continued research efforts to identify novel and reliable markers for these cells (Tallquist & Molkentin, 2017).

In monoculture, CMs and CFs are maintained in their own media. However, it is crucial to define a medium composition that allows for the viability of both cell types in a co-culture setting. The preliminary screening of cell viability in CM medium (**Fig. 3.1.6**) revealed that while dermal fibroblasts are viable and metabolically active in CM medium RPMI+B27C, this induces cytotoxicity in both hiPSC-CFs and haCFv. The presence of specific components in CF media, such as FibroGRO™ or FGM, highlights the importance of these factors for CF viability and function. For both media, the composition of the basal medium is proprietary however, important supplements contained are human serum albumin, linoleic acid, lecithin, ascorbic acid, insulin, L-glutamine, Hydrocortisone Hemisuccinate and 5ng/mL recombinant

human bFGF. Of these components, serum albumin, linoleic acid, insulin, and L-glutamine are also present in the RPMI+B27C medium; however, the proprietary media composition of the CF media does not allow us to determine in what concentration ranges these components are needed. As bFGF is a key factor to fibroblasts mitotic and survival activities, one approach was its addition to the RPMI+B27C medium, which however was not sufficient to sustain CFs viability. In an attempt to provide a sufficient amount of nutrients to the CFs, I mixed in a 3:1 ratio RPMI+B27C and FGM, which show reduced cytotoxicity and improved metabolic activity in fibroblasts (**Fig. 3.1.7**). This ratio was chosen to reflect the cell type ratio in the co-culture condition. The same media combinations were tested on hiPSC-CMs (**Fig. 3.1.8**), which showed an enhanced metabolic activity observed in the FGM and 3:1 mixed medium, indicating the influence of components in CF media on CM metabolism.

The tissue generation approach involves using spheroids as building blocks to achieve physiological densities, cell-cell contacts, 3D structural organization resembling heart tissue, and the ability to integrate other relevant cell types such as fibroblasts. The formation of tissue involves pre-generating cardiac spheroids from differentiated CMs and CFs, which then fuse into a uniaxially aligned cardiac muscle fibre. Testing the aggregation protocol with the different cell types (**Fig. 3.1.9**) revealed that both hiPSC-CMs and CFs alone formed irregular clumps, while phDF formed compacted, round spheroids that were resistant to shear stress. Adding phDF, to CMs improved aggregation, with a mixture of 25% phDF resulting in compact round spheroids of around 120 µm in diameter. The ratio of 75% CMs and 25% CFs was decided based on similar studies (Beauchamp et al., 2020; Giacomelli et al., 2020) and investigations of the heart composition (Banerjee et al., 2007; Dewing et al., 2022). Further analysis showed significant differences in spheroid compaction, with phDF-containing spheroids being smaller than those containing haCFv, which still resulted in loosely packed cells that could not bear sheer stress. Several other studies achieved spheroids generation with CMs and either hiPSC-derived or primary foetal CFs. However, their spheroids were generated by the hanging drop method or in a U- or V-shaped 96 wellplate, required high cell count / spheroids and several days of culture (4-7 days) to aggregate with regular media changes (Beauchamp et al., 2020; Giacomelli, Bellin, Sala, et al., 2017; Kahn-Krell et al., 2022). The strategy presented in this work relied instead on the AggreWell™ plate format which allows the high-throughput cardiac spheroid generation, with 1200 aggregates/well with only $0.5 \cdot 10^6$ cells, thus allowing formation of smaller aggregates. While this approach allows generation of spheroids within 24 hours, it is not suited for media change as the spheroids are easily displaced from their microwell by the sheer stress caused by pipetting or just by moving the plate, with subsequent fusion of the spheroids which come in contact with each other.

Based on the results of the media screening, the limited knowledge of CF media composition, and the inability to aggregate CMs with CFs, I decided to utilize dermal fibroblasts in the chemically defined RPMI+B27C medium for the subsequent development of the HoC model.

4.2 HoC platforms and tissue validation

Spheroid formation is a widely established technique yielding 3D tissues without the use of hydrogel; however, they cannot reproduce structural organization and cell alignment, recapitulating human physiology only partially. On the other hand, as illustrated in EHTs and HoCs, using single cells interspersed in a hydrogel with a defined shaped allows for recapitulation of tissue physiognomy. However, injection of cell-laden hydrogels yields low cell densities, is prone to clogging due to high viscosity and polymerization time and may lead to uneven cellular distribution. In contrast, when employing flow-based injection of cell suspensions, it is common to utilize retaining features to concentrate cells in specific geometries. However, these features are susceptible to clogging during the loading process, resulting in unpredictable loading pressures, flow interruption, and limited three-dimensionality of the cell distribution. In addition, both approaches require high cell densities to cast a single tissue. Generation of spheroids enables a precisely controlled cellular tissue composition by mixing defined ratios of different cell types, such as CMs and fibroblasts and allows for the formation of 3D tissues from pre-generated 3D building blocks, increasing tissue density compared to other commonly used approaches.

Two platform concepts were investigated for the injection of cardiac aggregates, with and without the addition of ECM components, for the formation of dense aligned cardiac tissues.

In the Centrifugal HoC, the centrifugal loading procedure relies solely on a conventional centrifuge commonly available in cell culture laboratories and allows the loading of multiple units in one centrifuge simultaneously (**Fig. 3.2.1**). The application of centrifugal forces during cell loading leads to consecutive loading of the chambers in a self-organized manner (Burger et al., 2012; Espulgar et al., 2015; Glynn et al., 2015; Park et al., 2017). This approach was previously used for the loading of single cell suspension within 8 adjacent chambers (O. Schneider et al., 2019). Furthermore, centrifugal loading provides the opportunity to tune the number of tissue replicates by modulating the cell number in suspension. By adapting chamber width and height it was possible to transfer this approach for the loading of cardiac spheroids in the *Centrifugal HoC* platform (**Fig. 3.2.2 A**).

As previously explained, cardiac ECM is predominantly composed of collagen fibres, and is essential for supporting CM adhesion, contraction, and maturation. Despite the successful loading of hydrogels within the *Centrifugal HoC* chamber (**Fig. 3.2.2 B**), centrifugation was found to be ineffective for co-loading both hydrogel and cardiac spheroids into the chip. Instead, the loading process was adapted to utilize hydrostatic pressure for the loading of spheroids and the subsequent injection of the hydrogel (**Fig. 3.2.3**). In order to incorporate a physiologically relevant ECM, a collagen I hydrogel (FibriCol®) was employed. It is important to mention that this loading method was specifically suitable for hydrogels with low viscosity, such as collagen I at concentrations up to 3mg/mL. This ensured that the hydrogel could effectively fill the spaces between the cardiac spheroids, promoting their structural integration within the tissue model. The limitation of using low concentrations of FibriCol® used for the hydrogel is that the resulting hydrogel has a nominal stiffness of 0.5 kPa. This stiffness is more similar to the embryonic stage of ECM stiffness (0.2 kPa) rather

than the stiffness observed in the adult heart (10-20 kPa) (Gaetani et al., 2020; Huyer et al., 2015).

Over 6 days of culture, the tissue remained viable (**Fig. 3.2.4; Fig. 3.2.5**) and displayed compaction and spontaneous beating, meaning that the hydrogel does not prevent cell migration and tissue formation. However, the tissue experienced collapse from the lower knob to the shaft region, likely due to collagen shrinkage. Despite this, the tissue retained its ability for spontaneous beating, although the motion vectors showed more disorganized displacement compared to day 3 and exhibited a much lower beating rate compared to non-hydrogel-embedded tissues (O. Schneider et al., 2019, 2022). As reviewed by Hameed and Manivasagam, several studies have reported the collagen hydrogels undergo gradual shrinkage when cultured *in vitro* (El-Fiqi et al., 2013; Galois et al., 2006; X. Liu et al., 1998; Velegol & Lanni, 2001). Cells cultured have been observed to cause contraction, shrinkage, and actuation of the hydrogel due to cell-generated traction forces exerted on collagen type 1 hydrogels (Bacakova et al., 2019). This can alter the mechanical properties of hydrogels, such as compressive strain energy, tensile modulus, and compressive modulus (Hameed & Manivasagam, 2021; Velegol & Lanni, 2001). To prevent shrinkage and collapse of the tissue, one potential solution is to apply a PDMS coating with polydopamine (S. Kim et al., 2022). This approach can help maintain the mechanical properties of the hydrogel, preserve tissue structure, and enable linear contraction motion in the cardiac system.

Overall, the loading of cardiac aggregates and hydrogel within the centrifugal platform was possible but the filling of all 8 tissue replicates was not consistent, as aggregates often caused the clogging of the chambers' shaft region, resulting in incomplete chamber loading.

The *Spheroflow HoC* platform (**Fig. 3.2.6; Fig 3.2.7**) incorporates side lying constrained channels that prevent excessive pressure buildup during cell injection, similar to the trapping system described by Bruzewicz *et al*. (Bruzewicz et al., 2008). This design avoids the need for uncontrolled manual pressure and ensures the use of defined hydrostatic pressures. Furthermore, the HoC tissue layer can be assembled on coverslips for high-resolution imaging and Raman imaging or on top of O_2 sensor PET substrates.

To provide an on-line real-time monitoring of oxygen tissue metabolism, optical O_2 sensors were integrated into the platform. As explained in the introduction (section 1.2.3), measurement of O_2 levels were determined by the $\Delta\varphi$. PDMS exhibits oxygen permeability, which implies that in a complete PDMS chip, oxygen can permeate through the bulk material in the tissue layer, thus affecting the measurement of oxygen levels. Furthermore, the polymer mixture used for O_2 sensors does not adhere well to the PDMS material. These two factors present challenges in integrating sensor spots into fully PDMS platforms. To overcome these limitations, the chip fabrication process involves casting a gas impermeable resin for the tissue layer, which allows for the placement of O_2 sensors beneath the tissue (**Fig. 3.2.7; Fig. 3.2.10 B**) within the tissue chamber. This design bypasses the limitations posed by PDMS. In this set up, the PDMS media permits oxygenation of the top layer, while the measured O_2 concentration at the tissue level corresponds to the remaining oxygen concentration after tissue consumption. This configuration enables reliable O_2 measurement

under a constant media flow. However, the thin glass substrate, which is ideal for microscopy, was unsuitable for sensor adhesion and had to be replaced with a PET foil.

The chip concept described in this study is not limited to a specific fabrication method and material, as explained in Section 2.3.2 of the Methods. HoCs were successfully assembled using PDMS for both the tissue and media layers, as well as resin-based combinations of tissue layer with PDMS or TPE media layers. All these materials were also compatible with organic and water-based imaging clearing solutions (**Supplementary Table 1**). The biocompatibility of the resin used in the resin-based assemblies was confirmed for CM culture (**Fig. 3.2.8**).

When building an OoC device, it is crucial to consider its adsorption and absorption properties. Understanding the extent to which the drug of interest is retained within the system allows for adjusting the starting concentration to achieve the desired concentration at the tissue interface. Few studies in OoC tried to determine material drug absorption by using fluorescence molecules (i.e., rodhamines, cyanine NHS ester, paclitaxel and nile red) and measuring fluorescence spreading within the material (Ongaro et al., 2020; S. Schneider et al., 2021). Despite providing predictive insight, each different compound may be retained differently based on their chemical properties, such as molecular weight, logP, and functional groups. Therefore, it is important to test each compound beforehand. Van Meer *et al*. and Mair at al. characterized PDMS absorption of different drug compounds by UV-Vis spectroscopy (van Meer et al., 2017), and Mair *et al*. proposed a PDMS-PEG co-polymer to prevent drug absorption (Mair et al., 2022). Nonetheless, all mentioned studies were executed in static conditions. However, parameters such as chip design (Shirure & George, 2017), perfusion flow rate, time, temperature, and solvent all influence drug retention (absorption and adsorption) in the material. Therefore, the analysis set up should closely resemble the experimental set up in order to take into account all the aforementioned parameters.

To investigate the potential retainment of two majorly used drug compounds for HoC validation, Verapamil and Isoproterenol, a HPLC analysis of the drugs´ concentration after passing through the chip platform at a constant flow rate was performed (**Fig. 3.2.9**). The results showed that both drugs were primarily retained by the plastic tubings used for perfusion, with significant differences compared to the stock solution. The drug retention by the chips of different materials was negligible compared to those of the tubings. These findings indicate that most of the drug retention occurs before reaching the chip. Further investigation with optimized HPLC protocols for verapamil and isoproterenol detection at a higher resolution (Leedahl, 2016; Özkan et al., 2000) is required to examine the differences in retention, absorption, and adsorption kinetics between chips of different materials.

In the *Spheroflow HoC* platform, a suspension of cardiac spheroids was loaded into the chamber using hydrostatic flow, completing the process within one minute. Unlike previous methods that trap individual spheroids in microfluidic environments (Bergström et al., 2015), this approach confines a relatively large number of spheroids (approx. 50 spheroids) within a single chamber (**Fig. 3.2.10 A**). However, a drawback of this loading strategy is that each chamber may contain a slightly different number of cardiac spheroids, resulting in variations

in cell numbers between different tissues without precise knowledge of the exact cell count per chamber. Research conducted by Kim *et al*. (2018) and Arai *et al*. (2020) demonstrated that these generated spheroids tend to merge spontaneously upon contact (Arai et al., 2020; T. Y. Kim et al., 2018). The microfluidic geometry guides the tissue's shape as the aggregates fuse over a 24-hour period (**Fig. 3.2.10 B**). By utilizing the approach of forming spheroids in microwells, it was possible to reliably generate a high number of spheroids (approx. 1200 spheroids/well) of uniform size, from 0.5 million cells. These 1200 spheroids enable the generation of 24 aligned cardiac tissues (with approximately 50 spheroids per tissue) after injection into the chip.

Achieving physiological cellular alignment is a key objective in cardiac tissue engineering. Both platforms, by confining introduced spheroids within dog bone-shaped tissue chambers, successfully generate 3D tissues with significant alignment, evident from the aligned sarcomeres observed in the shaft region of the tissue chamber (**Fig. 3.2.11 A-B**), similarly to what was previously achieved with single cell seeding (O. Schneider et al., 2019). As a result, the HoCs accurately replicate the microstructure found in native cardiac tissue. Furthermore, media perfusion ensures an effective diffusion of nutrients in both HoCs, sustaining tissue functionality (**Fig. 3.2.4; Fig. 3.2.5; Fig. 3.2.11 C-D**). In comparison to static culture with periodic media exchanges, both systems offer closer mimicry of human physiology.

Although this chip could also be loaded with hydrogels, like the centrifugal HoC, once again hydrogel viscosity constituted a limiting factor (data not shown). However, while the *Centrifugal HoC* loading approach did not offer the possibility to load two different spheroid types within the same chamber (i.e. healthy/diseased, atrial/ventricular) as the sequential loading of each chamber relies on the prior chamber being fully loaded; the *Spheroflow HoC* approach offers the possibility of producing hetero-tissues, similarly to the Biowire platform (E. Y. Wang et al., 2019). Heterogeneous tissue formation, contraction coupling and beating dynamics were investigated in the *Spheroflow HoC* by my colleagues Joanna Nowacka and Dr. Dominik Eckardt at Miltenyi Biotec and they are therefore not reported in this thesis.

One characteristic of the implemented spheroid loading approach is the incomplete filling of the tissue compartment when compared to single cell loading (O. Schneider et al., 2019). The spherical shape of the introduced spheroids results in empty spaces between individual spheroids. As the spheroids merge and further compact, the compartment remains partially unfilled. This altered filling may affect the fluid dynamics of the system, potentially enabling increased media flow through the membrane into the tissue compartment. While this additional flow may enhance nutrient supply by introducing a convective nutrient delivery component alongside diffusion, it can also potentially impact tissue functionality in unpredictable ways. To protect the tissue from shear forces after compaction, one possible solution is to inject and subsequently polymerize a hydrogel into the tissue chamber, effectively filling the void. In addition, the current system does not include endothelialisation of the tissue, as the endothelial barrier is simulated by the porous membrane. However, it offers the possibility to integrate ECs by seeding them in the media layer on top of the porous membrane, similarly to what is presented in many other organ models (Cipriano et al., 2022; Nawroth et al., 2021; Ronaldson-Bouchard et al., 2022; Si et al., 2021). Despite this, inner

vascularization of the tissue and cell-cell contact between CMs and ECs cannot be investigated in the current set up of the platforms. A possible approach to studing vascularization and CM-EC interaction consists of introducing a hydrogel mixture with interspersed ECs into a tissue chamber hosting pre-formed cardiac tissues containing ECs. As demonstrated by Ulgu *et al*., when the cardiac organoids are surrounded by a fibrin hydrogel containing ECs, over time, lumenized vascular networks spontaneously form around and inside the cardiac tissue through anastomosis (Arslan et al., 2023).

As previously explained, electrical actuation is one of the main stimulation approaches investigated to drive hiPSC-CMs maturation, as well as to verify changes in tissue contraction parameters in pathological conditions (i.e. arrythmia, fibrosis etc) and provide a defined baseline beating frequency for drug testing. Therefore, it is desirable to have an easy integration of electrodes into existing HoCs, without requiring changes in chip design and fabrication. This can be achieved by using the metal fluidic connectors to deliver electrical stimulation through the media compartment (**Fig. 3.3.12 A-B**). However, fluidic connectors limit the electrode material to the connector material, which in this case is stainless steel. This may not be optimal for electrophysiology and could potentially generate toxic byproducts. Nonetheless, compared to pacing in a static system, the existing media flow can assist in removing these toxic byproducts, allowing pacing to be conducted for longer durations (Tandon et al., 2011).

Simulation results indicate that both investigated HoCs exhibit a homogeneous electrical field in the shaft region. The predicted field strength of 0.8 V/cm (**Fig. 3.3.12 C**) is lower than the conventionally applied electrical fields of approximately 5 V/cm for pacing cardiac tissues, considering the chosen pacing parameters (Ruan et al., 2016; Tandon et al., 2009). Despite this, robust stimulation of the tissues was achieved, leading to precise control and adaption of observed tissue beating rate within a tissue-specific range (**Fig. 3.3.13**). In future scenarios where standardized non-metal connectors are used for media supply, it becomes possible to utilize the metal plugs, currently used for the sealing of the tissue channels as electrodes. This modification would result in a shorter distance between the electrodes and the tissue, potentially leading to an increased electrical field. Studies around electrical stimulation effects on CM maturity were carried out using high frequencies (up to 6 Hz), in some cases outside physiological range (Nunes et al., 2013; Ronaldson-Bouchard et al., 2018; Ruan et al., 2016). I therefore decided to apply continuous pacing from day 5 for day 14 at 1 Hz frequency, which represents the average beating frequency at rest in a human. For the duration of the pacing, the cells remained viable (**Fig. 3.3.14**) and functional. Paced tissues exhibited a higher beating rate on average but with comparable maximum contraction velocity to the control tissues (**Fig. 3.3.15**), similar to what was observed by Eng and colleagues (Eng et al., 2016).

4.3 Non-invasive monitoring of cardiac metabolic changes under external stimuli

The focus of this thesis was the establishment of non-invasive readout procedures for living tissue analysis. As mentioned before, in terminal assays, the sample is often irreversibly altered or destroyed during the assessment process, limiting further study opportunities. In

contrast, non-invasive assays enable repeated measurements on the same sample over time, maximizing data yield and reducing the need for additional resources. By employing non-invasive methods, researchers can track dynamic changes, responses to stimuli, and recovery processes within the same sample, minimizing the need for a large number of individual samples. This approach accelerates data collection, streamlines experimental workflows, and facilitates quicker results.

The integrated O_2 sensor spots within the *Spheroflow HoC* provided a continuous real-time measurement of O_2 levels. Prior to recording O_2 levels, the stability of the oxygen sensors over time and the potential impact of electrical current in the media were assessed (**Fig. 3.3.1**). The consistent O_2 levels observed in the empty perfused chamber indicate that the sensors maintain stability under continuous culture conditions. This finding denies the possibility of the resin used for tissue layer fabrication, specifically NOA81, exhibiting O_2 scavenging properties, as observed in chips fabricated from OSTEMER, a thiolene-based resin similar to NOA81 (Sticker et al., 2019). Moreover, sporadic spikes in O_2 concentration suggest that these sensors are capable of detecting transient air bubbles passing through the media layer during perfusion.

To ensure that electrical currents do not interfere with O_2 measurement, I paced empty chambers at different parameters and observed that O_2 levels remained unaffected. However, upon pacing the tissue, the results revealed an augmented O_2 consumption in cardiac tissues within the microphysiological system (**Fig. 3.3.2**). This finding aligns with a similar study conducted on O_2 consumption in myobundles undergoing electrical stimulation (B. N. Davis et al., 2019). The observed reductions in partial pressure of O_2 (pO2) were synchronized with the pacing onset and ending, strongly suggesting an influence of pacing onto the tissue metabolism. The increase in tissue beating frequency resulting from electrical stimulation may lead to an elevation in tissue O_2 consumption. As the pacing frequency increases, tissue metabolism and subsequent O_2 consumption also increase, thus providing an explanation for the observed correlation between O_2 consumption and pacing frequency. During long-term monitoring of O_2 levels under a continuous and constant pacing regimen (**Fig. 3.3.3**), the paced tissue exhibited an immediate drop in O_2 levels upon initiation of pacing. Although the O_2 levels remained lower than the initial level, there was a gradual but consistent increase in O_2, indicating a decrease in O_2 consumption. However, control tissue also displayed progressively higher O_2 levels. This finding suggests that the tissues still heavily rely on anaerobic glycolysis to fulfil their energy requirements; however, more replicates measurements are required to confirm this trend. Additionally, the overall set up should be simplified and improved to avoid sensors displacement as well as reduce the noise in the O_2 readings due to the current syringe pumping system.

Following the confirmation of a correlation between metabolic changes in cardiac tissues and the induced beating frequency through electrical stimulation, the objective was to examine whether drug compounds could also influence tissue respiration.

Measurements of OCR and ECAR are used extensively in the cardiac field to investigate metabolic changes in response to maturation approaches (Giacomelli et al., 2020; Ronaldson-Bouchard et al., 2018), cardiac disease modelling (Giacomelli et al., 2020;

Richards et al., 2020), and acute or chronic drug treatment (Fiserova et al., 2022; Mills et al., 2018, 2019). However, as explained in section 1.2.3, one of the challenges currently being tackled in the OoC platform is the application of such techniques to such closed systems. Therefore, similarly to what has been recently established by Busche *et al*. and Fuchs *et al*., I tried to establish the mitochondrial respiration assay within the platform under constant perfusion. In the Busche *et al*. paper, the perfusion was achieved by gravity flow and the addition of the assay drug compounds was performed by emptying the outlet reservoir and refilling the inlet reservoir with media containing the appropriate drug at each step of the assay (Busche et al., 2022). In contrast, in Fuchs *et al*., the perfusion was provided by syringe pumps; however, the drug administration was still performed manually by stopping the flow to exchange the syringes at each step (Fuchs et al., 2022). Additionally, the chip design consisted of a single channel with cells seeded at the bottom and the sensors were positioned on the top of the channel, with media flowing in the same channel. Therefore, the O_2 levels measured in absence or presence of drug, were kept constant by the continuous flow of oxygenated media. This means that, to measure the OCR and ECAR and to compare the measurements to the *Seahorse XF Analyzer*, the perfusion had to be stopped to measure a decrease in oxygen and an increase of the pH; with this approach they demonstrated the comparability between the assays in the OoC platform and the 2D well plated assay performed with the commercially available Seahorse Analyzer.

In this set up (**Supplementary Fig. 1**), the perfusion was kept at a constant flow rate and the drug injection was automated by using valve switches which can be programmed to assure a timely control of the drug injection. As one solution is pumped through the chip, the other tubing is primed with the next solution, preventing air bubble formation, which occur when manually disconnecting and connecting syringes. The system I had in place only used one 4-port microfluidic valve which only allows the perfusion of 2 solutions at the same time; and therefore still required manual syringe exchange. To have a fully automated system, a valve that provides the possibility to switch between multiple solution is required. An example of a commercially available option is the sequential fluid injection pack by Elveflow (A. Yang et al., 2023).

By following the same protocol published by Busche *et al*. (Busche et al., 2022), in terms of drug concentrations and incubation times, the appropriate tissue for all the drugs injected was confirmed (Oligomycin A, FCCP, Rotenone / Antimycin A) and I could extrapolate the all the relevant parameters of the mitochondrial respiration (**Fig. 3.3.4**). However, as it is not possible to know the exact cell number within the platform, and because I measured remaining O_2 levels in the media after cellular respiration, I could not provide an OCR as hPa/min*10000 cells, as reported in Fuchs *et al*. (Fuchs et al., 2022).

Another noteworthy distinction lies in the HoC platform, where I measure the OCR of a 3D tissue, in contrast to the aforementioned examples where hiPSCs and hepatocytes were cultured as monolayers in microfluidic channels. In a recent study by Magliaro *et al*., it was demonstrated that cells exhibit a reduction in their maximal OCR as cell density increases. Furthermore, it was revealed that in static culture, the average OCR decreases over time for a given cell density, indicating that cells adapt their OCR in response to the availability of oxygen (Ahluwalia, 2017; Magliaro et al., 2019). This study raises the significative

question of whether it is meaningful to compare the OCR and ECAR of 3D tissues subjected to constant perfusion with their 2D counterparts cultured under static conditions.

Despite these differences compared to other studies and the limitation of not having a defined cell number, this newly developed automated mitochondrial respiration assay on-chip would provide an important tool for future on-chip studies on the modulation of CM respiration in response to drug treatment as well as different nutritional regimes, as already investigated in static conditions (Angelini et al., 2021; Fiserova et al., 2022). Additionally, other optical sensors could be implemented to measure pH for glycolysis assays (ECAR) as well as monitor glycolysis and lactate production changes.

Upon validating the feasibility of quantifying drug-induced alterations in O_2 levels, I inquired whether pharmacological compounds influencing cardiac functionality would also incite changes in O_2 consumption. For this purpose, two known compounds, Verapamil and Isoproterenol were used. Verapamil, acting as a calcium channel blocker, elicits a negative chronotropic and ionotropic response, while Isoproterenol, a beta-adrenergic agonist, induces a positive chronotropic and ionotropic effect.

Initially, I assessed the functional response of the tissues to Verapamil and Isoproterenol, which are commonly used drugs in cardiac research. In order to avoid drug absorption by the tubings used for perfusion (explained in section 4.2), a pipette tip attached to the media inlet was employed as a reservoir while the tubing and syringe were connected to the media outlet. The chip was perfused by negative pressure (**Supplementary Fig. 2**) as pipette tips were confirmed to exhibit no retention of the studied drug compounds (**Supplementary Fig. 3**). The tissue's beating response was analysed using drug concentrations ranging from 0 to 10 µM, similarly a previous study utilizing a comparable HoC platform (Huebsch et al., 2016; Mathur et al., 2015). The experimental results (**Fig. 3.3.5**) revealed that the tissue's response to Verapamil closely resembled the findings of the previous study. Conversely, when Isoproterenol was applied, the tissue displayed a two-fold increase in contraction rate at a concentration as low as 10 nM, which differed from the previous studies where a similar magnitude of response was observed at concentrations close to 1 µM. To quantify the drug response, I calculated the Isoproterenol half-maximal effective concentration (EC_{50}) and the Verapamil half-maximal inhibitory concentration (IC_{50}) using the drug response curves. The obtained values align with the aforementioned study, the EC_{50} for Isoproterenol was 250 nM (compared to 315 nM in the previous study), and the IC_{50} for Verapamil was 1155 nM (compared to 950 nM).

After validating the tissue functional response to these drug compounds, I wanted to investigate if they also induce a metabolic change in cardiac tissues. To determine if the observed changes in tissue functionality corresponded to alterations in O_2 metabolism, O_2 levels were measured before and during treatment with 10 µM of Verapamil or 100 nM of Isoproterenol. The analysis (**Fig. 3.3.6**) indicated no significant difference in O_2 levels between the samples and their respective controls. This may suggest that both drugs, despite affecting tissue functionality, did not induce a change in cellular metabolism, at least in the short-term or that higher drug concentrations are needed to induce a significant decrease or increase in O_2 consumption in the short-term.

Commonly used non-invasive screening techniques rely on effluent analysis for biologically relevant metabolites. Not having integrated glucose and lactate sensors in the platform yet, I used commercially available kits to quantify glucose and lactate concentration in the media after perfusion. This approach is still non-invasive as it is based on effluent collection but does not provide real-time measurement as the effluent is only collected as specific time-points to monitor metabolic changes. Analysis of glucose levels in the media (**Fig. 3.3.7**), showed an overall higher glucose concentration compared to the nominal concentration of the media (11.11 mM). I hypothesise that media collection over 24 hours at such low flow rate (50 ul/hr) may result in partial evaporation of the media due to high surface area exposed to air. Possible evaporation points in the system are the tubings which have an internal diameter of 0.05 mm and are gas permeable, the PDMS media layer and the media droplets exiting the tubing and dropping into the empty reservoir at the beginning of collection. Additionally, the results highlighted that the QuantiChrom™ Glucose Assay Kit, which is suitable for detection of glucose in serum and plasma may not be suited for in-chip experiments. I assumed that the low consumption of the tissue and the one-way perfusion of the media resulted in a glucose consumption rate too low to detect any difference in glucose concentration in the scale of mM. Alternatives could be implementing a recirculation system of the media to detect overall progressive consumption as well as providing media with glucose concentration in the physiological range.

Another relevant analyte of CM metabolism is lactate. In this case, the Lactate-Glo™ Assay kit, was used, which worked within an appropriate concentration range (up to 200 µM) and a sensitivity of 0.2 µM. In the current experiment set up, tissues in which a higher beating frequency is induced maintained a higher glycolytic rate compared to control tissue (**Fig 3.3.8**). These results, in addition to the slight decrease in OCR measured over time in both control and paced tissues (**Fig. 3.3.3**), may confirm that, as reported by Magliaro *et al*., the tissues are adapting their metabolism to a reduced O_2 concentration (Magliaro et al., 2019). Tissues that were not subjected to continuous pacing exhibited a decline in beating rate (refer to **Fig. 3.2.15**) and a reduction in lactate secretion, which aligns with the observed decrease in oxygen consumption. Conversely, tissues subjected to pacing did not display a decrease in spontaneous beating rate and maintained a consistent production of lactate, despite experiencing a decline in oxygen consumption. Based on this, my hypothesis is that these tissues require sustained anaerobic respiration to support the induced beating rate of 1 Hz while also adapting their oxygen consumption to the surrounding oxygen levels. However, further investigation into the metabolic dynamics is required to elucidate the intricate interplay between various metabolic pathways and oxygen consumption in cardiac tissues. Additionally, the measurement of FA consumption could be included in these metabolic investigations to provide a comprehensive understanding of the metabolic processes involved.

Regrettably, in this particular study, the measurement of FAs was not feasible. The commercially available kits commonly employed for detecting fatty acids, such as the Free Fatty Acid Assay Kit - Quantification, are primarily designed for use with serum and plasma samples. Consequently, these kits offer a wider detection range (up to 600 µM) but have low sensitivity (> 2 µM) compared to what is typically found in cell culture media. I

approximatively calculated the FA concentrations in this experimental set up. Considering the original formulation of the B27 supplement, it is important to note that commercially available options do not provide precise concentrations of individual components. As a result, I estimated the composition of the current media, which consists of 2% B27 in RPMI medium, to contain approximately 3.56 µM of Linoleic acid, 3.6 µM of Linolenic acid, and 3.54 µM of Oleic acid (Hanna Lab Protocol – Weizmann Institute of Science, n.d.).

As previously mentioned, the incorporation of glucose, lactate, and pH sensors within the *Spheroflow HoC* platform holds the potential to provide valuable insights into metabolic modulation within cardiac tissue. However, careful considerations need to be made regarding the integration positions of these sensors. Specifically, the glucose sensor should be positioned within the tissue layer to accurately measure the remaining glucose levels after cellular metabolism, without being influenced by the influx of new glucose-rich media. Furthermore, since the currently developed sensor is sensitive to oxygen concentrations for measurement, modifications to the chip design are necessary (Fuchs et al., 2023). These modifications should include a compartment where the sensor can assess glucose concentration following cell metabolism, while simultaneously maintaining a constant level of oxygenation in the media. An additional critical aspect to consider with this sensor is its reliance on an enzyme. Despite being proven compatible with several sterilization techniques (i.e. plasma treatment, UV-exposure, and E-beam), it has not been tested against solvents (i.e. ethanol and isopropanol) and high temperature (> 60 °C) which are commonly used in OoC fabrication. Thus, meticulous attention must be given to these procedures to ensure that the sensor remains unaffected and functions optimally; moreover, the sensor's stability lasts only for up to 5 days at 37°C, limiting experimental time. Another strategy would be redesigning the *Spheroflow HoC* to host a plug-in sensors attachment so that sensors can be replaced at the end of their lifetime.

Sensors and effluent analysis offer a non-invasive method to monitor the uptake and secretion of tissue metabolites in media. In contrast, Raman spectroscopy provides a non-invasive imaging approach for characterizing live tissue, eliminating the need for dyes or cell-reporter lines. The advantage of the *Spheroflow HoC* design is that it enables direct contact between the tissue and the bottom glass coverslip, allowing for Raman spectroscopy analysis through the glass substrate without any potential interference from PDMS or plastic materials. High resolution imaging (1 x 1 µm) could be achieved within the platform and different biological fingerprints (**Fig. 3.3.9; Fig. 3.3.10; Fig. 3.3.11**) and the chip material fingerprints could be identified. The analysis of cardiac tissues revealed three additional cellular components in addition to DNA, lipids, and proteins (**Fig. 3.3.12**), two of which present fingerprints similar to glycogen and mitochondria respectively.

Despite the mainstream use of Raman spectroscopy for bulk material characterization (i.e. graphene) in material science, its application to biological samples is still a challenge as there is currently no extensive database of biological fingerprints and the conditions the biological sample (i.e. cryopreserve slice or paraffin-embedded) is in may also affect the fingerprint of biomolecules making their identification challenging. Currently very few studies have been performed to characterize cardiac differentiation and maturity (Brauchle et al.,

2016; Pascut et al., 2013; Shen et al., 2017). Brauchle and colleagues, from Katja Schenke-Layland's group, identified differences in Raman spectra between different CMs populations, atrial and ventricular and were able to distinguish by PCA of the Raman spectra between human embryonic stem cells (**hESC**), hESC-derived CMs and human foetal CMs (Brauchle et al., 2016). A subsequent study, from the same group, analysed the effects of strain on hESC-derived CMs maturation and compared them to primary human foetal CMs. While the PCA analysis showed hESC-CMs after 10 days of strain training as a distinctive cell population compared to primary CMs, after 20 days of training the hESC-CMs and the primary CMs population showed comparable Raman fingerprints (Shen et al., 2017), proving that dynamic strain was inducing cardiac maturation.

Similarly, to determine whether Raman imaging could be a useful tool for on-chip tissue analysis, I tried to analyse the differences between cardiac tissues at day 5 and at day 14 after a pacing regime. I focused on the 2 better characterised components, lipids and proteins. PCA analysis of the protein content (**Fig. 3.3.13**) revealed a partial separation of day 5 and day 14 spectra on the PC-2, with loading values ranging between -0.2 and 0.2; on the other hand, in the lipids PCA analysis (**Fig. 3.3.14**) the difference between the two conditions is less pronounced but they still present a significative difference on the PC-1 with loading values ranging between -0.1 and 0.3. Such small loading values in PCA analysis are due to the intrinsic variability of biological samples and are comparable to loading values obtained in the abovementioned studies on CMs. Therefore, I concluded that Raman imaging can effectively be applied on the microfluidic platform, is able to detect biological differences between samples and can be a valuable tool to monitor *in vivo* tissue changes over time.

4.4 Skeletal muscle tissue establishment

In this study, the *Spheroflow HoC* platform was presented as a suitable tool for investigating cardiac tissues, however due to their similarity in functionality and structure I investigated its potential to host skeletal muscle models as well.

As current challenges in skeletal muscle modelling from patient's primary cells is the ineffective differentiation of satellite cells into functional myotubules I tested a newly developed protocol (Dreher et al., 2023), which relies on IGF-1 as the main molecule driving myocytes fusion. The use of this novel protocol on 2D plates successfully generated electrically responsive myotubules in contrast to medium without IGF-1 (**Fig. 3.5.1**). This protocol was then successfully transferred to engineered 3D myobundles in fibrin hydrogel (**Fig. 3.5.2**), which displayed a uniaxial contraction response when prompted by electrical stimulation. Therefore, I used a similar approach to generate hydrogel embedded 3D myobundles in the *Spheroflow HoC* platform.

As mentioned before, the integration of hydrogels with cardiac spheroids presented challenges in this study, primarily due to the high viscosity of the hydrogels and the difficulty in achieving compact tissue using dispersed CMs, as these cells are not proliferative. However, the integration of Matrigel and collagen hydrogels in the chip was successfully

accomplished by loading a cell suspension of myocytes. Since satellite cells, which are proliferative, were included in the gel, they were allowed to expand within the platform for 3 days before initiating the differentiation protocol with IGF. This approach ensured that the tissue chambers were fully filled. Although this approach was feasible, it lacked robustness due to the rapid polymerization of temperature-sensitive hydrogels. Therefore, to enhance user-friendliness, alternative hydrogels that employ different gelation methods or adaptation of the OoC platform may be necessary.

Under phase contrast imaging, it was possible to see myotubules being formed in the IGF+ condition (**Fig. 3.5.3**). Furthermore, as skeletal muscle lacks constant spontaneous beating, the collagen hydrogel did not undergo shrinkage during the 14-day culture period. This observation supports the hypothesis that the contraction of cardiac tissue would exert sufficient strain on the collagen filaments to cause the collapse of the hydrogel. (See Discussion 4.2; **Fig. 3.2.5; Fig. 3.2.6**). Such formed skeletal muscle myotubules were functionally active and exhibited an organised uniaxial contraction of the tissue (**Fig. 3.5.4**).

Tissue characterization confirmed tissue viability at day 10 (**Fig 3.5.5 A**), under continuous perfusion of 50 µL/h. The orthogonal view of the tissue revealed a three-dimensional distribution of nuclei within the channel's height. Notably, a higher density of cells was observed closer to the membrane side of the chip compared to the chip bottom (**Fig. 3.5.5 B**). This phenomenon may be attributed to the hydrogel's impact on nutrient diffusion, slowing down the transfer of nutrients from the membrane to the chip's bottom. Consequently, the cells migrate towards the porous membrane region to access more nutrients and oxygen. Immunostaining of the tissues for F-actin and nuclei demonstrated the presence of multinucleated myotubules and aligned actin filaments in the shaft region of the chip (**Fig. 3.5.5 C**). This confirms that the skeletal muscle fibres generated on the chip replicate the 3D structural organization observed *in vivo*.

Overall, the viability, functionality, and structure of the myobundles engineered within the *Spheroflow HoC* system as a proof of concept, demonstrated that it is possible to form and culture primary skeletal muscle tissues within a perusable platform and lays the basis for further studies on the relation between metabolic disorders (i.e. Diabetes Type 2) and physical exercise as a one organ model. In future studies, the microfluidic platform could be connected to other OoC pathophysiological models (i.e. liver, pancreas, fat) to study cross-interaction between affected organs.

5 Outlook and Perspectives

Although proof-of-concept studies have been conducted in the field of HoC technology, the full potential of these systems has only been partially realized. Existing systems have primarily focused on tissue generation, with functional readouts such as contraction kinetics and electrophysiology primarily utilized for drug response assessment, maturation studies, or disease modelling. In most cases, the chip developers themselves are the primary users of these developed systems. To fully harness the tremendous potential of HoCs, it is crucial not only to advance the generation of more sophisticated model systems but also to incorporate different readouts and promote transferability. By enabling end-user investigators to probe and gain advanced insights into key biological questions, the transition from the development stage to real applications can be truly achieved.

The studies presented in this thesis aimed to validate the HoC platform and cardiac tissue model, and further explore novel tools and integration approaches for biophysical stimulation and probing metabolic responses in MPS. These investigations contribute to advancing the capabilities and understanding of HoCs, paving the way for their broader utilization in addressing important research questions and facilitating their transition into practical applications.

I focused first on cellular validation, aiming to achieve chemically defined culture conditions at all steps from hiPSC maintenance to chip culture. Despite being able to have all media components serum-free and chemically defined, hiPSC differentiation still relied on Matrigel coating as the use of recombinant human substrates (i.e. laminin-521 and vitronectin) did not sustain efficient hiPSC differentiation in CMs. Additionally, some animal components are still present: the ibidi Freezing media classic contains BSA and the B27 supplement also contains BSA and other proteins of animal origin; but xeno-free alternatives for both are commercially available even though far more expensive (e.g. B-27™ Supplement, XenoFree, A1486701, Gibco; StemMACS™ iPS-Brew XF, human, 130-104-368, Miltenyi).

I qualified our HoC platform by ensuring cellular biocompatibility and defining a protocol for detection of drug absorption. Often disregarded in OoC drug studies is how different materials in the experimental set up may retain drug compounds, therefore changing the drug concentration when it reaches the tissue. For this reason, it is important to test the drug retention of the experimental set up for each drug of interest and keep the set up consistent (tubing length, flow rate, temperature, humidity etc.) with each experiment. As immunocytochemistry is one of the most commonly used technique in biology, I also tested which microscopy clearing agents may compromise the platform material when performing standard staining techniques. I have developed a robust and user-friendly protocol for cellular loading that minimizes the wastage of valuable cell types, such as CMs.

The cardiac and skeletal muscle tissue models were validated by assessing their functionality and their structure. The HoC tissue model has been validated for different hiPSC-CMs lines: (i) the hiPSC line GM25256, (ii) the commercially available hiPSC line E1 (A18945; Thermofisher) and (iii) the commercially available hiPSC-derived ventricular CMs (male) (ax2508; AXOL Bioscience). All these cell lines allowed for the formation of

aggregates with a diameter within the required range and after loading in the chip, they all produced a fused cardiac fibre within 24 hrs. A minimal beat rate threshold could not be defined as spontaneous beat rate varies considerably between cell lines and differentiations; however, all the tissues are able to follow a physiological pacing frequency of 1 Hz at day 5. The tissue exhibits long-term (≥ 14 days under perfusion) viability and functionality (beating). The system can be easily challenged with electrochemical stimulation over an extensive period without inducing cytotoxicity.

I showed that the system is easy to use and allows reproducible and reliable tissue formation. The system, without sensors integration, has been already transferred to other laboratories (Miltenyi R&D) where proprietary hiPSC lines, different differentiation procedure and culture media are used and shown to be compatible with the system with little to no-optimization required. Despite being transferable, additional equipment is needed to work with the chip (syringe pumps, tubing etc.) which is not provided with the platform.

The system allows the measurement of several parameters in a non-invasive and real-time manner. The integrated O_2 sensors are stable during long term culture (>14 days) and are suitable for performing mitochondrial respiration assays, obtaining key respiration parameters. As it is not possible to tightly control the cell number present in every system, the basal O_2 consumption rate varies quite significantly, therefore you can only compare relative O_2 consumption values. Effluent analysis can also be exploited to obtain more insight on metabolic pathways such as lactate secretions. However, not all commercially available kits provide a suitable range for the analysis of OoC effluents as they are developed for detection in plasma or serum.

Finally, the developed platform demonstrates suitability for Raman imaging due to its utilization of a thin glass bottom layer. Raman imaging is an advantageous technique as it is non-invasive and not dependent on dyes, allowing the monitoring of tissue changes within the same sample over a period. Through my research, I have successfully demonstrated the platform's ability to detect tissue components and significant tissue changes under varying conditions.

In conclusion, I have established a toolkit of non-invasive readout technologies that enable the monitoring of live tissues, thereby facilitating the acquisition of extensive datasets from single samples. Furthermore, I have verified the transferability of the system to other laboratories, thereby laying the foundation for its broader application in addressing crucial research inquiries.

Despite these accomplishments, I acknowledge that this HoC model can still be enhanced from both a biological perspective and in terms of its readout capabilities. To render the cardiac tissue model more physiologically relevant, additional efforts should be devoted to integrating CFs and relevant vascular structures. Furthermore, the proof-of-concept for sensor integration and metabolism monitoring, as well as the development of an assay similar to *Seahorse Analyzer*'s mitochondrial respiration assay, opens up possibilities for the incorporation of other optical sensors that can read other analytes of cardiac significance, such as pH, glucose, and lactate. Such implementation would provide valuable insights into

the metabolic changes of CMs in response to chronic stimuli such as pacing and drug compounds.

With regards to non-invasive microscopy, it is worth noting that Raman spectroscopy currently suffers from a lack of a comprehensive and diverse spectral database for biological compounds, thus limiting the technique's potential. However, this limitation is expected to be resolved in the future as researchers in the field continue to collaborate and enrich the existing database. Another live imaging technique that can be applied to the chip, but was not examined in this study, is FLIM, which has the capacity to unveil alterations in oxidative phosphorylation by tracking the NADH/NAD+ ratio within individual cells.

Furthermore, a more thorough investigation of metabolic responses to drug compounds using the currently established readout techniques is required to further validate the utility of this HoC model for drug studies.

6 Summary

Cardiac spheroids and engineered tissues have risen in the past years as potential alternatives to animal models for cardiovascular research and drug development. Nevertheless, conventional spheroid models fail to accurately replicate the cellular organization observed in native cardiac tissue. Similarly, engineered heart models utilizing hydrogel-embedded cells have struggled to attain the high cell density characteristic of *in vivo* tissue. Addressing these challenges, Organ-on-a-Chip platforms have been developed with the aim of introducing the concept of nutrient perfusion to mimic the human vascular system and achieve a more accurate reproduction of physiological conditions.

With the concept of “making the most out of your samples” in mind, I aimed to develop a HoC model which provides a non-invasive toolkit of techniques for the analysis of the function of live tissues and their metabolism. This thesis presents an innovative Heart-on-Chip platform designed for robust 3D tissue generation of contractile tissues. Two different cell injection approaches were utilized to create cardiac and skeletal muscle tissues.

The initial *Centrifugal HoC* platform lacked robustness in the loading of spheroids and hydrogels. Therefore, a new HoC platform was developed, called *Spheroflow HoC*. *Spheroflow HoC* provided robust spheroid loading but was incompatible with co-loading of hydrogel and spheroids due to the high viscosity and quick gelation of hydrogels during injection. Nevertheless, the strategy proved successful for single cell loading of skeletal myocytes, which could proliferate, reach adequate cell density, and form myotubules, resulting in contractile tissue over a 10-day differentiation period. In addition to cultivation, the tissues were characterized by brightfield video microscopy for analysis of beating kinetics, and immunostaining to verify tissue morphology. Both tissues exhibited structural organization resembling their respective organs, with uniaxial alignment guided by the chamber geometry. They displayed full functionality and response to electrical stimulation.

With a specific focus on cardiac tissues, I established non-invasive measurements that could be applied to investigate different biological questions. To achieve this, electrodes were seamlessly integrated into the *Spheroflow HoC* platform, enabling successful electrical stimulation of both cardiac and skeletal muscle tissues. Additionally, the platform incorporated oxygen sensors, allowing real-time monitoring of oxygen consumption during stimulation. To enhance the versatility of the platform, an automated drug injection and readout procedure was implemented. This innovation facilitated not only potential drug screening but also the execution of respirometry analysis directly within the chip, eliminating the requirement for external machines or modifications to the chip design to accommodate the use of an analyser. The platform was compatible with non-invasive high resolution imaging techniques thanks to its thin glass bottom layer. I was able to detect tissue components and significant tissue changes under varying conditions by Raman spectroscopic imaging.

These features distinguish this Heart-on-Chip model from currently available models and enhance its capabilities for studying cardiac physiology and pathology metabolism in a more non-invasive manner.

German summary

Kardiale Sphäroide und künstlich hergestellte Gewebe haben sich in den letzten Jahren als mögliche Alternativen zu Tiermodellen für die kardiovaskuläre Forschung und Arzneimittelentwicklung etabliert. Herkömmliche Sphäroidmodelle können jedoch die im natürlichen Herzgewebe beobachtete Zellorganisation nicht genau nachbilden. Auch bei Herzmodellen mit in Hydrogelen eingebetteten Zellen ist es schwierig, die für *In vivo*-Gewebe charakteristische hohe Zelldichte zu erreichen. Um diesen Herausforderungen zu begegnen, wurden Organ-on-a-Chip-Plattformen entwickelt, die das Konzept der Nährstoffperfusion einführen, um das menschliche Gefäßsystem zu imitieren und eine genauere Rekapitulation der physiologischen Bedingungen zu erreichen.

Mit dem Konzept "das Beste aus den Proben herausholen" im Hinterkopf wollten wir ein Heart-on-Chip -Modell entwickeln, das ein nicht-invasives Repertoire an Techniken für die Analyse der Funktion lebender Gewebe und ihres Stoffwechsels bietet. In dieser Dissertation wird eine innovative Heart-on-Chip-Plattform vorgestellt, die für die robuste 3D-Gewebeerzeugung von kontraktilem Gewebe konzipiert wurde. Für die Herstellung von Herz- und Skelettmuskelgewebe wurden zwei verschiedene Zellinjektionsverfahren verwendet.

Der ursprünglichen Zentrifugal-HoC-Plattform mangelte es an Robustheit bei der Beladung von Sphäroiden und Hydrogelen. Daher wurde eine neue HoC-Plattform mit der Bezeichnung *Spheroflow HoC* entwickelt. *Spheroflow HoC* ermöglichte eine robuste Beladung mit Sphäroiden, war aber, aufgrund der hohen Viskosität und der schnellen Gelierung von Hydrogelen während der Injektion, nicht mit der gemeinsamen Beladung von Hydrogelen und Sphäroiden kompatibel. Nichtsdestotrotz erwies sich die Strategie als erfolgreich für die Einzelzell-Beladung des Systems mit Skelettmuskelzellen, die sich vermehren, eine angemessene Zelldichte erreichen und Myotubuli bilden konnten. Dies führte, über einen Differenzierungszeitraum von 10 Tagen, zur Bildung von kontraktilem Gewebe. Zusätzlich zur Kultivierung wurden die Gewebe durch Hellfeld-Videomikroskopie, zur Analyse der Schlagkinetik, und durch Immunfärbung, zur Histologischen Evaluation, charakterisiert. Beide Gewebe wiesen eine strukturelle Organisation auf, die ihren jeweiligen Organen ähnelte, wobei die uniaxiale Ausrichtung durch die Kammergeometrie vorgegeben war. Sie zeigten volle Funktionalität und reagierten auf elektrische Stimulation.

Mit besonderem Augenmerk auf Herzgewebe haben wir nicht-invasive Messungen entwickelt, die zur Untersuchung verschiedener biologischer Fragen eingesetzt werden können. Zu diesem Zweck wurden Elektroden nahtlos in die *Spheroflow HoC*-Plattform integriert, die eine erfolgreiche elektrische Stimulation sowohl von Herz- als auch von Skelettmuskelgewebe ermöglicht. Darüber hinaus wurden in die Plattform Sauerstoffsensoren integriert, die eine Echtzeitüberwachung des Sauerstoffverbrauchs während der Stimulation ermöglichen. Um die Vielseitigkeit der Plattform zu erhöhen, wurde ein automatisiertes Verfahren zur Injektion von Wirkstoffen und Ablesung der Messverfahren eingeführt. Diese Innovation erleichterte nicht nur das potenzielle Wirkstoffscreening, sondern auch die Durchführung von Experimenten zur Evaluierung des

Zellstoffwechsels direkt im Chip, so dass keine externen Geräte oder Änderungen am Chipdesign für die Verwendung eines externen Gerätes erforderlich waren. Die Plattform war dank ihrer dünnen Glasbodenschicht mit nicht-invasiven hochauflösenden Bildgebungsverfahren kompatibel. Wir waren in der Lage, Gewebekomponenten und signifikante Gewebeveränderungen unter verschiedenen Bedingungen durch Raman-spektroskopische Bildgebung zu erkennen.

Diese Eigenschaften unterscheiden unser Heart-on-Chip-Modell von den derzeit verfügbaren Modellen und verbessern seine Möglichkeiten zur Untersuchung der Herzphysiologie und des pathologischen Stoffwechsels auf nicht-invasive Weise.

7 Appendix

Material/Clearing Kit	Methanol:BABB (Renner et al., 2020)	MACS® Clearing Kit (130-126-719; Miltenyi Biotec)	RTF (Yu et al., 2018)
PDMS	Yes	Yes	Yes
PET membrane	Yes	Yes	Yes
NOA81	Yes	Yes	Yes
TPE	Yes	Yes	Yes
PMMA	NO (melted)	Yes	Yes

Supplementary Table 1 *Compatibility of different materials to clearing solutions.*

After being kept submerged for 3 days in the clearing solutions, the materials consistency and transparency was assessed. The material was deemed compatible if its original consistency and transparency were maintained.

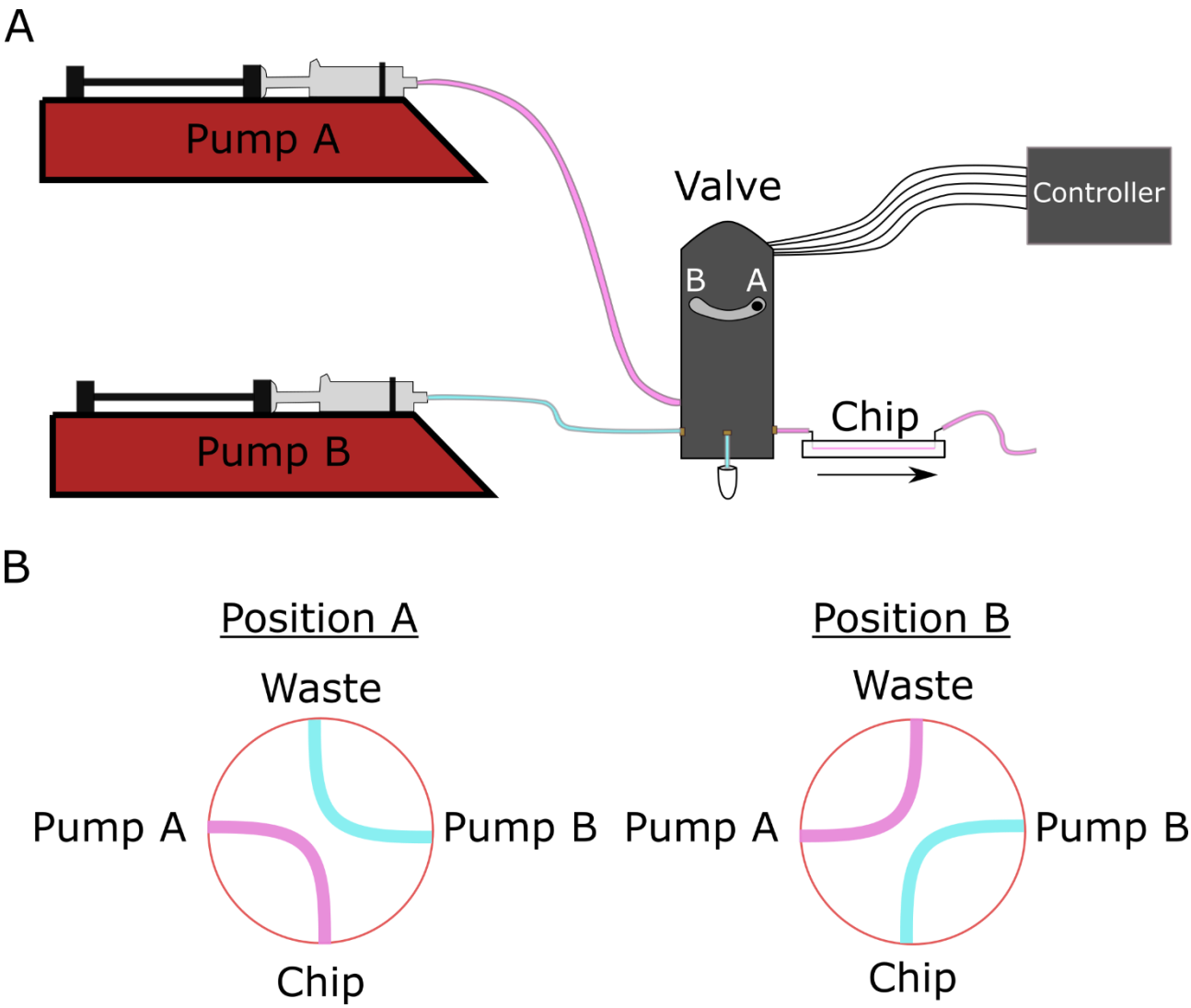

Supplementary Figure 1 *Automated injection set up.* ***(A)*** *Configuration of perfusion system with the pumps connected to the valve which deliver the media of one pump into the chip and of the other pump to the waste reservoir. The valve position is remotely regulated by a controller.* ***(B)*** *Valve position A: the chip is perfused by Pump A; Valve position B: the chip is perfused by Pump B.*

Two pumps, named pump A and pump B, are perfusing at the same time. In the first configuration, the valve is in position A and the pump A is perfusing into the chip, while the pump B is perfusing into a waste reservoir. When the valve is switched to position B, the pump B is now perfusing the solution into the chip while the pump A is perfusing into the waste reservoir. The switching between position A and B can be fully automated via the controller.

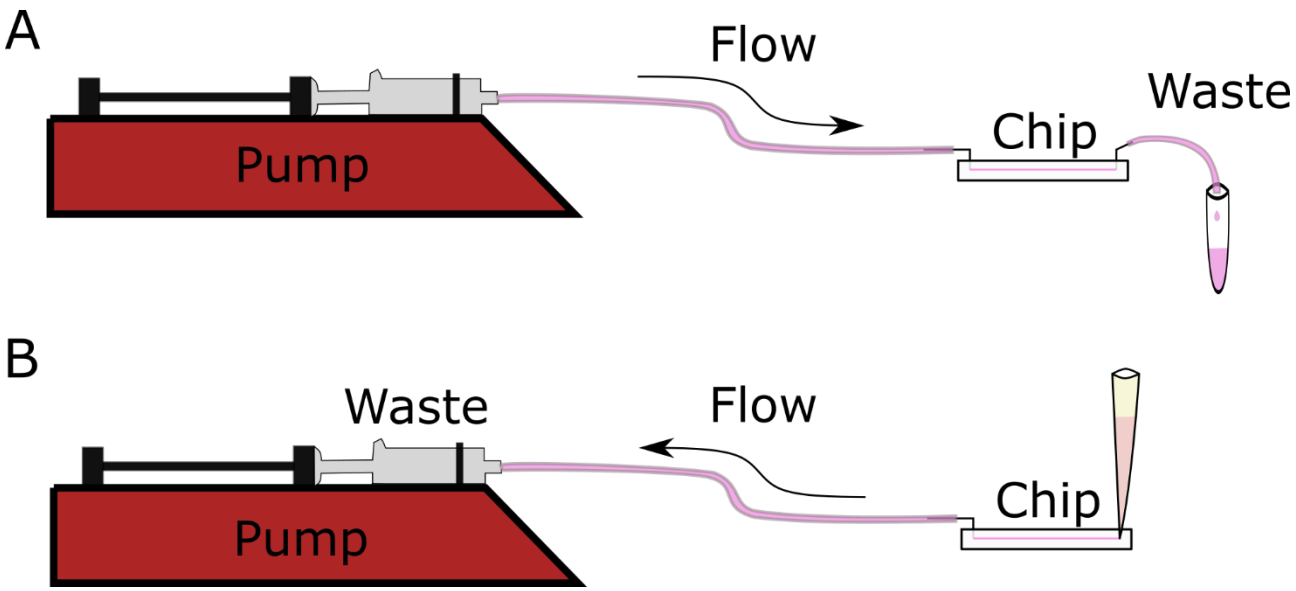

Supplementary Figure 2 *Perfusion set ups.* ***(A)*** *Standard set up.* ***(B)*** *Withdrawal set up.*

In the standard set up (A), the pump pushed the syringes pistons and perfuses media by positive pressure. In the withdrawal set up, a pipette tip is used as reservoir for the media. The pump pulls the syringes pistons, withdrawing media from the pipette tip by negative pressure.

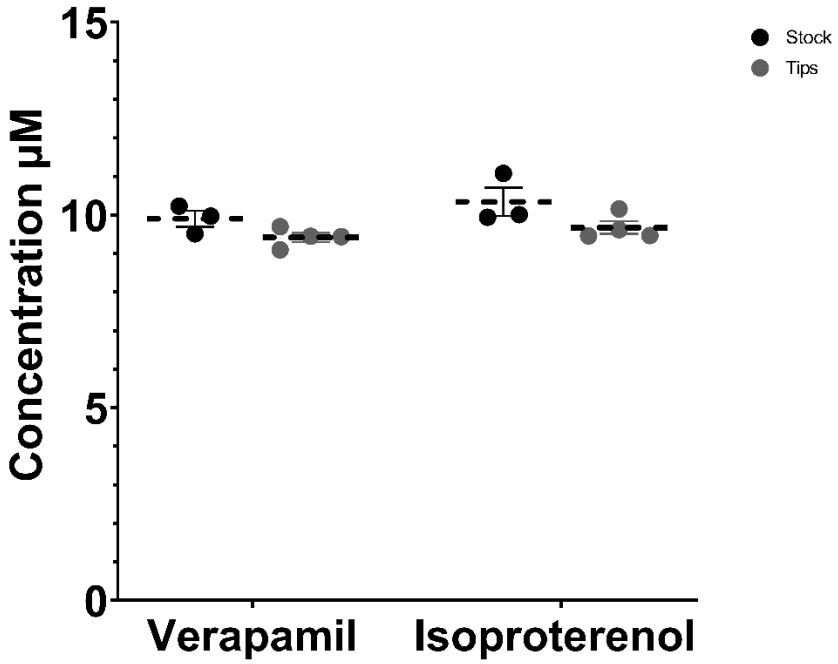

Supplementary Figure 3 *HPLC analysis of pipet tip plasticware absorbance of Verapamil and Isoproterenol.*

Drug solutions were kept in a 100 µL pipette tip for 2hr at 37°C 99% Hr, 5% CO_2 and subsequently collected. The samples were then analysed and compared to the initial concentration of the stock, demonstrating that the plastic of the tips does not retain either verapamil or isoproterenol.

8 Bibliography

Aas, V., Bakke, S. S., Feng, Y. Z., Kase, E. T., Jensen, J., Bajpeyi, S., Thoresen, G. H., & Rustan, A. C. (2013). Are cultured human myotubes far from home? *Cell and Tissue Research*, *354*(3), 671–682. https://doi.org/10.1007/s00441-013-1655-1

Aas, V., Hessvik, N. P., Wettergreen, M., Hvammen, A. W., Hallén, S., Thoresen, G. H., & Rustan, A. C. (2011). Chronic hyperglycemia reduces substrate oxidation and impairs metabolic switching of human myotubes. *Biochimica et Biophysica Acta (BBA) - Molecular Basis of Disease*, *1812*(1), 94–105. https://doi.org/10.1016/j.bbadis.2010.09.014

Abdelmoez, A. M., Sardón Puig, L., Smith, J. A. B., Gabriel, B. M., Savikj, M., Dollet, L., Chibalin, A. V., Krook, A., Zierath, J. R., & Pillon, N. J. (2020). Comparative profiling of skeletal muscle models reveals heterogeneity of transcriptome and metabolism. *American Journal of Physiology-Cell Physiology*, *318*(3), C615–C626. https://doi.org/10.1152/ajpcell.00540.2019

Abreu, C. M., Thomas, V., Knaggs, P., Bunkheila, A., Cruz, A., Teixeira, S. R., Alpuim, P., Francis, L. W., Gebril, A., Ibrahim, A., Margarit, L., Gonzalez, D., Freitas, P. P., Conlan, R. S., & Mendes Pinto, I. (2020). Non-invasive molecular assessment of human embryo development and implantation potential. *Biosensors and Bioelectronics*. https://doi.org/10.1016/j.bios.2020.112144

Agarwal, A., Goss, J. A., Cho, A., McCain, M. L., & Parker, K. K. (2013). Microfluidic heart on a chip for higher throughput pharmacological studies. *Lab on a Chip*, *13*(18), 3599. https://doi.org/10.1039/c3lc50350j

Agrawal, G., Aung, A., & Varghese, S. (2017). Skeletal muscle-on-a-chip: an in vitro model to evaluate tissue formation and injury. *Lab on a Chip*, *17*(20), 3447–3461. https://doi.org/10.1039/C7LC00512A

Ahadian, S., Civitarese, R., Bannerman, D., Mohammadi, M. H., Lu, R., Wang, E., Davenport-Huyer, L., Lai, B., Zhang, B., Zhao, Y., Mandla, S., Korolj, A., & Radisic, M. (2018). Organ-On-A-Chip Platforms: A Convergence of Advanced Materials, Cells, and Microscale Technologies. *Advanced Healthcare Materials*, *7*(2), 1–53. https://doi.org/10.1002/adhm.201700506

Ahluwalia, A. (2017). Allometric scaling in-vitro. *Scientific Reports*, *7*(1), 42113. https://doi.org/10.1038/srep42113

Aird, W. C. (2012). Endothelial cell heterogeneity. *Cold Spring Harbor Perspectives in Medicine*. https://doi.org/10.1101/cshperspect.a006429

American Diabetes Association. (2017). 2. Classification and Diagnosis of Diabetes. In *Diabetes Care* (Vol. 40, Issue Supplement_1). https://doi.org/10.2337/dc17-S005

Angelini, A., Saha, P. K., Jain, A., Jung, S. Y., Mynatt, R. L., Pi, X., & Xie, L. (2021). PHDs/CPT1B/VDAC1 axis regulates long-chain fatty acid oxidation in cardiomyocytes. *Cell Reports*, *37*(1), 109767. https://doi.org/10.1016/j.celrep.2021.109767

Arai, K., Murata, D., Takao, S., Nakamura, A., Itoh, M., Kitsuka, T., & Nakayama, K. (2020). Drug response analysis for scaffold-free cardiac constructs fabricated using bio-3D printer. *Scientific Reports*, *10*(1), 8972. https://doi.org/10.1038/s41598-020-65681-y

Archer, C. R., Sargeant, R., Basak, J., Pilling, J., Barnes, J. R., & Pointon, A. (2018). Characterization and validation of a human 3D cardiac microtissue for the assessment of changes in cardiac pathology. *Scientific Reports*. https://doi.org/10.1038/s41598-018-28393-y

Ardell, J. L., & Armour, J. A. (2016). Neurocardiology: Structure-Based Function. In *Comprehensive Physiology* (Vol. 6, Issue 4, pp. 1635–1653). John Wiley & Sons, Inc. https://doi.org/10.1002/cphy.c150046

Arslan, U., Brescia, M., Meraviglia, V., Nahon, D. M., van Helden, R. W. J., Stein, J. M., van den Hil, F. E., van Meer, B. J., Vila Cuenca, M., Mummery, C. L., & Orlova, V. V. (2023). Vascularized hiPSC-derived 3D cardiac microtissue on chip. *Stem Cell Reports*. https://doi.org/10.1016/j.stemcr.2023.06.001

Arslan, U., Moruzzi, A., Nowacka, J., Mummery, C. L., Eckardt, D., Loskill, P., & Orlova, V. V. (2022). Microphysiological stem cell models of the human heart. *Materials Today Bio*, *14*, 100259. https://doi.org/10.1016/j.mtbio.2022.100259

Askanas, V., & Engel, W. K. (1975). A new program for investigating adult human skeletal muscle grown aneurally in tissue culture. *Neurology*, *25*(1), 58–58. https://doi.org/10.1212/WNL.25.1.58

Ausoni, S., & Sartore, S. (2009). The cardiovascular unit as a dynamic player in disease and regeneration. *Trends in Molecular Medicine*, *15*(12), 543–552. https://doi.org/10.1016/j.molmed.2009.10.002

Bacakova, M., Pajorova, J., Broz, A., Hadraba, D., Lopot, F., Zavadakova, A., Vistejnova, L., Beno, M., Kostic, I., Jencova, V., & Bacakova, L. (2019). A two-layer skin construct consisting of a collagen hydrogel reinforced by a fibrin-coated polylactide nanofibrous membrane. *International Journal of Nanomedicine*, *Volume 14*, 5033–5050. https://doi.org/10.2147/IJN.S200782

Bailey, A. L., Dmytrenko, O., Greenberg, L., Bredemeyer, A. L., Ma, P., Liu, J., Penna, V., Winkler, E. S., Sviben, S., Brooks, E., Nair, A. P., Heck, K. A., Rali, A. S., Simpson, L., Saririan, M., Hobohm, D., Stump, W. T., Fitzpatrick, J. A., Xie, X., … Lavine, K. J. (2021). SARS-CoV-2 Infects Human Engineered Heart Tissues and Models COVID-19 Myocarditis. *JACC: Basic to Translational Science*, *6*(4). https://doi.org/10.1016/j.jacbts.2021.01.002

Bajpai, G., Schneider, C., Wong, N., Bredemeyer, A., Hulsmans, M., Nahrendorf, M., Epelman, S., Kreisel, D., Liu, Y., Itoh, A., Shankar, T. S., Selzman, C. H., Drakos, S.

G., & Lavine, K. J. (2018). The human heart contains distinct macrophage subsets with divergent origins and functions. *Nature Medicine*. https://doi.org/10.1038/s41591-018-0059-x

Bambot, S. B., Holavanahali, R., Lakowicz, J. R., Carter, G. M., & Rao, G. (1994). Phase fluorometric sterilizable optical oxygen sensor. *Biotechnology and Bioengineering*, *43*(11), 1139–1145. https://doi.org/10.1002/bit.260431119

Banerjee, I., Fuseler, J. W., Price, R. L., Borg, T. K., & Baudino, T. A. (2007). Determination of cell types and numbers during cardiac development in the neonatal and adult rat and mouse. *American Journal of Physiology-Heart and Circulatory Physiology*, *293*(3), H1883–H1891. https://doi.org/10.1152/ajpheart.00514.2007

Barnes, A. M., Holmstoen, T. B., Bonham, A. J., & Rowland, T. J. (2022). Differentiating Human Pluripotent Stem Cells to Cardiomyocytes Using Purified Extracellular Matrix Proteins. *Bioengineering*, *9*(12), 720. https://doi.org/10.3390/bioengineering9120720

Battey, E., Ross, J. A., Hoang, A., Wilson, D. G. S., Han, Y., Levy, Y., Pollock, R. D., Kalakoutis, M., Pugh, J. N., Close, G. L., Ellison-Hughes, G. M., Lazarus, N. R., Iskratsch, T., Harridge, S. D. R., Ochala, J., & Stroud, M. J. (2023). Myonuclear alterations associated with exercise are independent of age in humans. *The Journal of Physiology*. https://doi.org/10.1113/JP284128

Beauchamp, P., Jackson, C. B., Ozhathil, L. C., Agarkova, I., Galindo, C. L., Sawyer, D. B., Suter, T. M., & Zuppinger, C. (2020). 3D Co-culture of hiPSC-Derived Cardiomyocytes With Cardiac Fibroblasts Improves Tissue-Like Features of Cardiac Spheroids. *Frontiers in Molecular Biosciences*, *7*. https://doi.org/10.3389/fmolb.2020.00014

Beeton, C. (2018). Differences in ion channel phenotype and function between humans and animal models. *Frontiers in Bioscience*, *23*(1), 4581. https://doi.org/10.2741/4581

Benders, A. (1991). The biochemical and structural maturation of human skeletal muscle cells in culture: The effect of the serum substitute Ultroser G*1. *Experimental Cell Research*, *195*(2), 284–294. https://doi.org/10.1016/0014-4827(91)90375-5

Bergström, G., Christoffersson, J., Schwanke, K., Zweigerdt, R., & Mandenius, C.-F. (2015). Stem cell derived in vivo-like human cardiac bodies in a microfluidic device for toxicity testing by beating frequency imaging. *Lab on a Chip*, *15*(15), 3242–3249. https://doi.org/10.1039/C5LC00449G

Birket, M. J., & Mummery, C. L. (2015). Pluripotent stem cell derived cardiovascular progenitors - A developmental perspective. In *Developmental Biology*. https://doi.org/10.1016/j.ydbio.2015.01.012

Bishop, A., Gallup, B., Skeate, Y., & Dubowitz, V. (1971). Morphological studies on normal and diseased human muscle in culture. *Journal of the Neurological Sciences*, *13*(3), 333–350. https://doi.org/10.1016/0022-510X(71)90037-2

Blacker, T. S., Mann, Z. F., Gale, J. E., Ziegler, M., Bain, A. J., Szabadkai, G., & Duchen, M. R. (2014). Separating NADH and NADPH fluorescence in live cells and tissues using FLIM. *Nature Communications*, *5*(1), 3936. https://doi.org/10.1038/ncomms4936

Blau, H. M., & Webster, C. (1981). Isolation and characterization of human muscle cells. *Proceedings of the National Academy of Sciences*, *78*(9), 5623–5627. https://doi.org/10.1073/pnas.78.9.5623

Blazeski, A., Kostecki, G. M., & Tung, L. (2015). Engineered heart slices for electrophysiological and contractile studies. *Biomaterials*, *55*(1), 119–128. https://doi.org/10.1016/j.biomaterials.2015.03.026

Borisov, S. M., Nuss, G., & Klimant, I. (2008). Red Light-Excitable Oxygen Sensing Materials Based on Platinum(II) and Palladium(II) Benzoporphyrins. *Analytical Chemistry*, *80*(24), 9435–9442. https://doi.org/10.1021/ac801521v

Boulé, N. G., Haddad, E., Kenny, G. P., Wells, G. A., & Sigal, R. J. (2001). Effects of Exercise on Glycemic Control and Body Mass in Type 2 Diabetes Mellitus. *JAMA*, *286*(10), 1218. https://doi.org/10.1001/jama.286.10.1218

Brauchle, E., Knopf, A., Bauer, H., Shen, N., Linder, S., Monaghan, M. G., Ellwanger, K., Layland, S. L., Brucker, S. Y., Nsair, A., & Schenke-Layland, K. (2016). Non-invasive Chamber-Specific Identification of Cardiomyocytes in Differentiating Pluripotent Stem Cells. *Stem Cell Reports*, *6*(2), 188–199. https://doi.org/10.1016/j.stemcr.2015.12.007

Brauchle, E., & Schenke-Layland, K. (2013). Raman spectroscopy in biomedicine – non-invasive in vitro analysis of cells and extracellular matrix components in tissues. *Biotechnology Journal*, *8*(3), 288–297. https://doi.org/10.1002/biot.201200163

Breckenridge, R. A., Piotrowska, I., Ng, K.-E., Ragan, T. J., West, J. A., Kotecha, S., Towers, N., Bennett, M., Kienesberger, P. C., Smolenski, R. T., Siddall, H. K., Offer, J. L., Mocanu, M. M., Yelon, D. M., Dyck, J. R. B., Griffin, J. L., Abramov, A. Y., Gould, A. P., & Mohun, T. J. (2013). Hypoxic Regulation of Hand1 Controls the Fetal-Neonatal Switch in Cardiac Metabolism. *PLoS Biology*, *11*(9), e1001666. https://doi.org/10.1371/journal.pbio.1001666

Brutsaert, D. L. (2003). Cardiac Endothelial-Myocardial Signaling: Its Role in Cardiac Growth, Contractile Performance, and Rhythmicity. *Physiological Reviews*, *83*(1), 59–115. https://doi.org/10.1152/physrev.00017.2002

Bruzewicz, D. A., McGuigan, A. P., & Whitesides, G. M. (2008). Fabrication of a modular tissue construct in a microfluidic chip. *Lab on a Chip*, *8*(5), 663. https://doi.org/10.1039/b719806j

Burger, R., Kirby, D., Glynn, M., Nwankire, C., O'Sullivan, M., Siegrist, J., Kinahan, D., Aguirre, G., Kijanka, G., Gorkin, R. A., & Ducrée, J. (2012). Centrifugal microfluidics for cell analysis. *Current Opinion in Chemical Biology*, *16*(3–4), 409–414. https://doi.org/10.1016/j.cbpa.2012.06.002

Burridge, P. W., Matsa, E., Shukla, P., Lin, Z. C., Churko, J. M., Ebert, A. D., Lan, F., Diecke, S., Huber, B., Mordwinkin, N. M., Plews, J. R., Abilez, O. J., Cui, B., Gold, J. D., & Wu, J. C. (2014). Chemically defined generation of human cardiomyocytes. *Nature Methods*, *11*(8), 855–860. https://doi.org/10.1038/nmeth.2999

Busche, M., Rabl, D., Fischer, J., Schmees, C., Mayr, T., Gebhardt, R., & Stelzle, M. (2022). Continous, non-invasive monitoring of oxygen consumption in a parallelized microfluidic in vitro system provides novel insight into the response to nutrients and drugs of primary human hepatocytes. *EXCLI Journal*, *21*, 144–161. https://doi.org/10.17179/excli2021-4351

Busek, M., Nøvik, S., Aizenshtadt, A., Amirola-Martinez, M., Combriat, T., Grünzner, S., & Krauss, S. (2021). Thermoplastic Elastomer (TPE)–Poly(Methyl Methacrylate) (PMMA) Hybrid Devices for Active Pumping PDMS-Free Organ-on-a-Chip Systems. *Biosensors*, *11*(5), 162. https://doi.org/10.3390/bios11050162

Campostrini, G., Meraviglia, V., Giacomelli, E., van Helden, R. W. J., Yiangou, L., Davis, R. P., Bellin, M., Orlova, V. V., & Mummery, C. L. (2021). Generation, functional analysis and applications of isogenic three-dimensional self-aggregating cardiac microtissues from human pluripotent stem cells. *Nature Protocols*, *16*(4), 2213–2256. https://doi.org/10.1038/s41596-021-00497-2

Centers for Disease Control and Prevention. (2022). *National Diabetes Statistics Report.* . https://www.cdc.gov/diabetes/data/statistics/statistics-report.html.

Chen, X., Hou, S., Chu, J., Xiong, Y., Xiong, P., Liu, G., & Tian, Y. (2017). Observation Interface of PDMS Membrane in a Microfluidic Chip Based on One-Step Molding. *Micromachines*, *8*(3), 64. https://doi.org/10.3390/mi8030064

Christensen, R. K., von Halling Laier, C., Kiziltay, A., Wilson, S., & Larsen, N. B. (2020). 3D Printed Hydrogel Multiassay Platforms for Robust Generation of Engineered Contractile Tissues. *Biomacromolecules*, *21*(2), 356–365. https://doi.org/10.1021/acs.biomac.9b01274

Cipriano, M., Schlünder, K., Probst, C., Linke, K., Weiss, M., Fischer, M. J., Mesch, L., Achberger, K., Liebau, S., Mesquida, M., Nicolini, V., Schneider, A., Giusti, A. M., Kustermann, S., & Loskill, P. (2022). Human immunocompetent choroid-on-chip: a novel tool for studying ocular effects of biological drugs. *Communications Biology*, *5*(1), 52. https://doi.org/10.1038/s42003-021-02977-3

Cortezzi, S. S., Cabral, E. C., Trevisan, M. G., Ferreira, C. R., Setti, A. S., Braga, D. P. de A. F., Figueira, R. de C. S., Iaconelli, A., Eberlin, M. N., & Borges, E. (2013). Prediction of embryo implantation potential by mass spectrometry fingerprinting of the culture medium. *REPRODUCTION*, *145*(5), 453–462. https://doi.org/10.1530/REP-12-0168

Davidson, M., Nesti, C., Palenzuela, L., Walker, W., Hernandez, E., Protas, L., Hirano, M., & Isaac, N. (2005). Novel cell lines derived from adult human ventricular cardiomyocytes. *Journal of Molecular and Cellular Cardiology*, *39*(1), 133–147. https://doi.org/10.1016/j.yjmcc.2005.03.003

Davis, B. N. J., Santoso, J. W., Walker, M. J., Cheng, C. S., Koves, T. R., Kraus, W. E., & Truskey, G. A. (2017). Human, Tissue-Engineered, Skeletal Muscle Myobundles to Measure Oxygen Uptake and Assess Mitochondrial Toxicity. *Tissue Engineering Part C: Methods*, *23*(4), 189–199. https://doi.org/10.1089/ten.tec.2016.0264

Davis, B. N., Yen, R., Prasad, V., & Truskey, G. A. (2019). Oxygen consumption in human, tissue-engineered myobundles during basal and electrical stimulation conditions. *APL Bioengineering*, *3*(2), 026103. https://doi.org/10.1063/1.5093417

Dewing, J. M., Saunders, V., O'Kelly, I., & Wilson, D. I. (2022). Defining cardiac cell populations and relative cellular composition of the early fetal human heart. *PLOS ONE*, *17*(11), e0259477. https://doi.org/10.1371/journal.pone.0259477

Dostal, D., Glaser, S., & Baudino, T. A. (2015). Cardiac Fibroblast Physiology and Pathology. In *Comprehensive Physiology* (Vol. 5, Issue 2, pp. 887–909). John Wiley & Sons, Inc. https://doi.org/10.1002/cphy.c140053

Dowden, H., & Munro, J. (2019). Trends in clinical success rates and therapeutic focus. *Nature Reviews Drug Discovery*, *18*(7), 495–496. https://doi.org/10.1038/d41573-019-00074-z

Dreher, S. I., Grubba, P., Toerne, C. von, Moruzzi, A., Maurer, J., Goj, T., Birkenfeld, A. L., Peter, A., Loskill, P., Hauck, S., & Weigert, C. (2023). Engineering of human myotubes toward a mature metabolic and contractile phenotype. *BioRxiv*, 2023.06.12.544344. https://doi.org/10.1101/2023.06.12.544344

Dutta, P., & Nahrendorf, M. (2015). Monocytes in Myocardial Infarction. *Arteriosclerosis, Thrombosis, and Vascular Biology*, *35*(5), 1066–1070. https://doi.org/10.1161/ATVBAHA.114.304652

Egan, B., & Zierath, J. R. (2013). Exercise Metabolism and the Molecular Regulation of Skeletal Muscle Adaptation. *Cell Metabolism*, *17*(2), 162–184. https://doi.org/10.1016/j.cmet.2012.12.012

El-Fiqi, A., Lee, J. H., Lee, E.-J., & Kim, H.-W. (2013). Collagen hydrogels incorporated with surface-aminated mesoporous nanobioactive glass: Improvement of physicochemical stability and mechanical properties is effective for hard tissue engineering. *Acta Biomaterialia*, *9*(12), 9508–9521. https://doi.org/10.1016/j.actbio.2013.07.036

Ellis, B. W., Acun, A., Can, U. I., & Zorlutuna, P. (2017). Human iPSC-derived myocardium-on-chip with capillary-like flow for personalized medicine. *Biomicrofluidics*, *11*(2), 024105. https://doi.org/10.1063/1.4978468

Eng, G., Lee, B. W., Protas, L., Gagliardi, M., Brown, K., Kass, R. S., Keller, G., Robinson, R. B., & Vunjak-Novakovic, G. (2016). Autonomous beating rate adaptation in human stem cell-derived cardiomyocytes. *Nature Communications*, *7*(1), 10312. https://doi.org/10.1038/ncomms10312

Espulgar, W., Aoki, W., Ikeuchi, T., Mita, D., Saito, M., Lee, J.-K., & Tamiya, E. (2015). Centrifugal microfluidic platform for single-cell level cardiomyocyte-based drug profiling and screening. *Lab on a Chip*, *15*(17), 3572–3580. https://doi.org/10.1039/C5LC00652J

Evano, B., Khalilian, S., Le Carrou, G., Almouzni, G., & Tajbakhsh, S. (2020). Dynamics of Asymmetric and Symmetric Divisions of Muscle Stem Cells In Vivo and on Artificial Niches. *Cell Reports*, *30*(10), 3195-3206.e7. https://doi.org/10.1016/j.celrep.2020.01.097

Evans, R. D., & Heather, L. C. (2016). Metabolic pathways and abnormalities. *Surgery (Oxford)*, *34*(6), 266–272. https://doi.org/10.1016/j.mpsur.2016.03.010

Feric, N. T., Pallotta, I., Singh, R., Bogdanowicz, D. R., Gustilo, M. M., Chaudhary, K. W., Willette, R. N., Chendrimada, T. P., Xu, X., Graziano, M. P., & Aschar-Sobbi, R. (2019). Engineered Cardiac Tissues Generated in the Biowire II: A Platform for Human-Based Drug Discovery. *Toxicological Sciences*, *172*(1), 89–97. https://doi.org/10.1093/toxsci/kfz168

Ferrannini, E., Simonson, D. C., Katz, L. D., Reichard, G., Bevilacqua, S., Barrett, E. J., Olsson, M., & DeFronzo, R. A. (1988). The disposal of an oral glucose load in patients with non-insulin-dependent diabetes. *Metabolism*, *37*(1), 79–85. https://doi.org/10.1016/0026-0495(88)90033-9

Fink, C., Ergün, S., Kralisch, D., Remmers, U., Weil, J., & Eschenhagen, T. (2000). Chronic stretch of engineered heart tissue induces hypertrophy and functional improvement. *The FASEB Journal*, *14*(5), 669–679. https://doi.org/10.1096/fasebj.14.5.669

Fiserova, I., Trinh, M. D., Elkalaf, M., Vacek, L., Heide, M., Martinkova, S., Bechynska, K., Kosek, V., Hajslova, J., Fiser, O., Tousek, P., & Polak, J. (2022). Isoprenaline modified the lipidomic profile and reduced β-oxidation in HL-1 cardiomyocytes: In vitro model of takotsubo syndrome. *Frontiers in Cardiovascular Medicine*, *9*. https://doi.org/10.3389/fcvm.2022.917989

Frontera, W. R., & Ochala, J. (2015). Skeletal Muscle: A Brief Review of Structure and Function. *Calcified Tissue International*, *96*(3), 183–195. https://doi.org/10.1007/s00223-014-9915-y

Fuchs, S., Johansson, S., Tjell, A. Ø., Werr, G., Mayr, T., & Tenje, M. (2021). In-Line Analysis of Organ-on-Chip Systems with Sensors: Integration, Fabrication, Challenges, and Potential. *ACS Biomaterials Science & Engineering*, *7*(7), 2926–2948. https://doi.org/10.1021/acsbiomaterials.0c01110

Fuchs, S., Rieger, V., Tjell, A. Ø., Spitz, S., Brandauer, K., Schaller-Ammann, R., Feiel, J., Ertl, P., Klimant, I., & Mayr, T. (2023). Optical glucose sensor for microfluidic cell culture systems. *Biosensors and Bioelectronics*, *237*, 115491. https://doi.org/10.1016/j.bios.2023.115491

Fuchs, S., van Helden, R. W. J., Wiendels, M., de Graaf, M. N. S., Orlova, V. V., Mummery, C. L., van Meer, B. J., & Mayr, T. (2022). On-chip analysis of glycolysis and

mitochondrial respiration in human induced pluripotent stem cells. *Materials Today Bio*, *17*, 100475. https://doi.org/10.1016/j.mtbio.2022.100475

Furtado, M. B., Nim, H. T., Boyd, S. E., & Rosenthal, N. A. (2016). View from the heart: cardiac fibroblasts in development, scarring and regeneration. *Development*, *143*(3), 387–397. https://doi.org/10.1242/dev.120576

Gaetani, R., Zizzi, E. A., Deriu, M. A., Morbiducci, U., Pesce, M., & Messina, E. (2020). When Stiffness Matters: Mechanosensing in Heart Development and Disease. *Frontiers in Cell and Developmental Biology*, *8*. https://doi.org/10.3389/fcell.2020.00334

Galois, L., Hutasse, S., Cortial, D., Rousseau, C. F., Grossin, L., Ronziere, M.-C., Herbage, D., & Freyria, A.-M. (2006). Bovine chondrocyte behaviour in three-dimensional type I collagen gel in terms of gel contraction, proliferation and gene expression. *Biomaterials*, *27*(1), 79–90. https://doi.org/10.1016/j.biomaterials.2005.05.098

Galpin, A. J., Raue, U., Jemiolo, B., Trappe, T. A., Harber, M. P., Minchev, K., & Trappe, S. (2012). Human skeletal muscle fiber type specific protein content. *Analytical Biochemistry*, *425*(2), 175–182. https://doi.org/10.1016/j.ab.2012.03.018

Garoffolo, G., & Pesce, M. (2019). Mechanotransduction in the Cardiovascular System: From Developmental Origins to Homeostasis and Pathology. *Cells*, *8*(12), 1607. https://doi.org/10.3390/cells8121607

Giacomelli, E., Bellin, M., Orlova, V. V., & Mummery, C. L. (2017). Co-Differentiation of Human Pluripotent Stem Cells-Derived Cardiomyocytes and Endothelial Cells from Cardiac Mesoderm Provides a Three-Dimensional Model of Cardiac Microtissue. *Current Protocols in Human Genetics*, *95*(1), 21.9.1-21.9.22. https://doi.org/10.1002/cphg.46

Giacomelli, E., Bellin, M., Sala, L., van Meer, B. J., Tertoolen, L. G. J., Orlova, V. V., & Mummery, C. L. (2017). Three-dimensional cardiac microtissues composed of cardiomyocytes and endothelial cells co-differentiated from human pluripotent stem cells. *Development*. https://doi.org/10.1242/dev.143438

Giacomelli, E., Meraviglia, V., Campostrini, G., Cochrane, A., Cao, X., van Helden, R. W. J., Krotenberg Garcia, A., Mircea, M., Kostidis, S., Davis, R. P., van Meer, B. J., Jost, C. R., Koster, A. J., Mei, H., Míguez, D. G., Mulder, A. A., Ledesma-Terrón, M., Pompilio, G., Sala, L., … Mummery, C. L. (2020). Human-iPSC-Derived Cardiac Stromal Cells Enhance Maturation in 3D Cardiac Microtissues and Reveal Non-cardiomyocyte Contributions to Heart Disease. *Cell Stem Cell*, *26*(6), 862-879.e11. https://doi.org/10.1016/j.stem.2020.05.004

Glynn, M., Nwankire, C., Lemass, K., Kinahan, D. J., & Ducrée, J. (2015). Cluster size distribution of cancer cells in blood using stopped-flow centrifugation along scale-matched gaps of a radially inclined rail. *Microsystems & Nanoengineering*, *1*(1), 15018. https://doi.org/10.1038/micronano.2015.18

Godier-Furnémont, A. F. G., Duan, Y., Maidhof, R., & Vunjak-Novakovic, G. (2011). Tissue Engineering Strategies for Cardiac Regeneration. In *Regenerating the Heart* (pp. 443–475). Humana Press. https://doi.org/10.1007/978-1-61779-021-8_23

Goldfracht, I., Protze, S., Shiti, A., Setter, N., Gruber, A., Shaheen, N., Nartiss, Y., Keller, G., & Gepstein, L. (2020). Generating ring-shaped engineered heart tissues from ventricular and atrial human pluripotent stem cell-derived cardiomyocytes. *Nature Communications*, *11*(1), 75. https://doi.org/10.1038/s41467-019-13868-x

Gordon, J., Amini, S., & White, M. K. (2013). General overview of neuronal cell culture. In *Methods in Molecular Biology* (Vol. 1078, pp. 1–8). https://doi.org/10.1007/978-1-62703-640-5_1

Grist, S. M., Chrostowski, L., & Cheung, K. C. (2010). Optical Oxygen Sensors for Applications in Microfluidic Cell Culture. *Sensors*, *10*(10), 9286–9316. https://doi.org/10.3390/s101009286

Guo, X., Greene, K., Akanda, N., Smith, A. S. T., Stancescu, M., Lambert, S., Vandenburgh, H., & Hickman, J. J. (2014). In vitro differentiation of functional human skeletal myotubes in a defined system. *Biomater. Sci.*, *2*(1), 131–138. https://doi.org/10.1039/C3BM60166H

Guo, Y., & Pu, W. T. (2020). Cardiomyocyte Maturation. *Circulation Research*, *126*(8), 1086–1106. https://doi.org/10.1161/CIRCRESAHA.119.315862

Hameed, P., & Manivasagam, G. (2021). An overview of bio-actuation in collagen hydrogels: a mechanobiological phenomenon. *Biophysical Reviews*, *13*(3), 387–403. https://doi.org/10.1007/s12551-021-00804-x

Hanna Lab Protocol – Weizmann Institute of Science. (n.d.). *JACOB HANNA LAB - In house and custom production of B27 supplement*. Retrieved July 11, 2023, from https://hannalabweb.weizmann.ac.il/wp-content/uploads/2016/02/HANNA-LAB-B22-B27-PROTOCOL-V3.pdf

Harari, E., Guo, L., Smith, S. L., Braumann, R. E., Virmani, R., & Finn, A. V. (2017). Heart-resident macrophages: are they involved in the rhythm of every beat? *Journal of Thoracic Disease*, *9*(8), 2264–2267. https://doi.org/10.21037/jtd.2017.07.43

Hawley, J. A., & Lessard, S. J. (2007). Exercise training-induced improvements in insulin action. *Acta Physiologica*, *192*(1), 127–135. https://doi.org/10.1111/j.1748-1716.2007.01783.x

Henry, R. R., Abrams, L., Nikoulina, S., & Ciaraldi, T. P. (1995). Insulin Action and Glucose Metabolism in Nondiabetic Control and NIDDM Subjects: Comparison Using Human Skeletal Muscle Cell Cultures. *Diabetes*, *44*(8), 936–946. https://doi.org/10.2337/diab.44.8.936

Hoes, M. F., Grote Beverborg, N., Kijlstra, J. D., Kuipers, J., Swinkels, D. W., Giepmans, B. N. G., Rodenburg, R. J., van Veldhuisen, D. J., de Boer, R. A., & van der Meer, P. (2018). Iron deficiency impairs contractility of human cardiomyocytes through

decreased mitochondrial function. *European Journal of Heart Failure*, *20*(5), 910–919. https://doi.org/10.1002/ejhf.1154

Hoffmann, C., Höckele, S., Kappler, L., Hrabě de Angelis, M., Häring, H.-U., & Weigert, C. (2018). The effect of differentiation and TGFβ on mitochondrial respiration and mitochondrial enzyme abundance in cultured primary human skeletal muscle cells. *Scientific Reports*, *8*(1), 737. https://doi.org/10.1038/s41598-017-18658-3

Hoffmann, C., & Weigert, C. (2017). Skeletal Muscle as an Endocrine Organ: The Role of Myokines in Exercise Adaptations. *Cold Spring Harbor Perspectives in Medicine*, *7*(11), a029793. https://doi.org/10.1101/cshperspect.a029793

Hong, Y., Zhao, Y., Li, H., Yang, Y., Chen, M., Wang, X., Luo, M., & Wang, K. (2023). Engineering the maturation of stem cell-derived cardiomyocytes. *Frontiers in Bioengineering and Biotechnology*, *11*. https://doi.org/10.3389/fbioe.2023.1155052

Hookway, T. A., Butts, J. C., Lee, E., Tang, H., & McDevitt, T. C. (2016). Aggregate formation and suspension culture of human pluripotent stem cells and differentiated progeny. *Methods*, *101*, 11–20. https://doi.org/10.1016/j.ymeth.2015.11.027

Hoppeler, H., Luethi, P., Claassen, H., Weibel, E. R., & Howald, H. (1973). The ultrastructure of the normal human skeletal muscle. *Pfluegers Archiv European Journal of Physiology*, *344*(3), 217–232. https://doi.org/10.1007/BF00588462

Huebsch, N., Charrez, B., Neiman, G., Siemons, B., Boggess, S. C., Wall, S., Charwat, V., Jæger, K. H., Cleres, D., Telle, Å., Lee-Montiel, F. T., Jeffreys, N. C., Deveshwar, N., Edwards, A. G., Serrano, J., Snuderl, M., Stahl, A., Tveito, A., Miller, E. W., & Healy, K. E. (2022). Metabolically driven maturation of human-induced-pluripotent-stem-cell-derived cardiac microtissues on microfluidic chips. *Nature Biomedical Engineering*, *6*(4), 372–388. https://doi.org/10.1038/s41551-022-00884-4

Huebsch, N., Loskill, P., Deveshwar, N., Spencer, C. I., Judge, L. M., Mandegar, M. A., Fox, C. B., Mohamed, T. M. A., Ma, Z., Mathur, A., Sheehan, A. M., Truong, A., Saxton, M., Yoo, J., Srivastava, D., Desai, T. A., So, P. L., Healy, K. E., & Conklin, B. R. (2016). Miniaturized iPS-Cell-Derived Cardiac Muscles for Physiologically Relevant Drug Response Analyses. *Scientific Reports*, *6*(April), 1–12. https://doi.org/10.1038/srep24726

Hulsmans, M., Clauss, S., Xiao, L., Aguirre, A. D., King, K. R., Hanley, A., Hucker, W. J., Wülfers, E. M., Seemann, G., Courties, G., Iwamoto, Y., Sun, Y., Savol, A. J., Sager, H. B., Lavine, K. J., Fishbein, G. A., Capen, D. E., Da Silva, N., Miquerol, L., … Nahrendorf, M. (2017). Macrophages Facilitate Electrical Conduction in the Heart. *Cell*. https://doi.org/10.1016/j.cell.2017.03.050

Huyer, L. D., Montgomery, M., Zhao, Y., Xiao, Y., Conant, G., Korolj, A., & Radisic, M. (2015). Biomaterial based cardiac tissue engineering and its applications. *Biomedical Materials*, *10*(3), 034004. https://doi.org/10.1088/1748-6041/10/3/034004

Iberite, F., Gruppioni, E., & Ricotti, L. (2022). Skeletal muscle differentiation of human iPSCs meets bioengineering strategies: perspectives and challenges. *Npj Regenerative Medicine*, *7*(1), 23. https://doi.org/10.1038/s41536-022-00216-9

Iles, R. K., Sharara, F. I., Zmuidinaite, R., Abdo, G., Keshavarz, S., & Butler, S. A. (2019). Secretome profile selection of optimal IVF embryos by matrix-assisted laser desorption ionization time-of-flight mass spectrometry. *Journal of Assisted Reproduction and Genetics*, *36*(6), 1153–1160. https://doi.org/10.1007/s10815-019-01444-7

Israeli-Rosenberg, S., Manso, A. M., Okada, H., & Ross, R. S. (2014). Integrins and Integrin-Associated Proteins in the Cardiac Myocyte. *Circulation Research*, *114*(3), 572–586. https://doi.org/10.1161/CIRCRESAHA.114.301275

Jacob, R., & Khan, M. (2018). Cardiac Biomarkers: What Is and What Can Be. *Indian Journal of Cardiovascular Disease in Women WINCARS*, *03*(04), 240–244. https://doi.org/10.1055/s-0039-1679104

Jang, K.-J., Otieno, M. A., Ronxhi, J., Lim, H.-K., Ewart, L., Kodella, K. R., Petropolis, D. B., Kulkarni, G., Rubins, J. E., Conegliano, D., Nawroth, J., Simic, D., Lam, W., Singer, M., Barale, E., Singh, B., Sonee, M., Streeter, A. J., Manthey, C., … Hamilton, G. A. (2019). Reproducing human and cross-species drug toxicities using a Liver-Chip. *Science Translational Medicine*, *11*(517). https://doi.org/10.1126/scitranslmed.aax5516

Jongh, R., Spijkers, X. M., Pasteuning-Vuhman, S., Vulto, P., & Pasterkamp, R. J. (2021). Neuromuscular junction-on-a-chip: ALS disease modeling and read-out development in microfluidic devices. *Journal of Neurochemistry*, *157*(3), 393–412. https://doi.org/10.1111/jnc.15289

Jonsson, M. K. B., Hartman, R. J. G., Ackers-Johnson, M., Tan, W. L. W., Lim, B., van Veen, T. A. B., & Foo, R. S. (2016). A Transcriptomic and Epigenomic Comparison of Fetal and Adult Human Cardiac Fibroblasts Reveals Novel Key Transcription Factors in Adult Cardiac Fibroblasts. *JACC: Basic to Translational Science*, *1*(7), 590–602. https://doi.org/10.1016/j.jacbts.2016.07.007

Kahn-Krell, A., Pretorius, D., Guragain, B., Lou, X., Wei, Y., Zhang, J., Qiao, A., Nakada, Y., Kamp, T. J., Ye, L., & Zhang, J. (2022). A three-dimensional culture system for generating cardiac spheroids composed of cardiomyocytes, endothelial cells, smooth-muscle cells, and cardiac fibroblasts derived from human induced-pluripotent stem cells. *Frontiers in Bioengineering and Biotechnology*, *10*. https://doi.org/10.3389/fbioe.2022.908848

Kehat, I., Gepstein, A., Spira, A., Itskovitz-Eldor, J., & Gepstein, L. (2002). High-Resolution Electrophysiological Assessment of Human Embryonic Stem Cell-Derived Cardiomyocytes. *Circulation Research*, *91*(8), 659–661. https://doi.org/10.1161/01.RES.0000039084.30342.9B

Kim, H.-D. (1996). Expression of intermediate filament desmin and vimentin in the human fetal heart. *The Anatomical Record*, *246*(2), 271–278. https://doi.org/10.1002/(SICI)1097-0185(199610)246:2<271::AID-AR13>3.0.CO;2-L

Kim, S., Lee, H., Kim, J. Ah., & Park, T. H. (2022). Prevention of collagen hydrogel contraction using polydopamine-coating and alginate outer shell increases cell contractile force. *Biomaterials Advances*, *136*, 212780. https://doi.org/10.1016/j.bioadv.2022.212780

Kim, T. Y., Kofron, C. M., King, M. E., Markes, A. R., Okundaye, A. O., Qu, Z., Mende, U., & Choi, B. R. (2018). Directed fusion of cardiac spheroids into larger heterocellular microtissues enables investigation of cardiac action potential propagation via cardiac fibroblasts. *PLoS ONE*, *13*(5), e0196714. https://doi.org/10.1371/journal.pone.0196714

Kim, Y. Y., Ku, S.-Y., Liu, H.-C., Cho, H.-J., Oh, S. K., Moon, S. Y., & Choi, Y. M. (2011). Cryopreservation of Human Embryonic Stem Cells Derived-Cardiomyocytes Induced by BMP2 in Serum-Free Condition. *Reproductive Sciences*, *18*(3), 252–260. https://doi.org/10.1177/1933719110385130

Kirwan, J. P., Sacks, J., & Nieuwoudt, S. (2017). The essential role of exercise in the management of type 2 diabetes. *Cleveland Clinic Journal of Medicine*, *84*(7 suppl 1), S15–S21. https://doi.org/10.3949/ccjm.84.s1.03

Kolanowski, T. J., Busek, M., Schubert, M., Dmitrieva, A., Binnewerg, B., Pöche, J., Fisher, K., Schmieder, F., Grünzner, S., Hansen, S., Richter, A., El-Armouche, A., Sonntag, F., & Guan, K. (2020). Enhanced structural maturation of human induced pluripotent stem cell-derived cardiomyocytes under a controlled microenvironment in a microfluidic system. *Acta Biomaterialia*, *102*, 273–286. https://doi.org/10.1016/j.actbio.2019.11.044

Kolesová, H., Olejníčková, V., Kvasilová, A., Gregorovičová, M., & Sedmera, D. (2021). Tissue clearing and imaging methods for cardiovascular development. In *iScience* (Vol. 24, Issue 4). https://doi.org/10.1016/j.isci.2021.102387

Kondash, M. E., Ananthakumar, A., Khodabukus, A., Bursac, N., & Truskey, G. A. (2020). Glucose Uptake and Insulin Response in Tissue-engineered Human Skeletal Muscle. *Tissue Engineering and Regenerative Medicine*, *17*(6), 801–813. https://doi.org/10.1007/s13770-020-00242-y

Kong, M., Lee, J., Yazdi, I. K., Miri, A. K., Lin, Y.-D., Seo, J., Zhang, Y. S., Khademhosseini, A., & Shin, S. R. (2019). Cardiac Fibrotic Remodeling on a Chip with Dynamic Mechanical Stimulation. *Advanced Healthcare Materials*, *8*(3), 1801146. https://doi.org/10.1002/adhm.201801146

Konorov, S. O., Schulze, H. G., Piret, J. M., Aparicio, S. A., Turner, R. F. B., & Blades, M. W. (2011). Raman Microscopy-Based Cytochemical Investigations of Potential Niche-Forming Inhomogeneities Present in Human Embryonic Stem Cell Colonies. *Applied Spectroscopy*, *65*(9), 1009–1016. https://doi.org/10.1366/11-06312

Koobotse, M. O., Schmidt, D., Holly, J. M. P., & Perks, C. M. (2020). Glucose Concentration in Cell Culture Medium Influences the BRCA1-Mediated Regulation of the Lipogenic Action of IGF-I in Breast Cancer Cells. *International Journal of Molecular Sciences*, *21*(22), 8674. https://doi.org/10.3390/ijms21228674

Krützfeldt, J., Kausch, C., Volk, A., Klein, H. H., Rett, K., Häring, H. U., & Stumvoll, M. (2000). Insulin signaling and action in cultured skeletal muscle cells from lean healthy humans with high and low insulin sensitivity. *Diabetes*, *49*(6), 992–998. https://doi.org/10.2337/diabetes.49.6.992

Kuhn, T. C., Knobel, J., Burkert-Rettenmaier, S., Li, X., Meyer, I. S., Jungmann, A., Sicklinger, F., Backs, J., Lasitschka, F., Müller, O. J., Katus, H. A., Krijgsveld, J., & Leuschner, F. (2020). Secretome Analysis of Cardiomyocytes Identifies PCSK6 (Proprotein Convertase Subtilisin/Kexin Type 6) as a Novel Player in Cardiac Remodeling After Myocardial Infarction. *Circulation*, *141*(20), 1628–1644. https://doi.org/10.1161/CIRCULATIONAHA.119.044914

LaBarge, W., Mattappally, S., Kannappan, R., Fast, V. G., Pretorius, D., Berry, J. L., & Zhang, J. (2019). Maturation of three-dimensional, hiPSC-derived cardiomyocyte spheroids utilizing cyclic, uniaxial stretch and electrical stimulation. *PLOS ONE*, *14*(7), e0219442. https://doi.org/10.1371/journal.pone.0219442

Laflamme, M. A., Chen, K. Y., Naumova, A. V, Muskheli, V., Fugate, J. A., Dupras, S. K., Reinecke, H., Xu, C., Hassanipour, M., Police, S., O'Sullivan, C., Collins, L., Chen, Y., Minami, E., Gill, E. A., Ueno, S., Yuan, C., Gold, J., & Murry, C. E. (2007). Cardiomyocytes derived from human embryonic stem cells in pro-survival factors enhance function of infarcted rat hearts. *Nature Biotechnology*, *25*(9), 1015–1024. https://doi.org/10.1038/nbt1327

Lambernd, S., Taube, A., Schober, A., Platzbecker, B., Görgens, S. W., Schlich, R., Jeruschke, K., Weiss, J., Eckardt, K., & Eckel, J. (2012). Contractile activity of human skeletal muscle cells prevents insulin resistance by inhibiting pro-inflammatory signalling pathways. *Diabetologia*, *55*(4), 1128–1139. https://doi.org/10.1007/s00125-012-2454-z

Lamboley, C. R., Murphy, R. M., McKenna, M. J., & Lamb, G. D. (2014). Sarcoplasmic reticulum Ca2+ uptake and leak properties, and SERCA isoform expression, in type I and type II fibres of human skeletal muscle. *The Journal of Physiology*, *592*(6), 1381–1395. https://doi.org/10.1113/jphysiol.2013.269373

Lee, M.-O., Jung, K. B., Jo, S.-J., Hyun, S.-A., Moon, K.-S., Seo, J.-W., Kim, S.-H., & Son, M.-Y. (2019). Modelling cardiac fibrosis using three-dimensional cardiac microtissues derived from human embryonic stem cells. *Journal of Biological Engineering*, *13*(1), 15. https://doi.org/10.1186/s13036-019-0139-6

Leedahl, N. D. (2016). A Potential Cost Savings Strategy for Isoproterenol Hydrochloride Using Novel Stability Data. *Cardiology: Study & Research*, *3*(1), 1–3. https://doi.org/10.24966/CSR-768X/100011

Leonard, A., Bertero, A., Powers, J. D., Beussman, K. M., Bhandari, S., Regnier, M., Murry, C. E., & Sniadecki, N. J. (2018). Afterload promotes maturation of human induced pluripotent stem cell derived cardiomyocytes in engineered heart tissues. *Journal of*

Molecular and Cellular Cardiology, *118*(10), 147–158. https://doi.org/10.1016/j.yjmcc.2018.03.016

Li, R., Lv, X., Hasan, M., Xu, J., Xu, Y., Zhang, X., Qin, K., Wang, J., Zhou, D., & Deng, Y. (2016). A Rapidly Fabricated Microfluidic Chip for Cell Culture. *Journal of Chromatographic Science*, *54*(4), 523–530. https://doi.org/10.1093/chromsci/bmv176

Li, Y., Asfour, H., & Bursac, N. (2017). Age-dependent functional crosstalk between cardiac fibroblasts and cardiomyocytes in a 3D engineered cardiac tissue. *Acta Biomaterialia*, *55*, 120–130. https://doi.org/10.1016/j.actbio.2017.04.027

Lian, X., Zhang, J., Azarin, S. M., Zhu, K., Hazeltine, L. B., Bao, X., Hsiao, C., Kamp, T. J., & Palecek, S. P. (2013). Directed cardiomyocyte differentiation from human pluripotent stem cells by modulating Wnt/β-catenin signaling under fully defined conditions. *Nature Protocols*, *8*(1), 162–175. https://doi.org/10.1038/nprot.2012.150

Lind, J. U., Yadid, M., Perkins, I., O'Connor, B. B., Eweje, F., Chantre, C. O., Hemphill, M. A., Yuan, H., Campbell, P. H., Vlassak, J. J., & Parker, K. K. (2017). Cardiac microphysiological devices with flexible thin-film sensors for higher-throughput drug screening. *Lab Chip*, *17*(21), 3692–3703. https://doi.org/10.1039/C7LC00740J

Lindsey, S. E., Butcher, J. T., & Yalcin, H. C. (2014). Mechanical regulation of cardiac development. *Frontiers in Physiology*, *5 AUG*(August), 1–15. https://doi.org/10.3389/fphys.2014.00318

Liu, H., Qin, W., Ma, Z., Gao, B. Z., Shao, Y., Ye, T., & Borg, T. K. (2011). Myofibrillogenesis in live neonatal cardiomyocytes observed with hybrid two-photon excitation fluorescence-second harmonic generation microscopy. *Journal of Biomedical Optics*, *16*(12), 126012. https://doi.org/10.1117/1.3662457

Liu, X., Umino, T., Cano, M., Ertl, R., Veys, T., Spurzem, J., Romberger, D., & Rennard, S. I. (1998). Human bronchial epithelial cells can contract type I collagen gels. *American Journal of Physiology-Lung Cellular and Molecular Physiology*, *274*(1), L58–L65. https://doi.org/10.1152/ajplung.1998.274.1.L58

Lladó Maldonado, S., Panjan, P., Sun, S., Rasch, D., Sesay, A. M., Mayr, T., & Krull, R. (2019). A fully online sensor-equipped, disposable multiphase microbioreactor as a screening platform for biotechnological applications. *Biotechnology and Bioengineering*, *116*(1), 65–75. https://doi.org/10.1002/bit.26831

Lopaschuk, G. D., & Jaswal, J. S. (2010). Energy Metabolic Phenotype of the Cardiomyocyte During Development, Differentiation, and Postnatal Maturation. *Journal of Cardiovascular Pharmacology*, *56*(2), 130–140. https://doi.org/10.1097/FJC.0b013e3181e74a14

Lopez III, A. L., & Larina, I. V. (2019). Second harmonic generation microscopy of early embryonic mouse hearts. *Biomedical Optics Express*, *10*(6), 2898–2908. https://doi.org/10.1364/BOE.10.002898

Loskill, P., Marcus, S. G., Mathur, A., Reese, W. M., & Healy, K. E. (2015). µOrgano: A Lego®-Like Plug & Play System for Modular Multi-Organ-Chips. *PLOS ONE*, *10*(10), e0139587. https://doi.org/10.1371/journal.pone.0139587

Ma, C., Peng, Y., Li, H., & Chen, W. (2021). Organ-on-a-Chip: A New Paradigm for Drug Development. *Trends in Pharmacological Sciences*, *42*(2), 119–133. https://doi.org/10.1016/j.tips.2020.11.009

Madden, L., Juhas, M., Kraus, W. E., Truskey, G. A., & Bursac, N. (2015). Bioengineered human myobundles mimic clinical responses of skeletal muscle to drugs. *ELife*, *4*. https://doi.org/10.7554/eLife.04885

Magliaro, C., Mattei, G., Iacoangeli, F., Corti, A., Piemonte, V., & Ahluwalia, A. (2019). Oxygen Consumption Characteristics in 3D Constructs Depend on Cell Density. *Frontiers in Bioengineering and Biotechnology*, *7*. https://doi.org/10.3389/fbioe.2019.00251

Mair, D. B., Williams, M. A. C., Chen, J. F., Goldstein, A., Wu, A., Lee, P. H. U., Sniadecki, N. J., & Kim, D.-H. (2022). PDMS–PEG Block Copolymer and Pretreatment for Arresting Drug Absorption in Microphysiological Devices. *ACS Applied Materials & Interfaces*, *14*(34), 38541–38549. https://doi.org/10.1021/acsami.2c10669

Maoz, B. M., Herland, A., Henry, O. Y. F., Leineweber, W. D., Yadid, M., Doyle, J., Mannix, R., Kujala, V. J., FitzGerald, E. A., Parker, K. K., & Ingber, D. E. (2017). Organs-on-Chips with combined multi-electrode array and transepithelial electrical resistance measurement capabilities. *Lab on a Chip*, *17*(13), 2294–2302. https://doi.org/10.1039/C7LC00412E

Marsano, A., Conficconi, C., Lemme, M., Occhetta, P., Gaudiello, E., Votta, E., Cerino, G., Redaelli, A., & Rasponi, M. (2016). Beating heart on a chip: a novel microfluidic platform to generate functional 3D cardiac microtissues. *Lab on a Chip*, *16*(3), 599–610. https://doi.org/10.1039/C5LC01356A

Mastikhina, O., Moon, B., Williams, K., Hatkar, R., Gustafson, D., Mourad, O., Sun, X., Koo, M., Lam, A. Y. L., Sun, Y., Fish, J. E., Young, E. W. K., & Nunes, S. S. (2020). Human cardiac fibrosis-on-a-chip model recapitulates disease hallmarks and can serve as a platform for drug testing. *Biomaterials*, *233*, 119741. https://doi.org/10.1016/j.biomaterials.2019.119741

Mastrangeli, M., & van den Eijnden-van Raaij, J. (2021). Organs-on-chip: The way forward. *Stem Cell Reports*, *16*(9), 2037–2043. https://doi.org/10.1016/j.stemcr.2021.06.015

Mathur, A., Loskill, P., Shao, K., Huebsch, N., Hong, S., Marcus, S. G., Marks, N., Mandegar, M., Conklin, B. R., Lee, L. P., & Healy, K. E. (2015). Human iPSC-based Cardiac Microphysiological System For Drug Screening Applications. *Scientific Reports*, *5*(1), 8883. https://doi.org/10.1038/srep08883

Mathur, A., Ma, Z., Loskill, P., Jeeawoody, S., & Healy, K. E. (2016). In vitro cardiac tissue models: Current status and future prospects. In *Advanced Drug Delivery Reviews* (Vol. 96). https://doi.org/10.1016/j.addr.2015.09.011

Matsa, E., Ahrens, J. H., & Wu, J. C. (2016). Human Induced Pluripotent Stem Cells as a Platform for Personalized and Precision Cardiovascular Medicine. *Physiological Reviews*, *96*(3), 1093–1126. https://doi.org/10.1152/physrev.00036.2015

McDonaugh, B., & Whyte, M. (2020). The Evolution and Future Direction of The Cardiac Biomarker. *EMJ Cardiology*. https://doi.org/10.33590/emjcardiol/20-00045

Mdaki, K. S., Larsen, T. D., Weaver, L. J., & Baack, M. L. (2016). Age related bioenergetics profiles in isolated rat cardiomyocytes using extracellular flux analyses. *PLoS ONE*, *11*(2). https://doi.org/10.1371/journal.pone.0149002

Mellbin, L. G., Anselmino, M., & Lars, R. (2010). Diabetes, prediabetes and cardiovascular risk. *European Journal of Cardiovascular Prevention & Rehabilitation*, *17*(1_suppl), s9–s14. https://doi.org/10.1097/01.hjr.0000368192.24732.2f

Merz, K. E., & Thurmond, D. C. (2020). Role of Skeletal Muscle in Insulin Resistance and Glucose Uptake. In *Comprehensive Physiology* (pp. 785–809). Wiley. https://doi.org/10.1002/cphy.c190029

Mikoliunaite, L., Rodriguez, R. D., Sheremet, E., Kolchuzhin, V., Mehner, J., Ramanavicius, A., & Zahn, D. R. T. (2015). The substrate matters in the Raman spectroscopy analysis of cells. *Scientific Reports*, *5*(1), 13150. https://doi.org/10.1038/srep13150

Mills, R. J., Parker, B. L., Quaife-Ryan, G. A., Voges, H. K., Needham, E. J., Bornot, A., Ding, M., Andersson, H., Polla, M., Elliott, D. A., Drowley, L., Clausen, M., Plowright, A. T., Barrett, I. P., Wang, Q.-D., James, D. E., Porrello, E. R., & Hudson, J. E. (2019). Drug Screening in Human PSC-Cardiac Organoids Identifies Pro-proliferative Compounds Acting via the Mevalonate Pathway. *Cell Stem Cell*, *24*(6), 895-907.e6. https://doi.org/10.1016/j.stem.2019.03.009

Mills, R. J., Voges, H. K., Porrello, E. R., & Hudson, J. E. (2018). Disease modeling and functional screening using engineered heart tissue. *Current Opinion in Physiology*, *1*(3), 80–88. https://doi.org/10.1016/j.cophys.2017.08.003

Moorman, A. F. M., & Christoffels, V. M. (2003). Cardiac chamber formation: Development, genes, and evolution. In *Physiological Reviews* (Vol. 83, Issue 4, pp. 1223–1267). https://doi.org/10.1152/physrev.00006.2003

Morgan, C. G., & Mitchell, A. C. (1996). Fluorescence lifetime imaging: an emerging technique in fluorescence microscopy. *Chromosome Research*, *4*(4), 261–263. https://doi.org/10.1007/BF02263674

Mousavi Shaegh, S. A., De Ferrari, F., Zhang, Y. S., Nabavinia, M., Binth Mohammad, N., Ryan, J., Pourmand, A., Laukaitis, E., Banan Sadeghian, R., Nadhman, A., Shin, S. R., Nezhad, A. S., Khademhosseini, A., & Dokmeci, M. R. (2016). A microfluidic optical

platform for real-time monitoring of pH and oxygen in microfluidic bioreactors and organ-on-chip devices. *Biomicrofluidics*, *10*(4). https://doi.org/10.1063/1.4955155

Mu, C. J., Zhang, Z. Y., Lin, M., & Cao, X. C. (2015). Development of a simple and reliable PDMS interconnect for high throughput microfluidic applications. *Microsystem Technologies*, *21*(1), 147–154. https://doi.org/10.1007/s00542-013-2037-z

Narmoneva, D. A., Vukmirovic, R., Davis, M. E., Kamm, R. D., & Lee, R. T. (2004). Endothelial Cells Promote Cardiac Myocyte Survival and Spatial Reorganization. *Circulation*, *110*(8), 962–968. https://doi.org/10.1161/01.CIR.0000140667.37070.07

Nawroth, J. C., Petropolis, D. B., Manatakis, D. V., Maulana, T. I., Burchett, G., Schlünder, K., Witt, A., Shukla, A., Kodella, K., Ronxhi, J., Kulkarni, G., Hamilton, G., Seki, E., Lu, S., & Karalis, K. C. (2021). Modeling alcohol-associated liver disease in a human Liver-Chip. *Cell Reports*, *36*(3), 109393. https://doi.org/10.1016/j.celrep.2021.109393

Nikolić, N., Skaret Bakke, S., Tranheim Kase, E., Rudberg, I., Flo Halle, I., Rustan, A. C., Thoresen, G. H., & Aas, V. (2012). Electrical Pulse Stimulation of Cultured Human Skeletal Muscle Cells as an In Vitro Model of Exercise. *PLoS ONE*, *7*(3), e33203. https://doi.org/10.1371/journal.pone.0033203

Nunes, S. S., Miklas, J. W., Liu, J., Aschar-Sobbi, R., Xiao, Y., Zhang, B., Jiang, J., Massé, S., Gagliardi, M., Hsieh, A., Thavandiran, N., Laflamme, M. A., Nanthakumar, K., Gross, G. J., Backx, P. H., Keller, G., & Radisic, M. (2013). Biowire: a platform for maturation of human pluripotent stem cell–derived cardiomyocytes. *Nature Methods*, *10*(8), 781–787. https://doi.org/10.1038/nmeth.2524

Ogneva, I. V., Mirzoev, T. M., Biryukov, N. S., Veselova, O. M., & Larina, I. M. (2012). Structure and Functional Characteristics of Rat's Left Ventricle Cardiomyocytes under Antiorthostatic Suspension of Various Duration and Subsequent Reloading. *Journal of Biomedicine and Biotechnology*, *2012*, 1–11. https://doi.org/10.1155/2012/659869

Oleaga, C., Bernabini, C., Smith, A. S. T., Srinivasan, B., Jackson, M., McLamb, W., Platt, V., Bridges, R., Cai, Y., Santhanam, N., Berry, B., Najjar, S., Akanda, N., Guo, X., Martin, C., Ekman, G., Esch, M. B., Langer, J., Ouedraogo, G., … Hickman, J. J. (2016). Multi-Organ toxicity demonstration in a functional human in vitro system composed of four organs. *Scientific Reports*, *6*(1), 20030. https://doi.org/10.1038/srep20030

Oleaga, C., Lavado, A., Riu, A., Rothemund, S., Carmona-Moran, C. A., Persaud, K., Yurko, A., Lear, J., Narasimhan, N. S., Long, C. J., Sommerhage, F., Bridges, L. R., Cai, Y., Martin, C., Schnepper, M. T., Goswami, A., Note, R., Langer, J., Teissier, S., … Hickman, J. J. (2018). Long-Term Electrical and Mechanical Function Monitoring of a Human-on-a-Chip System. *Advanced Functional Materials*, 1805792. https://doi.org/10.1002/adfm.201805792

Oleaga, C., Riu, A., Rothemund, S., Lavado, A., McAleer, C. W., Long, C. J., Persaud, K., Narasimhan, N. S., Tran, M., Roles, J., Carmona-Moran, C. A., Sasserath, T., Elbrecht, D. H., Kumanchik, L., Bridges, L. R., Martin, C., Schnepper, M. T., Ekman, G., Jackson, M., … Hickman, J. J. (2018). Investigation of the effect of hepatic metabolism on off-

target cardiotoxicity in a multi-organ human-on-a-chip system. *Biomaterials*, *182*, 176–190. https://doi.org/10.1016/j.biomaterials.2018.07.062

Onakpoya, I. J., Heneghan, C. J., & Aronson, J. K. (2016). Post-marketing withdrawal of 462 medicinal products because of adverse drug reactions: a systematic review of the world literature. *BMC Medicine*, *14*(1), 10. https://doi.org/10.1186/s12916-016-0553-2

Ondatje, B. N., Sances, S., Workman, M. J., & Svendsen, C. N. (2022). Tissue clearing of human iPSC-derived organ-chips enables high resolution imaging and analysis. *Lab on a Chip*, *22*(21), 4246–4255. https://doi.org/10.1039/D2LC00116K

Ongaro, A. E., Di Giuseppe, D., Kermanizadeh, A., Miguelez Crespo, A., Mencattini, A., Ghibelli, L., Mancini, V., Wlodarczyk, K. L., Hand, D. P., Martinelli, E., Stone, V., Howarth, N., La Carrubba, V., Pensabene, V., & Kersaudy-Kerhoas, M. (2020). Polylactic is a Sustainable, Low Absorption, Low Autofluorescence Alternative to Other Plastics for Microfluidic and Organ-on-Chip Applications. *Analytical Chemistry*, *92*(9), 6693–6701. https://doi.org/10.1021/acs.analchem.0c00651

Onódi, Z., Visnovitz, T., Kiss, B., Hambalkó, S., Koncz, A., Ágg, B., Váradi, B., Tóth, V. É., Nagy, R. N., Gergely, T. G., Gergő, D., Makkos, A., Pelyhe, C., Varga, N., Reé, D., Apáti, Á., Leszek, P., Kovács, T., Nagy, N., … Varga, Z. V. (2022). Systematic transcriptomic and phenotypic characterization of human and murine cardiac myocyte cell lines and primary cardiomyocytes reveals serious limitations and low resemblances to adult cardiac phenotype. *Journal of Molecular and Cellular Cardiology*, *165*, 19–30. https://doi.org/10.1016/j.yjmcc.2021.12.007

Özkan, Y., Yılmaz, N., Özkan, S. A., & Biryol, İ. (2000). High-performance liquid chromatographic analysis of verapamil and its application to determination in tablet dosage forms and to drug dissolution studies. *Il Farmaco*, *55*(5), 376–382. https://doi.org/10.1016/S0014-827X(00)00054-9

Park, J., Lee, G.-H., Yull Park, J., Lee, J. C., & Kim, H. C. (2017). Hypergravity-induced multicellular spheroid generation with different morphological patterns precisely controlled on a centrifugal microfluidic platform. *Biofabrication*, *9*(4), 045006. https://doi.org/10.1088/1758-5090/aa9472

Pascut, F. C., Kalra, S., George, V., Welch, N., Denning, C., & Notingher, I. (2013). Non-invasive label-free monitoring the cardiac differentiation of human embryonic stem cells in-vitro by Raman spectroscopy. *Biochimica et Biophysica Acta (BBA) - General Subjects*, *1830*(6), 3517–3524. https://doi.org/10.1016/j.bbagen.2013.01.030

Passerieux, E., Rossignol, R., Letellier, T., & Delage, J. (2007). Physical continuity of the perimysium from myofibers to tendons: Involvement in lateral force transmission in skeletal muscle. *Journal of Structural Biology*, *159*(1), 19–28. https://doi.org/10.1016/j.jsb.2007.01.022

Passier, R., Oostwaard, D. W., Snapper, J., Kloots, J., Hassink, R. J., Kuijk, E., Roelen, B., de la Riviere, A. B., & Mummery, C. (2005). Increased Cardiomyocyte Differentiation

from Human Embryonic Stem Cells in Serum-Free Cultures. *STEM CELLS*, *23*(6), 772–780. https://doi.org/10.1634/stemcells.2004-0184

Picton, H. M., Elder, K., Houghton, F. D., Hawkhead, J. A., Rutherford, A. J., Hogg, J. E., Leese, H. J., & Harris, S. E. (2010). Association between amino acid turnover and chromosome aneuploidy during human preimplantation embryo development in vitro. *Molecular Human Reproduction*, *16*(8), 557–569. https://doi.org/10.1093/molehr/gaq040

Pillon, N. J., Gabriel, B. M., Dollet, L., Smith, J. A. B., Sardón Puig, L., Botella, J., Bishop, D. J., Krook, A., & Zierath, J. R. (2020). Transcriptomic profiling of skeletal muscle adaptations to exercise and inactivity. *Nature Communications*, *11*(1), 470. https://doi.org/10.1038/s41467-019-13869-w

Pointon, A., Harmer, A. R., Dale, I. L., Abi-Gerges, N., Bowes, J., Pollard, C., & Garside, H. (2015). Assessment of cardiomyocyte contraction in human-induced pluripotent stem cell-derived cardiomyocytes. *Toxicological Sciences*, *144*(2), 227–237. https://doi.org/10.1093/toxsci/kfu312

Pointon, A., Pilling, J., Dorval, T., Wang, Y., Archer, C., & Pollard, C. (2017). From the Cover: High-Throughput Imaging of Cardiac Microtissues for the Assessment of Cardiac Contraction during Drug Discovery. *Toxicological Sciences*, *155*(2), 444–457. https://doi.org/10.1093/toxsci/kfw227

Praet, S. F. E., & van Loon, L. J. C. (2008). Exercise: the brittle cornerstone of type 2 diabetes treatment. *Diabetologia*, *51*(3), 398–401. https://doi.org/10.1007/s00125-007-0910-y

Radisic, M., Park, H., Shing, H., Consi, T., Schoen, F. J., Langer, R., Freed, L. E., & Vunjak-Novakovic, G. (2004). Functional assembly of engineered myocardium by electrical stimulation of cardiac myocytes cultured on scaffolds. *Proceedings of the National Academy of Sciences*, *101*(52), 18129–18134. https://doi.org/10.1073/pnas.0407817101

Ren, L., Zhou, X., Nasiri, R., Fang, J., Jiang, X., Wang, C., Qu, M., Ling, H., Chen, Y., Xue, Y., Hartel, M. C., Tebon, P., Zhang, S., Kim, H., Yuan, X., Shamloo, A., Dokmeci, M. R., Li, S., Khademhosseini, A., … Sun, W. (2020). Combined Effects of Electric Stimulation and Microgrooves in Cardiac Tissue-on-a-Chip for Drug Screening. *Small Methods*, *4*(10), 2000438. https://doi.org/10.1002/smtd.202000438

Renner, H., Grabos, M., Becker, K. J., Kagermeier, T. E., Wu, J., Otto, M., Peischard, S., Zeuschner, D., TsyTsyura, Y., Disse, P., Klingauf, J., Leidel, S. A., Seebohm, G., Schöler, H. R., & Bruder, J. M. (2020). A fully automated high-throughput workflow for 3D-based chemical screening in human midbrain organoids. *ELife*, *9*. https://doi.org/10.7554/eLife.52904

Rennert, K., Steinborn, S., Gröger, M., Ungerböck, B., Jank, A.-M., Ehgartner, J., Nietzsche, S., Dinger, J., Kiehntopf, M., Funke, H., Peters, F. T., Lupp, A., Gärtner, C., Mayr, T., Bauer, M., Huber, O., & Mosig, A. S. (2015). A microfluidically perfused three

dimensional human liver model. *Biomaterials*, *71*, 119–131. https://doi.org/10.1016/j.biomaterials.2015.08.043

Ribeiro, A. J. S., Ang, Y. S., Fu, J. D., Rivas, R. N., Mohamed, T. M. A., Higgs, G. C., Srivastava, D., & Pruitt, B. L. (2015). Contractility of Single cardiomyocytes differentiated from pluripotent stem cells depends on physiological shape and substrate stiffness. *Proceedings of the National Academy of Sciences of the United States of America*, *112*(41), 12705–12710. https://doi.org/10.1073/pnas.1508073112

Ribeiro, M. C., Slaats, R. H., Schwach, V., Rivera-Arbelaez, J. M., Tertoolen, L. G. J., van Meer, B. J., Molenaar, R., Mummery, C. L., Claessens, M. M. A. E., & Passier, R. (2020). A cardiomyocyte show of force: A fluorescent alpha-actinin reporter line sheds light on human cardiomyocyte contractility versus substrate stiffness. *Journal of Molecular and Cellular Cardiology*, *141*, 54–64. https://doi.org/10.1016/j.yjmcc.2020.03.008

Ribeiro, M. C., Tertoolen, L. G., Guadix, J. A., Bellin, M., Kosmidis, G., D'Aniello, C., Monshouwer-Kloots, J., Goumans, M. J., Wang, Y. li, Feinberg, A. W., Mummery, C. L., & Passier, R. (2015). Functional maturation of human pluripotent stem cell derived cardiomyocytes invitro - Correlation between contraction force and electrophysiology. *Biomaterials*. https://doi.org/10.1016/j.biomaterials.2015.01.067

Richards, D. J., Li, Y., Kerr, C. M., Yao, J., Beeson, G. C., Coyle, R. C., Chen, X., Jia, J., Damon, B., Wilson, R., Starr Hazard, E., Hardiman, G., Menick, D. R., Beeson, C. C., Yao, H., Ye, T., & Mei, Y. (2020). Human cardiac organoids for the modelling of myocardial infarction and drug cardiotoxicity. *Nature Biomedical Engineering*, *4*(4), 446–462. https://doi.org/10.1038/s41551-020-0539-4

Richardson, D. S., & Lichtman, J. W. (2015). Clarifying Tissue Clearing. In *Cell* (Vol. 162, Issue 2). https://doi.org/10.1016/j.cell.2015.06.067

Richter, E. A., & Hargreaves, M. (2013). Exercise, GLUT4, and Skeletal Muscle Glucose Uptake. *Physiological Reviews*, *93*(3), 993–1017. https://doi.org/10.1152/physrev.00038.2012

Rienks, M., Papageorgiou, A.-P., Frangogiannis, N. G., & Heymans, S. (2014). Myocardial Extracellular Matrix. *Circulation Research*, *114*(5), 872–888. https://doi.org/10.1161/CIRCRESAHA.114.302533

Robert, A. W., Pereira, I. T., Dallagiovanna, B., & Stimamiglio, M. A. (2020). Secretome Analysis Performed During in vitro Cardiac Differentiation: Discovering the Cardiac Microenvironment. *Frontiers in Cell and Developmental Biology*, *8*, 49. https://doi.org/10.3389/fcell.2020.00049

Rogal, J., Binder, C., Kromidas, E., Roosz, J., Probst, C., Schneider, S., Schenke-Layland, K., & Loskill, P. (2020). WAT-on-a-chip integrating human mature white adipocytes for mechanistic research and pharmaceutical applications. *Scientific Reports*, *10*(1), 6666. https://doi.org/10.1038/s41598-020-63710-4

Ronaldson-Bouchard, K., Ma, S. P., Yeager, K., Chen, T., Song, L., Sirabella, D., Morikawa, K., Teles, D., Yazawa, M., & Vunjak-Novakovic, G. (2018). Advanced maturation of human cardiac tissue grown from pluripotent stem cells. *Nature*, *556*(7700), 239–243. https://doi.org/10.1038/s41586-018-0016-3

Ronaldson-Bouchard, K., Teles, D., Yeager, K., Tavakol, D. N., Zhao, Y., Chramiec, A., Tagore, S., Summers, M., Stylianos, S., Tamargo, M., Lee, B. M., Halligan, S. P., Abaci, E. H., Guo, Z., Jacków, J., Pappalardo, A., Shih, J., Soni, R. K., Sonar, S., … Vunjak-Novakovic, G. (2022). A multi-organ chip with matured tissue niches linked by vascular flow. *Nature Biomedical Engineering*, *6*(4), 351–371. https://doi.org/10.1038/s41551-022-00882-6

Ruan, J.-L., Tulloch, N. L., Razumova, M. V., Saiget, M., Muskheli, V., Pabon, L., Reinecke, H., Regnier, M., & Murry, C. E. (2016). Mechanical Stress Conditioning and Electrical Stimulation Promote Contractility and Force Maturation of Induced Pluripotent Stem Cell-Derived Human Cardiac Tissue. *Circulation*, *134*(20), 1557–1567. https://doi.org/10.1161/CIRCULATIONAHA.114.014998

Rubart, M., & Field, L. J. (2006). CARDIAC REGENERATION: Repopulating the Heart. *Annual Review of Physiology*, *68*(1), 29–49. https://doi.org/10.1146/annurev.physiol.68.040104.124530

Russell, W. M. S., & Burch, R. L. (1959). *The principles of humane experimental technique*. Methuen.

Sala, L., van Meer, B. J., Tertoolen, L. G. J., Bakkers, J., Bellin, M., Davis, R. P., Denning, C., Dieben, M. A. E., Eschenhagen, T., Giacomelli, E., Grandela, C., Hansen, A., Holman, E. R., Jongbloed, M. R. M., Kamel, S. M., Koopman, C. D., Lachaud, Q., Mannhardt, I., Mol, M. P. H., … Mummery, C. L. (2018). Musclemotion: A versatile open software tool to quantify cardiomyocyte and cardiac muscle contraction in vitro and in vivo. *Circulation Research*, *122*(3). https://doi.org/10.1161/CIRCRESAHA.117.312067

Sanford, J. A., Nogiec, C. D., Lindholm, M. E., Adkins, J. N., Amar, D., Dasari, S., Drugan, J. K., Fernández, F. M., Radom-Aizik, S., Schenk, S., Snyder, M. P., Tracy, R. P., Vanderboom, P., Trappe, S., Walsh, M. J., Adkins, J. N., Amar, D., Dasari, S., Drugan, J. K., … Rivas, M. A. (2020). Molecular Transducers of Physical Activity Consortium (MoTrPAC): Mapping the Dynamic Responses to Exercise. *Cell*, *181*(7), 1464–1474. https://doi.org/10.1016/j.cell.2020.06.004

Sarabia, V., Lam, L., Burdett, E., Leiter, L. A., & Klip, A. (1992). Glucose transport in human skeletal muscle cells in culture. Stimulation by insulin and metformin. *Journal of Clinical Investigation*, *90*(4), 1386–1395. https://doi.org/10.1172/JCI116005

Schneider, O. (2022). *Generation, probing and biophysical stimulation of human microtissues in microfluidic Organ-on-Chip platforms* [Doctoral Disertation]. University of Stuttgart.

Schneider, O., Moruzzi, A., Fuchs, S., Grobel, A., Schulze, H. S., Mayr, T., & Loskill, P. (2022). Fusing spheroids to aligned µ-tissues in a heart-on-chip featuring oxygen

sensing and electrical pacing capabilities. *Materials Today Bio*, *15*, 100280. https://doi.org/10.1016/j.mtbio.2022.100280

Schneider, O., Zeifang, L., Fuchs, S., Sailer, C., & Loskill, P. (2019). User-Friendly and Parallelized Generation of Human Induced Pluripotent Stem Cell-Derived Microtissues in a Centrifugal Heart-on-a-Chip. *Tissue Engineering Part A*, *25*(9–10), 786–798. https://doi.org/10.1089/ten.tea.2019.0002

Schneider, S., Brás, E. J. S., Schneider, O., Schlünder, K., & Loskill, P. (2021). Facile Patterning of Thermoplastic Elastomers and Robust Bonding to Glass and Thermoplastics for Microfluidic Cell Culture and Organ-on-Chip. *Micromachines*, *12*(5), 575. https://doi.org/10.3390/mi12050575

Serena, E., Zatti, S., Zoso, A., Lo Verso, F., Tedesco, F. S., Cossu, G., & Elvassore, N. (2016). Skeletal Muscle Differentiation on a Chip Shows Human Donor Mesoangioblasts' Efficiency in Restoring Dystrophin in a Duchenne Muscular Dystrophy Model. *Stem Cells Translational Medicine*, *5*(12), 1676–1683. https://doi.org/10.5966/sctm.2015-0053

Severinsen, M. C. K., & Pedersen, B. K. (2020). Muscle–Organ Crosstalk: The Emerging Roles of Myokines. *Endocrine Reviews*, *41*(4), 594–609. https://doi.org/10.1210/endrev/bnaa016

Shegokar, R. (2020). Preclinical testing—Understanding the basics first. In *Drug Delivery Aspects* (pp. 19–32). Elsevier. https://doi.org/10.1016/B978-0-12-821222-6.00002-6

Shen, N., Knopf, A., Westendorf, C., Kraushaar, U., Riedl, J., Bauer, H., Pöschel, S., Layland, S. L., Holeiter, M., Knolle, S., Brauchle, E., Nsair, A., Hinderer, S., & Schenke-Layland, K. (2017). Steps toward Maturation of Embryonic Stem Cell-Derived Cardiomyocytes by Defined Physical Signals. *Stem Cell Reports*, *9*(1), 122–135. https://doi.org/10.1016/j.stemcr.2017.04.021

Shin, S. R., Kilic, T., Zhang, Y. S., Avci, H., Hu, N., Kim, D., Branco, C., Aleman, J., Massa, S., Silvestri, A., Kang, J., Desalvo, A., Hussaini, M. A., Chae, S. K., Polini, A., Bhise, N., Hussain, M. A., Lee, H. Y., Dokmeci, M. R., & Khademhosseini, A. (2017). Label-Free and Regenerative Electrochemical Microfluidic Biosensors for Continual Monitoring of Cell Secretomes. *Advanced Science*, *4*(5). https://doi.org/10.1002/advs.201600522

Shinozawa, T., Nakamura, K., Shoji, M., Morita, M., Kimura, M., Furukawa, H., Ueda, H., Shiramoto, M., Matsuguma, K., Kaji, Y., Ikushima, I., Yono, M., Liou, S.-Y., Nagai, H., Nakanishi, A., Yamamoto, K., & Izumo, S. (2017). Recapitulation of Clinical Individual Susceptibility to Drug-Induced QT Prolongation in Healthy Subjects Using iPSC-Derived Cardiomyocytes. *Stem Cell Reports*, *8*(2), 226–234. https://doi.org/10.1016/j.stemcr.2016.12.014

Shirure, V. S., & George, S. C. (2017). Design considerations to minimize the impact of drug absorption in polymer-based organ-on-a-chip platforms. *Lab on a Chip*, *17*(4), 681–690. https://doi.org/10.1039/C6LC01401A

Shroff, T., Aina, K., Maass, C., Cipriano, M., Lambrecht, J., Tacke, F., Mosig, A., & Loskill, P. (2022). Studying metabolism with multi-organ chips: new tools for disease modelling, pharmacokinetics and pharmacodynamics. *Open Biology*, *12*(3). https://doi.org/10.1098/rsob.210333

Shulman, G. I., Rothman, D. L., Jue, T., Stein, P., DeFronzo, R. A., & Shulman, R. G. (1990). Quantitation of Muscle Glycogen Synthesis in Normal Subjects and Subjects with Non-Insulin-Dependent Diabetes by 13C Nuclear Magnetic Resonance Spectroscopy. *New England Journal of Medicine*, *322*(4), 223–228. https://doi.org/10.1056/NEJM199001253220403

Si, L., Bai, H., Rodas, M., Cao, W., Oh, C. Y., Jiang, A., Moller, R., Hoagland, D., Oishi, K., Horiuchi, S., Uhl, S., Blanco-Melo, D., Albrecht, R. A., Liu, W.-C., Jordan, T., Nilsson-Payant, B. E., Golynker, I., Frere, J., Logue, J., … Ingber, D. E. (2021). A human-airway-on-a-chip for the rapid identification of candidate antiviral therapeutics and prophylactics. *Nature Biomedical Engineering*, *5*(8), 815–829. https://doi.org/10.1038/s41551-021-00718-9

Silva, A. C., Pereira, C., Fonseca, A. C. R. G., Pinto-do-Ó, P., & Nascimento, D. S. (2021). Bearing My Heart: The Role of Extracellular Matrix on Cardiac Development, Homeostasis, and Injury Response. *Frontiers in Cell and Developmental Biology*, *8*(January), 1–18. https://doi.org/10.3389/fcell.2020.621644

Silvani, G., Romanov, V., Cox, C. D., & Martinac, B. (2021). Biomechanical Characterization of Endothelial Cells Exposed to Shear Stress Using Acoustic Force Spectroscopy. *Frontiers in Bioengineering and Biotechnology*, *9*. https://doi.org/10.3389/fbioe.2021.612151

Skardal, A., Murphy, S. V., Devarasetty, M., Mead, I., Kang, H.-W., Seol, Y.-J., Shrike Zhang, Y., Shin, S.-R., Zhao, L., Aleman, J., Hall, A. R., Shupe, T. D., Kleensang, A., Dokmeci, M. R., Jin Lee, S., Jackson, J. D., Yoo, J. J., Hartung, T., Khademhosseini, A., … Atala, A. (2017). Multi-tissue interactions in an integrated three-tissue organ-on-a-chip platform. *Scientific Reports*, *7*(1), 8837. https://doi.org/10.1038/s41598-017-08879-x

Smith, J. A. B., Murach, K. A., Dyar, K. A., & Zierath, J. R. (2023). Exercise metabolism and adaptation in skeletal muscle. *Nature Reviews Molecular Cell Biology*. https://doi.org/10.1038/s41580-023-00606-x

Sticker, D., Rothbauer, M., Ehgartner, J., Steininger, C., Liske, O., Liska, R., Neuhaus, W., Mayr, T., Haraldsson, T., Kutter, J. P., & Ertl, P. (2019). Oxygen Management at the Microscale: A Functional Biochip Material with Long-Lasting and Tunable Oxygen Scavenging Properties for Cell Culture Applications. *ACS Applied Materials & Interfaces*, *11*(10), 9730–9739. https://doi.org/10.1021/acsami.8b19641

Taegtmeyer, H., Young, M. E., Lopaschuk, G. D., Abel, E. D., Brunengraber, H., Darley-Usmar, V., Des Rosiers, C., Gerszten, R., Glatz, J. F., Griffin, J. L., Gropler, R. J., Holzhuetter, H.-G., Kizer, J. R., Lewandowski, E. D., Malloy, C. R., Neubauer, S.,

Peterson, L. R., Portman, M. A., Recchia, F. A., … Wang, T. J. (2016). Assessing Cardiac Metabolism. *Circulation Research*, *118*(10), 1659–1701. https://doi.org/10.1161/RES.0000000000000097

Tallquist, M. D., & Molkentin, J. D. (2017). Redefining the identity of cardiac fibroblasts. *Nature Reviews Cardiology*, *14*(8), 484–491. https://doi.org/10.1038/nrcardio.2017.57

Tandon, N., Cannizzaro, C., Chao, P.-H. G., Maidhof, R., Marsano, A., Au, H. T. H., Radisic, M., & Vunjak-Novakovic, G. (2009). Electrical stimulation systems for cardiac tissue engineering. *Nature Protocols*, *4*(2), 155–173. https://doi.org/10.1038/nprot.2008.183

Tandon, N., Marsano, A., Maidhof, R., Wan, L., Park, H., & Vunjak-Novakovic, G. (2011). Optimization of electrical stimulation parameters for cardiac tissue engineering. *Journal of Tissue Engineering and Regenerative Medicine*, *5*(6), e115–e125. https://doi.org/10.1002/term.377

Tang, H., Yao, H., Wang, G., Wang, Y., Li, Y., & Feng, M. (2007). NIR Raman spectroscopic investigation of single mitochondria trapped by optical tweezers. *Optics Express*, *15*(20), 12708. https://doi.org/10.1364/OE.15.012708

Tanumihardja, E., Slaats, R. H., van der Meer, A. D., Passier, R., Olthuis, W., & van den Berg, A. (2021). Measuring Both pH and O 2 with a Single On-Chip Sensor in Cultures of Human Pluripotent Stem Cell-Derived Cardiomyocytes to Track Induced Changes in Cellular Metabolism. *ACS Sensors*, *6*(1), 267–274. https://doi.org/10.1021/acssensors.0c02282

Taylor, K. (2019). A summary of EU national statistical reports of animal experiments in 2014-2016. *ALTEX*, 314–319. https://doi.org/10.14573/altex.1812211

TeSlaa, T., & Teitell, M. A. (2014). Techniques to Monitor Glycolysis. In *Methods in Enzymology* (Vol. 542, pp. 91–114). https://doi.org/10.1016/B978-0-12-416618-9.00005-4

Thiebaud, D., Jacot, E., Defronzo, R. A., Maeder, E., Jequier, E., & Felber, J.-P. (1982). The Effect of Graded Doses of Insulin on Total Glucose Uptake, Glucose Oxidation, and Glucose Storage in Man. *Diabetes*, *31*(11), 957–963. https://doi.org/10.2337/diacare.31.11.957

Thompson, C. L., Fu, S., Heywood, H. K., Knight, M. M., & Thorpe, S. D. (2020). Mechanical Stimulation: A Crucial Element of Organ-on-Chip Models. *Frontiers in Bioengineering and Biotechnology*, *8*. https://doi.org/10.3389/fbioe.2020.602646

Tirziu, D., Giordano, F. J., & Simons, M. (2010). Cell Communications in the Heart. *Circulation*, *122*(9), 928–937. https://doi.org/10.1161/CIRCULATIONAHA.108.847731

Torres, M. J., Zhang, X., Slentz, D. H., Koves, T. R., Patel, H., Truskey, G. A., & Muoio, D. M. (2022). Chemotherapeutic drug screening in 3D-Bioengineered human myobundles provides insight into taxane-induced myotoxicities. *IScience*, *25*(10), 105189. https://doi.org/10.1016/j.isci.2022.105189

Trietsch, S. J., Israëls, G. D., Joore, J., Hankemeier, T., & Vulto, P. (2013). Microfluidic titer plate for stratified 3D cell culture. *Lab on a Chip*, *13*(18), 3548. https://doi.org/10.1039/c3lc50210d

Trinh, K. T. L., Thai, D. A., Chae, W. R., & Lee, N. Y. (2020). Rapid Fabrication of Poly(methyl methacrylate) Devices for Lab-on-a-Chip Applications Using Acetic Acid and UV Treatment. *ACS Omega*, *5*(28), 17396–17404. https://doi.org/10.1021/acsomega.0c01770

Trotter, J. A., & Purslow, P. P. (1992). Functional morphology of the endomysium in series fibered muscles. *Journal of Morphology*, *212*(2), 109–122. https://doi.org/10.1002/jmor.1052120203

Ulmer, B. M., & Eschenhagen, T. (2020). Human pluripotent stem cell-derived cardiomyocytes for studying energy metabolism. *Biochimica et Biophysica Acta (BBA) - Molecular Cell Research*, *1867*(3), 118471. https://doi.org/10.1016/j.bbamcr.2019.04.001

van den Berg, C. W., Elliott, D. A., Braam, S. R., Mummery, C. L., & Davis, R. P. (2014). *Differentiation of Human Pluripotent Stem Cells to Cardiomyocytes Under Defined Conditions* (pp. 163–180). https://doi.org/10.1007/7651_2014_178

van der Ven, P. F. M., Schaart, G., Jap, P. H. K., Sengers, R. C. A., Stadhouders, A. M., & Ramaekers, F. C. S. (1992). Differentiation of human skeletal muscle cells in culture: maturation as indicated by titin and desmin striation. *Cell and Tissue Research*, *270*(1), 189–198. https://doi.org/10.1007/BF00381893

van Meer, B. J., de Vries, H., Firth, K. S. A., van Weerd, J., Tertoolen, L. G. J., Karperien, H. B. J., Jonkheijm, P., Denning, C., IJzerman, A. P., & Mummery, C. L. (2017). Small molecule absorption by PDMS in the context of drug response bioassays. *Biochemical and Biophysical Research Communications*, *482*(2), 323–328. https://doi.org/10.1016/j.bbrc.2016.11.062

van Meer, B. J., Sala, L., Tertoolen, L. G. J., Smith, G. L., Burton, F. L., & Mummery, C. L. (2018). Quantification of Muscle Contraction In Vitro and In Vivo Using MUSCLEMOTION Software: From Stem Cell-Derived Cardiomyocytes to Zebrafish and Human Hearts. *Current Protocols in Human Genetics*, *99*(1), e67. https://doi.org/10.1002/cphg.67

Velegol, D., & Lanni, F. (2001). Cell Traction Forces on Soft Biomaterials. I. Microrheology of Type I Collagen Gels. *Biophysical Journal*, *81*(3), 1786–1792. https://doi.org/10.1016/S0006-3495(01)75829-8

Vickovic, S., Eraslan, G., Salmén, F., Klughammer, J., Stenbeck, L., Schapiro, D., Äijö, T., Bonneau, R., Bergenstråhle, L., Navarro, J. F., Gould, J., Griffin, G. K., Borg, Å., Ronaghi, M., Frisén, J., Lundeberg, J., Regev, A., & Ståhl, P. L. (2019). High-definition spatial transcriptomics for in situ tissue profiling. *Nature Methods*, *16*(10), 987–990. https://doi.org/10.1038/s41592-019-0548-y

Vis, M. A. M., Ito, K., & Hofmann, S. (2020). Impact of Culture Medium on Cellular Interactions in in vitro Co-culture Systems. *Frontiers in Bioengineering and Biotechnology*, *8*. https://doi.org/10.3389/fbioe.2020.00911

Vivas, A., IJspeert, C., Pan, J. Y., Vermeul, K., van den Berg, A., Passier, R., Keller, S. S., & van der Meer, A. D. (2022). Generation and Culture of Cardiac Microtissues in a Microfluidic Chip with a Reversible Open Top Enables Electrical Pacing, Dynamic Drug Dosing and Endothelial Cell Co-Culture. *Advanced Materials Technologies*, *7*(7), 2101355. https://doi.org/10.1002/admt.202101355

Votteler, M., Carvajal Berrio, D. A., Pudlas, M., Walles, H., Stock, U. A., & Schenke-Layland, K. (2012). Raman spectroscopy for the non-contact and non-destructive monitoring of collagen damage within tissues. *Journal of Biophotonics*, *5*(1), 47–56. https://doi.org/10.1002/jbio.201100068

Vučković, S., Dinani, R., Nollet, E. E., Kuster, D. W. D., Buikema, J. W., Houtkooper, R. H., Nabben, M., van der Velden, J., & Goversen, B. (2022). Characterization of cardiac metabolism in iPSC-derived cardiomyocytes: lessons from maturation and disease modeling. *Stem Cell Research & Therapy*, *13*(1), 332. https://doi.org/10.1186/s13287-022-03021-9

Wake, E., & Brack, K. (2016). Characterization of the intrinsic cardiac nervous system. *Autonomic Neuroscience : Basic & Clinical*, *199*, 3–16. https://doi.org/10.1016/j.autneu.2016.08.006

Wallace, S. J., Morrison, J. L., & Botting, K. J. (2015). Second-harmonic generation and two-photon-excited autofluorescence microscopy of cardiomyocytes : quantification of cell volume and myosin filaments. *Journal of Biomedical Optics*, *13*(6), 13–17. https://doi.org/10.1117/1.3027970

Wan, L., Flegle, J., Ozdoganlar, B., & LeDuc, P. (2020). Toward Vasculature in Skeletal Muscle-on-a-Chip through Thermo-Responsive Sacrificial Templates. *Micromachines*, *11*(10), 907. https://doi.org/10.3390/mi11100907

Wang, E. Y., Rafatian, N., Zhao, Y., Lee, A., Lai, B. F. L., Lu, R. X., Jekic, D., Davenport Huyer, L., Knee-Walden, E. J., Bhattacharya, S., Backx, P. H., & Radisic, M. (2019). Biowire Model of Interstitial and Focal Cardiac Fibrosis. *ACS Central Science*, *5*(7), 1146–1158. https://doi.org/10.1021/acscentsci.9b00052

Wang, F., Flanagan, J., Su, N., Wang, L.-C., Bui, S., Nielson, A., Wu, X., Vo, H.-T., Ma, X.-J., & Luo, Y. (2012). RNAscope. *The Journal of Molecular Diagnostics*, *14*(1), 22–29. https://doi.org/10.1016/j.jmoldx.2011.08.002

Warram, J. H. (1990). Slow Glucose Removal Rate and Hyperinsulinemia Precede the Development of Type II Diabetes in the Offspring of Diabetic Parents. *Annals of Internal Medicine*, *113*(12), 909. https://doi.org/10.7326/0003-4819-113-12-909

White, S. M., Constantin, P. E., & Claycomb, W. C. (2004). Cardiac physiology at the cellular level: use of cultured HL-1 cardiomyocytes for studies of cardiac muscle cell structure

and function. *American Journal of Physiology-Heart and Circulatory Physiology*, *286*(3), H823–H829. https://doi.org/10.1152/ajpheart.00986.2003

Wiesinger, A., Li, J., Fokkert, L., Bakker, P., Verkerk, A. O., Christoffels, V. M., Boink, G. J., & Devalla, H. D. (2022). A single cell transcriptional roadmap of human pacemaker cell differentiation. *ELife*, *11*. https://doi.org/10.7554/eLife.76781

Wikswo, J. P. (2014). The relevance and potential roles of microphysiological systems in biology and medicine. *Experimental Biology and Medicine*, *239*(9), 1061–1072. https://doi.org/10.1177/1535370214542068

Xin, M., Olson, E. N., & Bassel-Duby, R. (2013). Mending broken hearts: cardiac development as a basis for adult heart regeneration and repair. *Nature Reviews Molecular Cell Biology*, *14*(8), 529–541. https://doi.org/10.1038/nrm3619

Yamamoto, T., Minamikawa, T., Harada, Y., Yamaoka, Y., Tanaka, H., Yaku, H., & Takamatsu, T. (2018). Label-free Evaluation of Myocardial Infarct in Surgically Excised Ventricular Myocardium by Raman Spectroscopy. *Scientific Reports*, *8*(1), 14671. https://doi.org/10.1038/s41598-018-33025-6

Yang, A., Lein, F. N., Weiler, J., Drechsel, J., Schumann, V., Erichson, F., Streek, A., & Börner, R. (2023). Pressure-controlled microfluidics for automated single-molecule sample preparation. *HardwareX*, *14*, e00425. https://doi.org/10.1016/j.ohx.2023.e00425

Yang, H., Schmidt, L. P., Wang, Z., Yang, X., Shao, Y., Borg, T. K., Markwald, R., Runyan, R., & Gao, B. Z. (2016). Dynamic Myofibrillar Remodeling in Live Cardiomyocytes under Static Stretch. *Scientific Reports*, *6*, 1–12. https://doi.org/10.1038/srep20674

Yang, Wang, Zang, Tang, & Li. (2012). Cell-Based Assays in High-Throughput Screening for Drug Discovery. *International Journal of Biotechnology for Wellness Industries*. https://doi.org/10.6000/1927-3037.2012.01.01.02

Yang, Y., Creer, A., Jemiolo, B., & Trappe, S. (2005). Time course of myogenic and metabolic gene expression in response to acute exercise in human skeletal muscle. *Journal of Applied Physiology*, *98*(5), 1745–1752. https://doi.org/10.1152/japplphysiol.01185.2004

Yasin, R., Van Beers, G., Nurse, K. C. E., Al-Ani, S., Landon, D. N., & Thompson, E. J. (1977). A quantitative technique for growing human adult skeletal muscle in culture starting from mononucleated cells. *Journal of the Neurological Sciences*, *32*(3), 347–360. https://doi.org/10.1016/0022-510X(77)90018-1

Ye, L., Ni, X., Zhao, Z.-A., Lei, W., & Hu, S. (2018). The Application of Induced Pluripotent Stem Cells in Cardiac Disease Modeling and Drug Testing. *Journal of Cardiovascular Translational Research*, *11*(5), 366–374. https://doi.org/10.1007/s12265-018-9811-3

Yin, F., Zhang, X., Wang, L., Wang, Y., Zhu, Y., Li, Z., Tao, T., Chen, W., Yu, H., & Qin, J. (2021). HiPSC-derived multi-organoids-on-chip system for safety assessment of

antidepressant drugs. *Lab on a Chip*, *21*(3), 571–581. https://doi.org/10.1039/D0LC00921K

Yoon, J.-K., Kim, H. N., Bhang, S. H., Shin, J.-Y., Han, J., La, W.-G., Jeong, G.-J., Kang, S., Lee, J.-R., Oh, J., Kim, M. S., Jeon, N. L., & Kim, B.-S. (2016). Enhanced Bone Repair by Guided Osteoblast Recruitment Using Topographically Defined Implant. *Tissue Engineering Part A*, *22*(7–8), 654–664. https://doi.org/10.1089/ten.tea.2015.0417

Yu, T., Zhu, J., Li, Y., Ma, Y., Wang, J., Cheng, X., Jin, S., Sun, Q., Li, X., Gong, H., Luo, Q., Xu, F., Zhao, S., & Zhu, D. (2018). RTF: a rapid and versatile tissue optical clearing method. *Scientific Reports*, *8*(1), 1964. https://doi.org/10.1038/s41598-018-20306-3

Zahid, A., Dai, B., Hong, R., & Zhang, D. (2017). Optical properties study of silicone polymer PDMS substrate surfaces modified by plasma treatment. *Materials Research Express*, *4*(10), 105301. https://doi.org/10.1088/2053-1591/aa8645

Zbinden, A., Marzi, J., Schlünder, K., Probst, C., Urbanczyk, M., Black, S., Brauchle, E. M., Layland, S. L., Kraushaar, U., Duffy, G., Schenke-Layland, K., & Loskill, P. (2020). Non-invasive marker-independent high content analysis of a microphysiological human pancreas-on-a-chip model. *Matrix Biology*, *85–86*, 205–220. https://doi.org/10.1016/j.matbio.2019.06.008

Zhang, H., Tian, L., Shen, M., Tu, C., Wu, H., Gu, M., Paik, D. T., & Wu, J. C. (2019). Generation of Quiescent Cardiac Fibroblasts From Human Induced Pluripotent Stem Cells for In Vitro Modeling of Cardiac Fibrosis. *Circulation Research*, *125*(5), 552–566. https://doi.org/10.1161/CIRCRESAHA.119.315491

Zhang, J., Tao, R., Campbell, K. F., Carvalho, J. L., Ruiz, E. C., Kim, G. C., Schmuck, E. G., Raval, A. N., da Rocha, A. M., Herron, T. J., Jalife, J., Thomson, J. A., & Kamp, T. J. (2019). Functional cardiac fibroblasts derived from human pluripotent stem cells via second heart field progenitors. *Nature Communications*, *10*(1), 2238. https://doi.org/10.1038/s41467-019-09831-5

Zhang, X., Hong, S., Yen, R., Kondash, M., Fernandez, C. E., & Truskey, G. A. (2018). A system to monitor statin-induced myopathy in individual engineered skeletal muscle myobundles. *Lab on a Chip*, *18*(18), 2787–2796. https://doi.org/10.1039/C8LC00654G

Zhang, Y. S., Aleman, J., Arneri, A., Bersini, S., Piraino, F., Shin, S. R., Dokmeci, M. R., & Khademhosseini, A. (2015). From cardiac tissue engineering to heart-on-a-chip: beating challenges. *Biomedical Materials*, *10*(3), 034006. https://doi.org/10.1088/1748-6041/10/3/034006

Zhang, Y. S., Aleman, J., Shin, S. R., Kilic, T., Kim, D., Mousavi Shaegh, S. A., Massa, S., Riahi, R., Chae, S., Hu, N., Avci, H., Zhang, W., Silvestri, A., Sanati Nezhad, A., Manbohi, A., De Ferrari, F., Polini, A., Calzone, G., Shaikh, N., … Khademhosseini, A. (2017). Multisensor-integrated organs-on-chips platform for automated and continual in situ monitoring of organoid behaviors. *Proceedings of the National Academy of Sciences*, *114*(12). https://doi.org/10.1073/pnas.1612906114

Zhao, Y., Rafatian, N., Feric, N. T., Cox, B. J., Aschar-Sobbi, R., Wang, E. Y., Aggarwal, P., Zhang, B., Conant, G., Ronaldson-Bouchard, K., Pahnke, A., Protze, S., Lee, J. H., Davenport Huyer, L., Jekic, D., Wickeler, A., Naguib, H. E., Keller, G. M., Vunjak-Novakovic, G., … Radisic, M. (2019). A Platform for Generation of Chamber-Specific Cardiac Tissues and Disease Modeling. *Cell*, *176*(4), 913-927.e18. https://doi.org/10.1016/j.cell.2018.11.042

Zhao, Y., Rafatian, N., Wang, E. Y., Feric, N. T., Lai, B. F. L., Knee-Walden, E. J., Backx, P. H., & Radisic, M. (2020). Engineering microenvironment for human cardiac tissue assembly in heart-on-a-chip platform. *Matrix Biology*, *85–86*, 189–204. https://doi.org/10.1016/j.matbio.2019.04.001

Zimmermann, W. H., Schneiderbanger, K., Schubert, P., Didié, M., Münzel, F., Heubach, J. F., Kostin, S., Neuhuber, W. L., & Eschenhagen, T. (2002). Tissue Engineering of a Differentiated Cardiac Muscle Construct. *Circulation Research*, *90*(2), 223–230. https://doi.org/10.1161/hh0202.103644

Zipes, D. P., Jalife, J., & Stevenson, W. G. (2017). Cardiac Electrophysiology: From Cell to Bedside: Seventh Edition. In *Cardiac Electrophysiology: From Cell to Bedside: Seventh Edition*. https://doi.org/10.1161/01.cir.0000146800.76451.65

Zuppinger, C., Gibbons, G., Dutta-Passecker, P., Segiser, A., Most, H., & Suter, T. M. (2017). Characterization of cytoskeleton features and maturation status of cultured human iPSC-derived cardiomyocytes. *European Journal of Histochemistry*. https://doi.org/10.4081/ejh.2017.2763

9 Declaration of own contribution

The work was carried out in the institutes *Fraunhofer IGB* and *NMI Naturwissenschaftliches und Medizinisches Institut* under the supervision of Prof. Dr. Peter Loskill.

The study was designed by Alessia Moruzzi, experiments were carried out in collaboration with:
- Dr. Ing. Oliver Schneider: designed and established the resin-PDMS based fabrication process of the *Spheroflow HoC* with O_2 sensors, Easypace development, electrical field simulation. Spheroid formation, spheroid injection, electrical stimulation, sensor spot readout experiments published in Schneider et al., 2022 were a collaborative effort.

- Daniel Carvajal Berrio: Raman imaging and PCA analysis.

- Marina Shirokikh: HPLC data acquisition.

- Dr rer. nat. Simon Dreher: performed skeletal myocytes biopsy and skeletal muscles myobundle formation and culture; provided the developed protocol for the myocytes maturation; collaborated in the experimental procedures for tissue injection and culture on the *Spheroflow HoC*.

I certify that I have written the manuscript independently with the guidance of Prof. Dr. Peter Loskill and that I have not used any sources other than those indicated by me.

Tübingen, The

10 Publications

Arslan U., Moruzzi A., Nowacka J., Mummery C.L., Eckardt D., Loskill P., Orlova V.V., MICROPHYSIOLOGICAL STEM CELL MODELS OF THE HUMAN HEART, review, *Mater Today Bio*. 2022 March; 14: 100259. Doi: 10.1016/j.mtbio.2022.100259.

Schneider O., Moruzzi A., Fuchs S., Grobel A., Schulze H.S., Mayr T., Loskill P., Fusing Spheroids to Aligned µ-Tissues in a Heart-on-Chip Featuring Oxygen Sensing and Electrical Pacing Capabilities. *Mater Today Bio*. 2022 June; 15:100280. Doi: 10.1016/j.mtbio.2022.100280.

Moruzzi A., Shroff T., Keller S., Loskill, P., Cipriano M., Training the Next Generation of Researchers in the Organ-on-Chip Field. *Educ. Sci.* 2023 January; 13:144. Doi: 10.3390/educsci13020144.

Dreher S.I., Grubba P., von Toerne C., Moruzzi A., Maurer J., Goj T., Birkenfeld A.L., Peter A., Loskill P., Hauck S., Weigert C., Engineering of human myotubes towards a mature metabolic and contractile phenotype. (Submitted to American Journal of Physiology-Cell Physiology).

11 Acknowledgement

I would like to express my deepest gratitude to the individuals who have supported and guided me throughout my PhD journey. First and foremost, I am immensely grateful to Prof. Dr. Peter Loskill, my thesis supervisor, for his invaluable guidance, mentorship, and unwavering support throughout these three years. His expertise and wisdom have been instrumental in shaping my research and personal growth.

I would also like to extend my heartfelt appreciation to my co-supervisors, Prof. Dr. Christine Mummery from LUMC, Netherlands, and Prof. Dr. Robert Lukowski from the University of Tübingen. Their guidance, honest feedback, and collaborative spirit have greatly contributed to the success of this project.

I am deeply indebted to the entire µOrgano Lab for providing a stimulating and multidisciplinary environment that fostered growth, creativity, and diverse perspectives. I would like to acknowledge the contributions of Dr. Madalena Cipriano and Dr. Eduardo Bras, who served as mentors and provided invaluable insights and troubleshooting strategies. I am also grateful to Dr. Oliver Schneider for his camaraderie, inventive thinking, and the countless memorable pranks we shared during our first year. I extend my appreciation to the brilliant students in the lab, Henrike, Svenja, and Benedikt, whose quick learning abilities and dedicated efforts significantly advanced the project. The invaluable support of the laboratory staff scientists, Julia Roosz, Lena Scheying, and Cristhian Rojas, is also deeply appreciated. I would like to express my gratitude to my office mates, Tanvi Shroff, Katharina Schlünder, Fulya Ersoy, Matthijs van der Moolen, and Hannah Graf, for their friendship, cultural exchange, and for generously sharing delicious snacks from their home countries. Furthermore, I would like to thank Dr. Silke Keller, Elena Kromidas, Ibrahim Maulana Tengkyu, Dr. Claudia Teufel, Franziska Kern, Dr. Stefan Schneider, and all the other lab members for their support, camaraderie, and valuable advice.

I am immensely thankful to be part fo the EUROoCS ITN, and I would like to express my appreciation to Joanna Nowacka, Anders Tjell Orts, Mara Luchetti, Ulgu Arslan, and all my ITN companions for the shared experiences and the opportunity to learn from esteemed leaders in the field. I am grateful to Prof. Dr. Andries van der Meer, Dr. Susanne Brendler-Schwaab, Prof. Dr. Maria Tenje, Dr. Dominik Eckardt, and the numerous advisors who provided guidance to the ITN researchers.

I would like to extend my special thanks to my project collaborators: Stefanie Fuchs and Prof. Torsten Mayr from TU Graz for their assistance with oxygen sensors and troubleshooting integration in the platform and data readouts; Bilge Şen Elçi and Prof. Dr. Matthias Lütolf for hosting me at EPFL and imparting their knowledge on working with natural and synthetic hydrogels; Daniel Alejandro Carvajal Berrio and Dr. Julia Marzi for sharing their expertise in Raman spectroscopy; and Dr. Simon Dreher and Prof. Dr. Cora Weigert for actively contributing to the development of the skeletal muscle on chip proof-of-concept model.

I am grateful to Prof. Dr. Katja Schenke-Layland and Dr. Markus Wolperdinger, leaders of the NMI and Fraunhofer Institutes respectively, for creating productive work environments

that allowed me to focus entirely on my research as well as to Dr. Inka Montero and Dr. Lina Maria Cajamara for their invaluable support in navigating the program and bureaucracy of the Experimental Medicine PhD program at the University of Tübingen.

To my family and friends, Ada, Silvia, Maria-Anna, Bazzi, Adriano, Andrea, and my significant other, Mike, I am deeply grateful for their occasional distractions from work and their unwavering support and encouragement throughout this journey. I cannot forget to mention my long-lasting loyal Dungeon & Dragons companions, Claudio, David, Valerio, Chiara, and Sandro, who offered me a weekly escape from reality. Lastly, I want to express my heartfelt thanks to my cats (Pinky and Brain), whose unconditional love and nighttime cuddles and zoomies ensured that I never missed an opportunity to wake up during the night.